

Multiphase Flow Effects on Naphthenic Acid Corrosion of Carbon Steel

A dissertation presented to
the faculty of
the Russ College of Engineering and Technology of Ohio University

In partial fulfillment
of the requirements for the degree
Doctor of Philosophy

Nicolas Jauseau

December 2012

© 2012 Nicolas Jauseau. All Rights Reserved.

This dissertation titled
Multiphase Flow Effects on Naphthenic Acid Corrosion of Carbon Steel

by
NICOLAS JAUSEAU

has been approved for
the Department of Chemical and Biomolecular Engineering
and the Russ College of Engineering and Technology by

Srdjan Nesic
Professor of Chemical and Biomolecular Engineering

Dennis Irwin
Dean, Russ College of Engineering and Technology

ABSTRACT

NICOLAS JAUSEAU, Ph.D., December 2012, Chemical Engineering

Multiphase Flow Effects on Naphthenic Acid Corrosion of Carbon Steel

Director of Dissertation: Srdjan Nesic

Because of increasing oil prices and the continuous need for improving business margins, the refining industry faces new challenges by processing cheaper oils, such as "opportunity crudes". These usually contain higher amounts of corrosive sulfur compounds and naphthenic acids (NAP) which, at high velocity multiphase flow conditions, can impair the integrity of transfer lines in crude distillation units. Previous studies have shown that NAP corrosion is particularly aggressive in the presence of a liquid phase at the metal surface. Although the effect of flow was previously assessed in single-phase flow conditions, a high velocity multiphase flow has been suggested to occur in the transfer lines. Therefore, this study investigates the multiphase flow effect on NAP corrosion of carbon steel in the presence or absence of an iron sulfide corrosion product layer, at elevated temperature and fluid flow velocities, using a small-scale annular flow rig (AFR). In parallel, it examines the hydrodynamics of a multiphase flow mixture at room temperature and high flow velocities in a large-scale cold flow rig (CFR), in order to identify the flow patterns and their characteristics. A mechanistically derived gas-liquid two-phase flow model is additionally developed to predict the flow

regimes and related characteristics, and for its application to the operating conditions in the AFR to understand what may control the NAP corrosion rate.

Results show a multiphase flow effect on the NAP corrosion rate at superficial gas velocities in the range of 1–10 m/s, where a decrease in the corrosion rate by 60% occurred at a constant liquid velocity of 0.1 m/s and a total acid number of 2 mg KOH / g oil. The iron sulfide scale built during sulfidation conferred some protection in single phase flow, but none in multiphase flow. The main predicted flow patterns were: annular, stratified, intermittent and bubble. The oil wetting is suggested to be the main mechanism controlling pure NAP corrosion in multiphase flow; the dominant pattern in the AFR was most likely a mist flow, leading to lower wetted wall fractions and, consequently, reduced corrosion rates.

ACKNOWLEDGMENTS

I would like to express my gratitude to Professor Srdjan Nesic, my PhD advisor, for his guidance, encouragements and the relative freedom I had for conducting my own research during the course of this study. Even if he masters a broad scientific knowledge, being a recognized authority in the field of CO₂ corrosion, he is, at the same time, a warm, understanding and fair person who has encouraged me to express my ideas and exert my skills.

My appreciation goes to Valerie Young, Lauren McMills, Howard Dewald and Dusan Sormaz for accepting to serve as members in my dissertation committee, and also to the former committee members, Daniel Gulino and Martin Kordesch.

This study would not have been possible without the financial support from ExxonMobil Research and Engineering Company (EMRE). I would like to thank Alan Wolf, supervising the Naphthenic Acid Project, for his constant support and availability to discuss about the difficulties encountered along this research, Katie Walker for analyzing the oil samples and consultant Saul Blum (ex-EMRE) for the technical discussions and valuable suggestions related to corrosion.

I would also like to thank Dingrong Qu and Gheorghe Bota for their involvement in the Naphthenic Acid Project at the Institute of Corrosion and Multiphase Technology (ICMT), with a special mention of Gheorghe Bota for his help with the AFR work in 2009.

Many thanks I would like to address to the ICMT staff for technical support:

Bruce Brown, Marc Singer, Sonja Richter, Albert “Al” Schubert (thanks for our engaging talks about History too), Cody Shafer (thanks for your promptness and empathy during my daily work in the lab) and technicians Daniel Cain, John Goettge, Philip Bullington and Steve Upton who worked on my experimental loops. I am also grateful to Eddie Chalfant and Rebbeca “Becky” Gill for their administrative support and especially, to Deborah “Debbie” Bullington for her valuable help with the ICMT database. In particular, I am indebted to David Young for revising the manuscript of my dissertation.

My thankful thoughts also go to my colleagues whom I had the opportunity to meet and work with in the ICMT, particularly François Ayello, Marijan Babic, Christian Canto and Vanessa Fajardo.

I thank my parents, my sister and the rest of my family for their support and encouragements during these long years far away from them.

I dearly thank my wife, Loredana, for her patience, care, and support during this long journey.

TABLE OF CONTENTS

| | Page |
|---|------|
| Abstract..... | 3 |
| Acknowledgments..... | 5 |
| Table of Contents | 7 |
| List of Tables | 12 |
| List of Figures..... | 13 |
| CHAPTER 1 Introduction..... | 21 |
| CHAPTER 2 Literature Review and Research Objectives | 24 |
| 2.1 Naphthenic acids: properties and corrosion features..... | 24 |
| 2.2 Interactions between naphthenic acid and sulfidation corrosion phenomena..... | 27 |
| 2.3 Factors influencing naphthenic acid corrosion..... | 29 |
| 2.3.1 The corrosiveness of naphthenic acids..... | 29 |
| 2.3.2 The effect of sulfur compounds | 31 |
| 2.3.3 The effect of temperature | 33 |
| 2.3.4 The effect of physical state and boiling points..... | 34 |
| 2.3.5 The effect of test duration | 35 |
| 2.3.6 The effect of pressure | 36 |
| 2.3.7 The effect of metallurgy | 36 |
| 2.4 The flow effect on naphthenic acid corrosion..... | 38 |
| 2.4.1 NAP corrosion in transfer lines..... | 39 |
| 2.4.2 Experimental equipment | 40 |
| 2.4.3 Fluid velocity vs. wall shear stress..... | 43 |
| 2.4.4 NAP corrosion features in multiphase flow systems | 45 |
| 2.4.5 Multiphase flow modeling | 47 |
| 2.5 Research hypotheses and objectives | 48 |
| CHAPTER 3 Experimental Study of Corrosion | 52 |
| 3.1 Description of the Flow Through Mini Autoclave (FTMA)..... | 53 |

| | | |
|--|---|-----|
| 3.1.1 | Overview of the FTMA and its working fluids..... | 53 |
| 3.1.2 | Description of the FTMA test sections | 56 |
| 3.2 | Description of the Annular Flow Rig..... | 61 |
| 3.2.1 | Overview of the AFR and working fluids..... | 61 |
| 3.2.2 | Description of the AFR test sections..... | 67 |
| 3.3 | Revamping of the AFR | 71 |
| 3.3.1 | The history of the AFR until June 2008..... | 71 |
| 3.3.2 | New design of the AFR..... | 73 |
| 3.4 | Methodology | 82 |
| 3.4.1 | Definitions..... | 83 |
| 3.4.2 | Preparation of metal samples | 84 |
| 3.4.3 | Sulfidation (FTMA) | 85 |
| 3.4.4 | Pure NAP corrosion or challenge (AFR) | 90 |
| 3.4.5 | Presulfidation-challenge (FTMA-AFR)..... | 98 |
| 3.4.6 | Surface analysis of metal samples..... | 100 |
| 3.5 | Results and Discussion..... | 101 |
| 3.5.1 | Sulfidation corrosion..... | 101 |
| 3.5.2 | Pure NAP corrosion | 106 |
| 3.5.3 | Presulfidation-challenge corrosion..... | 130 |
| 3.6 | Summary | 140 |
| CHAPTER 4 Experimental Study of Hydrodynamics..... | | 141 |
| 4.1 | Overview of the Cold Flow Rig and working fluids..... | 141 |
| 4.2 | Description of the CFR test section..... | 144 |
| 4.3 | Instrument calibration | 147 |
| 4.4 | Experimental procedure for CFR experiments..... | 149 |
| 4.5 | Results and discussion..... | 151 |
| 4.5.1 | Flow patterns and entrainment onset..... | 152 |
| 4.5.2 | Flow characteristics..... | 156 |
| 4.6 | Summary | 161 |
| CHAPTER 5 Gas-Liquid Two-Phase Flow Modeling..... | | 162 |
| 5.1 | Description of flow patterns in multiphase flow..... | 162 |
| 5.1.1 | Stratified flow..... | 162 |

| | | |
|-------|--|-----|
| 5.1.2 | Annular-dispersed flow | 164 |
| 5.1.3 | Intermittent flow | 166 |
| 5.1.4 | Bubble flow | 167 |
| 5.2 | Friction model | 168 |
| 5.2.1 | Definition of the Reynolds number | 168 |
| 5.2.2 | Correlations for gas-wall friction factors | 169 |
| 5.3 | Predictions of flow pattern transitions | 170 |
| 5.3.1 | Introduction | 170 |
| 5.3.2 | Transition stratified/non-stratified..... | 172 |
| 5.3.3 | Transition stratified/annular at steep downward inclinations | 173 |
| 5.3.4 | Transition stratified-smooth/stratified-wavy..... | 174 |
| 5.3.5 | Transitions from bubbly flow..... | 175 |
| 5.3.6 | Transitions from dispersed bubble | 177 |
| 5.3.7 | Transitions annular / intermittent | 180 |
| 5.4 | Modeling of the entrainment onset transition | 182 |
| 5.4.1 | Description of droplets entrainment mechanisms | 182 |
| 5.4.2 | Definition of the entrainment onset..... | 184 |
| 5.4.3 | Modeling of the entrainment onset transition | 185 |
| 5.4.4 | Limiting cases | 189 |
| 5.5 | Modeling of the stratified flow..... | 190 |
| 5.5.1 | Model “Taitel Dukler Modified” (TDM) | 191 |
| 5.5.2 | Model “Low liquid Loading” (LLL)..... | 195 |
| 5.5.3 | Stability analysis on a multiple roots system | 199 |
| 5.6 | Modeling of the annular flow | 200 |
| 5.6.1 | Momentum balance equations..... | 200 |
| 5.6.2 | Definition of geometrical properties | 201 |
| 5.6.3 | Calculations of shear stresses and in situ velocities | 202 |
| 5.6.4 | Friction factors correlations | 203 |
| 5.6.5 | Entrainment fraction correlations..... | 204 |
| 5.6.6 | Determination of pressure drop and holdup | 207 |
| 5.7 | Modeling of the bubble flow | 207 |
| 5.7.1 | Dispersed bubble flow..... | 208 |
| 5.7.2 | Bubbly flow..... | 209 |

| | |
|--|-----|
| | 10 |
| 5.8 Modeling of the intermittent flow (slug flow) | 210 |
| 5.8.1 Mass Balances | 213 |
| 5.8.2 Hydrodynamics in the film region | 214 |
| 5.8.3 Hydrodynamics in the slug region..... | 215 |
| 5.8.4 Closure relationships | 216 |
| 5.8.5 Calculation of lengths LU and LF | 218 |
| 5.8.6 Determination of holdup and pressure drop over the slug unit | 218 |
| 5.8.7 Liquid slug frequency..... | 219 |
| 5.8.8 Direction of the liquid film in slug flow | 219 |
| 5.9 Structure of the flow model..... | 220 |
| CHAPTER 6 Flow Model Results and Validation | 228 |
| 6.1 The gas-liquid two-phase flow database | 228 |
| 6.2 Statistical tools | 230 |
| 6.3 Evaluation of flow pattern prediction models | 231 |
| 6.3.1 Evaluation of the FLOPAT model | 231 |
| 6.3.2 Evaluation of the entrainment onset model..... | 239 |
| 6.4 Evaluation of flow pattern models | 243 |
| 6.4.1 Stratified flow model..... | 244 |
| 6.4.2 Annular flow model | 249 |
| 6.4.3 Intermittent flow model..... | 252 |
| 6.4.4 Bubble flow model | 255 |
| 6.5 Summary | 256 |
| CHAPTER 7 Corrosion Model Validation | 258 |
| 7.1 Description of the corrosion model..... | 258 |
| 7.2 Model evaluation..... | 260 |
| 7.2.1 Prediction of the sulfidation corrosion rate | 263 |
| 7.2.2 Prediction of the pure NAP corrosion rate | 264 |
| CHAPTER 8 Conclusions and Recommendations | 269 |
| References..... | 277 |
| Nomenclature | 295 |

| | | |
|------------|--|-----|
| APPENDIX A | Procedure of Processing Metal Samples for SEM/EDX Analyses | 302 |
| APPENDIX B | Chemical Analysis of Oil Samples | 308 |
| APPENDIX C | Uncertainty Analysis of the AFR and CFR Experiments | 312 |
| APPENDIX D | Sulfidation Experimental Data (FTMA)..... | 315 |
| APPENDIX E | Pure NAP Corrosion Experimental Data (AFR)..... | 316 |
| APPENDIX F | Presulfidation-Challenge Experimental Data (FTMA – AFR)..... | 319 |
| APPENDIX G | Calculation of the Superficial Gas Velocity (AFR)..... | 321 |
| APPENDIX H | Calculation of the Superficial Liquid Velocity (AFR) | 324 |
| APPENDIX I | Calibration Curves of the Superficial Gas Velocity (CFR) | 326 |
| APPENDIX J | Study of Hydrodynamics – Experimental Data (CFR)..... | 327 |

LIST OF TABLES

| | Page |
|---|------|
| Table 3.1: Physical properties of the fluids used in the corrosion study. | 55 |
| Table 3.2: Test matrix for sulfidation reference experiments. | 90 |
| Table 3.3: Test matrix for pure NAP corrosion experiments. | 97 |
| Table 3.4: Test matrix for presulfidation-challenge experiments. | 100 |
| Table 3.5: Average corrosion rates due to sulfidation. | 103 |
| Table 3.6: Flow conditions encountered in different flow loops for pure NAP corrosion tests (TAN 4). | 126 |
| Table 4.1: The CFR test matrix for air-water experimental cases (EO is the Entrainment Onset). | 151 |
| Table 6.1: The gas-liquid two-phase flow database. | 229 |
| Table 6.2: Flow pattern predictions using Shoham's (1982) experimental data. | 232 |
| Table 6.3: Flow pattern predictions of other datasets than Shoham's. | 238 |
| Table 6.4: Experimental data used for the entrainment onset model validation. | 240 |
| Table 6.5: Performance evaluation of the entrainment onset model. | 241 |
| Table 6.6: Validation data for each flow pattern model. | 243 |
| Table 6.7: Performance evaluation of the stratified flow model. | 244 |
| Table 6.8: Performance evaluation of the annular flow model. | 249 |
| Table 6.9: Performance evaluation of the intermittent flow model. | 253 |
| Table 6.10: Overall performance of the gas-liquid two-phase flow model. | 257 |
| Table 7.1: Experimental conditions for sulfidation used for corrosion model validation. | 262 |
| Table 7.2: Experimental conditions for pure NAP corrosion used for corrosion model validation. | 262 |
| Table 7.3: Flow characteristics conditions encountered in the autoclave, the FTMA, and the AFR. | 262 |

LIST OF FIGURES

| | Page |
|---|------|
| Figure 2.1: Examples of chemical structures of naphthenic acid molecules. | 25 |
| Figure 3.1: Overview of the Flow Through Mini-Autoclave flow (Kanukuntla, 2008)... | 54 |
| Figure 3.2: True boiling point curve of a commercial naphthenic acids mixture (data from Wolf, 2010b)..... | 56 |
| Figure 3.3: External view of the set up used in the FTMA for presulfidation (May–December 2010)..... | 57 |
| Figure 3.4: Internal structure of the test section (Figure 3.3) with temperature measurement set up (May–December 2010). The samples are within the yellow spacers in this design. | 58 |
| Figure 3.5: Overview of the FTMA test section set up used during the test NJ18 (February 2011). Samples and test sections are named according to their position or function in the AFR (Figure 3.14)..... | 59 |
| Figure 3.6: Overview of the FTMA test section used for tests NJ19–NJ50. Samples and test sections are named according to their position or function in the AFR (Figure 3.14). The zoom view represents the cross section of the thermocouple inserted in the multiphase flow test section #1..... | 60 |
| Figure 3.7: Cross section of the multiphase flow test section (only the straight part) with heating element (red coil) and insulation layers. Heat was provided to the samples through the spacers by heat transfer. | 61 |
| Figure 3.8: Overview of the Annular Flow Rig (front view). Note that the acid injection system is not included in this drawing..... | 63 |
| Figure 3.9: Overview of the Annular Flow Rig using a recycling set up for the liquid phase (rear view)..... | 64 |
| Figure 3.10: Process and Flow Diagram of the Annular Flow Rig (with liquid recycling). | 65 |
| Figure 3.11: Process and Flow Diagram of the Annular Flow Rig (without liquid recycling) used for testing with pure NAP naphthenic acids injection in the saturation column..... | 66 |
| Figure 3.12: Overview of the single oil phase and multiphase flow test sections as within January–June 2010 (adapted from Bota, 2010a). | 67 |
| Figure 3.13: Overview of the single oil phase and multiphase flow test sections: (a) July–August 2010; (b) September 2010–January 2011. | 68 |
| Figure 3.14: Overview of the single oil phase and multiphase flow test sections as in March 2011–March 2012. | 69 |

| | |
|---|-----|
| Figure 3.15: (a) Details of the gas-liquid mixing section using the 1/8” annulus design during April 2008–August 2010. (b) Overview of the gas-liquid mixing section as after September 2010..... | 70 |
| Figure 3.16: Corrosion rates before (NJ09) and after (NJ11) changes in the mixing section..... | 70 |
| Figure 3.17: Overview of the Annular Flow Rig during 2006–2008 (adapted from Schubert, 2008). A zoom shows the mixing and the test sections as they were in Spring 2008 (adapted from Qu, 2008)..... | 72 |
| Figure 3.18: Overview of the saturation column (left) with a zoom on the gas inlet. Column cross section with temperature probes and heater (right). | 75 |
| Figure 3.19: Overview of the vessel used to preheat the oil phase in the AFR (left). The column cross section showing the temperature probes and heating element (right). | 78 |
| Figure 3.20: Overview of the Annular Flow Rig control panel..... | 79 |
| Figure 3.21: The acid injection system set up in the research facility..... | 80 |
| Figure 3.22: The AFR set up after coolers: (a) with liquid recycling; (b) without liquid recycling and with oil sampling device (zoom view). Green arrows indicate the flow direction..... | 81 |
| Figure 3.23: Exploded view of a carbon steel sample with its compression fittings..... | 85 |
| Figure 3.24: Process and Flow Diagram of the Flow Through Mini-Autoclave (FTMA). | 86 |
| Figure 3.25: The set up used to inject the Clarke solution (HCl) and the DI water (water) in the sample without altering its outer surface. | 88 |
| Figure 3.26: Calibration of the actual liquid flow rate delivered by a Zenith pump B9000-9.0 cc/rev..... | 93 |
| Figure 3.27: Modification and transfer of the single phase (green dashed line) and multiphase flow test sections (red dashed line) from the FTMA set up (a) to the AFR set up (d). The FTMA test section was split in two main parts (a to b). The multiphase flow test section was readjusted (b to c) before insertion in the AFR with the single phase test section (c to d). | 98 |
| Figure 3.28: Longitudinal (a) and radial (b) cross sections of a CS sample used in the SEM/EDX surface analysis. | 101 |
| Figure 3.29: Corrosion rates measured during the sulfidation process in the FTMA. Averages ($n \leq 7$) are reported by sample type or ID as it was used in experiments. The error bars represent 2 standard deviations. | 103 |
| Figure 3.30: Longitudinal cross-section of a CS sample (magnified 1000X). The FeS scale was built with yellow oil in the FTMA for 24 hrs and at 316 °C. | 104 |

- Figure 3.31: Longitudinal cross-section of a CS sample (magnified 5000X). (a) SEM picture; (b) backscattering. The FeS was built with yellow oil in the FTMA for 24 hrs and at 316 °C. 105
- Figure 3.32: (a) EDX analysis across the longitudinal cross-section of a CS sample. The FeS scale was built with yellow oil in the FTMA for 24 hrs and at 316 °C. (b) Equivalent EDX analysis re-plotted with absolute values showing that oxygen content is only an artifact. 106
- Figure 3.33: Temperature control on the corrosion rate check in the test sections. The experiments NJ09 and NJ10 were run at the respective temperatures of 318 °C and 282 °C. 108
- Figure 3.34: The inhibiting effect of corrosion by-products (iron concentration) on NAP corrosion. 109
- Figure 3.35: Evolution of the TAN concentration loss in the saturation column, before and after experiments. 111
- Figure 3.36: TAN and Fe concentrations in the multiphase flow mixture measured at the outlet of the AFR during an experiment (NJ48). 112
- Figure 3.37: TAN concentrations of a multiphase flow mixture measured at the outlet of the AFR during experiments NJ48 and NJ50. 115
- Figure 3.38: Iron concentrations of a multiphase flow mixture measured at the outlet of the AFR during experiments NJ48 and NJ50. 116
- Figure 3.39: Measurements of corrosion rates for different acid media in the saturation column. Superficial gas and liquid velocities are 10 and 0.1 m/s for each condition. 116
- Figure 3.40: Corrosion rates measured using non-presulfided samples with different geometries and TAN concentrations. The multiphase flow conditions are $U_{SG} = 20$ m/s; $U_{SL} = 0.1$ m/s. For a better visualization, the multiphase flow corrosion rates are slightly displaced to the left and right from the corresponding tick mark of TAN (actually, they overlap). 118
- Figure 3.41: Corrosion rates measured using non-presulfided samples with different geometries at different superficial gas velocities. Measurements were performed with a concentration TAN 2 and a superficial liquid velocity of 0.1 m/s. Corrosion rates in elbows are slightly displaced to the right of the gas velocity tick mark for a better visualization (they actually overlap with the ones from straight samples). 120
- Figure 3.42: Flow map of a CO₂ / White oil mixture at P = 3.8 bar, T = 343 °C using a ¼” horizontal line. The point marks represent different multiphase flow conditions used in the AFR. 122
- Figure 3.43: Corrosion rates measured on straight samples in multiphase flow and predicted entrainment fraction of liquid droplets vs. superficial gas velocity... 123

- Figure 3.44: Corrosion rates under multiphase flow conditions at different superficial liquid velocities..... 125
- Figure 3.45: Corrosion rates by flow loops. Results are from single phase and multiphase flow conditions (TAN 4 and 343 °C). 127
- Figure 3.46: Corrosion rates measured using presulfided samples of different geometry and TAN concentrations. In multiphase flow, $U_{SG} = 20$ m/s and $U_{SL} = 0.1$ m/s. Corrosion rates displayed at TAN 0.1 represent the average sulfidation corrosion rate in the FTMA. (The point-values are slightly displaced to the left or right of the TAN corresponding tick mark for a better visualization; the actual point-values overlap). 131
- Figure 3.47: Corrosion rates measured in single phase flow conditions ($U_{SL} = 0.1$ m/s) at different TAN concentrations using non-presulfided (hollow marks) and presulfided (full marks) samples. 133
- Figure 3.48: Corrosion rates measured in multiphase flow conditions ($U_{SG} = 20$ m/s; $U_{SL} = 0.1$ m/s) at different TAN concentrations using non-presulfided (hollow marks) and presulfided (full marks) samples and various piping geometries. 134
- Figure 3.49: Corrosion rates expressed as a function of the superficial gas velocity using a TAN 2 solution and presulfided samples of various piping geometry in multiphase flow. The corrosion rate at $U_{SG} = 0$ m/s was measured in single phase flow conditions. 135
- Figure 3.50: SEM images (magnified 1000X) showing the radial cross-sections of a CS sample: (a) bottom; (b) top. The FeS scale was formed with yellow oil in the FTMA for 24 hrs at 316 °C, then challenged in the AFR by a TAN 2 solution for 6 hrs at 343 °C in multiphase flow conditions ($U_{SG} = 10$ m/s; $U_{SL} = 0.1$ m/s). 137
- Figure 3.51: SEM images magnified 4000X to see in detail the radial cross-sections of a CS sample from Figure 3.50. 137
- Figure 3.52: Backscattered images (magnified 4000X) showing the radial cross-sections of a CS sample: (a) bottom; (b) top. The FeS scale was formed with yellow oil in the FTMA for 24 hrs at 316 °C, then challenged in the AFR by a TAN 2 solution for 6 hrs at 343 °C in multiphase flow conditions ($U_{SG} = 10$ m/s; $U_{SL} = 0.1$ m/s). The thickness measurements appear in orange. 138
- Figure 3.53: (a) EDX analysis across the top of the radial cross-section of the CS sample presented in Figure 3.51. (b) The equivalent EDX analysis re-plotted with absolute values showing that the oxygen content of the scale at this location of the sample is only an artifact. 139
- Figure 3.54: SEM image (magnified 4000X) of a longitudinal cross section of a CS sample: (a) typical SEM view; (b) backscattered SEM image with marked thickness measurements. The FeS scale was formed with yellow oil in the FTMA for 24 hrs at 316 °C, then challenged in the AFR by a TAN 2 solution for 6 hrs at 343 °C in multiphase flow conditions ($U_{SG} = 10$ m/s; $U_{SL} = 0.1$ m/s). 139

| | |
|---|-----|
| Figure 4.1: Overview of the Cold Flow Rig with a zoom on the gas-liquid separation. | 142 |
| Figure 4.2: Process and flow diagram of the Cold Flow Rig..... | 143 |
| Figure 4.3: Set up of the conductivity probes at the pipe wall, connected to the circuit board (in the background)..... | 145 |
| Figure 4.4: Borescope setup in the CFR. The PVC deflector (black) protecting the borescope camera from liquid droplets (lower left corner). | 146 |
| Figure 4.5: Longitudinal and radial views of the collector mouths placed at the extremity of the inner pipe in the gas-liquid separation section. | 147 |
| Figure 4.6: The CFR test matrix superimposed on an air-water flow map in horizontal flow using a 0.154 m pipe diameter..... | 151 |
| Figure 4.7: The 6-step droplets entrainment-deposition mechanism of the flow transition stratified to annular-dispersed. The pipe cross sections are: stratified-wavy flow (a), droplets atomization (b), droplets deposition (c), formation of liquid rivulets (d), continuous liquid film built along the top of the pipe wall (d/e), annular-dispersed flow (f)..... | 153 |
| Figure 4.8: Experimental observations represented on a flow pattern map of an air / water mixture in a 0.154 m horizontal pipe..... | 155 |
| Figure 4.9: Experimental measurements of the entrainment onset..... | 155 |
| Figure 4.10: The pressure drop ΔP trends at different superficial liquid velocities. | 156 |
| Figure 4.11: Wettability measurements at the inner wall of the pipe (red = wet, blue = dry) for a superficial gas velocity range of 15–55 m/s and at a constant liquid flow rate $Q_L = 18.92$ L/min. The liquid level at the bottom is expressed as the liquid height h_L | 157 |
| Figure 4.12: The wetted wall fraction θ_L at different superficial liquid velocities..... | 158 |
| Figure 4.13: The liquid height at the bottom of the pipe h_0 at different superficial liquid velocities..... | 159 |
| Figure 4.14: The entrainment fraction FE at different superficial liquid velocities. | 160 |
| Figure 5.1: Representation of stratified and intermittent flow patterns observed at horizontal and near horizontal pipe inclinations (adapted from Shoham (2006). © 2006 Society of Petroleum Engineers) | 163 |
| Figure 5.2: Representation of annular-dispersed (annular and wavy-annular) and dispersed-bubble flow patterns observed at horizontal and near horizontal pipe inclinations (adapted from Shoham (2006). © 2006 Society of Petroleum Engineers)..... | 164 |
| Figure 5.3: Representation of flow patterns observed at vertical and sharply vertical pipe inclinations (adapted from Shoham (2006). © 2006 Society of Petroleum Engineers)..... | 165 |

| | |
|---|-----|
| Figure 5.4: Air-water flow map at standard conditions in horizontal flow with a 0.154 m pipe diameter. | 173 |
| Figure 5.5: Air-water flow map at standard conditions in downward flow ($\beta = -70^\circ$) with a 0.154 m pipe diameter..... | 174 |
| Figure 5.6: Air-water flow map at standard conditions in upward flow ($\beta = +70^\circ$) with a 0.154 m pipe diameter. | 177 |
| Figure 5.7: Mechanisms of droplets formation: (a) bubble burst and (b) droplet impingement at the gas-liquid interface (reprinted with permission from Ishii and Grolmes (1975). © 1975 American Institute of Chemical Engineers)..... | 183 |
| Figure 5.8: Mechanisms of droplets formation by wave entrainment: (a) wave coalescence, (b) wave undercutting, (c) ripple wave shearing-off (reprinted with permission from Han and Gabriel (2007). © 2007 American Society of Mechanical Engineers). | 183 |
| Figure 5.9: Top view (a) and side view (b) of a wave (adapted from Mantilla, 2008)... | 185 |
| Figure 5.10: Geometry of the pipe cross section in a stratified flow pattern..... | 192 |
| Figure 5.11: Geometry of the pipe cross section of the annular flow pattern (liquid droplets entrained in the gas core are not shown here)..... | 202 |
| Figure 5.12: Longitudinal pipe cross section illustrating the slug flow pattern (reprinted from Shoham (2006). © 2006 Society of Petroleum Engineers)..... | 211 |
| Figure 5.13: General structure of the flow model..... | 221 |
| Figure 5.14: Algorithm of the entrainment onset model..... | 223 |
| Figure 5.15: Algorithms of the stratified flow model using and the LLL approach (left) and the TDM approach (right)..... | 224 |
| Figure 5.16: Algorithm of the annular flow model..... | 225 |
| Figure 5.17: Algorithms of the dispersed-bubble (left) and the bubbly (right) flow models..... | 226 |
| Figure 5.18: Algorithm of the intermittent (slug) flow model..... | 227 |
| Figure 6.1: Flow pattern maps for downward inclinations (-90° , -5° , -1°) of a 0.051 m pipe diameter at standard conditions. The points represent experimental observations of flow patterns. The transitions lines are generated with the FLOPAT model. | 234 |
| Figure 6.2: Flow pattern maps for upward inclinations ($+1^\circ$, $+5^\circ$, $+90^\circ$) of a 0.051 m pipe diameter at standard conditions. The points represent experimental observations of flow patterns. The transitions lines are generated with the FLOPAT model..... | 235 |
| Figure 6.3: Flow pattern maps for horizontal pipes of 0.051 m and 0.025 m diameters at standard conditions. The points represent experimental observations of flow patterns. The transitions lines are generated by the FLOPAT model..... | 236 |

- Figure 6.4: The effect of pipe diameter on flow pattern transitions using the same conditions encountered in the AFR (CO₂ / Tufflo mixture at T = 343 °C and P = 377 kPa). The operating conditions in transfer lines of oil refineries are contained in the red rectangle..... 237
- Figure 6.5: Experimental measurements of the entrainment onset (this work) plotted on a flow map with entrainment onset predictions generated by the model in this study and another model from literature 240
- Figure 6.6: Comparison between predicted and experimental entrainment onset values expressed as superficial gas velocity U_{SG}..... 242
- Figure 6.7: Comparison between predicted and measured pressure drop in stratified flow conditions (Data source: Table 6.1, Ref. Nr. 2-3; 6; 9; 11; 13-14; 20; 24). 246
- Figure 6.8: Comparison between predicted and measured liquid holdup in stratified flow conditions (Data source: Table 6.1, Ref. Nr. 1; 3; 6; 8-9; 14-16; 20)..... 246
- Figure 6.9: Comparison between predicted and measured wetted wall fraction in stratified flow conditions (Data source: Table 6.1, Ref. Nr. 6; 14; 24). 247
- Figure 6.10: Comparison between predicted and measured liquid height in stratified flow conditions (Data source: Table 6.1, Ref. Nr. 2; 6; 13; 14; 24). 248
- Figure 6.11: Comparison between predicted and measured pressure drop in annular flow conditions (Data source: Table 6.1, Ref. Nr. 2-3; 9; 11-14; 24)..... 250
- Figure 6.12: Comparison between predicted and measured liquid holdup in annular flow conditions (Data source: Table 6.1, Ref. Nr. 1; 3; 8-9; 12; 14; 16)..... 251
- Figure 6.13: Comparison between predicted and measured entrainment fraction in annular flow conditions (Data source: Table 6.1, Ref. Nr. 5; 10-14; 17; 22-24). 252
- Figure 6.14: Comparison between predicted and measured pressure drop in intermittent flow conditions (Data source: Table 6.1, Ref. Nr. 2-3; 7; 9-11)..... 254
- Figure 6.15: Comparison between predicted and measured liquid holdup in intermittent flow conditions (Data source: Table 6.1, Ref. Nr. 1; 3; 7-9; 16)..... 254
- Figure 6.16: Comparison between predicted and measured liquid holdup in bubble flow conditions (Data source: Table 6.1, Ref. Nr. 3-4; 8). 256
- Figure 7.1: Corrosion processes occurring at the metal surface in naphthenic acid (RCOOH) and organo-sulfur compounds (RS) containing environments (adapted from Nesic and Qu, 2008). 260
- Figure 7.2: Overview of the inputs window of Crudecorp V5.1 for single phase flow conditions..... 261
- Figure 7.3: Sulfidation corrosion rates as a function of temperature. Experimental data were measured in autoclave and in the FTMA using either Kanukuntla (2008) set up or this study's set up (tubing samples). 263

- Figure 7.4: Pure NAP corrosion rates as a function of TAN concentration in autoclaves and FTMA operating conditions..... 265
- Figure 7.5: Pure NAP corrosion rates as a function of TAN concentration. Measurements were taken in the AFR in single phase and multiphase flow conditions (superficial velocities $U_{SG} = 20$ m/s; $U_{SL} = 0.1$ m/s)..... 266
- Figure 7.6: Pure NAP corrosion rates expressed as a function of the in situ oil velocity. Experiments were performed in the AFR with a liquid flow rate $Q_L = 80$ mL/min. The corrosion rate corresponding to the in situ velocity $U_L = 0.1$ m/s represents single phase flow conditions..... 268

CHAPTER 1 INTRODUCTION

The processing of petroleum fluids in oil refineries has become an increasingly challenging task due to the combined strains exerted by high oil prices and a lower world demand for refined products, as well as a continuous need for maintaining or improving the refining margins. As a direct consequence of this economic situation, refiners have looked to the processing of cheaper crude oils, also called “opportunity crudes”. However, these crudes are usually characterized by higher sulfur and/or naphthenic acid contents, which can promote sulfidation (or sulfidic) corrosion and naphthenic acid (NAP) corrosion at processing temperatures. Although NAP corrosion has been combated by refiners for almost a century (Derungs, 1956), NACE International¹ still has not issued a standard documenting in depth this problem (as was done for sulfidation or overhead corrosion). Likewise, NAP corrosion can endanger the integrity of the refinery assets, as for example, the crude distillation units (CDU)².

Some locations of the CDU, such as the atmospheric and vacuum transfer lines, and particularly the bends, can experience severe NAP corrosion in multiphase flow conditions at high flow velocities. To date, refiners (Gutzeit, 1977) have only guessed which flow conditions might occur in the pipe in order to design the transfer lines, but no systematic investigation was pursued to confirm this point. Only a few experimental

¹ NACE® International is the largest professional organization dedicated to the study and control of all kinds of corrosion.

² Another main corrosion process (NACE International, 2009), called *Overhead Corrosion*, mainly due to the hydrolysis of magnesium and calcium chloride salts forming hydrochloric acid (HCl), also occurs in crude distillation units but at a much lower range of temperatures. Therefore, it is not considered in the present study.

studies (Kane and Cayard, 2002; Wu et al., 2002) have focused on the flow effect, but the flow conditions were always limited to a single liquid phase using a jet impingement device through which the liquid phase could impinge on the surface of the metal samples. This approach virtually ignored the co-existing multiphase flow conditions in transfer lines, and so, omitted the effect that a liquid phase impinging on the wall of the pipe could have on the corrosion rate. Therefore, the aims of this study are to closely reproduce the flow conditions occurring in transfer lines of oil refineries in order to study the effect of a multiphase flow mixture on NAP corrosion of carbon steel at high flow velocities and temperature. Furthermore, as an additional goal, the presence of a gas-oil mixture necessitates the characterization of the flow hydrodynamics existing in the pipe, which can be approached in a larger-scale rig, where a similar two-phase flow can be safely and simply visualized at room temperature. Results from this research project can inform corrosion management decisions dealing with particular opportunity crudes in transfer lines of oil refineries.

This dissertation is divided into eight chapters and multiple appendices. The next chapter comprises an extensive literature review about naphthenic acids and their properties, their possible interactions with sulfur compounds in refining processes, the main factors controlling NAP corrosion and on flow effects; the research goals and objectives of this work are presented at the end of the chapter. The third chapter describes the equipment used and related designs, as well as the experimental methodologies employed during the corrosion study to evaluate the NAP corrosion of carbon steel using a multiphase flow mixture at high temperature. The results are presented and discussed at

the end of the chapter. The fourth chapter centers on the hydrodynamic study, describing the equipment design and operation, as well as characterizing the main features of a multiphase flow mixture occurring at similar flow conditions to those encountered in transfer lines of oil refineries. Different flow parameters are recorded during the flow experiments and discussed. The following three chapters deal with the modeling work. The fifth chapter is entirely dedicated to the conception and development of a gas-liquid two-phase flow model, the mechanisms involved, the assumptions made and the model architecture. Given the complexity of the model, the sixth chapter is entirely assigned for its validation and performance evaluation using experimental data produced during this work or from other data sources. Aside from the flow model, the modeling work is extended in the seventh chapter by including corrosion rate predictions using an existing refining corrosion simulator, which was tested against corrosion data produced in this work. The dissertation closes with the eighth chapter, concluding about the work done in this study and its applicability and offering some recommendations and guidelines for future research.

Given the increasing use of opportunity crudes that are highly sour, derived from oil sands or have high acidity, the research described in this dissertation will have significant utility in not just corrosion management but materials selection for refinery design.

CHAPTER 2 LITERATURE REVIEW AND RESEARCH OBJECTIVES

Two types of corrosion processes may occur in crude distillation units of oil refineries at high temperatures: *naphthenic acid corrosion* and *sulfidation corrosion*. In this study, the operating temperature range is between 200 and 450 °C, excluding the ash fuel and oxidation corrosion that usually occur at much higher temperatures.

Based on the reviewed literature, this chapter introduces the theory beyond the naphthenic acids compounds and naphthenic acid (NAP) corrosion. The chapter further develops on the interaction between naphthenic acids and sulfur compounds to emphasize this effect on the corrosiveness of naphthenic acids. Then, the main factors controlling the NAP corrosion of steel are discussed. A particular attention in this work was given to the effect of flow on NAP corrosion from two different perspectives, experimental and modeling; hence, the chapter treats this subject separately from the other factors influencing corrosion. The emergent questions from literature and the main objectives of this research are formulated at the end of this chapter.

2.1 Naphthenic acids: properties and corrosion features

The term *naphthenic acids* refer to a broad family of organic acids containing the functional carboxylic group COOH. Their molecules can be expressed by the chemical formula $R - (CH_2)_n - COOH$. These organic acids generally contain two to six saturated rings, each consisting of five or six carbon atoms (Figure 2.1). The naphthenic acids have

a density close to that of water ($d = 0.98$) and are insoluble in water, but very soluble in organic solvents (i.e., toluene). Their flash points vary from 138 to 180 °C.

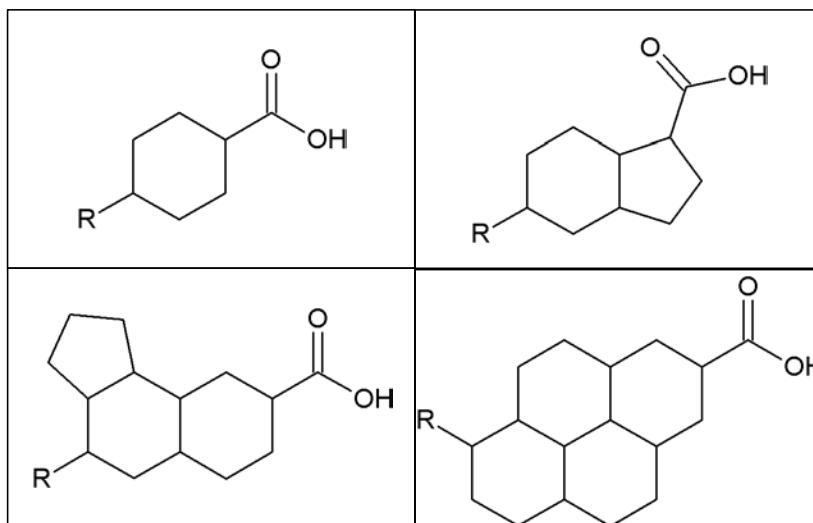


Figure 2.1: Examples of chemical structures of naphthenic acid molecules.

The molecular weights of naphthenic acids can vary greatly from 150 to 900 g/mol with a peak around 200–400 g/mol (Derungs, 1956; Piehl, 1988). As a comparison, the commercial naphthenic acids have much narrower ranges of molecular weights (Hsu et al., 2000) since they are extracted from petroleum distillates (mainly kerosene, light gas oil and heavy gas oil) boiling at temperatures, such as 180–360 °C (Jones and Pujado, 2006). Besides such a variety of existing chemical structures, the crude oils can also contain a very large number of naphthenic acid species of unknown molecular structure. For example, Seifert's (1975) study revealed the presence of around 1500 NAP compounds in a California crude demonstrating the complexity of characterizing their properties. Different analytical techniques, based on mass spectrometry (MS), have been

used to assess the distribution of NAP molecular weights, such as chemical ionization (Dzidic et al., 1988; Hsu et al., 2000), atmospheric pressure chemical ionization (APCI–MS) (Hsu et al., 2000), Fourier transform ion cyclotron resonance (FTICR–MS) (Barrow et al., 2003), electrospray ionization (ESI–MS) (Clemente and Fedorak, 2005; Qian et al., 2008; Rogers et al., 2002).

NAP corrosion can occur in many locations of the crude distillation units, such as furnace tubes, side cut pipings, reboilers, pumps, the lower section of atmospheric towers, the vacuum tower, internals of distillation towers (packing, trays), bottom heat exchangers, and vacuum and atmospheric transfer lines, particularly in bends (Blanco F. and Hopkinson, 1983; Slavcheva et al., 1999).

Corrosion conditions are so aggressive that only a “tarnish film” can be observed at the steel surface (Babaian-Kibala et al., 1993). At these locations, the morphology of the metal surface shows the signs of localized attacks. The patterns have the appearance of “sharp-edged holes” in quiescent flow conditions, but become more like “sharp-edged streamlined grooves” in higher flow velocity areas (Derungs, 1956; Jayaraman et al., 1986). In other cases, such as condensed vapor regions, the surface morphology looked like an “orange peel” due to the thinning of the metal (Babaian-Kibala et al., 1993).

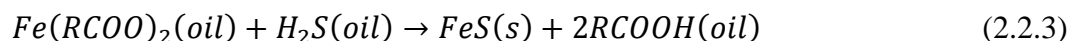
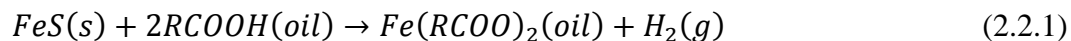
The corrosion conditions and surface morphology described above can be observed if the naphthenic acids are the only corrosive species present in the processed fluid. In oil refining, other species can be present and interact with naphthenic acids, such as sulfur compounds. Such interactions can be described by other corrosion mechanisms than that of pure NAP corrosion.

2.2 Interactions between naphthenic acid and sulfidation corrosion phenomena

In oil refining, the NAP and sulfidation corrosion phenomena cannot be easily distinguished due to multiple chemical interactions existing between the two processes. It has been widely recognized that the natural presence of sulfur compounds in crude oils may inhibit NAP corrosion at the steel surface (Hau, 2009; Slavcheva et al., 1999). Compared to NAP corrosion, sulfidation corrosion can generate a uniform iron sulfide scale (FeS) at the steel surface that confers some degree of protection against the naphthenic acids. Babaian-Kibala et al. (1993) pointed out three possible interactions between NAP and sulfidation corrosions. Craig (1996) developed further this concept and classified these interactions into three types. Type I corresponds to a pure NAP corrosion situation characterized by either the absence of a film or, at best, the presence of a very thin film at the steel surface. Type II characterizes the sulfidation corrosion in the presence of a reduced concentration of naphthenic acids. Type III represents the case of NAP corrosion inhibited by the presence of sulfur compounds. At given operating conditions, Type I would be considered as the worst case scenario in terms of corrosion rate. Types II and III would represent the respective domains of predominance of sulfidation corrosion and NAP corrosion.

Both corrosion mechanisms can simultaneously exist in oil refineries and, therefore, are concurrent. Although the mechanisms are not very well understood, many authors generally agree upon the dominant chemical reactions (Babaian-Kibala et al., 1993; Slavcheva et al., 1999). The naphthenic acids $RCOOH$ react with iron Fe and produce iron naphthenates $Fe(RCOO)_2$, which are soluble in oil (eq 2.2.1). Hydrogen

sulfide H_2S , considered the most reactive sulfur compound, may also react with iron to form iron sulfide FeS (eq 2.2.2). This latter phase is insoluble in oil and can form a scale at the steel surface. Finally, the iron naphthenates and hydrogen sulfide can react together and regenerate naphthenic acids that will start another “cycle” (eq 2.2.3).



In order to evaluate the dominant corrosion process, Craig (1996) developed the concept of *naphthenic acid corrosion index* (NACI). NACI is calculated as the ratio between the corrosion rate (mpy³) and the weight of the corrosion scale formed at the sample surface (mg/cm²). A predominant sulfidation corrosion would be characterized by a NACI smaller than 10, while a pure NAP corrosion process would be defined by a NACI more than 100. Between these two critical values, the NAP corrosion is considered to be partially inhibited by H_2S . Nevertheless, the index was developed for quiescent flow conditions using carbon steel samples, and more research is needed before making any further conclusions.

The interactions between sulfur compounds and naphthenic acids can be minimized in lab conditions when studying the effect of a specific variable on the corrosion of steel. Unlike crude oil fractions containing thousands of compounds, many researchers (Chambers et al., 2012; Gutzeit, 1977; Harrell et al., 2009; Kanukuntla et al., 2008; Smart et al., 2002) have been using model oils (i.e., white oil) spiked with known

³ The unit mpy “mils per year” is used in UK and US unit systems to measure the corrosion rate. It can be converted to mm/y (SI system) by multiplying its value by the factor 0.0254 (1 mpy = 0.0254 mm/y).

mixtures of naphthenic acids or/and sulfur compounds. In this way the undesired effects can be eliminated or at least isolated (i.e., inhibition) limiting the number of unknowns in the test matrix and helping to improve the understanding of primary controls on NAP corrosion.

As shown before, the corrosiveness of the naphthenic acids depends on the composition of the crude oil, but also on other parameters, such as temperature, metallurgy, time, or flow conditions. These controlling factors are presented in the next sections of this chapter.

2.3 Factors influencing naphthenic acid corrosion

The main factors controlling NAP corrosion are discussed in this section. The flow effect and related modeling are treated in a separate section.

2.3.1 The corrosiveness of naphthenic acids

In the refining industry, the corrosiveness of naphthenic acids is quantified by the acid concentration in crudes, commonly referred to as *Total Acid Number* (TAN). TAN corresponds to the amount of potassium hydroxide (mg) required to neutralize the acidity in 1 g of crude oil. It can be measured by various analytical procedures, such as standards ASTM D974 and ASTM D664. ASTM D974 uses a colorimetric titration by KOH while ASTM D664 is based on a potentiometric procedure (ASTM International, 2011a; ASTM

International, 2012b). The latter gives TAN values higher⁴ (up to 80%) than those with the colorimetric method, but is usually the preferred analytical technique for measuring the TAN (Piehl, 1988).

Based on field data, the industry developed rules of thumb to assess the NAP corrosion in processing fluids. Crude oils and refined fractions were considered to be corrosive if their respective TAN values were greater than 0.5 and 1.5 mg KOH / g oil. However, numerous exceptions contradicted such rules (Craig Jr., 1996; Messer et al., 2004; Slavcheva et al., 1999).

Many authors (Bota et al., 2010; Dettman et al., 2009; Groysman et al., 2007; Turnbull et al., 1998) also agreed that TAN was not an appropriate way to measure the corrosiveness of a crude oil. For example, Turnbull et al. (1998) demonstrated that, at equivalent operating conditions, a liquid phase (either model oil or HVGO) spiked with an isolated carboxylic acid or a mixture of naphthenic acids at the same TAN number had a different corrosivity on steel. They suggested that the corrosiveness could be influenced by the structure of the naphthenic acids, such as the steric hindrance.

The correlation between the corrosivity of naphthenic acids and their molecular structures was, therefore, investigated. Using crude fractions from Athabasca oil sands, Messer et al. (2004) suggested the existence of two different naphthenic acids fractions. The first one, including low molecular weight compounds (125–425 g/mol), is regarded as corrosive while the second fraction, gathering higher molecular weights molecules (325–900 g/mol), as non-corrosive or even possessing inhibitive properties. Dettman et

⁴ The ASTM D664 procedure also considers all the acidic species present in the medium, which includes inorganic acids, acid gases, salts of weak bases, and heavy metals (ASTM International, 2011a).

al. (2009) demonstrated that the corrosiveness of naphthenic acids cannot be correlated with their molecular weights, but they found that an increase in the rings number (more than 1) within a molecule starts diminishing the NAP corrosion. Furthermore, similar molecular structures (i.e., either 2 n-alkyl carboxylic acids, 2 carboxylic acids with cycloalkyl groups or 2 carboxylic acids with phenyl groups) exhibit similar corrosivities, although this latter generally tends to decrease when the steric hindrance increases. The distribution and the type of naphthenic acids are closely related to the distribution of their boiling points. The effects of the latter are further developed in section 2.3.4, also dealing with the effect of the physical state of naphthenic acids.

2.3.2 The effect of sulfur compounds

As mentioned earlier, the sulfur compounds can interact chemically with naphthenic acids. Likewise, different types of sulfur and organo-sulfur compounds can be present in crudes and refined fractions during the refining process. They include elemental sulfur, hydrogen sulfide, thiols (also called mercaptans), sulfides, polysulfides, aliphatic and aromatic disulfides, and thiophenes. The modified McConey curves (McConey, 1963) have been used as a predictive tool by the petroleum industry to assess sulfidation corrosion for different metallurgies, such as CS, 5Cr, 9Cr (NACE International, 2004). The corrosion rate is correlated to the total sulfur content (in a range of 0–3%) using a corrective factor. However, the modified McConey curves are generally considered very conservative leading to an overdesign of the corrosion resistant alloys. They do not account for the presence of hydrogen and multiphase flow conditions

(Kane, 2006). Instead, the Couper-Gorman curves can be used to capture the effect of hydrogen content on sulfidation corrosion (NACE International, 2004).

In oil refining media, sulfidation corrosion occurs in a temperature range of 230-425 °C (Rebak, 2011) and usually is uniform at the metal surface. Hydrogen sulfide (H_2S) is the most reactive sulfur compound in crude oils, but also the one reacting with iron to form an iron sulfide (FeS) scale at the metal surface. This scale can protect to some extent the steel surface against corrosion by limiting the transport of corrosive species to the surface (diffusion). Using model oils and/or crude fractions (VGO, 650+) several researchers (Bota et al., 2010; Kanukuntla et al., 2008) demonstrated that the corrosivity of crudes cannot be correlated to the properties of the iron sulfide scale, such as porosity, thickness or morphology.

Many authors (Hau, 2009; Kapusta et al., 2004; Messer et al., 2004; Tebbal and Kane, 1996) recognize that the total sulfur content is not appropriate to evaluate sulfidation corrosion. Instead, they recommend using the reactive sulfur content which plays a true interaction role with NAP compounds. However, the reactive sulfur content depends on the sulfur speciation in crude fractions, whose ratio changes as a function of temperature. Mercaptans are the dominant species in low boiling fractions ($T < 100$ °C); in higher boiling fractions ($T > 300$ °C), thiophenes, which are non-corrosive compounds, dominate representing 2/3 of the sulfur species while the remaining species are mainly “sulfidic” (Robbins, 2000).

Other researchers (Dettman et al., 2012; Kane and Cayard, 1999) suggest that the ability of sulfur compounds to generate H_2S by thermal degradation during the refining

process may be the key to assess the corrosivity of NAP compounds in the presence of sulfur. A few techniques, i.e., the ASTM D5705 method (ASTM International, 2012a), are currently evaluated to confidently measure the H_2S content in high boiling points fractions (Lywood, 2012; Murray, 2010).

2.3.3 The effect of temperature

Naphthenic acids are particularly reactive between 220 and 400 °C (Blanco F. and Hopkinson, 1983; Craig Jr., 1995; Craig Jr., 1996; Jayaraman et al., 1986; Kanukuntla et al., 2008; Piehl, 1988; Qu et al., 2006; Turnbull et al., 1998). However, in the upper range of 350–400 °C, their activity starts weakening due to thermal decomposition; at 400 °C and above, no naphthenic acid corrosion has been observed in refineries (Derungs, 1956; Gutzeit, 1977). In some cases, NAP corrosion was observed in unusually lower temperature ranges, such as 190–210 °C, due to the presence of low boiling points NAP species in crude oil (Groysman et al., 2005; Groysman et al., 2007).

The corrosion rate increases as a function of temperature (Craig Jr., 1996; Gutzeit, 1977; Turnbull et al., 1998). For instance, Gutzeit (1977) pointed out that the corrosion rate tripled every 55 K for most of the steels used during experiments. In the same study, the author also suggested that the kinetics of NAP corrosion follows the Arrhenius law equation. Hence, the associated activation energy would depend on the type of naphthenic acids present in the crude oil (Slavcheva et al., 1999), but it seems to be insensitive to the metallurgy of the pipe.

2.3.4 The effect of physical state and boiling points

Some researchers (Derungs, 1956; Groysman et al., 2007; Gutzeit, 1977) noticed that naphthenic acids are the most aggressive when they are close to their boiling points in liquid phase conditions. Gutzeit (1977) demonstrated that the high corrosion rates measured in the vapor phase could be attributed to the films of condensates formed at the steel surface and not to the vapors themselves. In these conditions, any equipment located in the vicinity of the flashing zone in the distillation units could be subjected to severe NAP corrosion attacks, such as those reported by Hopkinson and Penuela (1997).

The high corrosive potential of the naphthenic acids at their boiling points explains why no particular temperature within the range of 220–400 °C corresponds to a peak of NAP corrosion rate. But it helps to correlate the corrosivity with the distribution of naphthenic acids species present in the crude oil.

For corrosion management and safe refining purposes, it is important to measure the TAN and the TAN boiling point distribution in the whole crude oil and its distilled fractions. However, it requires the distillation of each fraction of interest using a gas chromatography simulation distillation (GCSD) and, then, to measure the TAN concentration by titration. This procedure may not be totally accurate due to the thermal degradation of the naphthenic acids during the distillation. Instead, Qian et al. (2008) proposed to use an ESI-MS method that is faster, minimizes the chemical alterations and measures the composition and the structure of the acids. Once the structure and molecular weights of the acids are determined, their boiling points are calculated using a structure-oriented lumping model (Altgelt and Boduszynski, 1992; Quann and Jaffe, 1992).

2.3.5 The effect of test duration

The experiments assessing the effect of test duration on naphthenic acid corrosion should not only account for the time necessary for the chemical medium to reach steady state conditions, but also make sure that no thermal degradation occurs during the test (Turnbull et al., 1998). Independent studies (Kanukuntla et al., 2008; Kanukuntla, 2008; Turnbull et al., 1998) show that 24 hours are usually sufficient to fulfill the first condition. The thermal decomposition of naphthenic acids and organo-sulfur compounds introduces a “chemistry effect” by modifying the chemical composition of the oil media. Although this effect is seldom considered in experimental test matrices, it can be observed in closed systems, such as stirred autoclaves, where conditions may become more aggressive due to H₂S generation (Kanukuntla et al., 2008).

Several studies reported similar results showing a decrease in corrosion rate with respect to time (Kanukuntla et al., 2008; Kanukuntla, 2008; Turnbull et al., 1998). Turnbull et al. (1998) interpreted this decrease by a decomposition of the naphthenic acids at high temperature. This explanation cannot stand when using Kanukuntla and coworkers’ experimental set up since the fluid was continuously refreshed in the test section during the experiment. Their data show that the mitigation of NAP corrosion could be attributed to the formation of a protective iron sulfide scale and, therefore, suggests that the kinetics of NAP corrosion attack was faster than that of the iron sulfide scale formation on a bare metal surface.

2.3.6 The effect of pressure

The pressure has a limited effect on naphthenic acid corrosion (Derungs, 1956; Gutzeit, 1977; Slavcheva et al., 1999). A change in pressure may have an indirect effect on the boiling point distribution of naphthenic acids, which has a major influence on the corrosivity of the acids (section 2.3.4). However, no experimental evidence has been reported to support such an assumption.

2.3.7 The effect of metallurgy

In oil refining, different techniques can be applied to mitigate naphthenic acid corrosion, such as removal of acids (pre-topping), neutralization, injection of inhibitors, blending of different feedstocks, and material selection (Blanco F. and Hopkinson, 1983; Derungs, 1956; Scattergood et al., 1987). The latter relies on the choice of the most adequate alloy given the actual corrosion (i.e., type I, II or III), operating conditions and, eventually, economic constraints. The most commonly encountered alloys in crude distillations units (CDU) are carbon steels (CS), low chromium steels (5Cr–0.5Mo and 9Cr–1Mo), and different types of stainless steels (AISI 410, AISI 304, AISI 316, AISI 317).

Carbon steel, mainly for economical reasons, represents 80% of the steel alloys used in oil refining (Farraro and Stellina Jr., 1996). It usually gives a good resistance to naphthenic acid corrosion at temperatures below 230°C and at low flow conditions (Derungs, 1956; Slavcheva et al., 1999).

Chromium alloys usually offer a better resistance to naphthenic acid corrosion than carbon steel. An increase in the chromium content makes the alloys more resistant to NAP corrosion, although some field cases reported severe pitting corrosion on chromium alloys (Nugent and Dobis, 1998). In the absence of NAP corrosion, Blanco and Hopkinson (1983) advised the use of chromium cladding with a 5–12% chromium content to mitigate sulfidation corrosion. Regarding the operating temperature, several authors (Blanco F. and Hopkinson, 1983; NACE International, 2004; Rebak, 2011) agree with the use of carbon steel for temperatures lower than 288 °C, 5Cr alloy for temperatures up to 343 °C, 9Cr alloy for temperatures up to 400 °C, and AISI 410 (containing 12Cr) for beyond 400 °C (hydrogen free conditions).

Martensitic stainless steel 410 is considered to be more resistant than carbon steel or low chromium content alloys (Derungs, 1956; Gutzeit, 1977). However, severe corrosion was reported in a few cases when using either AISI 410 or carbon steel clad with AISI 410 at different locations of the crude distillation units, such as the HVGO pump, furnace outlet elbow, or vacuum tower internals near the flash zone (Blanco F. and Hopkinson, 1983; Hopkinson and Penuela, 1997; Nugent and Dobis, 1998). In the case of failure, AISI 410 was replaced by stainless steel 316.

The austenitic stainless steel series 300 (also called 18/8 stainless steels for their chromium/nickel content) have a superior resistance to NAP corrosion compared to the other alloys mentioned above, because of the presence of a passive chromium oxide layer Cr_2O_3 at the steel surface. A rule of thumb states that the alloy should at least contain 2.5% molybdenum to be resistant to NAP corrosion, such as AISI 316 (2–3%) or AISI

317 (3–4%), although Gallo and Edmondson (2008) pointed out that this threshold value is not supported by some experimental studies (Craig Jr., 1996; Wu et al., 2004b). Others (Derungs, 1956; Piehl, 1988) considered AISI 304 as unreliable because of severe localized corrosion observed in some cases. Furthermore, field data (Nugent and Dobis, 1998; Piehl, 1988) usually reported higher corrosion rates with AISI 304 compared to AISI 316/317. Only in rare cases uniform and/or localized NAP corrosion of AISI 316 and AISI 317 were reported; subsequently, both materials were upgraded to AISI 316Ti alloy (Hopkinson and Penuela, 1997).

Higher grade alloys, such as Inconel 600 and Hastelloy B with high nickel contents (65–70%), show a high resistance to NAP corrosion; however, their performance is not significantly different from that of AISI 316, the latter being preferred for economic reasons (Derungs, 1956; Farraro and Stellina Jr., 1996). Aluminum and aluminum alloys also show a good resistance to NAP corrosion when replacing distillation tower internals (Farraro and Stellina Jr., 1996). On the other hand, Derungs (1956) does not recommend the use of copper and copper alloys in NAP corrosion environments since they start corroding at 150 °C.

2.4 The flow effect on naphthenic acid corrosion

The flow (fluid flow and turbulence) can enhance corrosion. This process is commonly referred as the flow accelerated corrosion and can be explained by different mechanisms, such as mass transport controlled corrosion, erosion-corrosion or cavitation corrosion (Heitz, 1991; Roberge, 2004; Weber, 1992). In the present case, the

combination of NAP corrosion and flow will be referred as *Flow Induced Naphthenic Acid Corrosion* (FINAC).

This section first revisits in more details the locations where NAP corrosion was or could be enhanced by flow conditions. Then, it reviews the different pieces of equipment used for the experimental studies investigating the flow effect on NAP corrosion. In addition, the variables used to correlate crude's corrosivity to the flow are also brought into focus. Finally, the existing flow models to predict the corrosion rates due to NAP corrosion are reviewed.

2.4.1 NAP corrosion in transfer lines

Tebbal (1999) suggested that the pure NAP corrosion mechanism (Type I) depends on the flow velocity, this mainly occurs in locations such as furnaces (tubes and heaters) and oil transfer lines. The transfer lines are large pipes linking the furnaces to the vacuum and atmospheric distillation towers. In these locations, the stream velocity rapidly increases due to the pressure drop and the thermal expansion of the gas phase and can easily reach up to 100–120 m/s or even more, promoting corrosion. To avoid having the streams flowing at a sonic velocity, the pipe diameters are enlarged between the inlet (furnace) and the outlet (distillation tower) of the transfer lines. They are commonly in the range of 0.2–1.2 m, but in some cases can be as large as 1.8 m.

For both atmospheric and vacuum transfer lines, the use of AISI 316 piping or AISI 317 clad piping is generally recommended, although some refineries can operate with atmospheric transfer lines made of low chromium alloys (Blanco F. and Hopkinson,

1983; Hopkinson and Penuela, 1997; Nugent and Dobis, 1998; Scattergood et al., 1987). The most severe NAP corrosion has been encountered in the bends of transfer lines, such as furnace outlet elbows, and other flow disturbances: thermowells, tees, and valves. For the furnace outlet elbow, different materials initially designed with CS, 5Cr, 9Cr or AISI 304L experienced severe NAP corrosion (Blanco F. and Hopkinson, 1983; Hopkinson and Penuela, 1997; Jayaraman et al., 1986; Nugent and Dobis, 1998; Piehl, 1988). A field case reported a corrosion rate up to 12 mm/y at a CS elbow which failed after 6 months of service (Blanco F. and Hopkinson, 1983). These materials were all replaced by AISI 316 and no corrosion was reported thereafter. The thermowells, located downstream of the heater outlets in transfer lines, were severely corroded or, in some cases, failed because of the local turbulence or droplets impingement (Babaian-Kibala et al., 1998; Nugent and Dobis, 1998; Piehl, 1988). In all these cases, a high velocity multiphase flow mixture was present at these locations.

2.4.2 Experimental equipment

Various types of equipment can be employed to investigate the effect of flow on corrosion processes (Roberge, 2004). Only the equipment used to study the flow effect on NAP corrosion is presented in this section.

2.4.2.1 Rotating cylinder

The rotating cylinder (RC) is usually a constant inventory apparatus or in some cases can include a continuous flow-through capability. In the latter case, which amounts

to a better design as it avoids buildup of corrosion products, the testing fluid stored in a feed tank is pumped, preheated and directed through the RC test section, usually mounted in a heated autoclave vessel, before exiting and being cooled down and collected in a waste tank (Bota, 2010b). In the RC autoclave, elevated pressure conditions are maintained to avoid the vaporization of light compounds. The corrosion samples can be either mounted on a rotor shaft rotating up to 2000 RPM (Bota et al., 2010; Smart et al., 2002) or set up in the vicinity of the stirrer (Gutzeit, 1977). In this way, peripheral velocities in a range of 0.5–8.5 m/s are generated at the surface of the samples creating low shear stress conditions (< 300 Pa). Given the low range of flow velocities the rotating cylinder would not be suitable to simulate multiphase flow conditions encountered in transfer lines.

2.4.2.2 Jet impingement

A jet impingement apparatus generally involves a single phase flow loop system with liquid recycling (Kane and Cayard, 2002; Tebbal and Kane, 1997; Wu et al., 2002; Wu et al., 2004a; Wu et al., 2004c). The testing solution is pumped from a feed tank, heated and directed to a test section, the jet impingement chamber, before being cooled down and redirected back to the feed tank. In the test section, the nozzle of the submerged impingement jet can deliver a high velocity stream on a target surface (stagnation region) placed adjacent to the nozzle nose where the corrosion samples are located (Efird, 2006; Roberge, 2004). In contrast to rotating cylinder systems, a jet impingement configuration can generate higher shear stress conditions (> 1000 Pa) at

the target surface. However, mass transfer characteristics are only well-determined in the stagnation region with a jet impingement perpendicular to the target surface (Roberge, 2004). Furthermore, the eventual presence of undesired gas bubbles in the stream would enhance mass transfer conditions at the sample surface (Poulson, 1983).

2.4.2.3 Flow loop

Flow loops have been rarely used in experimental studies investigating naphthenic acid corrosion controlling factors (Johnson et al., 2003). Besides involving much higher costs, this type of equipment presents more technical challenges. Fluid management (feed and waste), heat transfer control (heater design and insulation), pumping, material selection without mentioning potential leaks (and its coking consequences) illustrate some of these challenges.

No experimental study was carried out simulating a multiphase flow mixture with liquid droplets fractions entrained in a gas phase, such as those suggested to occur in transfer lines of oil refineries, particularly in bends. A multiphase flow loop developing a gas-oil mixture would have the advantage to simulate more faithfully the field conditions since only a fraction of the liquid phase (some of the droplets) actually impinge the pipe walls. In a case of a jet impingement, the fully liquid phase impinges on the corrosion sample leading to higher corrosion rates than happening in the field since the multiphase flow nature is not accounted for.

2.4.3 Fluid velocity vs. wall shear stress

While it is broadly accepted that naphthenic acid corrosion depends on fluid flow and turbulence, authors do not really agree on how to properly correlate them with the corrosivity of crude oils (Hau et al., 1999; Tebbal and Kane, 1996; Tebbal, 1999).

Usually, the fluid velocity represents the experimental variable used to evaluate the flow effect on NAP corrosion and, thereby, it was the first used to correlate the fluid flow to corrosion rate (Blanco F. and Hopkinson, 1983; Derungs, 1956; Gutzeit, 1977; Piehl, 1988; Tebbal, 1999). However, experimental studies led to contradictory results. Some researchers (Craig Jr., 1995; Qu et al., 2005) observed that the corrosion rate linearly increased with respect to fluid velocity, while others (Gutzeit, 1977; Hau, 2009; Qu et al., 2005) sustain that there is a velocity threshold above which FINAC may happen.

Using a rotating cylinder electrode, Craig (1995) demonstrated that the corrosion rate can be expressed as a function of velocity, such as $CR = \varphi(U^{0.7})$, and concluded that the corrosion process is controlled by mass transfer.

Kane and Cayard (2002) studied the velocity effect on NAP corrosion of different alloys (low chromium 5Cr, 9Cr, AISI 410) using the jet impingement technique and a model oil spiked with different TAN and H₂S concentrations. They only observed FINAC at high acid numbers (TAN > 1.5) and high velocity (U > 15 m/s) in the case of low chromium alloys. Still, the effect of H₂S content on FINAC remains uncertain since the NAP attack could be either inhibited by a protective FeS scale formed at the metal surface or be very aggressive due to the impingement and destruction of the FeS scale.

Using Kane and Cayard's data, Hau (2009) demonstrated that the effect of flow velocity in the range of 15–60 m/s is not very significant.

Qu et al. (2005) also investigated the flow effect of NAP corrosion using a jet impingement. Depending on TAN concentration and the type of alloy used, they observed that the corrosion rate can either increase linearly with the velocity or exhibit a velocity threshold above which the corrosion rate sharply increases. These results confirm that FINAC depends on both the line metallurgy and oil corrosiveness.

Tebbal and Kane (1996) propose to replace the velocity by the wall shear stress, which can be directly correlated with the crude corrosivity “through the removal of protective films” formed at the metal surface. They justify their choice based on the work of Efird (1993) related out erosion-corrosion in CO_2 aqueous corrosion systems. It should be noted that Efird (1993) stated that his experimental results needed further verification before being extrapolated to other types of corrosion.

Schmitt et al. (1996) studied the mechanical properties of iron carbonate $FeCO_3$ scales pointing out the existence of two types of stresses, *intrinsic* and *extrinsic*. He demonstrated that intrinsic stresses ($10^6 - 3 \cdot 10^7$ Pa) produced during the scale growth at the metal surface are the primary cause of scale fracture, while extrinsic stresses, such as the wall shear stress (10 – 1000 Pa), are too weak to damage the scale. Using two different Atomic Force Microscopes (AFM), Xiong (2011) demonstrated that only high stress levels ($10^6 - 10^7$ Pa) were able to remove the protective iron carbonate layer and inhibitor films (i.e., quaternary amines, imidazole salts) from the metal surface and pointed out that the fluid flow alone could not remove such films mechanically. Using a

multiphase flow loop, Canto (to be published) generated a turbulent standing slug flow (turbulence similar to that of a slug front region) exactly at the location of an Electrochemical Quartz Microbalance (EQCM) probe, whose surface was initially covered by a corrosion inhibitor (imidazoline and quaternary amine), and proved that the shear stress did not mechanically damage the inhibitor film established before the slug was present.

It should be emphasized that for all the experiments involving shear stress considerations in lines, the actual wall shear stress was never measured, but only calculated with correlations depending, among others, on the device's geometry (Nesic et al., 1997; Silverman, 1984; Silverman, 2003; Silverman, 2004). Despite some on-going research on this topic (Sheverev et al., 2011), this technical limitation (no direct measurements of shear stress) keeps fueling confusion and contradictions in the current literature about the use of the shear stress.

2.4.4 NAP corrosion features in multiphase flow systems

Directed experimental works in research laboratories to study the flow effect on NAP corrosion have exclusively been performed in single phase flow environments, regardless of the equipment used (Craig Jr., 1995; Gutzeit, 1977; Kane and Cayard, 2002; Qu et al., 2005). The multiphase flow effects, such as those found in transfer lines of oil refineries, have been ignored; this partially explains the present lack of understanding of the flow induced NAP corrosion.

The terms “fluid velocity” and “wall shear stress” are commonly encountered in describing single phase flow conditions. Furthermore, most of the authors keep using the same terminology when referring to multiphase flow conditions, which is not accurate. In the present case, the term *in situ liquid velocity* is carefully chosen instead of “fluid velocity”⁵ avoiding any confusion or misunderstanding. In the same manner, the *liquid-wall shear stress* should be used instead of “wall shear stress”.

In many studies (Kane, 2006; Rebak, 2011; Tebbal, 1999) it has been recognized that the degree of vaporization and its resulting features (multiphase flows) play an important role in naphthenic acid corrosion in field conditions. An increase in the degree of vaporization determines an increase in the gas-liquid interfacial shear stress; a higher shear stress leads to a higher *in situ liquid velocity*, which promotes the mass transfer of corrosive species at the pipe wall. The presence of light hydrocarbons or water in crude oils also promotes higher degrees of vaporization and fluid velocities (Tebbal, 1999).

The field inspections after a pipe failure or a pipe replacement due to severe NAP corrosion are the only available information to describe the existing flow pattern in transfer lines. Gutzeit (1977) argued that due to the kinetics of sulfidation and naphthenic acid corrosion, a protective scale cannot reasonably form under high velocity conditions. More interestingly, he suggested that only a flow induced corrosion mechanism with droplet impingement on the metal surface can damage a passive layer of AISI 410 stainless steels. In multiphase flow, a flow pattern with such characteristics may correspond, in some aspects, to an annular-dispersed flow. Therefore, more experimental

⁵ In multiphase flow mixtures, a fluid can be treated as either a liquid or a gas/vapor. Since NAP corrosion occurs in liquid phase and, at a much lower extent, in vapor phase, a clear distinction should be made between the two phases.

studies of multiphase flow (gas-liquid) effects on NAP corrosion are needed to confirm Gutzeit' hypothesis.

2.4.5 Multiphase flow modeling

As mentioned earlier, the transfer lines of oil refineries encompass a broad range of pipe diameters. Therefore, multiphase flow modeling becomes very useful to predict the flow pattern occurring in the pipe and its related characteristics, such as the pressure drop and liquid holdup.

The effect of flow on NAP corrosion has been hardly explored at all from a modeling point of view. Therefore, the reference list is rather limited for this particular topic. Tebbal and Kane (1998) suggested using simple empirical correlations developed for single phase flow conditions in order to quantify the flow effect through the calculation of the wall shear stress. These correlations were, however, applied to multiphase flow scenarios with high degrees of vaporization (30–70%) and yielded inconsistent results in terms of shear stress.

At the other extremity of the flow modeling spectrum, Gabetta et al. (2003) used computational fluid dynamics (CFD) tools to simulate the flow hydrodynamics in a U-shape furnace tube at high temperatures. Simulation results indicated the existence of a multiphase flow mixture with a degree of vaporization of 45% and a liquid phase flowing as dispersed liquid droplets in the gas core.

An intermediary approach using 1D multiphase modeling can be a good compromise between accuracy and extensive computational 3D developments. It would

provide indications about the existing flow pattern and, by extension, the distribution of the liquid phase in the line. The latter is very important for a corrosion engineer since NAP corrosion mainly occurs in the liquid phase. The current refinery corrosion simulators, such as Crudecorp V5 developed by the Institute for Corrosion and Multiphase Technology (ICMT) at Ohio University, are all proprietary tools, and can handle single phase flow conditions. Combining a refinery corrosion simulator with a multiphase flow prediction model would represent an important next step for developing predictive models in this field.

2.5 Research hypotheses and objectives

The naphthenic acid corrosion occurring in transfer lines of oil refineries is not very well-understood by refiners because it requires a good grasp of the corrosion processes and a fair understanding of the multiphase flow conditions existing in these environments. Simulating such chemical and hydrodynamic conditions in a laboratory represents a big technical challenge because of the large scale of the lines transporting the fluids, and the high temperatures involving volatile/explosive media. These conditions can never be fully reproduced in a laboratory. Therefore, in order to address the discrepancy between lab and field conditions, experiments need to be conducted on a much smaller scale and modeling was used to connect the two scenarios.

In the present research, the study of the effect of flow on naphthenic acid corrosion is split into two independent experimental studies. The first research hypothesis was: a particular two-phase flow pattern characterized by the liquid droplets impingement

drives the corrosion process occurring at high flow velocities in transfer lines of oil refineries; thus, an annular-dispersed flow is assumed to be the dominant flow pattern. To verify this hypothesis, the first study focused on the determination of hydrodynamics of gas/liquid flow using “cold flow” conditions (room temperature and atmospheric pressure), with a particular attention to the distribution of the liquid phase in the line.

This part of the work focused on the following objectives:

- Design and build a new large-scale experimental rig, the *Cold Flow Rig* (CFR), for simulating a horizontal gas-liquid two-phase flow at high flow velocities similar to those encountered in transfer lines of oil refineries.
- Determine the flow patterns and eventual flow pattern transitions taking place at these operating conditions in straight pipe sections.
- Measure the hydrodynamic characteristics of the corresponding flow patterns (pressure drop, wetted wall fraction) in straight pipe sections.

The second research hypothesis assumes that there is a flow effect on NAP corrosion, particularly in the bends of transfer lines. Therefore, the second experimental study directly focused on the evaluation of the naphthenic acids' corrosivity on carbon steel in the absence or presence of an FeS scale at the metal surface in two-phase flow conditions. The operating conditions needed to mimic the flow conditions encountered in transfer lines of oil refineries using a similar oil chemistry and high temperature multiphase flow environment, albeit all on a much smaller scale. The work was broken down using the following objectives:

- Upgrade an existing small-scale flow rig, the *Annular Flow Rig* (AFR), to assess the corrosion of naphthenic acids in single phase and multiphase flow conditions at high temperatures.
- Conceive an experimental procedure to assess the corrosiveness of the naphthenic acids in the absence and presence of the iron sulfide scale at the metal surface in multiphase flow conditions.
- Determine the influence of phase velocities and pipe geometry on corrosion rates due to naphthenic acids.

Furthermore, linking an experimental corrosion study on a small-scale to a multiphase flow study on a large-scale required the use of corrosion and flow modeling tools to scale-up/down these conditions and eventually relate them to the transfer lines of oil refineries. Scaling the flow hydrodynamics implies the design, development and validation of a gas-liquid two-phase model. The specific objectives to achieve such a goal were:

- Create a model capable of predicting the flow pattern and its main characteristics occurring at given flow conditions in relatively low pressure systems (similar to those in transfer lines of oil refineries).
- Validate the model with flow data generated in this study and/or from other in-house and open literature sources.
- Specifically focus on a “missing link” which liquid droplets entrainment onset in a horizontal line; develop and validate a model for this scenario.

To complement this flow modeling, a recently developed corrosion model to predict NAP corrosion in liquid phase will be used and connected with the present work, and evaluated with corrosion experimental data produced in this study.

CHAPTER 3 EXPERIMENTAL STUDY OF CORROSION

Two experimental flow systems were built to achieve this goal. The first small scale flow loop, Annular Flow Rig (AFR), primarily focused on creating the representative corrosion conditions, while the second larger flow system Cold Flow Rig (CFR) was used primarily for the two-phase flow study.

The presence of sulfur compounds in transfer lines implied that the metal surface is covered by an FeS scale. Therefore, a third auxiliary small scale flow system, called the Flow Through Mini Autoclave (FTMA), was customized and used to create an iron sulfide scale on the steel surface. Such pre-sulfided steel samples were moved to the custom built AFR which was assigned for studying the high velocity multiphase flow effects on NAP corrosion. The AFR could generate a very fast moving gas-oil mixture flow at very high temperature and set up corrosive environments, necessary to assess the aggressiveness of the NAP attack in the presence of the FeS scale at the metal surface.

The first sections of this chapter describe the equipment used for studying the NAP corrosion in the FTMA and the AFR. Because both flow systems existed previously, but have been significantly modified and improved to meet the technical specifications for this particular study, details regarding the modifications (AFR, FTMA) or the design of added features (AFR) are also provided. The following section introduces the methodologies used for building the iron sulfide scale and testing for the NAP corrosion. In the end, the results of the corrosion testing are presented and discussed.

3.1 Description of the Flow Through Mini Autoclave (FTMA)

3.1.1 Overview of the FTMA and its working fluids

Prior to this work, the FTMA was extensively used to study the iron scale formation rate and corrosion rate of carbon steel and alloyed steel in environments containing sulfur compounds and naphthenic acids (Kanukuntla, 2008). In the present study, the FTMA was used to build an iron sulfide scale at the metal surface of the samples, which were then transferred into the AFR.

A drawing of the FTMA set up is given in Figure 3.1. The FTMA is made of stainless steel AISI 316 with a 1/8" tubing diameter. The testing solution consisted of a mineral oil containing sulfur compounds spiked with a mixture of naphthenic acids. The mineral oil called here *Yellow Oil* was Americas Core 600 produced by Imperial Oil (2009). The naphthenic acids compounds came from a pure mixture of naphthenic acids with an initial concentration TAN 230 (Tokyo Chemical Industry Corp., 2011). Before each experimental run, the oil lines and the test sections were preheated using the non-corrosive mineral oil Tufflo 6056 called here *White Oil* (CITGO Petroleum Corp., 2006a; CITGO Petroleum Corp., 2006b).

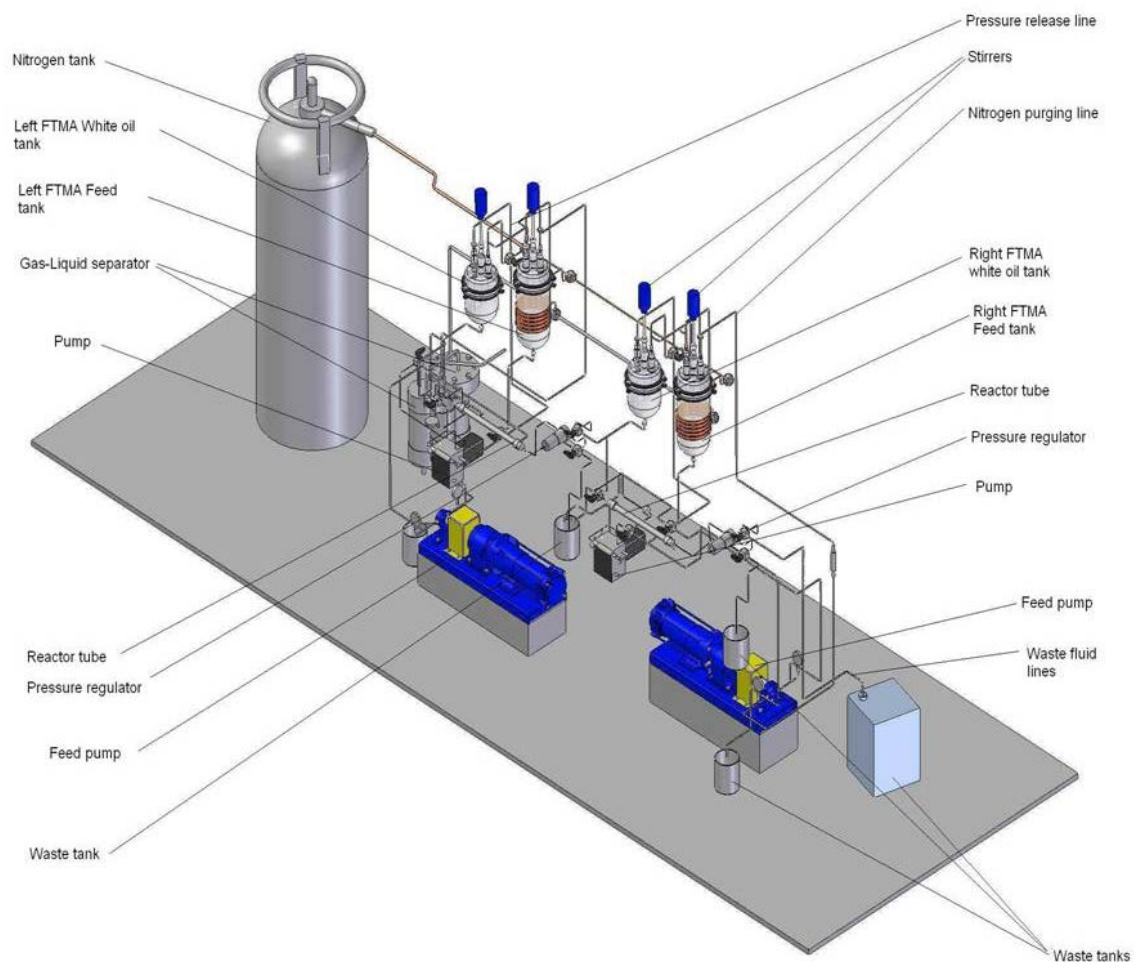


Figure 3.1: Overview of the Flow Through Mini-Autoclave flow (Kanukuntla, 2008).

Physical and chemical properties of these compounds are provided in Table 3.1. Given the importance of the boiling points on NAP corrosion, a true boiling point distribution of the naphthenic acids mixture used in this study was determined by gas chromatography simulated distillation (GCSD) following the ASTM D2887 standard (ASTM International, 2008) and is provided in Figure 3.2 (Wolf, 2010b). The curve shows that at 343 °C (operating conditions) ca. 80% of the naphthenic acids have flashed into the vapor phase.

Table 3.1: Physical properties of the fluids used in the corrosion study.

| Physical properties | White oil ^a | Yellow oil ^b | Naphthenic acids ^c |
|---------------------------------|------------------------|-------------------------|-------------------------------|
| Specific gravity (15.6/15.6 °C) | 0.876 | 0.879 | 0.98 |
| Kinematic viscosity (cSt): | | | |
| at 40 °C | 108 | 111.5 | - |
| at 100 °C | 12.0 | 11.8 | - |
| Molecular weight (g/mol) | 530 | - | - |
| TAN (mg KOH / g oil) | - | - | 230 |
| Flash point (°C) | 254 | 270 | 176 |
| Distillation curve (°C): | | | |
| IBP | 388 | - | 233 |
| 5% | 431 | - | 255 |
| 50% | 507 | - | 296 |
| 95% | 571 | - | 400 |
| FBP | 604 | - | 499 |

^a CITGO Petroleum Corp., 2006a; CITGO Petroleum Corp., 2006b.

^b Imperial Oil, 2009.

^c Tokyo Chemical Industry Corp., 2011; Wolf, 2010b.

The white oil was pumped from a preheated glass tank using a high pressure metering pump Eldex model AA-100-S with a liquid flow rate range of 0.2–10 mL/min (Eldex Laboratories Inc., 2007). When the temperature in the test section reached 316 °C, the liquid flow was switched to using the test solution, the Yellow Oil. The Yellow Oil was pumped from another preheated glass tank by a metering pump Zenith model B9000-0.05 cc/rev with a liquid flow rate range up to 8 mL/min (Colfax Corp., 2012). The flow rate was measured by oil sampling and adjusted if necessary. In order to suppress any gas phase formation during the test, a back pressure valve was set up downstream of the test section to keep the pressure in the range $P = [9.3; 11.4]$ bar. Then, the liquid phase was directed to a waste tank. It should be pointed out that the continuous refreshment of the corrosive species in the FTMA minimized solution degradation and contamination by

corrosion products and the effect on the corrosion rate results; it ensured more or less stable chemical conditions during the sulfidation testing.

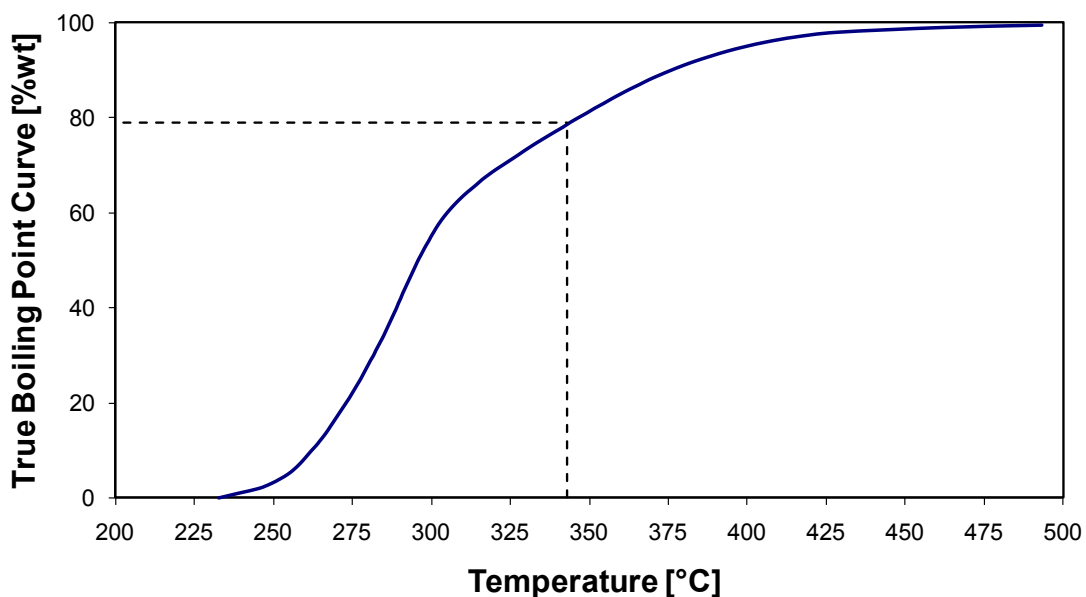


Figure 3.2: True boiling point curve of a commercial naphthenic acids mixture (data from Wolf, 2010b).

3.1.2 Description of the FTMA test sections

The original design of the FTMA test section used by Kanukuntla (2008) was modified to allow the insertion of cylindrical samples. Three different configurations were designed during this study to presulfide the samples. The first design had two FTMA reactors in series as shown in Figure 3.3: the first reactor was used as a preheater to overcome the important heat losses prior to or around the test section while the second was the actual test section in which three samples could be inserted.

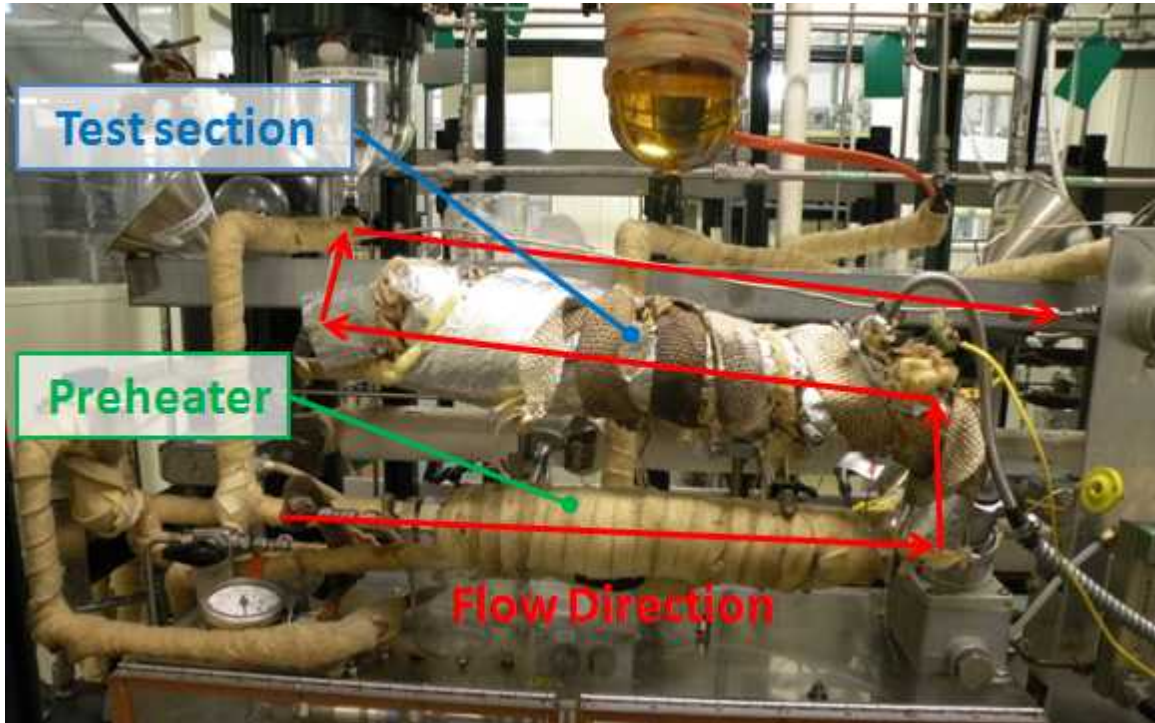


Figure 3.3: External view of the set up used in the FTMA for presulfidation (May–December 2010).

Both FTMA control temperatures were set up at 343 °C. In this design, the temperature of the fluid at the test section was not measured directly in the fluid but at the spacer surface outside the sample, as shown in Figure 3.4. Because of the combined effect of heat loss and difficult temperature sensor location, compared to the original design, more heat had to be provided to the test section to reach the temperature specification (343 °C). Corrosion was more aggressive at the outer and inner surfaces of the samples. On their external surface, the samples exhibited traces of high temperature oxidation, which were undesirable for this study. The inner surface of the samples was exposed to a much more aggressive form of sulfidation corrosion (corrosion rates 0.8–1.2

mm/y) since this latter linearly increases with temperature in the range of 260–350 °C (NACE International, 2004). For these reasons the original design had to be modified.

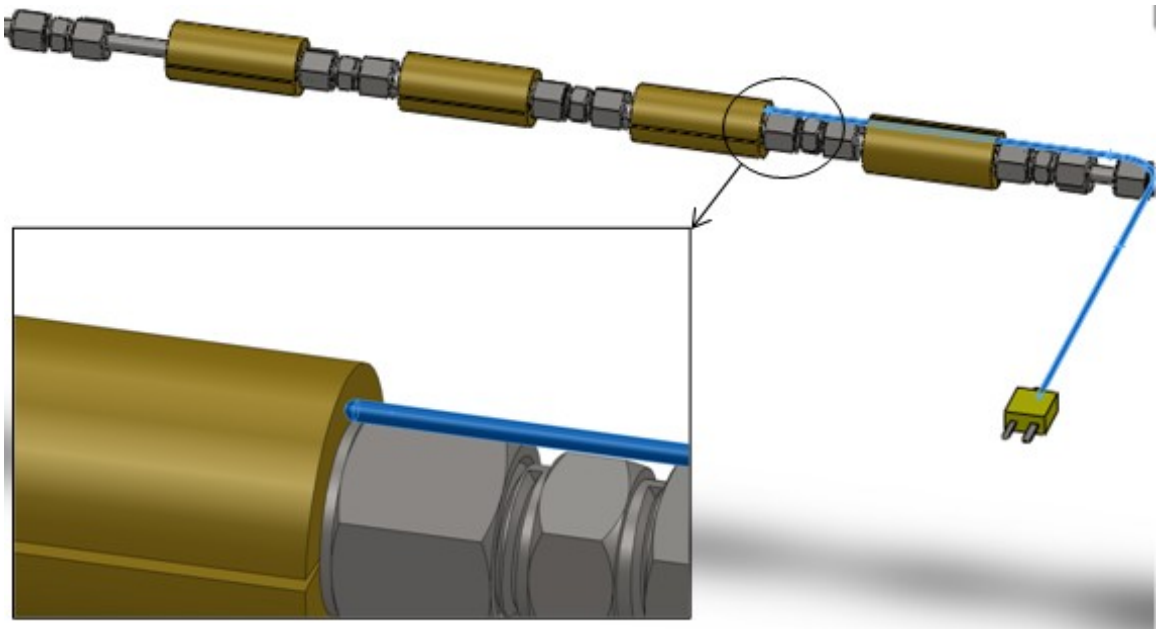


Figure 3.4: Internal structure of the test section (Figure 3.3) with temperature measurement set up (May–December 2010). The samples are within the yellow spacers in this design.

A second design was proposed and showed major improvements (Figure 3.5). For instance, the capacity for presulfidation was doubled and more samples could be added in the new test section. Four samples (type M) were assigned to be transferred in the multiphase flow test section of the AFR while the other two (type S) to be transferred to the single phase flow test section of the AFR.

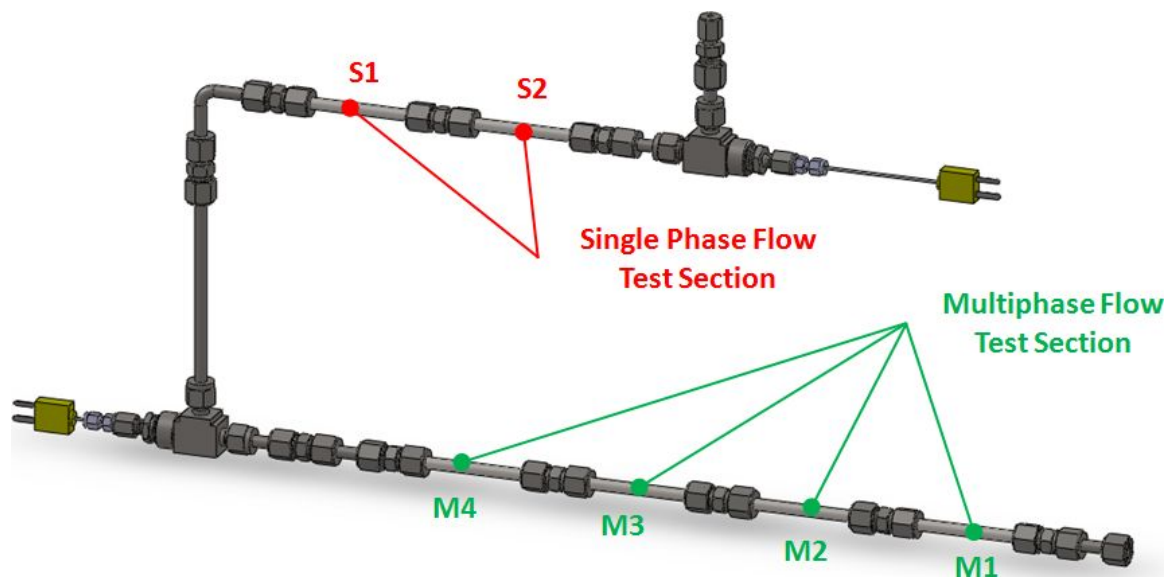


Figure 3.5: Overview of the FTMA test section set up used during the test NJ18 (February 2011). Samples and test sections are named according to their position or function in the AFR (Figure 3.14).

The control temperature in the preheater was kept at 343 °C, while the control temperature in the test section was reduced to 316 °C to avoid overheating the samples. The fluid temperatures were directly measured in the fluid by immersing a thermocouple in the piping (locations M2 and S1). Furthermore, a second layer of insulation was added on the test sections to limit the heat losses. The design gave encouraging results regarding the so-called *multiphase flow test section*, but needed to be upgraded because of the lack of temperature control (originally only manual) in the *single phase flow test section* (Figure 3.5).

The third design as shown in Figure 3.6 had all the “upgrades” made in the second design, but included a few more changes. The sulfidation capacity was increased even more by adding two 90° elbow samples. The eight samples (six straight and two bends) were arranged in series and controlled by two different heating systems.

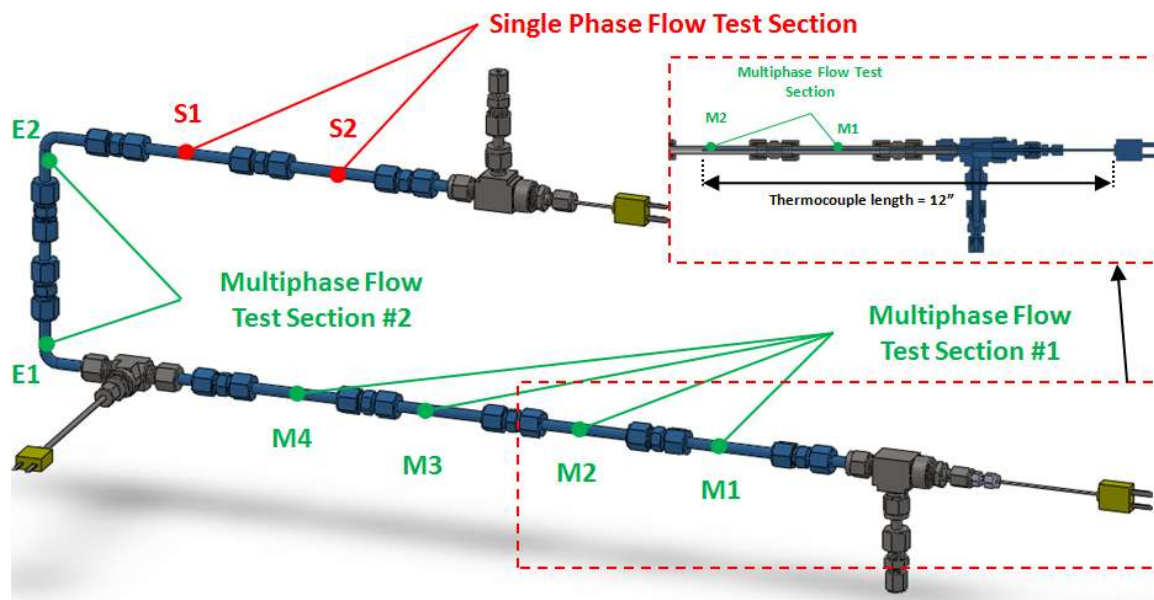


Figure 3.6: Overview of the FTMA test section used for tests NJ19–NJ50. Samples and test sections are named according to their position or function in the AFR (Figure 3.14). The zoom view represents the cross section of the thermocouple inserted in the multiphase flow test section #1.

The type M samples were heated using the FTMA reactor modified with spacers mounted on the samples for heat transfer purposes (Figure 3.7) while the other samples (type E & S) were heated using an ultra high temperature heating tape type Omega STH101. The fluid temperature of each heating system was measured by a 30 cm (12”) long thermocouple with a 1.6 mm (1/16”) sheath diameter immersed in the testing solution. A cross section of the thermocouple inserted in the FTMA reactor is shown in the upper right corner of Figure 3.6. The whole test section was also triply insulated to minimize the heat loss during the test. This last design was used for the rest of the sulfidation reference and presulfidation tests.

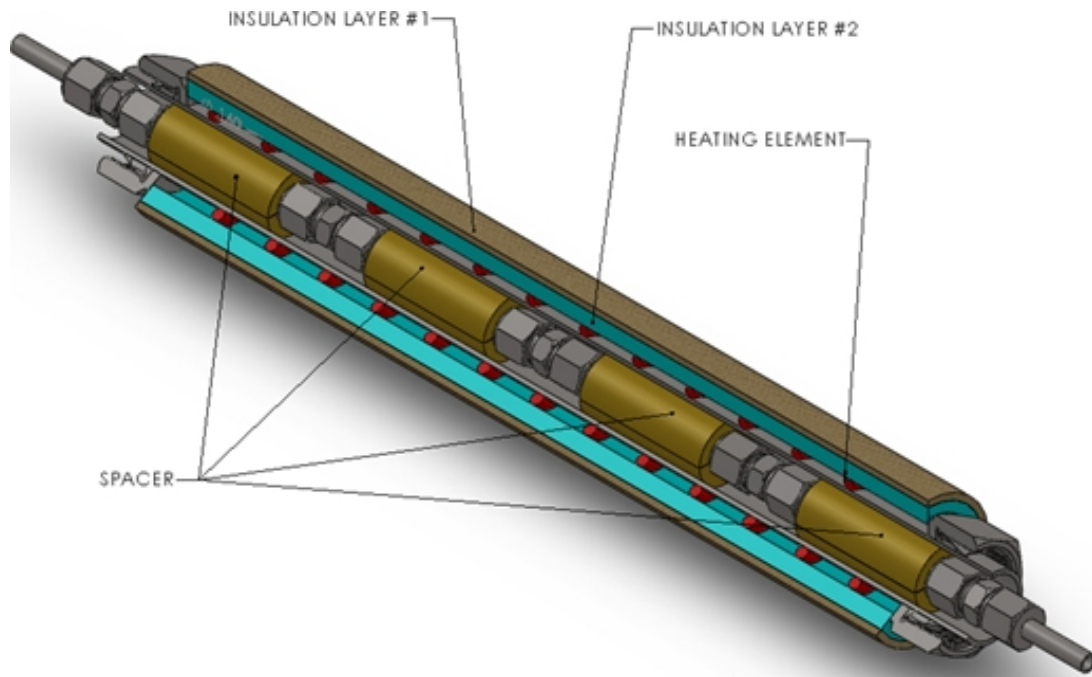


Figure 3.7: Cross section of the multiphase flow test section (only the straight part) with heating element (red coil) and insulation layers. Heat was provided to the samples through the spacers by heat transfer.

3.2 Description of the Annular Flow Rig

3.2.1 Overview of the AFR and working fluids

The AFR was designed to study the effects of NAP corrosion in single phase and gas-oil multiphase flow systems at high temperatures (343 °C) under high flow velocity conditions (1–40 m/s). A general description of this small scale flow loop with the final set up achieved during this work (within 2010-2012) is given in Figure 3.8 and Figure 3.9. A comprehensive diagram of the AFR system can be seen in Figure 3.10.

The AFR lines were made of either stainless steel AISI 316 or Inconel 600 using 4.6 mm (1/4" tube) to 12.7 mm (1/2" pipe) inner diameters, depending on the location and the transported fluid. The testing solution consisted of non-corrosive mineral white oil

spiked with a mixture of naphthenic acids. Both white oil and naphthenic acids mixture had the same origin as the one used for the testing in the FTMA (section 3.1.1). The liquid phase was pumped from a polyethylene storage tank using a metering pump Zenith model B9000-9.0 cc/rev at a liquid flow rate range up to 2 L/min. The fluid was directed to the oil vessel where the liquid phase was preheated to 343 °C with a plug heater. Before reaching the gas-liquid mixing section, the testing solution flowed through the single oil phase test section. At the mixing section, a gas-oil mixture was created and went to the multiphase flow test section, and then, was cooled down through three coolers arranged in series (countercurrent heat-exchangers). The liquid phase could be either recycled in the storage tank (Figure 3.10) or sent to a waste tank (Figure 3.11), while the gas phase was vented out to the atmosphere. For the majority of tests, the AFR set up with recycling was used. The gas phase consisted of pure carbon dioxide. The gas flow was measured with either a rotameter FL5651G for low gas flow, a rotameter FL-5671ST for medium gas flow or a rotameter FL-5681T for high gas flow. It was, then, heated to a temperature of 343 °C with a plug heater and bubbled through a column containing the same white oil used for the liquid phase. The oil present in the saturation column could be either spiked or not with naphthenic acids. The hot gas phase saturated with compounds contained in the column was directed to the gas-liquid mixing section (Figure 3.14) to create multiphase flow conditions. All the piping lines located after the oil vessel and the gas heaters were wrapped with heating tapes and insulated with three layers of insulation to minimize temperature losses. Test sections benefited of one more insulation layers for a better control of temperature.

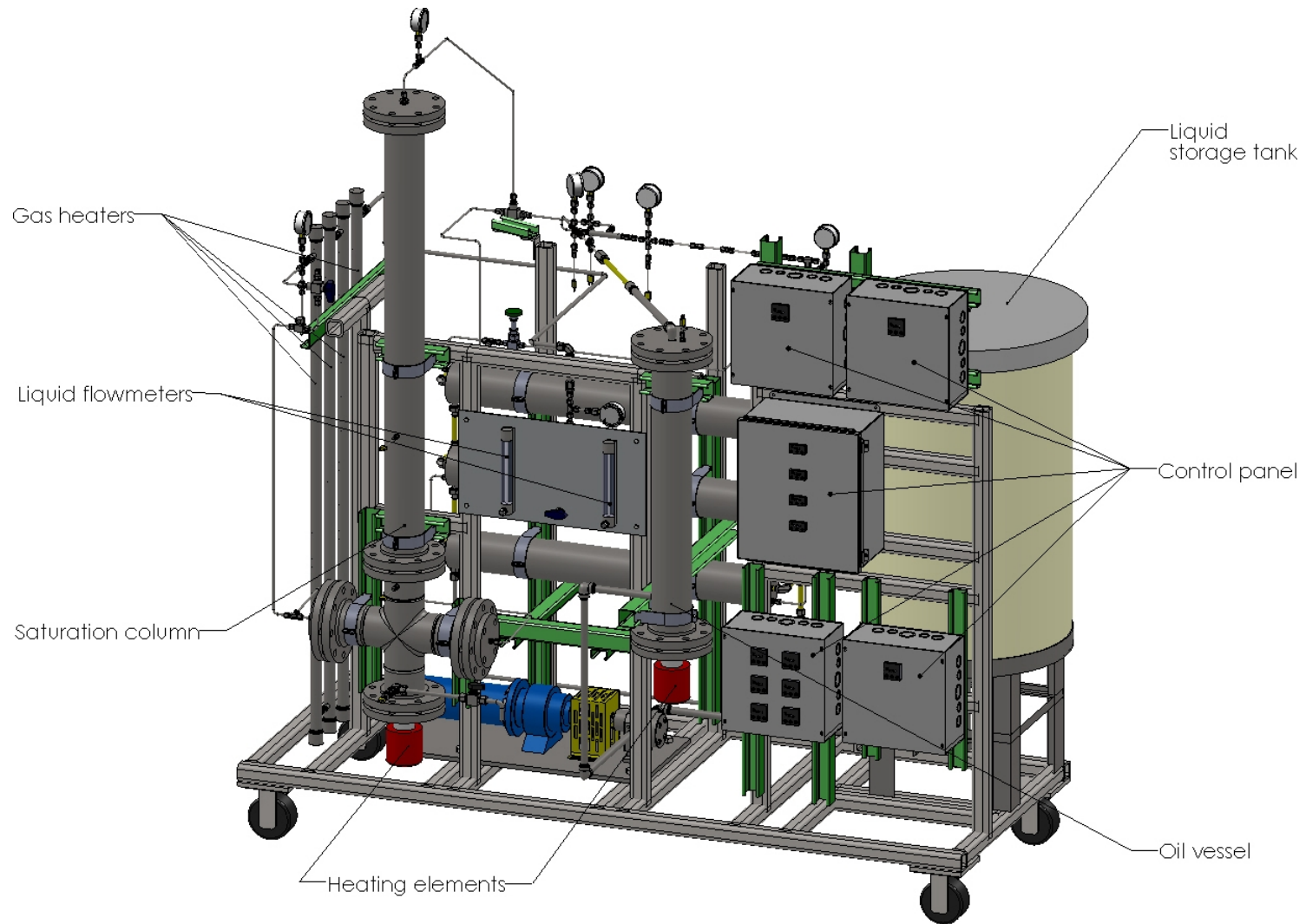


Figure 3.8: Overview of the Annular Flow Rig (front view). Note that the acid injection system is not included in this drawing.

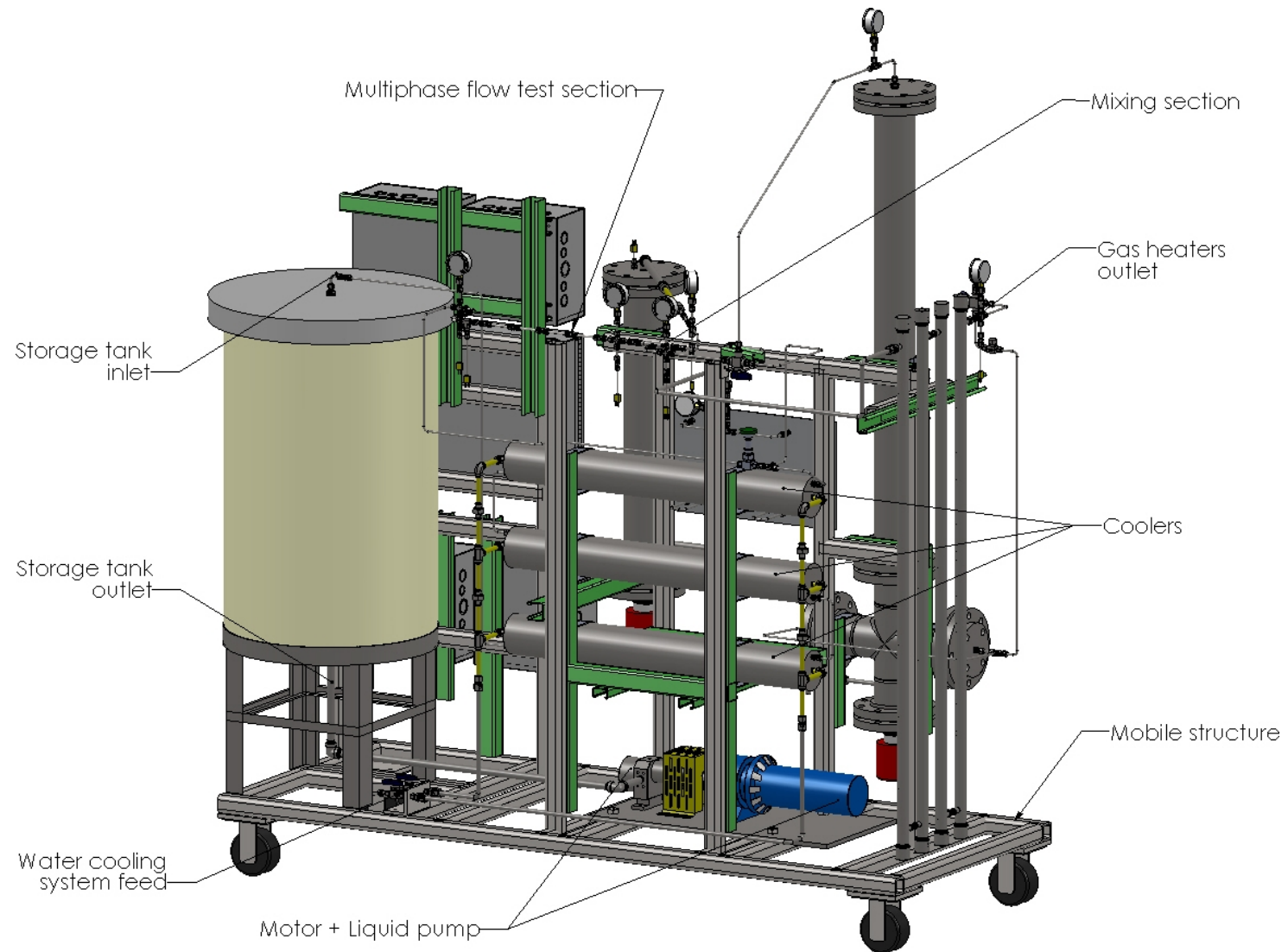


Figure 3.9: Overview of the Annular Flow Rig using a recycling set up for the liquid phase (rear view).

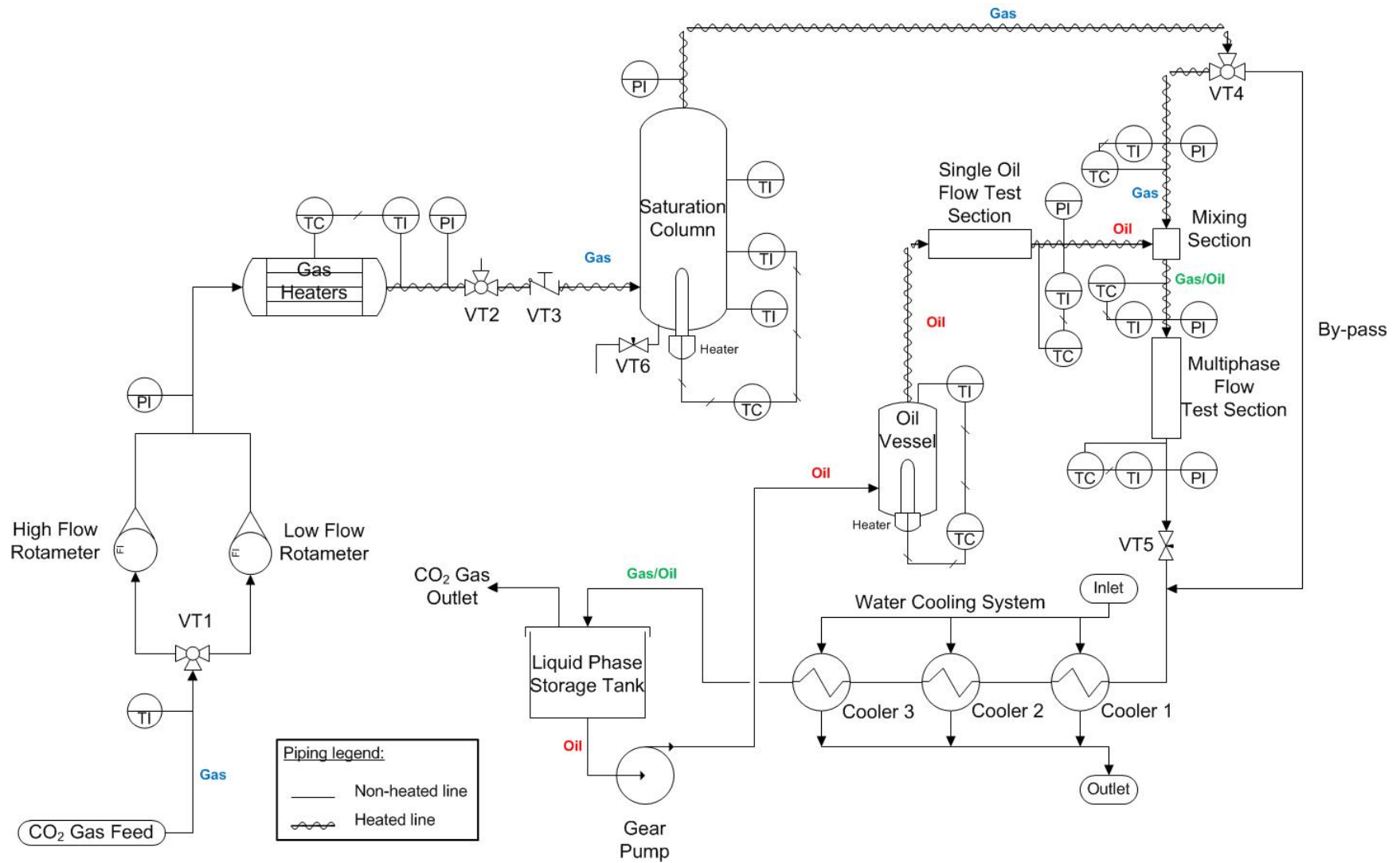


Figure 3.10: Process and Flow Diagram of the Annular Flow Rig (with liquid recycling).

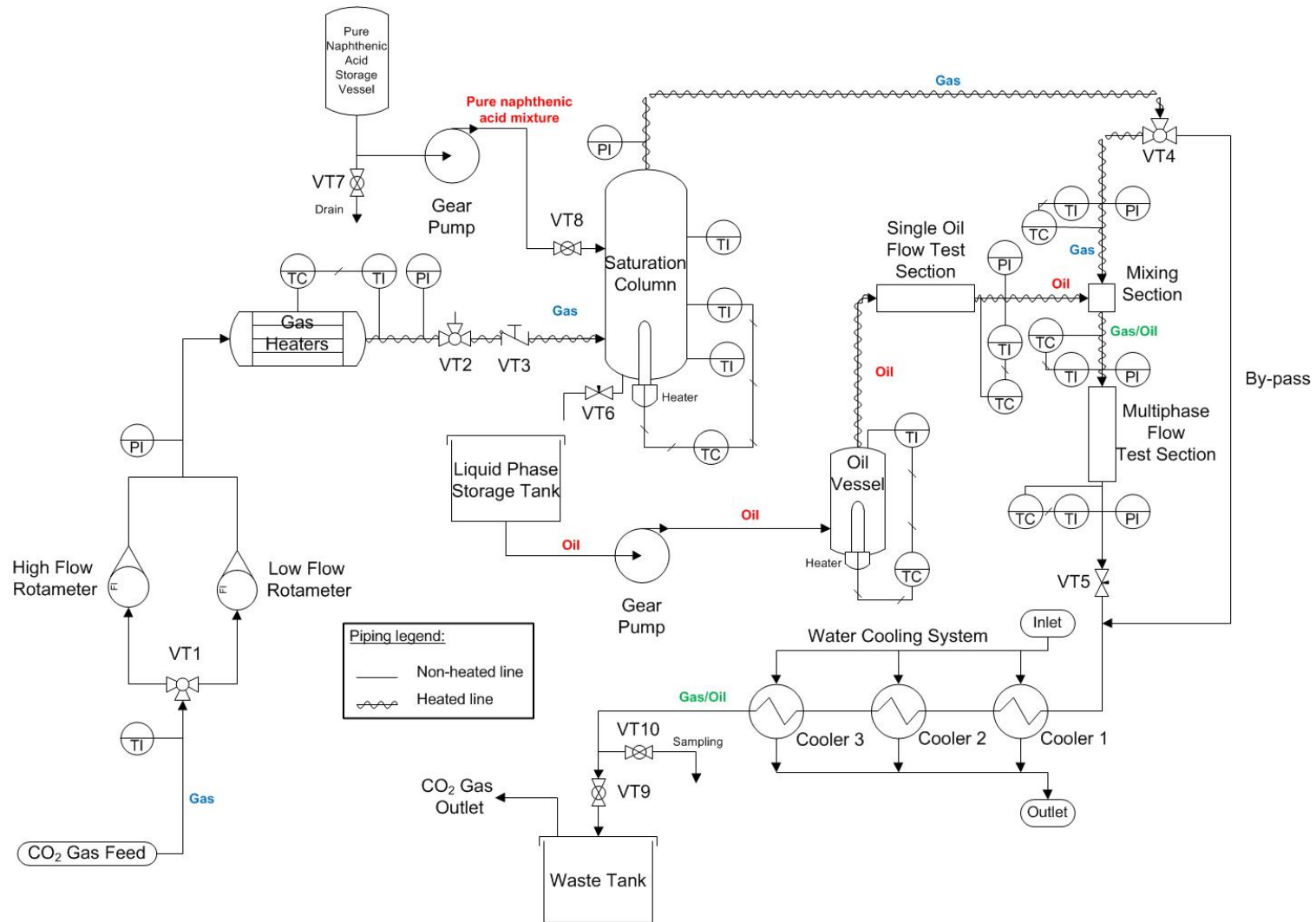


Figure 3.11: Process and Flow Diagram of the Annular Flow Rig (without liquid recycling) used for testing with pure NAP naphthenic acids injection in the saturation column.

3.2.2 Description of the AFR test sections

The structure of the test sections in single oil phase and multiphase flow was modified several times during the course of this study. The single phase flow test section was created for one sample, then extended to comprise two samples (named “0” and “V” in Figure 3.12) during Winter 2010. In July 2010, the piping in the mixing section area was completely redesigned to reduce the heat loss and the samples were gathered and relocated upstream of the mixing section (named “S1” and “S2” in Figure 3.13 and Figure 3.14). The multiphase flow test section was extended from three to six samples in early 2011 to study the effect of piping geometry and save samples for the surface analysis. Figure 3.14 shows how the test section appeared after modifications.

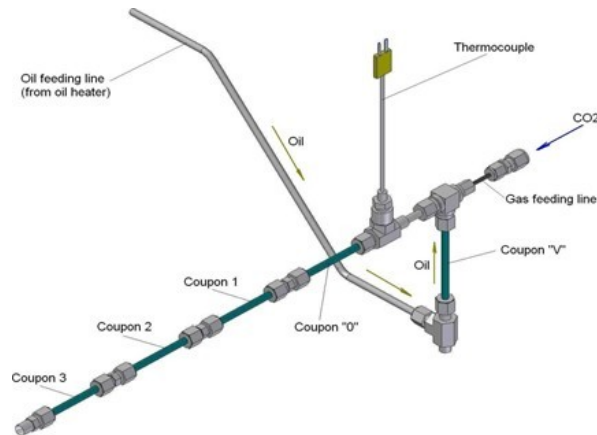


Figure 3.12: Overview of the single oil phase and multiphase flow test sections as within January–June 2010 (adapted from Bota, 2010a).

In the test sections, each sample made of carbon steel A106 was 80 mm long with a 6.35 mm outer diameter ($\frac{1}{4}$ " tube OD) and a wall thickness of 0.90 mm (0.035"). In the single phase test section, all samples had a straight shape while the multiphase flow

included straight or 90° elbow shaped samples to study the flow effects in bends. In multiphase flow test section, the straight samples (type M) were heated using the FTMA reactor modified with spacers mounted on the samples for heat transfer purposes (Figure 3.7) while the other samples (type E & S) were heated using ultra high temperature heating tapes (type Omega STH101).

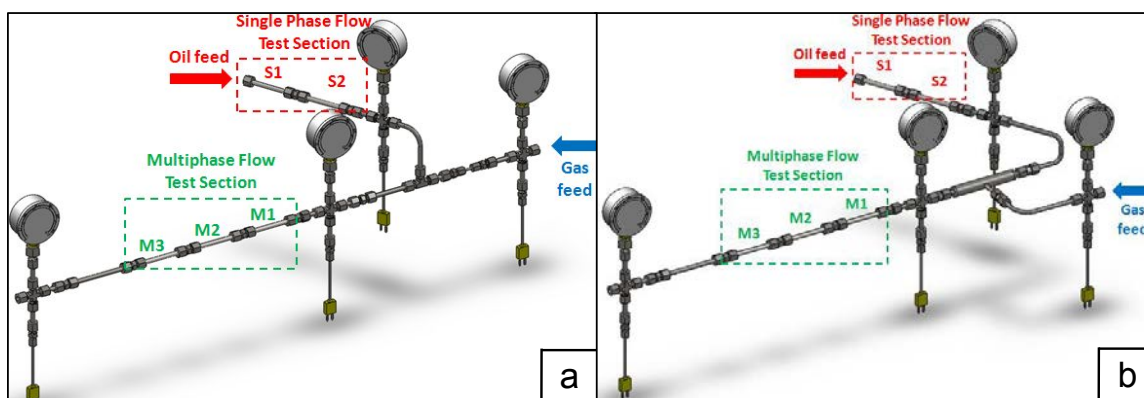


Figure 3.13: Overview of the single oil phase and multiphase flow test sections: (a) July–August 2010; (b) September 2010–January 2011.

In single phase conditions (oil), the pressure and temperature were measured downstream of the single phase test section. In multiphase conditions (gas-oil), the pressure gauges and thermocouples were located upstream and downstream of the multiphase test section. An additional thermocouple was inserted between the straight samples and the 90° elbow samples for a better temperature control (Figure 3.14). A novelty for this study was that the samples were integral parts of the flow line (the actual piping), while in all other experimental studies the samples are immersed in the chemical medium inside the operating unit.

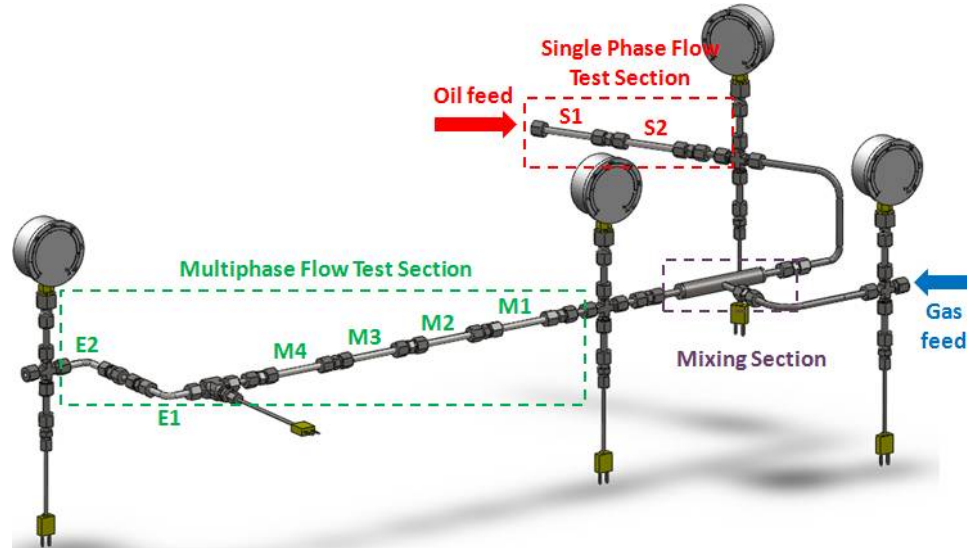


Figure 3.14: Overview of the single oil phase and multiphase flow test sections as in March 2011–March 2012.

Because of its location in the AFR, the mixing section is described together with the test sections. Two different designs of the mixing section were used during the testing (Figure 3.15). The *annulus* design, used within April 2008–August 2010, was based on the idea to create an artificial annular flow since this flow pattern was initially believed to occur in the transfer lines. The gas phase was injected through a 1/8" OD tubing in the core of a 1/4" OD tubing and mixed with the liquid phase coming from the annulus region, as shown in Figure 3.15a. However, this design generated too high pressure drop in the flow line when increasing the liquid or the gas flow rates. A second mixing section was designed to reduce the pressure losses and is presented in Figure 3.15b. By using larger tubing diameters, the new design considerably reduced the frictional pressure drop in pipes and at the bend locations (e.g., restriction and enlargement). The testing was done to check if the modification in the mixing section could affect the corrosion rate in

the multiphase flow test section. Under the same flow and chemical operating conditions, the change in the mixing section had no significant effect on the corrosion rate, as shown in Figure 3.16.

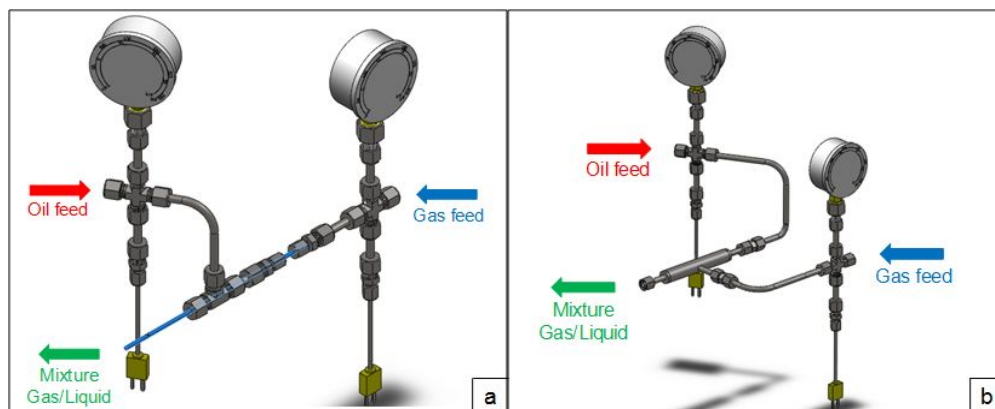


Figure 3.15: (a) Details of the gas-liquid mixing section using the 1/8" annulus design during April 2008–August 2010. (b) Overview of the gas-liquid mixing section as after September 2010.

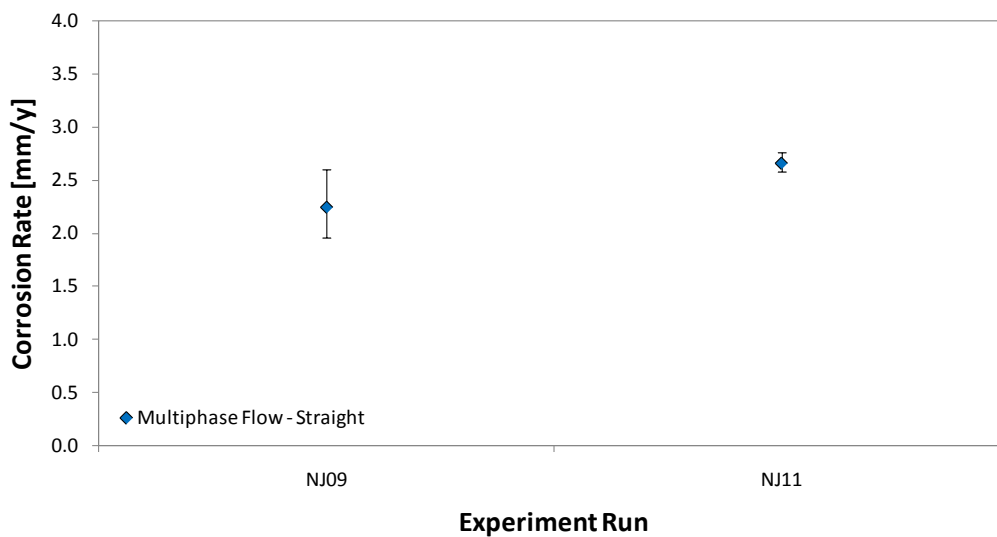


Figure 3.16: Corrosion rates before (NJ09) and after (NJ11) changes in the mixing section.

A by-pass line was set up in parallel with the test section (revisit Figure 3.10) such that in the presulfidation-challenge testing, the iron scale formed at the metal surface during the presulfidation phase could be protected from the preheated gas phase prior to the experiment.

3.3 Revamping of the AFR

3.3.1 The history of the AFR until June 2008

The first years of work on the AFR (2005–2007) consisted of designing, buying equipment and building the flow system. Figure 3.17 shows how the flow rig initially looked like around June 2008.

In 2007, the flow rig was hooked on an existing device, the FTMA, which provided the liquid phase to the AFR needed to produce the multiphase flow mixture. At that time, the yellow oil was commonly used as the liquid phase which was delivered at a flow rate of 8 mL/min by the FTMA pump. The testing solution was preheated to the required test temperature with an FTMA reactor before it reached the mixing section. The gas phase, pure CO₂, was compressed by two compressors arranged in series (only one of the compressors is shown in Figure 3.17), stored in a gas tank and pre-heated by going through a series of heaters before reaching the mixing section. The initial design of the mixing section was a simple tee in which the gas entered through the straight arm and the oil through the side arm. It was completely replaced by an *annulus* in Spring 2008, a design similar to the one in Figure 3.15a.

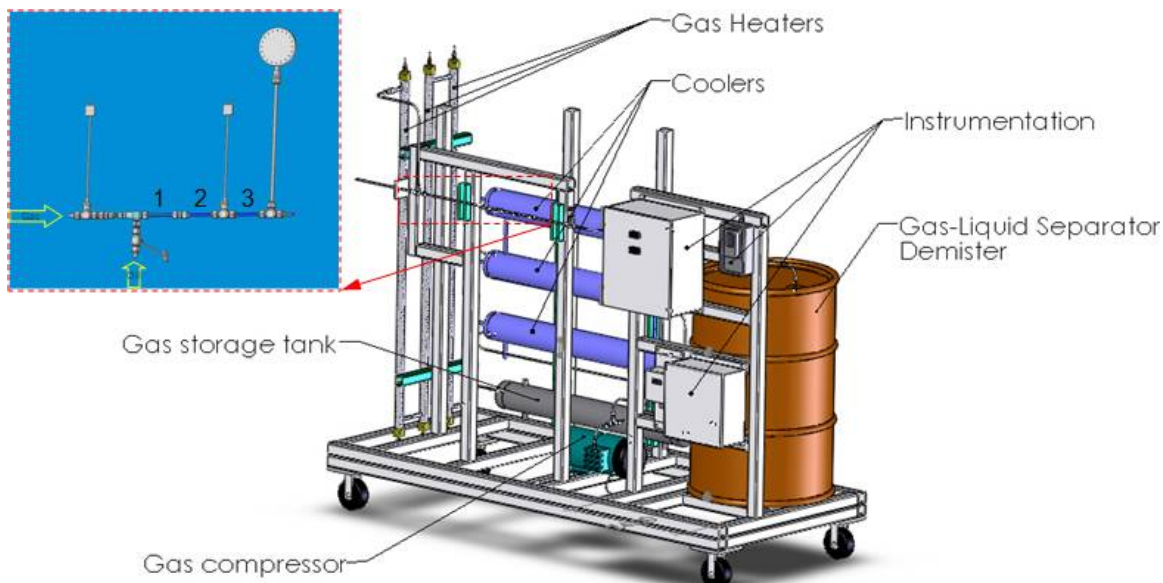


Figure 3.17: Overview of the Annular Flow Rig during 2006–2008 (adapted from Schubert, 2008). A zoom shows the mixing and the test sections as they were in Spring 2008 (adapted from Qu, 2008).

Note that the first sample of the test section (“1”) was exposed to single liquid phase flow conditions only, while the other two samples (“2” and “3”) were exposed to multiphase flow conditions. The test section (see the zoomed view in Figure 3.17) was composed of three straight carbon steel samples (4.6 mm inner diameter tubing and 8 cm length). The other operating conditions in the test section were usually maintained constant: a temperature of 343 °C, an estimated superficial gas velocity between 30 and 55 m/s, and a test duration between 3 and 24 hrs.

The first experiments, started in April 2007, revealed that corrosion rates in single liquid phase flow were similar to those measured in the FTMA. Either little or no corrosion was measured on the samples exposed to multiphase flow conditions; however, some cocking was observed at the surface of these samples. At that time, it was thought

that the type of carbon steel used for testing could be an issue for the experiment (more resistant to corrosion?), but results did not support that assumption. Because 70% of the flow loop was redesigned after June 2008, the experimental results prior to this date were not considered relevant for future work; therefore, they are not included in this study.

3.3.2 New design of the AFR

The annular flow rig has some newly designed parts to make it suitable for the purposes of this study. In this work, important changes in the AFR design occurred between June 2008 and December 2009. It featured not only the revamping of the equipment (liquid pump, storage tank) but also the design of new functionalities (saturation column, oil heater). A better control system, new instrumentation and the acid injection system were added later. Before presenting the numerous add-ons and modifications made during this period one should note that the following AFR parts presented in Figure 3.17 became obsolete and were removed between November 2008 and March 2009: gas compressors, gas storage tank, and demister.

3.3.2.1 Saturation column

Before the addition of the saturation column to the AFR flow loop, coking residues (from the thermal degradation of the oil) were recovered from samples in the multiphase flow test section, although very little corrosion was measured on these samples. It was found that the use of a dry gas phase contributed to these conditions; therefore, a *saturation column* was designed and added upstream of the gas-liquid mixing

section in order to pre-saturate the gas phase with the volatiles from the test solution (white oil sometimes spiked with naphthenic acids).

The saturation column was designed to operate at a maximal temperature of 343 °C and a standard gas flow rate of $Q_{CO_2}^0 = 1.97 \cdot 10^{-3} \text{ Sm}^3/\text{s}$. It was entirely made of stainless steel AISI 316 and included 5 and 10 cm flanges at the gas injection location, a 10 cm flanged cross, and a 132 cm long flanged pipe with a 10 cm inner diameter (Figure 3.18). All parts were machined to resist high temperature and corrosive conditions.

A 3 kW plug heater with an Incoloy® sheath resistant to naphthenic acid corrosion was inserted at the bottom of the vessel and completely immersed in the liquid phase. Three temperature probes were located at different locations (high, middle, low) of the column to measure the temperature. The “middle” probe was connected to a CN76000 controller which controlled the fluid temperature in the vessel; the entire column was insulated to reduce the heat losses. The gas phase was injected on the lateral sides of the pipe cross using eight sintered spargers (the zoomed view in Figure 3.18) made of stainless steel AISI 316 to enhance the mass transfer ($d_{max} = 100 \mu\text{m}$) and to maintain a low pressure drop through the column ($\Delta P \approx 0.03 \text{ bar}$). The saturation column contained ca. 9 L oil solution having the same fluid properties as the liquid phase used for tests in the flow system in order to reach more easily a thermodynamic equilibrium with respect to the gas/liquid conditions.

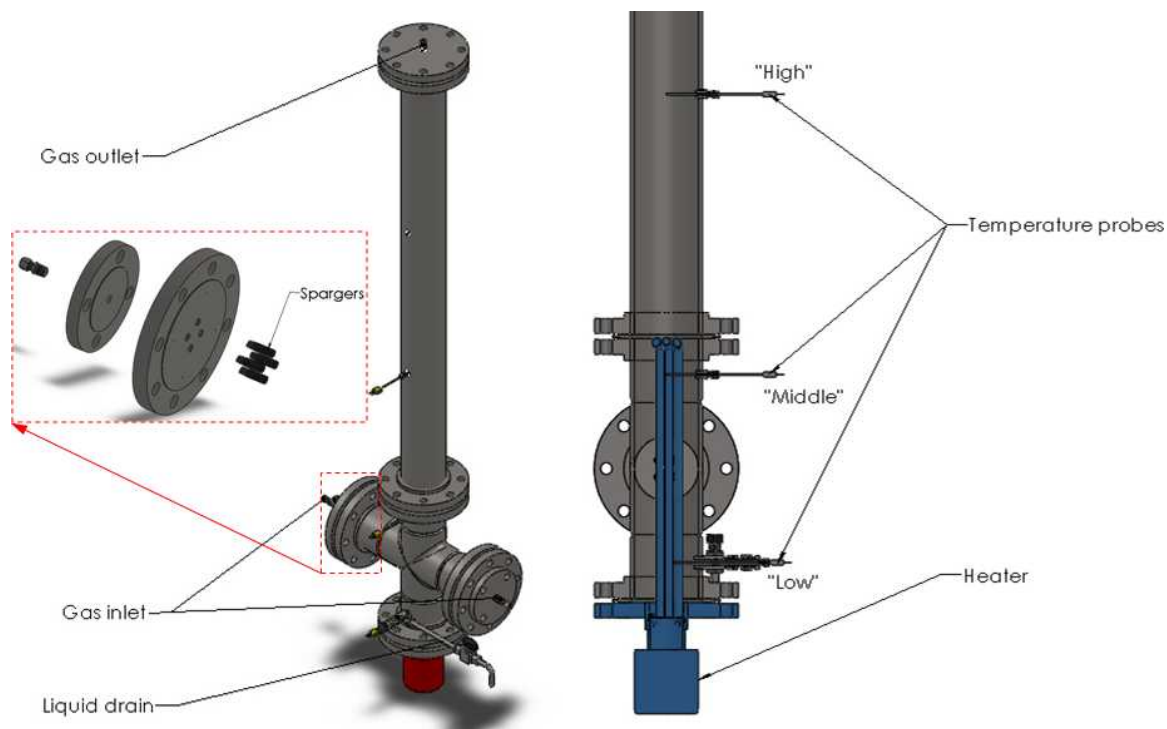


Figure 3.18: Overview of the saturation column (left) with a zoom on the gas inlet. Column cross section with temperature probes and heater (right).

Note that the upper section of the column (equivalent volume of 6.5 L) was “liquid free” to prevent any liquid entrainment in the gas phase. Some steel wool made of stainless steel AISI 316 was also placed just before the gas outlet to catch any large droplets entrained by the gas phase.

3.3.2.2 Liquid pump

Under the operating conditions before January 2009, the maximum liquid flow rate delivered by the Zenith pump was $Q_L = 8$ mL/min, representing a liquid volume fraction of ca. 0.02% when using a gas velocity of 40 m/s. The flow rate delivered by the pump was insufficient for measuring any corrosion in multiphase flow conditions since

naphthenic acid corrosion mainly occurs in the presence of a liquid phase. Therefore, the pump needed to be upgraded to meet the following specifications:

- The pump should be made from alloys that are resistant to NAP corrosion,
- The liquid flow rate should reach a liquid fraction of 1–3% for a range of gas velocity $U_{SG} = [1 - 60]$ m/s; in other words, the pump should ensure delivery of a liquid flow rate up to 1.77 L/min.

To save time for the electrical engineering design, the same pump's brand was selected (Zenith Gear). To ensure the required liquid flow rate, a Zenith Precision model B9000-9.0 cc/rev Precision Metering Pump (Colfax Corp., 2012) with a reducer ratio RR of 11:1 and a maximal liquid flow rate available calculated by eq. 3.1.1 was selected:

$$Q_{L,max} = \frac{RPM_{pump}}{RR} \cdot QC_{pump} \quad (3.3.1)$$

where RPM_{pump} is the pump rotating speed (RPM), and QC_{pump} is the pump capacity (mL/min). Using model B9000-9.0 for the pump, $RPM_{pump} = 1800$ RPM, and $QC_{pump} = 9$ mL/min, the calculated theoretical maximum liquid flow rate is:

$$Q_{L,max} = 1472 \text{ mL/min} \quad (3.3.2)$$

However, when measuring the liquid flow rate, the pump could actually deliver up to 2000 mL/min.

3.3.2.3 Oil storage tank

By selecting a high flow rate pump, a design condition was imposed for a tank in which the liquid solution could be pumped and stored. The volume of the tank was designed to be twice as large as the volume of the solution needed to fill all the piping of

the flow loop and the volume of solution needed to run one hour long experiments. Finally, the tank had a volume of 245 L (55 gal), a height of 96.5 cm and a diameter of 58.4 cm (Figure 3.8). To reduce the impact of corrosion, the material selected was polyethylene with a wall thickness of 6.4 mm (¼"). For a better drainage and cleaning of the testing solution, the bottom of the tank has a conic shape.

3.3.2.4 Oil preheater

Because of the increased liquid pumping capacity (section 3.3.2.2), the temperature of the liquid phase could no longer reach 343 °C at the test section with the previous setup (the one shown in Figure 3.17); therefore, a new oil preheater was designed to ensure the required temperature, similar to the one used in the saturation column since the heating element was in direct contact with the fluid (Figure 3.19).

The oil preheater ensured the heating from 21 °C (room temperature) to 343 °C of an 185 mL/min liquid flow rate. The oil phase was contained in a 6.5 L stainless steel AISI 316 vessel with an inner diameter of 10 cm and a height of 80 cm. A 3kW plug heater with an Incoloy® sheath resistant to NAP corrosion was inserted at the bottom of the vessel and was completely immersed in the liquid phase. The fluid temperature was controlled by a CN77000 controller, while the entire vessel was insulated to limit the heat losses.

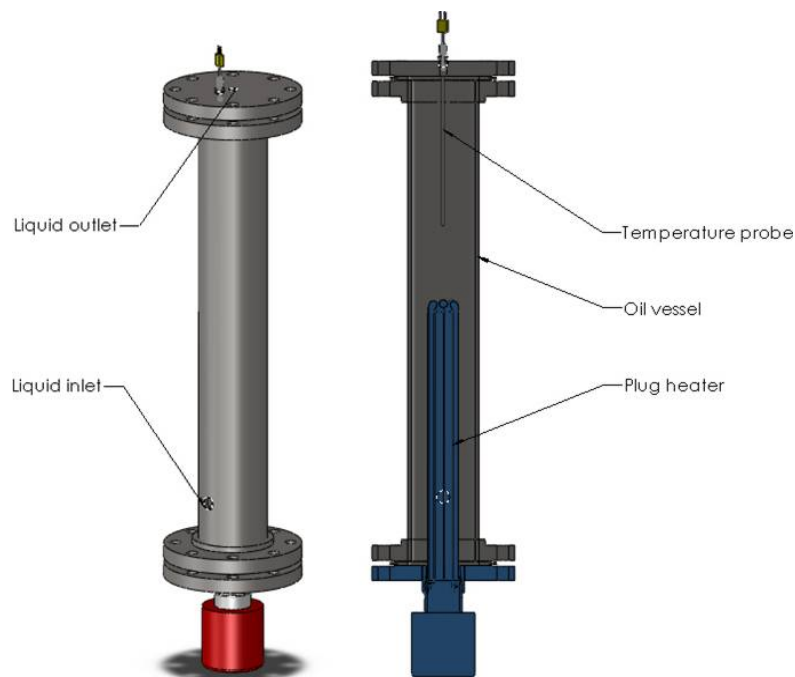


Figure 3.19: Overview of the vessel used to preheat the oil phase in the AFR (left). The column cross section showing the temperature probes and heating element (right).

3.3.2.5 Instrumentation and process control

The main instrumentation used in the AFR consisted of pressure gauges and thermocouples. Most of them were added (after June 2010) in the test and mixing sections to better control the process and easily control the eventual temperature losses. All the stream lines situated between the oil and gas pre-heaters, and the multiphase flow test section were wrapped with heavily insulated STH101 heating tapes (Figure 3.10). In most of the tests, the rheostats were manually set up by the user for controlling the heat power provided to the heating tapes. A new control panel was designed (Figure 3.20). The variable transformers were replaced by temperature controllers to rapidly reach and maintain steady state conditions (September 2011). At the same time, five skin

temperature probes were also set up in direct contact with the wrapped heating tapes and wired up to the temperature controllers for safety purposes.

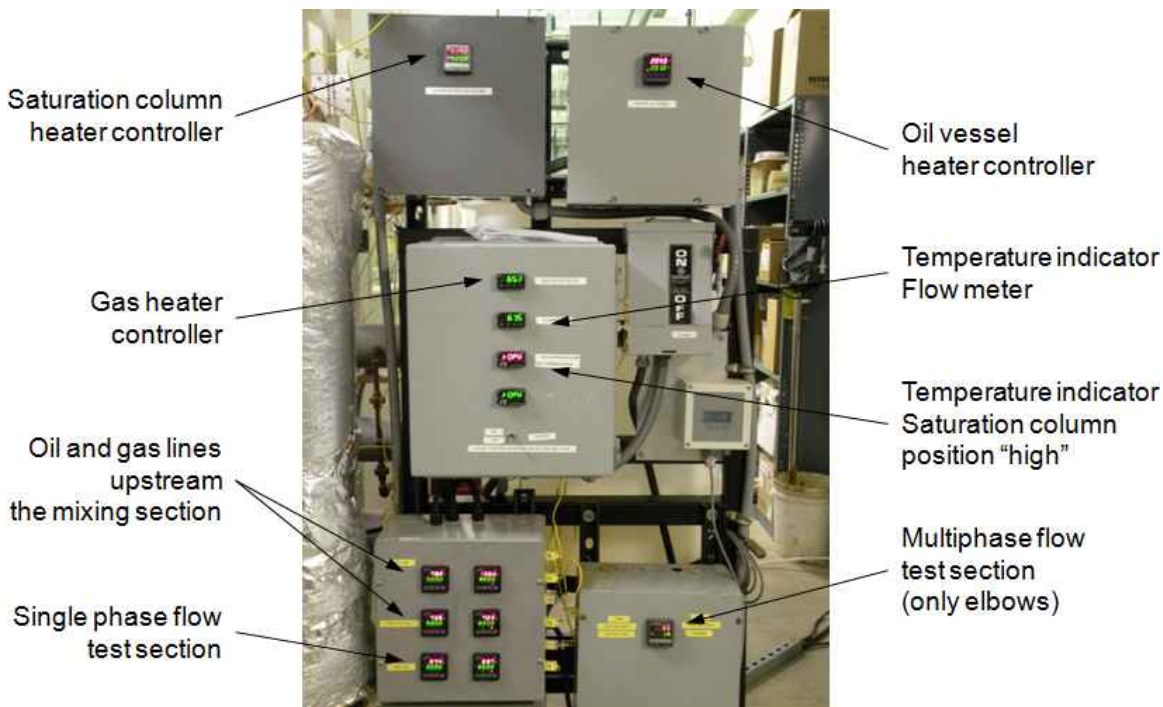


Figure 3.20: Overview of the Annular Flow Rig control panel.

3.3.2.6 Acid injection system

3.3.2.6.1 Acid injection system and recycling

The acid injection system represented the last major addition to the annular flow rig. During testing, it was observed that the naphthenic acids initially present in the saturation column were lost – as they were vaporized and entrained in the gas stream (section 3.5.2.2.1). A multiple batch injection of pure naphthenic acids into the saturation column was retained as an option to keep the acid concentration relatively constant in the

saturation column during the experiments. A schematic of the injection system is provided in Figure 3.11. While designing the acid injection system, a special attention was given to the material selection since a pure naphthenic acid mixture was used as a feed. The fluid was stored in a 500 mL stainless steel AISI 316 vessel with an inner diameter of 76 mm, then pumped with an Eldex model AA-100-S gear pump delivering a flow rate range of 0.2–10 mL/min (Figure 3.21). The pump was especially designed for corrosive environments (internals were made of stainless steel AISI 316) and rated for high pressure conditions to avoid any backflow from the column to the naphthenic acid storage vessel. All the lines were made of Inconel 600 using an inner diameter tubing of 1/8". The stainless steel AISI 316 valve (VT8 in Figure 3.11) was designed to be resistant to high temperature and corrosive environments (up to $T = 454\text{ }^{\circ}\text{C}$).

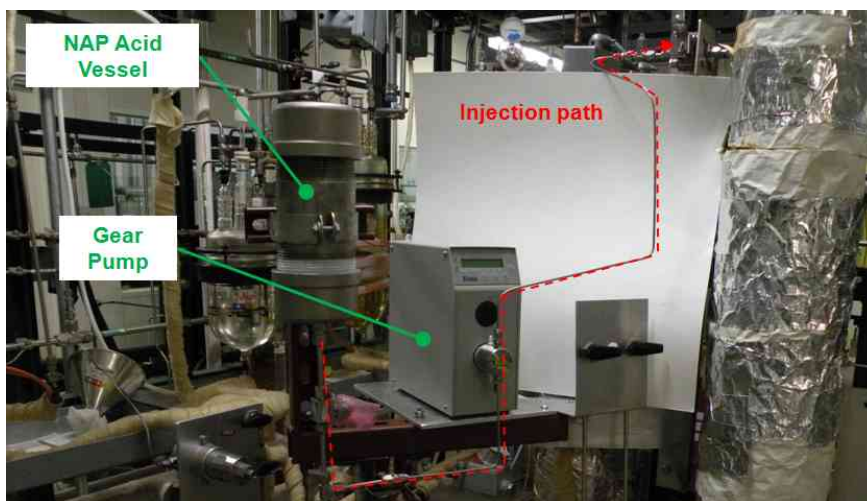


Figure 3.21: The acid injection system set up in the research facility.

3.3.2.6.2 Design without recycling

The entrained NAP vapors flowing through the multiphase test section were re-condensed in coolers and dissolved in the liquid phase. Consequently, the overall acidity of the liquid phase increased resulting in the liquid solution to be more aggressive than as initially prepared. Therefore, it was decided that the liquid phase should not be recycled when the naphthenic acids were initially present or were injected in the saturation column during the testing. In this context, the AFR design was modified by removing the recycling part after the coolers and replacing it by a non-recycling set up as shown in Figure 3.22b.

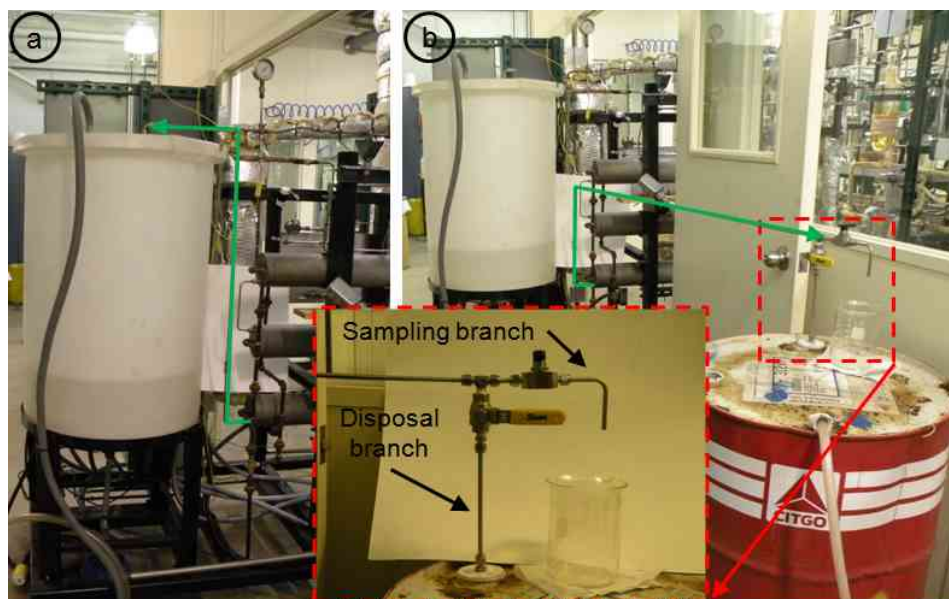


Figure 3.22: The AFR set up after coolers: (a) with liquid recycling; (b) without liquid recycling and with oil sampling device (zoom view). Green arrows indicate the flow direction.

The storage tank for the liquid phase was used as a feed tank, while another tank was added to recover the used oil. In order to perform high frequency sampling, a device was mounted before the waste tank inlet to quickly sample oil without altering the fluid flow in the AFR. During a normal run, valves VT9 and VT10 were in positions OPEN and CLOSED, respectively (Figure 3.11). When a sample was taken, the valve VT10 was first open and purged for a few seconds to eliminate any fluid left from the last sampling. Then, the oil was sampled. While sampling, the valve VT9 could be partially closed to speed up the sampling operation. Experimental results using the non-recycling set up are detailed in section 3.5.2.2.

3.4 Methodology

Leading with the definitions of the corrosion experiments done in this study and a description of the procedure used to prepare the metal samples undergoing corrosion during experiments, this section continues by describing the calibration of the instruments and the experimental procedures, including the post-processing of metal and oil samples (oil sampling only after the challenge test). In addition to these descriptions, see APPENDIX A (for the procedure used to prepare the metal samples for SEM/EDX analysis) and APPENDIX B (for the results from chemical analysis of the oil sampled in the AFR). Finally, the calculation methods used to determine the corrosion rates experienced by the metal samples are elaborated.

3.4.1 Definitions

The experiments conducted in the FTMA aimed to build up an iron sulfide (FeS) scale on the metal surface. Therefore, the experimental protocol related to this flow loop is called here *sulfidation* or *presulfidation*. On the other side, the experiments performed in the AFR were designed to assess the corrosiveness of the naphthenic acid species in the presence or absence of the iron sulfide scale; thus, the procedure is referred as *challenge* (figuratively because of “challenging” the resistance of the sulfide scale to corrosive species).

Three types of experiments were performed in this study by using the FTMA and AFR. Their definitions are detailed in this section since the same vocabulary is used as for the whole corrosion study:

- *Sulfidation Reference* is a single-step experiment in the FTMA aimed to quantify the contribution of sulfidation corrosion to the total corrosion.
- *Pure NAP Corrosion* is also a single-step experiment, designed to evaluate the NAP attack in the absence of the iron sulfide scale. This test was considered as the worst scenario in terms of corrosion rates for given operating conditions.
- *Presulfidation-challenge* is a two-step test consisting of a sulfidation experiment in the FTMA followed by a challenge experiment in the AFR. This test is considered the most complex because it requires a careful manipulation of the metal samples during their transfer from one flow loop to the other.

3.4.2 Preparation of metal samples

Only new carbon steel samples were used for each test to maintain the test reproducibility and avoid the formation of streamlines grooves due to a combination of high velocities and other operating conditions favoring NAP corrosion in the AFR.

The metal samples were cut from 2 m long carbon steel lines using a tubing cutter with a length of $L = 80.0 \pm 1.1$ mm. Both extremities of the sample were machined with a steel countersink mounted on a drill press to enlarge the inner diameter of the tubing and create a clean chamfer. Furthermore, the shims at the extremities of the sample were removed with a similar 6.35 mm outer diameter cylinder hone (600 grit) used to polish the inner surface of the samples. The final dimension of the sample inner diameter was $D = 4.29 \pm 0.03$ mm (average of 261 measured samples). Then, the metal samples were marked according to their future position in the AFR flow loop. The outer surface of each sample was polished with 400 and 600 grit papers while the inner surface (the only one actually exposed to corrosion) with a cylinder hone mounted in a drill machine. The hone had a 6.35 mm outer diameter with a 600 grit paper at its outer surface. Both polishings were carried out under isopropanol flushing. Then, the samples were dried with a flow of nitrogen.

At that stage, some of the polished straight tubings were eventually bent with a tubing bender to obtain a 90° elbow shape. Only after the bending, nuts and compression fittings (front and back sleeves) were inserted on each sample and tightened (Figure 3.23). Finally, the samples were weighed and the values recorded as the initial sample weight m_i .

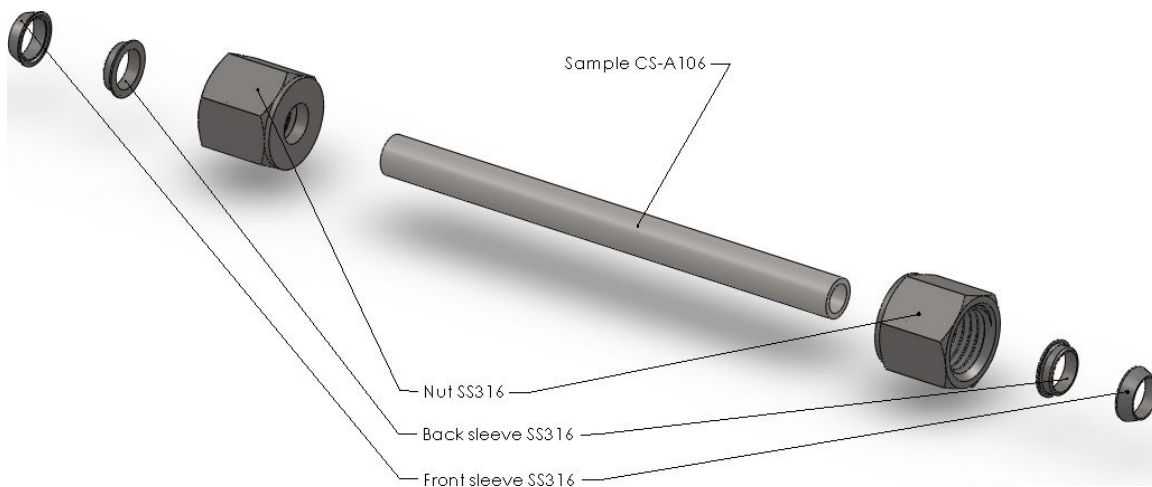


Figure 3.23: Exploded view of a carbon steel sample with its compression fittings.

3.4.3 Sulfidation (FTMA)

3.4.3.1 Instrument calibration

The main variables measured in this type of experiments were: temperature, pressure (both at different locations in the flow loop), the liquid flow rate, and the weight loss of the metal samples. The fluid temperature was measured using K-type thermocouple probes with an AISI 304 stainless steel sheath. As described in Figure 3.6, three probes were located in the multiphase flow test section #1 (sample M2), between two samples (M4 and E1), and in the single phase flow test section (sample S1). The pressure was measured using a pressure gauge calibrated by the manufacturer with a range of 1–70 bar and a measurement uncertainty of ± 0.7 bar. The pressure gauge was located upstream of the test section. The yellow oil flow rate was evaluated at the beginning of each test by measuring the volume of oil with a graduated cylinder within about 5–6 minutes. A typical flow rate of 1.5 ± 0.1 mL/min was used in experiments. The

corrosion rates were determined with the weight loss method using an analytical balance Mettler Toledo AT201. The balance was calibrated once a year by a licensed contractor with a repeatability uncertainty of ± 0.015 mg.

3.4.3.2 Experimental procedure during sulfidation

After preparation (see section 3.4.2), the metal samples were assembled together to create two different test sections (#1 and #2) as shown in Figure 3.24, inserted in the flow loop, wrapped around with heating elements and insulated.

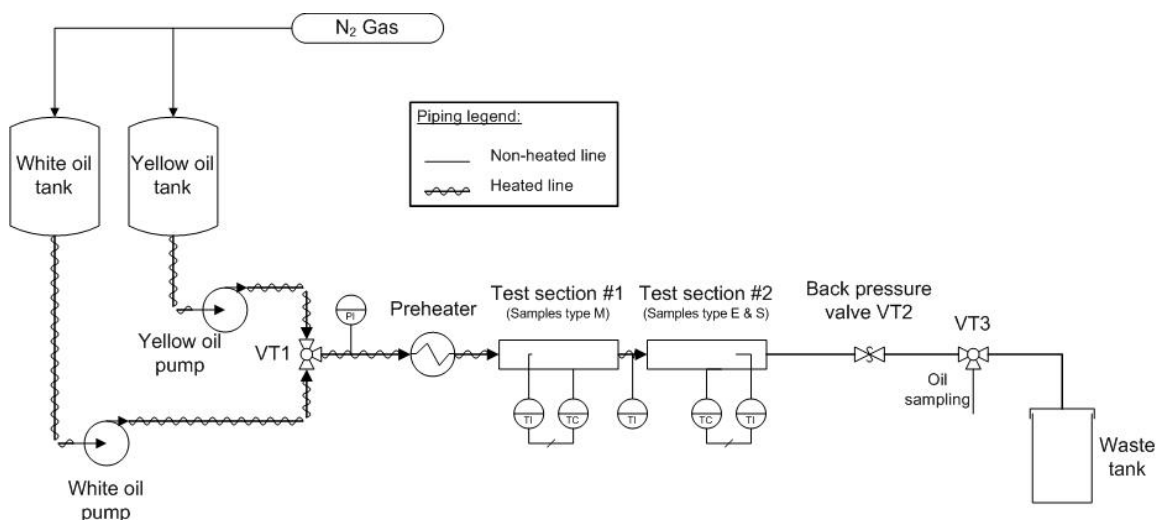


Figure 3.24: Process and Flow Diagram of the Flow Through Mini-Autoclave (FTMA).

Prior to starting the experiment, all thermocouples and power supply cables were plugged in and the vent hood was turned on. During the whole test duration, nitrogen gas was bubbled in both feed tanks containing white oil and yellow oil solutions to flush out any oxygen. The corresponding bubble rate ranged from 60 to 100 bubbles/min. The

valves VT1 and VT3 were switched to “white oil tank” and “waste tank” positions, respectively (Figure 3.24). Then, the white oil pump was turned on and all oil lines started being preheated. A few minutes later a sample was taken at the end of the FTMA to make sure that oil continuously flowed through the rig. The preheater located upstream of the test sections and the heaters of the test sections were turned on to increase the temperature in the test sections up to 316 °C in increments of 25 °C. Once the specified temperature was reached in the test sections, the white oil pump was turned off, the valve VT1 was switched to “yellow oil tank” position, and the yellow oil pump was turned on. This moment was considered to be the beginning of a 24 hrs experiment. Within the first minutes of the test, the yellow oil flow rate was measured by oil sampling (using valve VT3) and adjusted if necessary to 1.5 mL/min. After 24 hrs, the yellow oil pump was turned off, the valve VT1 was switched to “white oil tank” position, and the white oil pump was turned on. The preheater and heating elements were turned off while the white oil was flushing the test section for half an hour.

3.4.3.3 Corrosion rates assessment

The day after the experiment, both test sections were withdrawn from the flow loop and disassembled. Then, the inner surface of each sample was mechanically and chemically treated to remove any corrosion product (including the FeS scale) formed on the metal surface.

The mechanical treatments consisted of rinsing and rubbing operations. First, the samples were rinsed with toluene and acetone, dried with nitrogen gas, and then weighed.

This weight is commonly called “rinsing weight”. Then, the samples underwent rubbing with a plastic brush wetted by toluene, rinsed with toluene and acetone, dried with nitrogen gas and weighed again. This second weight value is called “rubbing weight”.

Subsequently, a chemical treatment using the ASTM G 1-90 standard (ASTM International, 2011b) and commonly called *Clarke solution* was applied to the inner surface of the sample to ensure that any corrosion product was completely removed. The Clarke solution prepared for this study consisted of 84 mL of concentrated hydrochloric acid (HCl), 2 g antimony trioxide (Sb_2O_3), and 5 g stannous chloride (SnCl_2). Since only the inner surface of the samples was exposed to NAP corrosion, only the inner surface of the samples was treated with this solution. Therefore, the Clarke solution contained in a syringe was injected by plugging a piece of tygon tubing in the sample (Figure 3.25), held 20 s inside the sample, and finally drained.



Figure 3.25: The set up used to inject the Clarke solution (HCl) and the DI water (water) in the sample without altering its outer surface.

A volume of 60 mL deionized water contained in another similar syringe was immediately injected in the sample right after draining the Clarke solution to flush the remnant hydrochloric acid. Next, the sample was thoroughly rinsed with acetone, dried with nitrogen gas and finally weighed. During the drying step, one should bear in mind that the compression fittings of the samples tend to trap liquid droplets and, hence, they require more attention. The whole Clarke-ing operation was usually repeated four times. The weight measured after the last Clarke-ing was considered as the final sample weight m_f .

The total corrosion rate CR is proportional to the sample weight loss $\Delta m = m_i - m_f$ and can be calculated by the following relationship:

$$CR = 10 \cdot 24 \cdot 365 \cdot \frac{m_i - m_f}{\rho_{Fe} \cdot A \cdot t} \quad (3.4.1)$$

where CR is the total corrosion rate (mm/y), m_i and m_f are the initial and final weight of the sample (g), ρ_{Fe} is the iron density (g/cm^3) taken as $\rho_{Fe} = 7.860 \text{ g/cm}^3$, A is the inner surface of the sample (cm^2), and t is the test duration (hrs).

In this work, the corrosion rate contribution due to sulfidation was referred as:

$$CR_T = CR_{Sulf} \quad (3.4.2)$$

3.4.3.4 Test matrix

The purpose of sulfidation experiments in the FTMA is to build an iron sulfide film on the surface of metal samples; therefore, the operating conditions are designed accordingly: a quiescent liquid flow with low concentrations of corrosive species. The

full range of operating conditions (the same were used in the presulfidation step of the presulfidation-challenge type of experiments) is given in Table 3.2.

Table 3.2: Test matrix for sulfidation reference experiments.

| Parameters | Conditions | |
|--------------------------------|-------------------------------|-------------------------------|
| | Design #2 | Design #3 |
| Liquid phase | Yellow oil | Yellow oil |
| Gas phase | N/A | N/A |
| Pipe material | Carbon steel A106 | Carbon steel A106 |
| TAN (mg KOH / g oil) | 0.1 | 0.1 |
| Test duration (hrs) | 24 | 24 |
| Temperature (°C) | 316 | 316 |
| Pipe diameter (mm) | 4.2 | 4.2 |
| Sample geometry / number | Straight / 6 90° Elbow / 0 | Straight / 6 90° Elbow / 2 |
| Liquid flow rate (mL/min) | 1.5 | 1.5 |
| Superficial gas velocity (m/s) | N/A | N/A |

3.4.4 Pure NAP corrosion or challenge (AFR)

3.4.4.1 Instrument calibration

The main parameters monitored during the pure NAP corrosion experiments in the AFR are similar to the ones measured during the sulfidation experiments in the FTMA (section 3.4.3.1.) except for the gas flow rate. The same instrumentation was also used to measure the fluid temperature. In the gas stream, the temperature probes were located at the inlet of the gas rotameter, the outlet of gas heaters, and on the saturation column (3 probes) as shown in Figure 3.18, as well as upstream of the mixing section

(Figure 3.14). In the liquid stream, one probe was placed in the oil vessel to control the temperature of the preheated oil (Figure 3.19). Several temperature probes were also inserted in the test sections. As can be seen in Figure 3.14, one probe was placed at the outlet of the single phase flow test section, with the other three in the upstream, middle and downstream of the multiphase flow test section.

Before September 2011, the heating elements wrapped around the stream lines, situated between the oil and gas pre-heaters and the multiphase flow test section, were manually controlled using variable AC transformers. After the upgrade of the control system, each temperature line was controlled by a specific controller. All temperature controllers were calibrated by the manufacturer. A CN76000 controller with an uncertainty of ± 2.8 °C was used for the multiphase flow test section consisting of type E samples, while CN7800 controllers with a uncertainty of ± 3.8 °C were used for the other test sections (single phase - type S samples and multiphase - type M samples), the mixing section, and the oil and gas lines located upstream of the mixing section.

The pressure in the AFR system was measured using pressure gauges calibrated by the manufacturer, with a range of 1–21 bar and a measurement uncertainty of ± 0.5 bar. In the gas stream, the pressure gauges were placed at the pressure regulator (located at the gas feed of the flow loop), the flow meter outlet, the gas heaters outlet, the top of the saturation column, and upstream of the mixing section. In the liquid stream, pressure gauges were added to the outlet of the single phase flow test section and the inlet/outlet of the multiphase test section (Figure 3.14). The readings in the pressure gauges were between 1 and 7.2 bar, depending on the gas velocity chosen for the operating conditions.

The total pressure drop across the flow loop when running the gas-oil mixture was around 0.3 bar.

Gas flow rates were measured with rotameters of serial type FL5000. Depending on the superficial gas velocity desired in the multiphase flow test section, one of the following three rotameters was used: FL5651G for low flow, FL5671ST for medium flow or FL5681T for high flow. Flow rates were between 0 and 66370 mL/min (for air considered as the gas phase). The flow meters were calibrated by the manufacturer with a measurement uncertainty of 3%.

The liquid flow rate was delivered by a Zenith B9000-9.0 cc/rev metering pump. A series of tests were run to determine a correlation between the pump controller value and the actual liquid flow rate delivered by the pump. The flow measurements were performed in single liquid phase conditions. For each measurement, the volume of oil accumulated in a graduated cylinder and the time were recorded. A 250 mL graduated cylinder was used for small volumes, while a 1000 mL for larger volumes. For each controller value, three measurements of the flow rate were performed. A linear regression of the actual measured flow rate vs. the controller reading gave the following calibration line (Figure 3.26):

$$Q_L = (13.24 \pm 0.07) \cdot PCV_{pump} + (14.89 \pm 6.02) \quad (3.4.3)$$

where Q_L is the liquid flow rate (mL/min) and PCV_{pump} is the pump controller value (-). Because the volumetric liquid flow rate Q_L is a function of the temperature, the temperature was also recorded and was always in the range $T = 31.6 \pm 3.9$ °C (average of 56 measurements).

The corrosion rates were determined with the weight loss method using an analytical balance Mettler Toledo AT201. The balance was calibrated once a year by a private contractor with a repeatability uncertainty of ± 0.015 mg.

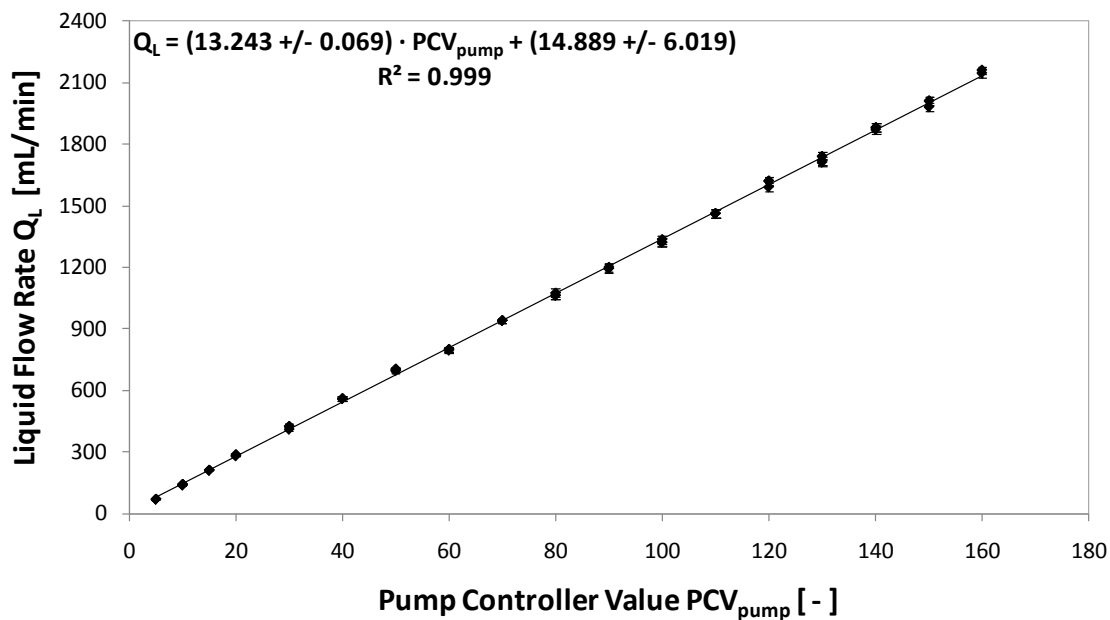


Figure 3.26: Calibration of the actual liquid flow rate delivered by a Zenith pump B9000-9.0 cc/rev.

The uncertainty analysis for each piece of the equipment used in the AFR is provided in APPENDIX C. A special attention was given to the calculation of the corrosion rate error.

3.4.4.2 Experimental procedure for pure NAP corrosion

The metal samples were assembled in two different test sections (single phase and multiphase) as depicted in Figure 3.14, inserted in the flow loop, wrapped around with heating elements and insulated. The FTMA reactor was modified to increase the heating of type M samples, a technique consisting of heat transfer through spacers. Before each experimental run, all thermocouples and power supply cables were plugged in the AFR. The vent hood was turned on and valves supplying water for the cooling system were opened. The valve VT1 was set according to the gas flow conditions used for the test (Figure 3.10). Valves VT2, VT4 and VT5 were positioned as “closed”, “by-pass” and “closed”, respectively. Then, the power was turned on. The fluids in the saturation column and the oil vessel started being preheated. To avoid overheating (and eventually, coking) the oil, temperature in both vessels was increased in increments of 25 °C. The liquid phase in the oil vessel was preheated to 343 °C in the test sections. The fluid present in the saturation column was preheated to 260 °C (when no naphthenic acids are present in the column) or 343 °C (when the liquid solution was spiked with naphthenic acids). When the target temperature was reached in the saturation column, the valve VT2 was switched to the column stream. The gas phase was bubbled through the saturation column while the gas heaters and other heating elements wrapped around the gas lines were turned on. A temperature drop was usually observed in the column due to the initial injection of the cold gas. After a few minutes, the specified temperature was reached again. This moment marked the end of the preheating phase.

In the next step, both gas and liquid phases were allowed to flow through the test sections. The valve VT5 was first opened, and then, the valve VT4 was switched to the test section line to direct the gas phase through the test section line instead of by-passing it. Immediately after, the liquid pump, preset for the desired flow rate, was turned on and the liquid phase started flowing through the two test sections (single phase and multiphase). The heaters wrapped around the oil line (between the oil vessel and the single phase flow test section), the mixing line area (from the single phase flow test section to the upstream of the entrance of the multiphase flow test section) and the multiphase flow test section (including the FTMA reactor modified for heating type M samples) were activated and set to reach the operating temperature in increments of 25 °C. The starting point of the experiment was considered when the temperature at the entrance of the multiphase flow test section reached 288 °C. A previous study using similar fluids concluded that below this temperature, NAP corrosion was less important (Kanukuntla, 2008); therefore, this study ignored the contribution of NAP corrosion occurring at temperatures below 288 °C. It took around 15 min to stabilize the heating temperature (steady state) in the test sections from the moment when the liquid pump had started. The setup of the desired gas flow rate (using a rotameter valve) was synchronized with the setup of the controlling temperature.

The entire test lasted 6 hrs during which the gas flow rate, temperature and pressure were regularly observed and recorded.

At the end of the test, all heating elements were turned off, but the liquid and gas phases kept flowing for a few minutes to avoid coking the oil on the hot metal surfaces.

Then, the liquid pump was stopped to allow the gas phase purge the liquid from the test sections lines. Five minutes later, valve VT4 was switched to the “by-pass” line and valve VT5 was closed. For safety reasons, the gas phase was allowed to flow through the gas heaters until their outlet temperatures dropped below 149 °C. Only then, the gas stream could be turned off and all the power sources shut down.

3.4.4.3 Corrosion rates assessment

Although the same procedure was used to prepare the metal samples for measuring the total corrosion rates as in section 3.4.3.3, in this case the total corrosion rate was a result of pure NAP corrosion only:

$$CR_T = CR_{NAP} \quad (3.4.4)$$

3.4.4.4 Oil sampling

Most of the experiments were carried out with some liquid recycling. Therefore, the oil was sampled in the saturation column and the tank storing the liquid phase, before and after each test. These oil samplings helped to control the TAN, dissolved iron and sulfur concentrations in the liquid solutions. In cases when these concentrations varied too much, the whole liquid solution had to be renewed. For instance, if the iron concentration was too high, the whole liquid solution had to be changed because the NAP corrosion could have been inhibited by the corrosion by-products (described in section 3.5.2.1). The TAN concentration was determined with a potentiometric method, ASTM D664 (ASTM International, 2011a). The dissolved iron concentration was obtained with

an Inductively Coupled Plasma (ICP) method. Since the level of sulfur was very low in the liquid stream, the sulfur concentration was measured using the X-Ray Fluorescence (XRF) technique.

3.4.4.5 Test matrix

The main monitored parameters, such as temperature, test duration, reactive sulfur content, pipe diameter, and metallurgy were not varied among the tests. The separate (or combined) effects of TAN concentration, sample geometry, flow rate, and multiphase flow on NAP corrosion were analyzed. The operating conditions for challenge testing are detailed in Table 3.3. Note that the experiments using a liquid flow rate of 185 mL/min were only performed at a superficial gas velocity of 20 m/s and a TAN 4 concentration.

Table 3.3: Test matrix for pure NAP corrosion experiments.

| Parameters | Conditions |
|--------------------------------|--------------------|
| Liquid phase | White oil |
| Gas phase | CO ₂ |
| Pipe material | Carbon steel A106 |
| TAN (mg KOH / g oil) | 2, 4 |
| Reactive sulfur content (wt%) | 0 |
| Test duration (hrs) | 6 |
| Temperature (°C) | 343 |
| Pipe diameter (mm) | 4.2 |
| Liquid flow rate (mL/min) | 80, 185 |
| Superficial gas velocity (m/s) | 0, 1.5, 10, 20, 33 |

3.4.5 Presulfidation-challenge (FTMA-AFR)

3.4.5.1 Experimental procedure for combined sulfidation and NAP corrosion

This two-step procedure includes the sulfidation (presulfidation) of metal samples in the FTMA and the subsequent exposure of these samples to the conditions favoring NAP corrosion (challenge) in the AFR. Figure 3.27 illustrates the different setups of the test sections in the FTMA and AFR and their transfer from one loop to another.

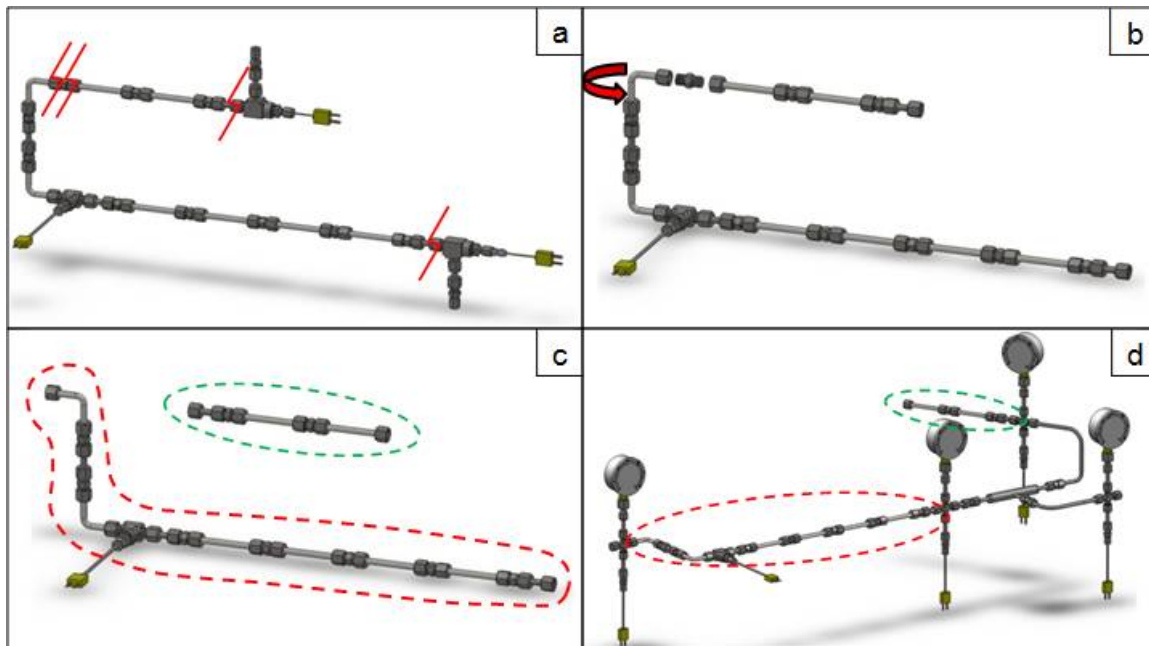


Figure 3.27: Modification and transfer of the single phase (green dashed line) and multiphase flow test sections (red dashed line) from the FTMA set up (a) to the AFR set up (d). The FTMA test section was split in two main parts (a to b). The multiphase flow test section was readjusted (b to c) before insertion in the AFR with the single phase test section (c to d).

After removing the insulation (in the FTMA), the piping was disconnected at three different locations: between samples E2 and S1, upstream from the thermocouple of

the multiphase flow test section and downstream from the single phase flow test section (Figure 3.27a). Then, the liquid solution trapped in the test sections was drained out; the connection fittings at the extremities of each test section were carefully cleaned (if necessary) from oil to avoid any coking during the subsequent challenge in the AFR. Finally, both test sections were inserted in the AFR as can be seen in Figure 3.27d. The pure NAP corrosion experiment was run according to the description in section 3.4.4.2.

3.4.5.2 Corrosion rates assessment

After the challenge in the AFR, the corrosion rates were determined following the procedure described in section 3.4.4.3. The total corrosion rate (CR_T) measured included the contributions of sulfidation corrosion (CR_{Sulf}) and NAP corrosion (CR_{NAP}). Therefore, the corrosiveness of the naphthenic acid attack in the presence of an iron sulfide scale was assessed as follows:

$$CR_{NAP} = CR_T - CR_{Sulf} \quad (3.4.5)$$

Note that there was no intermediary corrosion rate measured after presulfidation because the procedure would have damaged the iron sulfide scale freshly built. Instead, the sulfidation corrosion rate CR_{Sulf} was taken as the average of all sulfidation reference tests.

3.4.5.3 Test matrix

As in the challenge, the parameters monitored during the combined presulfidation-challenge experiments, were constant among experiments. These

parameters are: temperature, test duration, sulfur content, pipe diameter and metallurgy. Table 3.4 summarizes the operating conditions in the two flow loops. The presence of the iron sulfide scale at the metal surface and the effects of TAN concentration, sample geometry, and multiphase flow on NAP corrosion were studied through this type of experiments.

Table 3.4: Test matrix for presulfidation-challenge experiments.

| Parameters | Presulfidation | Challenge |
|--------------------------------|-----------------------|-------------------|
| Liquid phase | Yellow oil | White oil |
| Gas phase | N/A | CO ₂ |
| Pipe material | Carbon steel A106 | Carbon steel A106 |
| TAN (mg KOH / g oil) | 0.1 | 2, 4 |
| Reactive sulfur content (wt%) | 0.25 | 0 |
| Test duration (hrs) | 24 | 6 |
| Temperature (°C) | 316 | 343 |
| Pipe diameter (mm) | 4.2 | 4.2 |
| Liquid flow rate (mL/min) | 1.5 | 80 |
| Superficial gas velocity (m/s) | N/A | 0, 10, 20 |

3.4.6 Surface analysis of metal samples

Some samples were preserved for surface analyses after sulfidation or presulfidation-challenge testing using a scanning electron microscope (SEM) and energy-dispersive X-ray spectrometry (EDX) techniques. Because of their tubular geometry, only sample cross sections were prepared for surface analyses following a new procedure

described in APPENDIX A. For each sample, the longitudinal (XL) and radial (XR) cross sections were analyzed (Figure 3.28).



Figure 3.28: Longitudinal (a) and radial (b) cross sections of a CS sample used in the SEM/EDX surface analysis.

3.5 Results and Discussion

Previous sections provided information about the type of experiments and the procedures used to study the corrosion of carbon steel samples, either due to sulfidation, naphthenic acids or a combination of both. Other factors influencing corrosion were also studied, such as TAN concentration and flow velocity. Results are reported separately, in this section, for each type of experiments. Full experimental data is provided in APPENDIX D, 0 and APPENDIX F.

3.5.1 Sulfidation corrosion

The corrosion rate of metal samples due to sulfur compounds and the formation of

the iron sulfide scale by-product were assessed from sulfidation experiments and described in section 3.4.3.3. Previously, it was mentioned that the test sections experienced three different designs in order to properly serve sulfidation experiments (section 3.1.2). Reliable results were obtained with designs #2 and #3; therefore, only these results are reported here. Only one single experimental run (NJ18) was performed using the design #2. The corrosion rates of the samples located in the multiphase flow test section were considered as reliable while corrosion rates measured in single phase flow test section (Figure 3.5) were discarded due to too high temperature conditions leading to a very aggressive form of sulfidation corrosion. Design #3, representing an improvement of #2, served to run more trustworthy sulfidation experiments (NJ19 - NJ23 and NJ38). Results are plotted in Figure 3.29 while experimental data is available in APPENDIX D.

As shown in Figure 3.29, the M samples (M2, M3 and M4) heated by the FTMA reactor exhibited higher corrosion rates than E & S samples (E1, E2, S1 and S2), heated with heating tape. The small differences between these corrosion rates can be attributed to the use of different heating systems. Although sample M1 was heated as any other M-sample, the related corrosion rate measurements among experiments were consistently lower than the ones obtained from homologous samples. These lower values suggested that the fluid temperature at the entrance of the FTMA reactor (where sample M1 was located) was lower than 316°C; consequently, the sulfidation corrosion was less aggressive at this particular location.

The average corrosion rates from Figure 3.29 are also reported in Table 3.5. These values will serve as references in the presulfidation-challenge testing to account for the

contribution of sulfidation to the total corrosion. They were subtracted from the total corrosion rates measured after the presulfidation-challenge test so that the corrosion rate only due to the naphthenic acid attack could be assessed.

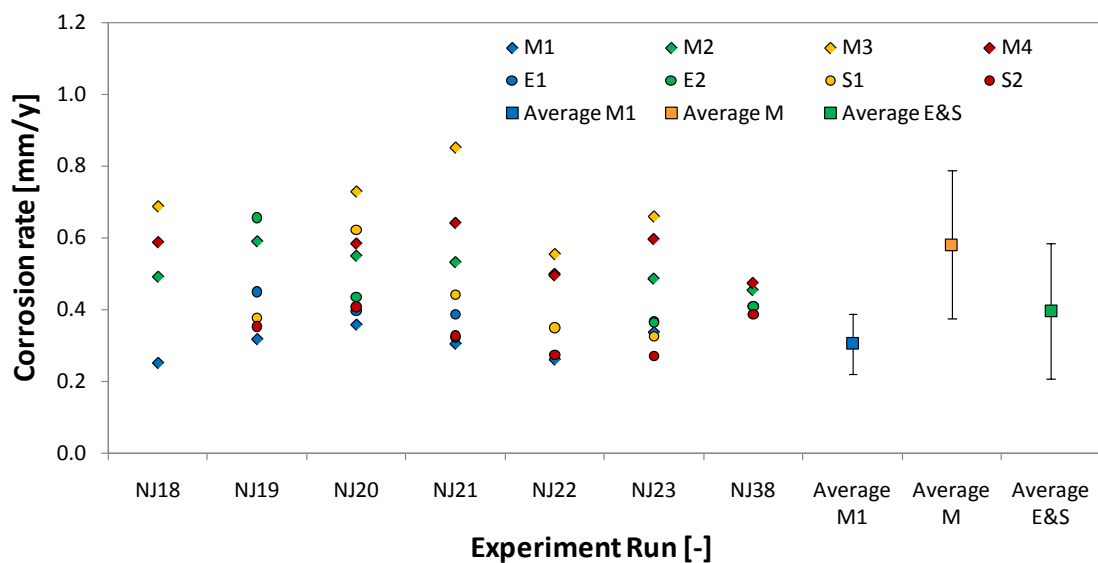


Figure 3.29: Corrosion rates measured during the sulfidation process in the FTMA. Averages ($n \leq 7$) are reported by sample type or ID as it was used in experiments. The error bars represent 2 standard deviations.

Table 3.5: Average corrosion rates due to sulfidation.

| Sample type | Corrosion rate (mm/y) | Corrosion rate error (mm/y) |
|----------------|-----------------------|-----------------------------|
| M1 | 0.30 | 0.08 |
| M2, M3, M4 | 0.58 | 0.20 |
| S1, S2, E1, E2 | 0.40 | 0.19 |

Three samples (M1, M3, S1) used in test NJ38 were preserved for the SEM/EDX surface analysis. Samples were specifically selected according to their position in the

FTMA in order to observe the influence of heating method on the formation of the iron sulfide scale during the sulfidation process.

Two cross sections of each sample - longitudinal (XL) and radial (XR) - were analyzed. There was no difference between the cross sections used in the SEM/EDX analysis. The scale thickness and morphology were similar among the three samples, suggesting that the different heating methods use did not affect the formation of the scale. Therefore, it was decided that the longitudinal cross section of sample S1 could be used as reference for all sulfidation experiments. The SEM analysis, performed at different magnitudes, signaled the presence of a thin scale (1-3 μm) at the metal surface visualization of which was enhanced using the SEM backscattering feature (Figure 3.30 and Figure 3.31).

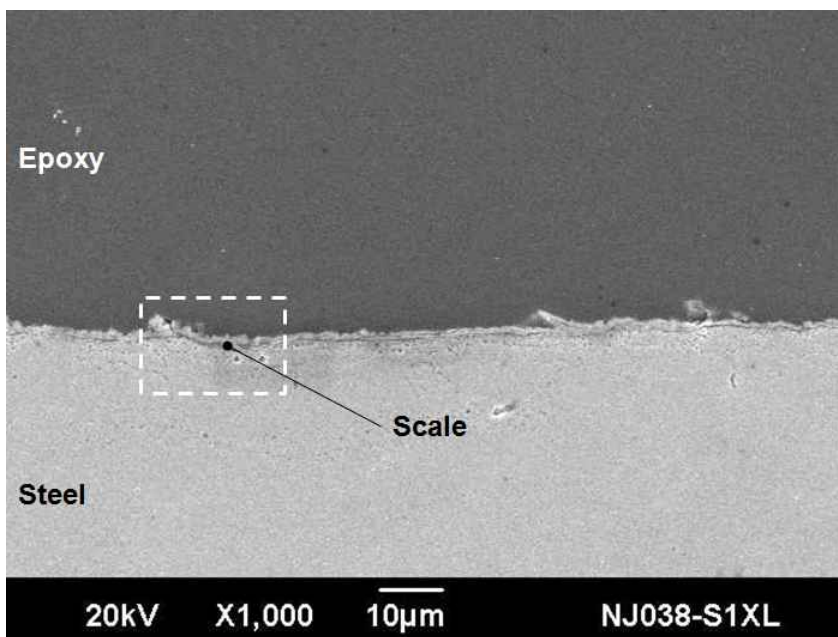


Figure 3.30: Longitudinal cross-section of a CS sample (magnified 1000X). The FeS scale was built with yellow oil in the FTMA for 24 hrs and at 316 °C.

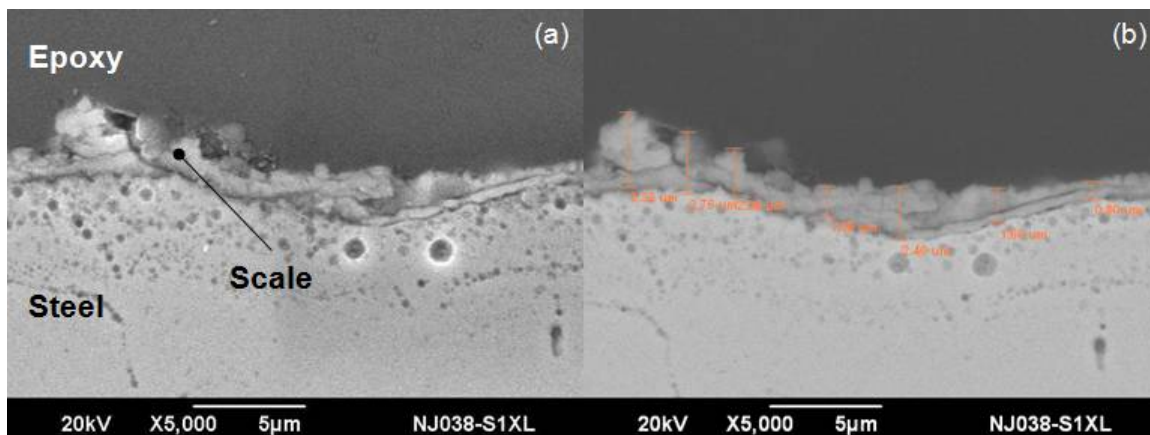


Figure 3.31: Longitudinal cross-section of a CS sample (magnified 5000X). (a) SEM picture; (b) backscattering. The FeS was built with yellow oil in the FTMA for 24 hrs and at 316 °C.

The EDX analysis confirmed the presence of an iron sulfide scale. In Figure 3.32a, the elemental profiles through the scale suggested a high oxygen content, and implicitly, the presence of an oxide layer at the metal surface. In the EDX analysis, the oxygen content is usually plotted relative to the highest content of oxygen. When plotting the absolute oxygen values with the other species (Figure 3.32b), the oxygen content is almost negligible. This artifact could be seen in most of the EDX analyses done in this work; that is why the absolute values of each element were systematically plotted to check if there was really any oxygen in the scale. The eventual presence of oxygen in the scale could be attributed to the exposure of samples to air during the time between polishing and inserting them into the flow loop.

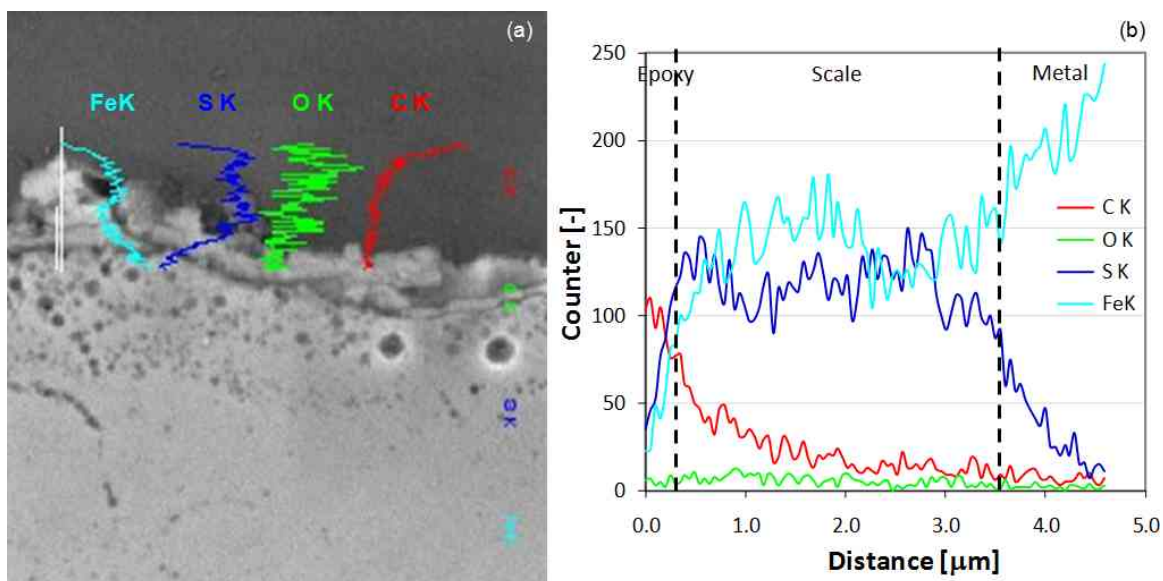


Figure 3.32: (a) EDX analysis across the longitudinal cross-section of a CS sample. The FeS scale was built with yellow oil in the FTMA for 24 hrs and at 316 °C. (b) Equivalent EDX analysis re-plotted with absolute values showing that oxygen content is only an artifact.

3.5.2 Pure NAP corrosion

Preliminary tests were run to calibrate some of the instruments on the flow loop, identify eventual technical limitations by improving the AFR design, and document all the necessary running procedures related to the flow loop. These tests focused mainly on temperature control, mixing section design (section 3.2.2), corrosion inhibition, and testing reproducibility. Unless specified, the liquid phase was continuously recycled in the AFR during all the experiments. The loss of naphthenic acids in the saturation column was separately treated (section 3.5.2.2.) from the other preliminary tests since the topic was more thoroughly investigated (i.e., flashing effects).

Furthermore, the effects of TAN concentration, superficial gas velocity, and piping geometry on NAP corrosion were also analyzed and detailed in the subsequent

sections. The corrosion rates obtained in this section constitute the baseline of the presulfidation–challenge experiments. Operating conditions, corrosion rate measurements and experimental chronology are all reported in 0.

3.5.2.1 Preliminary tests

The primary operating unit designated to study the NAP corrosion was tested prior to running the experiments given the complexity of the factors that may interact and affect the final corrosion rate. Few main issues were encountered, which are further discussed.

The heat loss and control of temperature

A common issue to all preliminary tests was the heat loss in the AFR test sections and nearby. Two conditions were necessary and sufficient for a better control of temperature: (1) ensure sufficient heating in the feed lines upstream of the test sections; (2) minimize the heat transfer along these lines. An illustration of temperature variability during this phase is shown in Figure 3.33. Here it appears that a drop in temperature by 36 °C determined a decrease in corrosion rate by a factor of 1.8, in the single phase flow environment. On the contrary, the temperature has a less strong effect on the corrosion rate under multiphase flow conditions (a decrease by a factor of 1.4) being usually much lower than in single phase flow conditions.

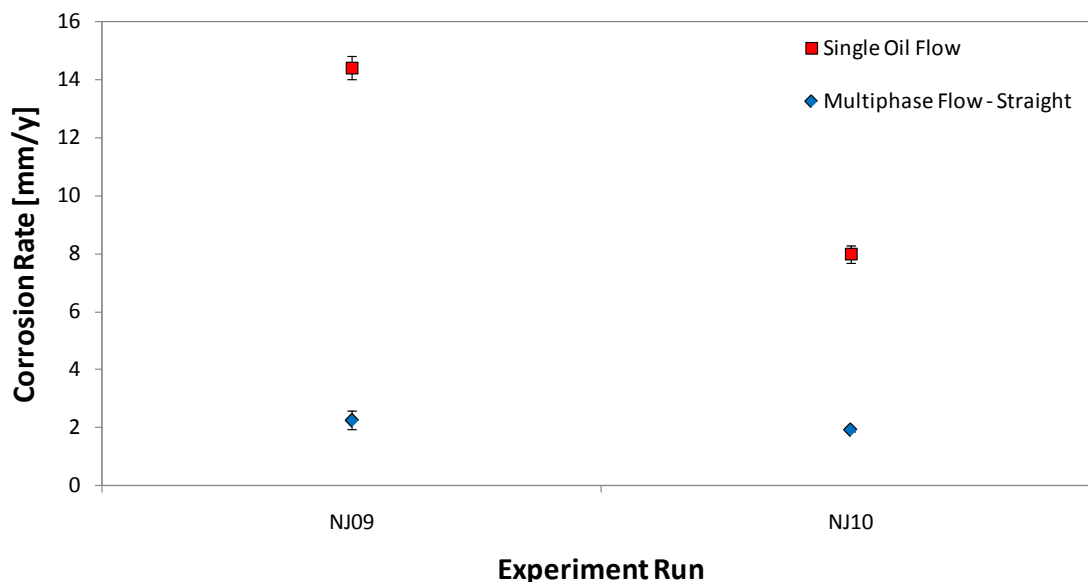


Figure 3.33: Temperature control on the corrosion rate check in the test sections. The experiments NJ09 and NJ10 were run at the respective temperatures of 318 °C and 282 °C.

The inhibition of NAP corrosion

Other issues, apparently masked by the heat loss and temperature control discussed above, came out from the preliminary tests. For instance, it was observed that at relatively similar operating conditions, the corrosion rate decreased in both single and multiphase flow conditions over time. However, the TAN concentration - in parallel, chemical analyses of oil samples taken from the liquid phase after each experiment (APPENDIX B) yielded TAN and Fe concentrations - remained constant meaning that the corrosiveness of the liquid phase was maintained. On the other hand, the Fe concentration increased due to recycling the liquid in the AFR (Figure 3.34). All these observations suggest that the presence of corrosion by-products, such as iron naphthenates, formed during previous runs in the flow system may have partially

inhibited the NAP corrosion. Hereafter, the iron concentration was monitored after each experiment to keep the iron concentrations in the liquid phase low.

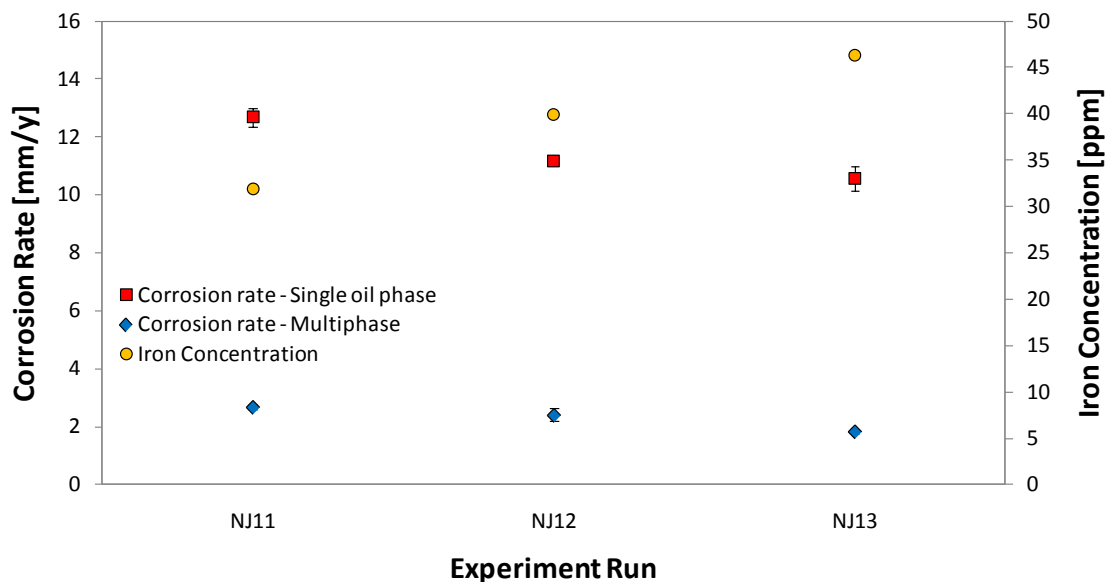


Figure 3.34: The inhibiting effect of corrosion by-products (iron concentration) on NAP corrosion.

3.5.2.2 The effect of flashing

Contrary to the filed experience, where reported corrosion is more aggressive in multiphase than in single phase flow conditions, the reverse was found in the laboratory. For example, the measured corrosion rates were up to six times higher in single phase than in multiphase flow conditions. One of the working hypotheses suggested that, in multiphase flow environments, a fraction of the corrosive species present in the liquid phase could be flashed in the vapor phase, where little NAP corrosion has been reported (Blum, 2011). In this case the loss of naphthenic acids from the liquid phase at operating

conditions (343 °C) would lead to a less in-situ acidic content of the liquid phase and, hence, to a lower corrosivity. Therefore, the section below focuses on this hypothesis and summarizes the work done in this regard.

3.5.2.2.1 The naphthenic acids loss in the saturation column

In the initial experimental design (Dec 2008 – Jun 2010), the liquid solutions present in the saturation column and the storage tank were identical in order to create similar thermodynamics conditions in the multiphase flow test section. The first samplings of liquid solutions from both devices were taken in May 2010. For similar starting solutions, spiked with naphthenic acids at TAN 4 (calculated value during the preparation of the solution), results from chemical analysis indicated that TAN concentrations after the experiment were 4.11 and 0.28 mg KOH / g oil in the liquid phase stored in the tank and saturation column, respectively (Wolf, 2010a). Since the present work did not have any historical oil sampling, the acid loss in the saturation column was not well understood; therefore, it was further investigated before moving on with the experimental program.

The first approach focused on identifying the mechanism of naphthenic acids loss in the saturation column. In Figure 3.35, the analysis of oil samples revealed that most of the NAP compounds were present after heating the saturation column (blank test NJ05) but were *flushed and flushed* by the gas stream bubbling in the liquid phase during another blank test (NJ06). Then, a test with metal samples (NJ08) was run to measure the final TAN concentrations of both liquid solutions in the column and tank. Mass balances

on naphthenic acid species from both liquid phases confirmed that the acidic vapors were recondensed in the AFR cooling section and recovered in the liquid solution present in the storage tank (Jauseau, 2011). This finding implied that under such conditions, the experiments on the AFR loop could not be reproduced using a recycled liquid phase in the presence of naphthenic acids in the column. Hence, the AFR design was modified to run one flow-through in each test.

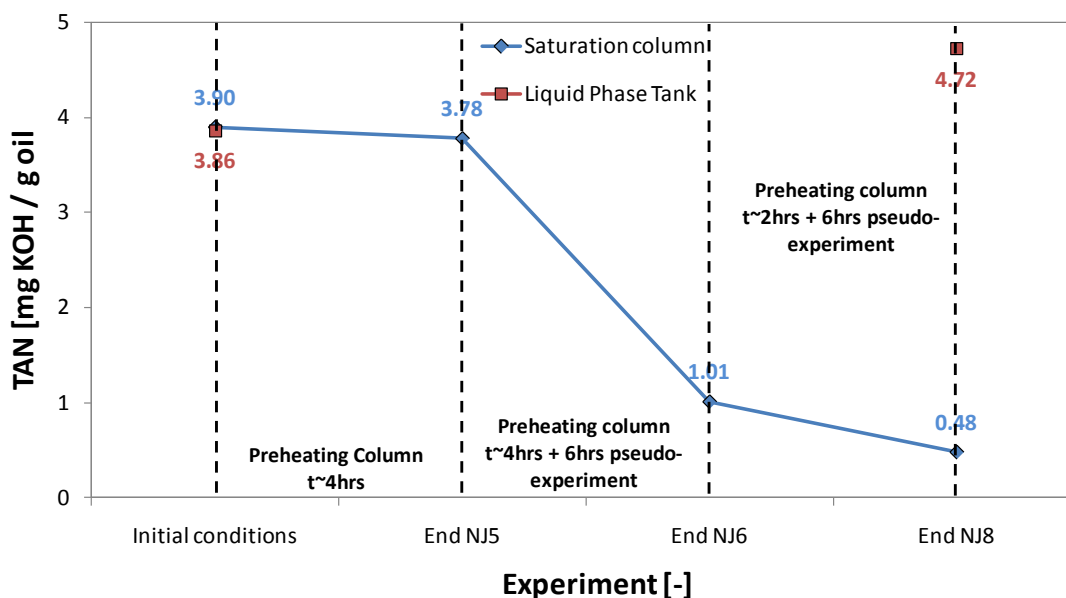


Figure 3.35: Evolution of the TAN concentration loss in the saturation column, before and after experiments.

Using an AFR set up without recycling (Figure 3.11), a second approach focused on measuring the flashing rate of NAP compounds in the saturation column. The initial TAN concentration of the liquid phase in the storage tank was TAN 2, while that of the liquid phase in the saturation column was TAN 3. The latter was higher to ensure that its

acidic contribution could be detected during the oil sample analysis, and eventually increase the corrosion rate. As described in section 3.3.2.6.2, the AFR set up was modified to carry out high frequency samplings during the testing. At the AFR outlet, the fluid was sampled every 5 minutes for the first two hours, every 15 minutes for the third hour and once at the end of the test. Because of safety hazards, samples from the saturation column were taken only before and after the experiment. Results of TAN and Fe concentrations of the multiphase flow mixture are plotted in Figure 3.36. Horizontal lines represent the reference TAN and Fe concentrations as they would be if NAP species from the feed tank were the only acids present in the liquid stream.

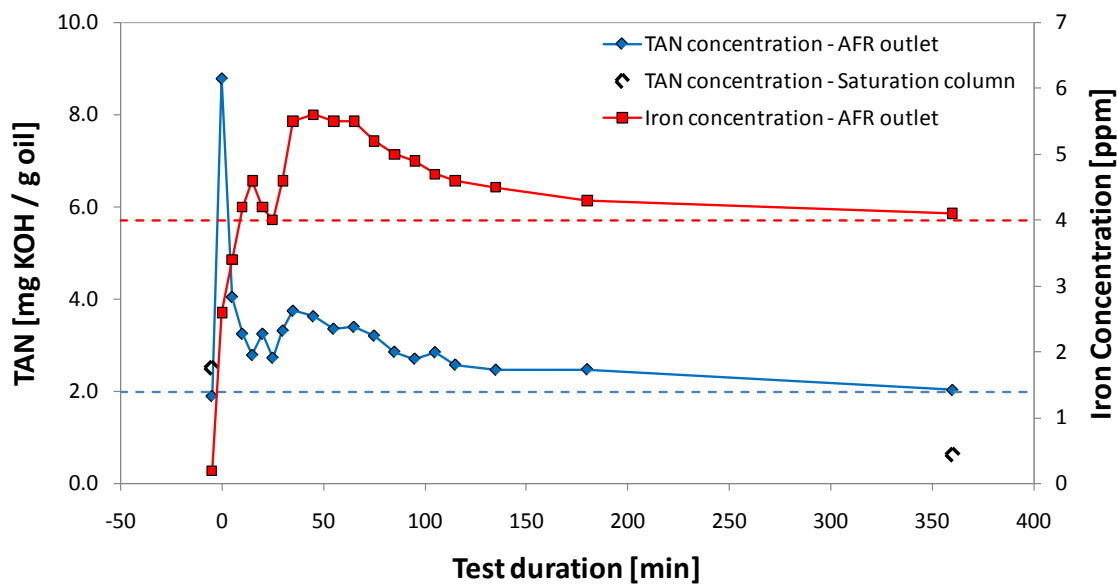


Figure 3.36: TAN and Fe concentrations in the multiphase flow mixture measured at the outlet of the AFR during an experiment (NJ48).

The TAN concentration peaked at 8.79 mg KOH / g oil. This high value suggested that the NAP vapors, formed while warming up the fluids present in the saturation column before the test (2.5–3.5 hrs) and condensed in coolers when the gas phase started flowing through the flow loop, were flushed at the beginning of the experiment. After this peak-value, the TAN concentration was about 3–4 mg KOH / g oil during the first 75–80 minutes of the test and declined asymptotically to the end of the test with a value corresponding to the initial concentration measured in the feed tank. The chemical analysis also revealed the presence of acidic vapors coming from the saturation column and their ability to increase the corrosiveness of the liquid stream after recondensation in coolers. The iron concentration profile having a similar trend throughout the experiment suggested a more aggressive corrosion occurring during the first 75–80 min of the experiments with a concentration exceeding 5 ppm. Therefore, it can be assumed that after minutes 75-80, no naphthenic acids from the saturation column could contribute to corrosion. The final TAN concentration in the saturation column confirmed that most of the acids initially present had been flashed during the test (final $TAN = 0.62$ mg KOH / g oil).

3.5.2.2.2 The batch injection of naphthenic acids in the saturation column

Because of the loss of naphthenic acids from the saturation column, multiple batches of NAP solutions were injected in the column to maintain the acidity level in the vapor phase flowing through test sections during the test. The injection mode had to account for safety issues because the operating temperature in the column was above the

flashing point of white oil. Besides, strong concerns about potential corrosion issues were raised related to high TAN concentration and the injection time of the corrosive fluids, and the possibility to have high TAN concentrations localized nearby the injection outlet, in the saturation column. A localized corrosion at TAN 4 was reported to occur at the furnace outlet with transfer lines made of stainless steel AISI 316 (Wolf, 2011). Therefore, a batch injection was preferred instead of a continuous feed, and the pure NAP mixture was injected through a tubing coil ending in the middle section (not at the wall) of the saturation column in the liquid solution.

In a particular experiment (NJ50), the initial TAN concentration used for the liquid solution in the saturation column was TAN 3, while for the one in the feed tank, TAN 2. Based on the available mixing volume⁶ of the saturation column, ca. 30 mL naphthenic acids were necessary to be injected in the column to reach again TAN 3. Given the complexity of the test, the injection volume was oversized by 25% to ensure an efficient injection. The injections of pure NAP were performed every 80 min until a volume of 40 mL was added to the liquid solution in the saturation column.

Figure 3.37 shows the TAN concentration following the same trend as the one in Figure 3.35, where no additional acid number from the saturation column was measured after 80 minutes of experiment NJ48; therefore, in experiment NJ50, the acids were injected after this critical point, every 80 minutes until the end of the experiment.

Figure 3.38 also superimposes the two iron concentration trends (NJ48 and NJ50) with marked times of injections. Both TAN and Fe concentrations did not seem to

⁶ The mixing volume was the available volume in which the naphthenic acids could be diluted. It included the volume of the column situated above the sparger's level (Figure 3.18).

increase after injecting more naphthenic acids in the saturation column. On the other hand, a much larger volume injection boosting the TAN concentration in the gas phase would have shifted the chemical operating conditions needed to be simulated in these experiments and could have affected irreversibly the integrity of the equipment used.

When comparing the corrosion rates measured with naphthenic acids either initially present or injected in the saturation column during the tests with those using a blank solution in the column, no significant difference was observed (Figure 3.39).

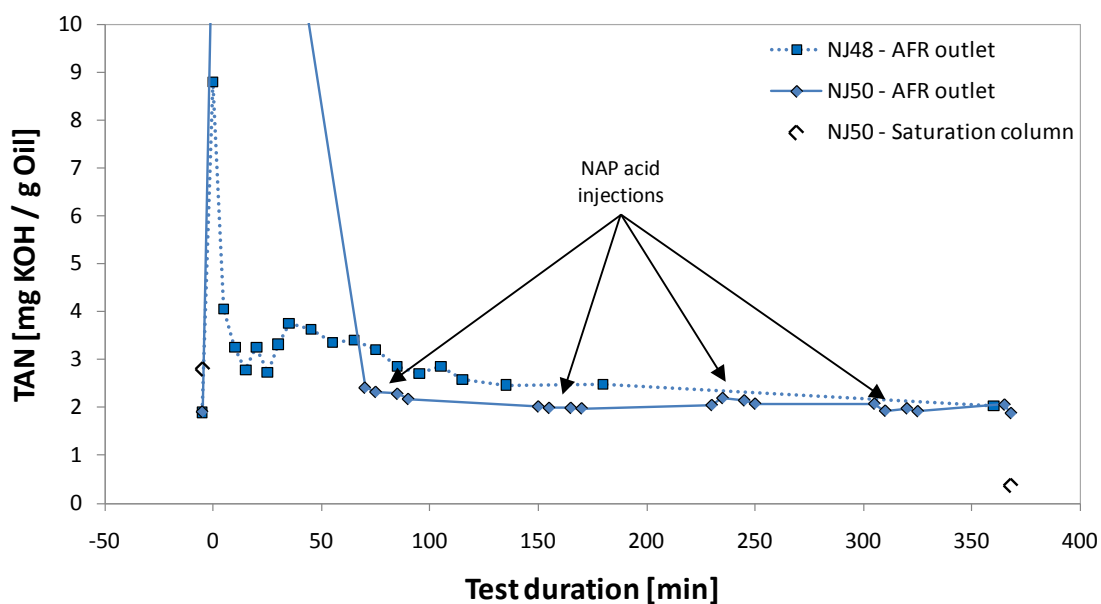


Figure 3.37: TAN concentrations of a multiphase flow mixture measured at the outlet of the AFR during experiments NJ48 and NJ50.

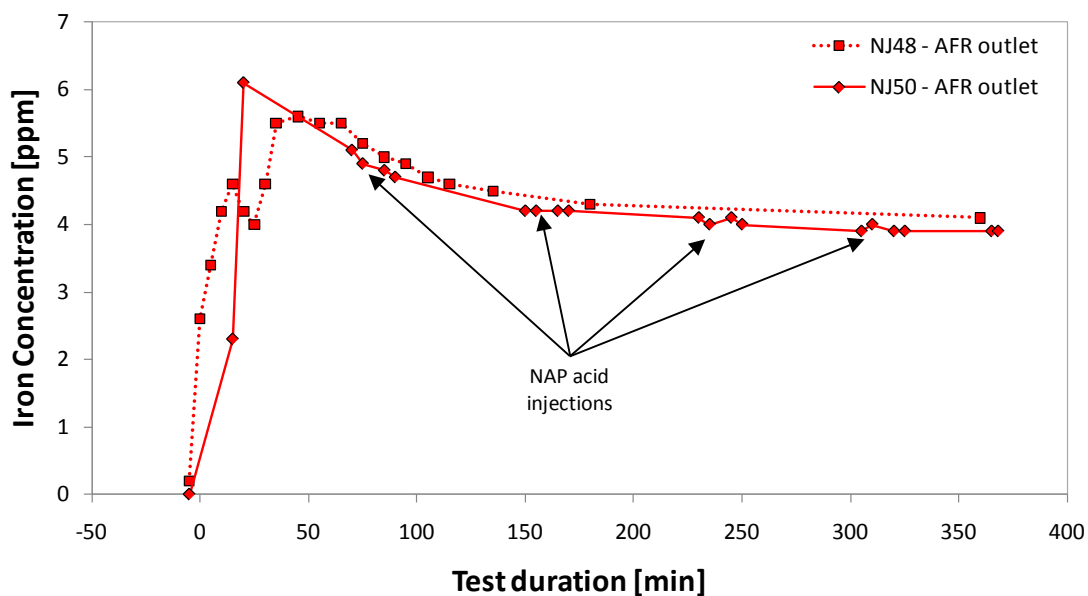


Figure 3.38: Iron concentrations of a multiphase flow mixture measured at the outlet of the AFR during experiments NJ48 and NJ50.

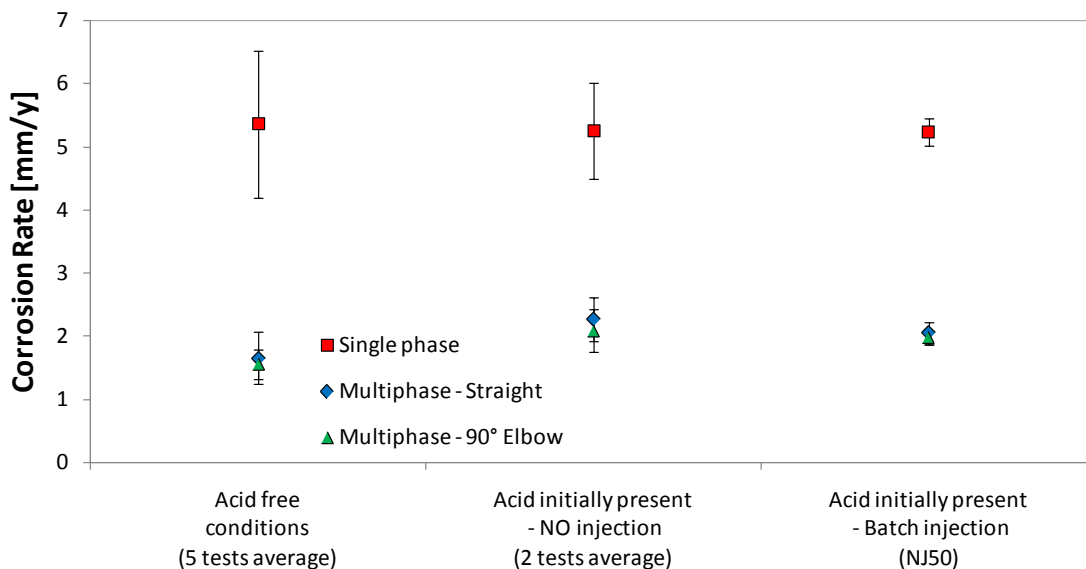


Figure 3.39: Measurements of corrosion rates for different acid media in the saturation column. Superficial gas and liquid velocities are 10 and 0.1 m/s for each condition.

In the present case (Figure 3.39), it is assumed that flashing of the corrosive species occurred in the saturation column as is seen in the transfer lines of oil refineries. However, this could not explain the difference between the corrosion rates measured in single- and multiphase flow conditions despite the overdosing of the acid injection volume. Since the addition of naphthenic acids in the saturation column did not affect the corrosion rate, the injection operation was dropped for further experiments. Consequently, the liquid phase in the AFR could be recycled without significantly changing the TAN concentration for the next tests (Figure 3.10).

3.5.2.3 The effect of TAN concentration

The initial choice of the chemical composition of the liquid phase was guided by the work of Bota (2010b). Using the same fluids (white oil spiked with naphthenic acids), he demonstrated that the FeS scale showed some kind of protection on the CS samples at a TAN concentration less than 5.

All experiments were repeated two or three times to ensure a good reproducibility of the results. The corrosion rates of CS samples were measured in single phase flow and multiphase flow conditions. In gas-oil conditions, the straight and 90° elbow samples were used and compared to assess any potential flow induced corrosion that might have occurred in bends. The test conditions were according to the test matrix presented in Table 3.3. The first test conditions foresaw a liquid solution spiked with TAN 4 at superficial gas and liquid velocities of 20 and 0.1 m/s, respectively.

The resulted corrosion rates at TAN 4 are presented in Figure 3.40.

No effect of piping geometry (straight vs. 90° elbow) in multiphase flow conditions was observed on these corrosion rates. Furthermore, the single phase flow conditions were unexpectedly much more aggressive than the multiphase flow conditions, exhibiting measured corrosion rates about 4–7 times higher in the first case. The operating conditions (flow and chemistry) were obviously too aggressive. Therefore, the acidity of the solution was reduced to TAN 2, while the flow conditions remained the same.

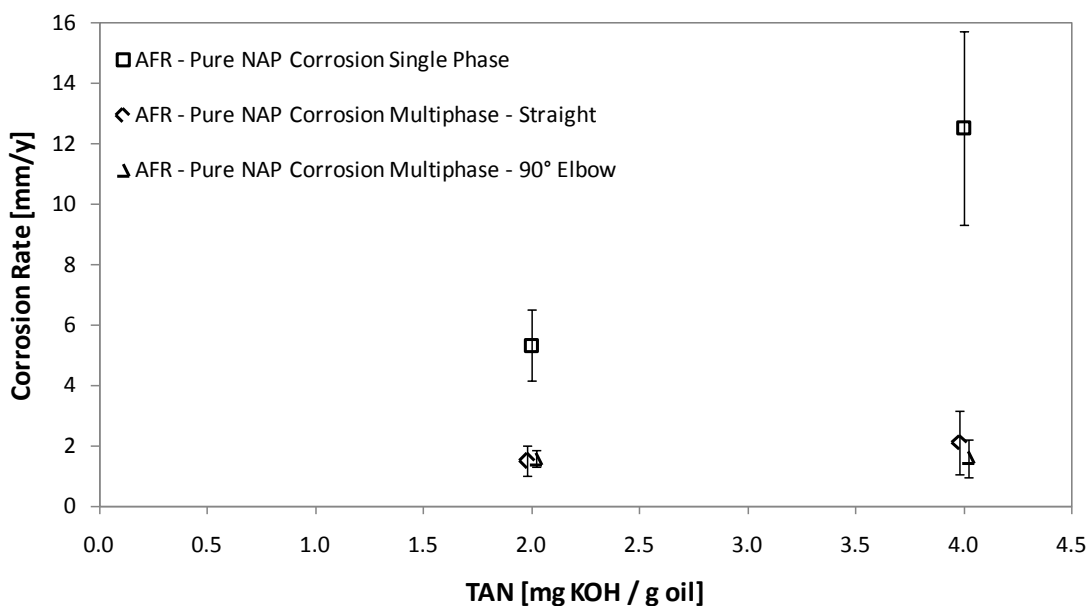


Figure 3.40: Corrosion rates measured using non-presulfided samples with different geometries and TAN concentrations. The multiphase flow conditions are $U_{SG} = 20$ m/s; $U_{SL} = 0.1$ m/s. For a better visualization, the multiphase flow corrosion rates are slightly displaced to the left and right from the corresponding tick mark of TAN (actually, they overlap).

Prior to run the experiment series at TAN 2, a new liquid phase was prepared. In single phase flow, the corrosion rates decreased when reducing the TAN concentration

because the NAP attack on the metal surface was less aggressive. When the TAN concentration was doubled, the corrosion rate increased by a factor of 2.3, which is in good agreement with the observations reported by Gutzeit (1977). However, in multiphase flow conditions, the TAN concentration and piping geometry did not affect the corrosion rate.

3.5.2.4 The effect of flow velocity

3.5.2.4.1 Superficial gas velocity

In the previous section, it was found that the piping geometry and TAN concentration did not affect the corrosion rates measured in gas-oil environments. Henceforth, the focus shifted to the effect of superficial gas velocity on corrosion. In the experiments assigned to investigate this effect, the TAN concentration of the liquid phase and the superficial liquid velocity were kept the same, TAN 2 and $U_{SL} = 0.1$ m/s, respectively. During the experiments, it was noticed that the pressure in the flow loop was proportional to the gas flow rate. Because some of the instrumentation could not be operated at high pressure (i.e., gas heaters, flow meters), a superficial gas velocity of $U_{SG,max} = 40$ m/s was considered as the maximal operating gas velocity in the AFR. Furthermore, the risk of liquid flowing back to the saturation column limited the superficial gas velocity to values no smaller than 1 m/s ($U_{SG,min} = 1$ m/s). Therefore, the gas flow conditions could vary in the range of $U_{SG} = [1 - 40]$ m/s. Experiments were carried out at superficial gas velocities of 1.5, 10 and 33 m/s. Since excellent

reproducibility of the preliminary tests was achieved at $U_{SG} = 20$ m/s, only two experiments were run at identical operating conditions.

The corrosion rate was plotted against the superficial gas velocity in Figure 3.41. Note that the superficial gas velocity $U_{SG} = 0$ m/s corresponds to the actual single oil phase flow conditions.

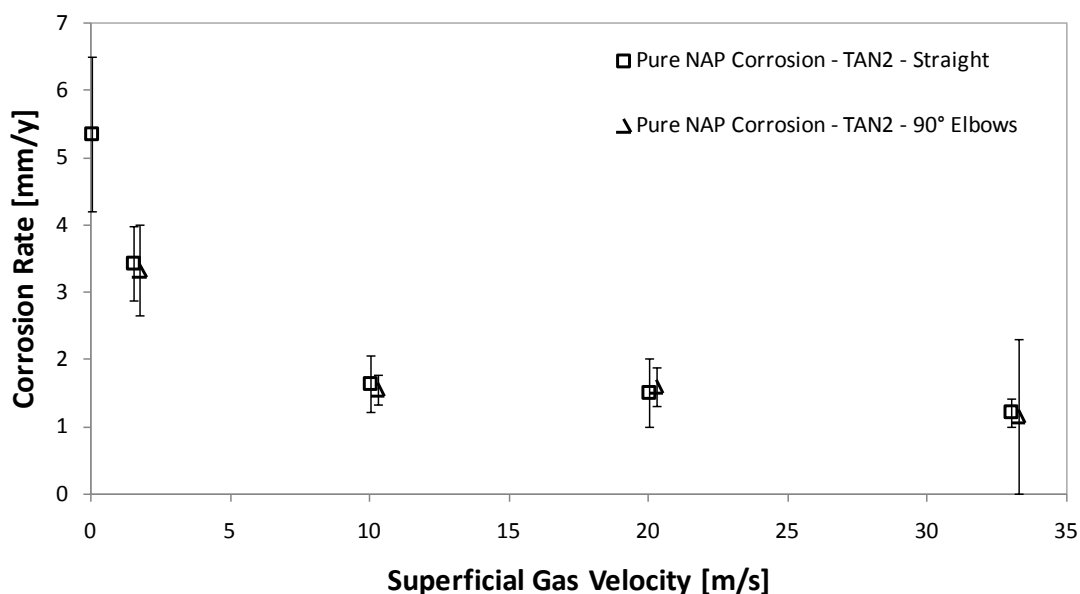


Figure 3.41: Corrosion rates measured using non-presulfided samples with different geometries at different superficial gas velocities. Measurements were performed with a concentration TAN 2 and a superficial liquid velocity of 0.1 m/s. Corrosion rates in elbows are slightly displaced to the right of the gas velocity tick mark for a better visualization (they actually overlap with the ones from straight samples).

When the gas velocity was varied from 0 m/s to a critical value $U_{SG,crit} = 10$ m/s, the corrosion rate decreased from 5.4 mm/y to 1.6 mm/y. Beyond $U_{SG,crit}$, the corrosion rate did not vary much so that at $U_{SG,crit} = 33$ m/s it reduced to 1.2 mm/y. This trend was common to both sample types, straight or 90° elbow, reassuring that the piping geometry

did not influence the corrosion rate. Contrary, the superficial gas velocity seems to have an effect when varying it from 1 to 10 m/s.

Visual observations of the gas-liquid mixture at the sampling station show that an annular-dispersed flow under the dominant mist form occurred in the AFR. At high temperature, the mist combined with some liquid containing entrained gas could be observed. The fraction of recovered liquid appeared to be more important at low than at high gas velocity. Contrary, at room temperature, the mist flow in the presence of a more important liquid film could be seen. This difference may be attributed to the absence of vaporization/condensation usually occurring at high temperatures.

The experimental conditions were also simulated using the gas-liquid two-phase flow model developed in CHAPTER 5. The model inputs required the piping properties, fluid properties, and flow rates or superficial velocities corresponding to the operating conditions. The point model was run for a horizontal line with an absolute pipe roughness of $\varepsilon = 4.5 \cdot 10^{-5}$ m. The fluid properties of the gas and liquid phases used as inputs for the flow model were assumed to be pure CO₂ and pure white oil. For unknown liquid petroleum fractions at low pressure, the correlation proposed by Ritter et al. (1958) was used to calculate the liquid density while the viscosity was computed with the relationship from Singh et al. (1990). Computations of superficial liquid and gas velocities are detailed in APPENDIX G and APPENDIX H.

The model predictions included a flow map generated for this specific gas-oil mixture and presented in Figure 3.42. The flow map shows that all the AFR operating conditions tested fell into the annular dispersed region, meaning that only a small fraction

of the liquid phase was flowing at the pipe wall (liquid film), while the rest of the liquid phase was transported into the gas phase in the form of entrained droplets (mist).

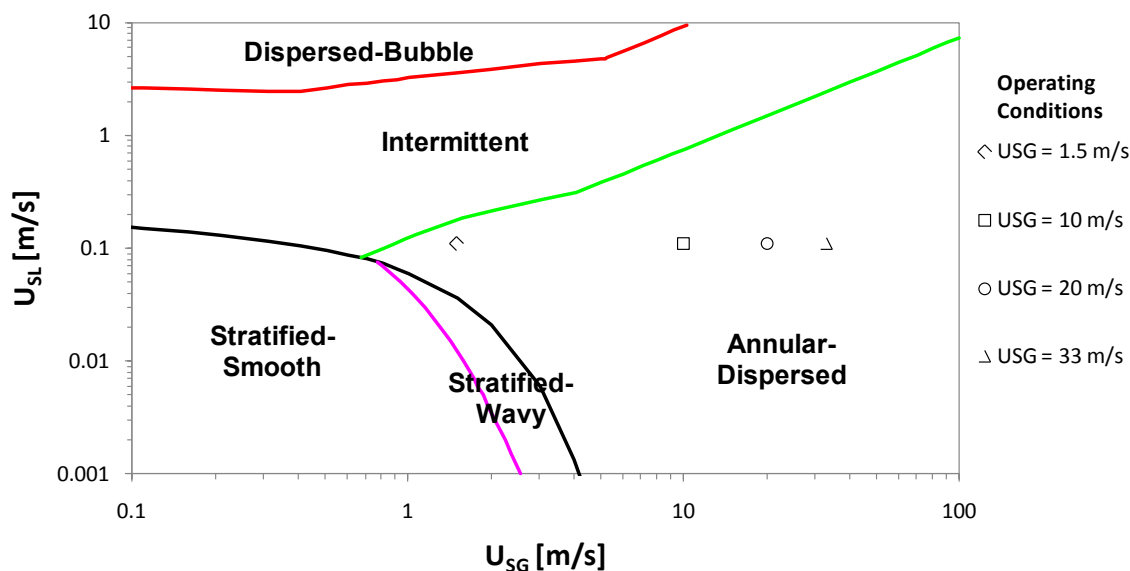


Figure 3.42: Flow map of a CO₂ / White oil mixture at P = 3.8 bar, T = 343 °C using a ¼” horizontal line. The point marks represent different multiphase flow conditions used in the AFR.

From Figure 3.43 it can be inferred that at $U_{SG} \geq 10$ m/s, most of the liquid was transported in the gas phase as entrained droplets. The entrainment predicted by the flow model presented in CHAPTER 5 tends to confirm that the dominant flow pattern was most likely the mist flow. Although the model still predicts annular-dispersed flow at $U_{SG} \approx 1.5$ m/s, (Figure 3.42), the actual operating conditions may be closer to the intermittent (slug) to annular flow transition and, thus, the flow pattern could be more a transition state (i.e., wavy-annular). Under such conditions, more liquid can be in contact with the wall when pseudo-slugs flow in the pipe. The flow model also predicted a lower

entrainment fraction (ca. 38%) at $U_{SG} = 1.5$ m/s, confirming the presence of a liquid film at the pipe wall. In other words, a higher wetted wall fraction may enhance the NAP attack on the steel surface.

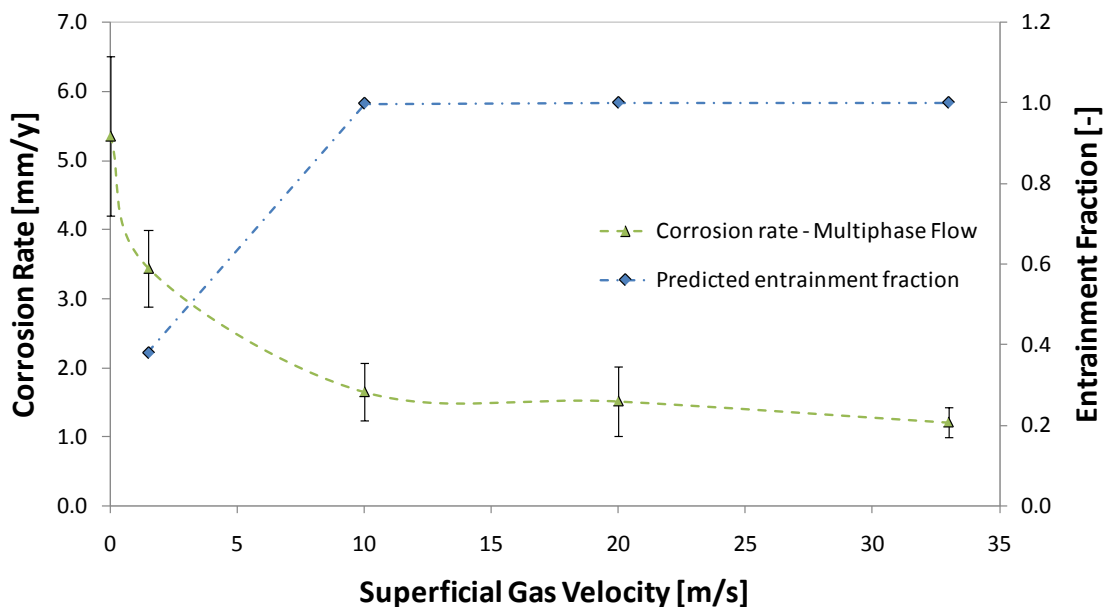


Figure 3.43: Corrosion rates measured on straight samples in multiphase flow and predicted entrainment fraction of liquid droplets vs. superficial gas velocity.

3.5.2.4.2 Superficial liquid velocity

Several experiments were done by varying both superficial liquid and gas velocities in the AFR (tests GB123 to NJ08 in 0). During the preliminary testing, the first runs occurred at $U_{SG} = 20$ m/s and $U_{SL} = 0.2$ m/s (liquid flow rate $Q_L = 185$ mL/min). Preliminary results (section 3.5.2.1) from single phase flow conditions were not reliable because of a combination of both the lack of temperature control in the test sections and the partial corrosion inhibition due to corrosion by-products (iron naphthenates). On the

contrary, results from multiphase flow conditions were reliable (due to an excellent reproducibility) despite the temperature control issues. Experiments related to the variation of superficial liquid velocity in the AFR system were done on straight CS samples only because at that time the inclusion of elbows had not been considered yet.

Results displayed in Figure 3.44 suggest that corrosion was more aggressive at higher liquid flow rates. The average corrosion rate measured at a superficial liquid velocity $U_{SL} = 0.2$ m/s was $CR_1 = 5.1$ mm/y; at about half the velocity, the average corrosion rate was $CR_2 = 2.2$ mm/y.

Interestingly, there is a factor of 2.3 between the corrosion rates at the two different velocities. If the ratio of the two corrosion rates was compared to that of the two liquid flow rates, it yielded similar results:

$$\frac{CR_1}{CR_2} = 2.3 \text{ and } \frac{Q_{L,1}}{Q_{L,2}} = 2.1 \quad (3.5.1)$$

However, more experiments at various liquid flow rates would be necessary to confirm the proportionality between the corrosion rates and liquid flow rates.

In this study, the liquid flow rate corresponded to the refreshment rate of the liquid solution in the test sections. Therefore, a higher liquid velocity would ensure a faster renewal of the corrosive species in the test sections. Moreover, in single phase flow, it would also increase the mass transfer of corrosive species to the steel surface and simultaneously remove corrosion by-products (i.e., iron naphthenates) away from the metal surface. In gas-oil conditions, an augmented corrosion could be explained by a totally different mechanism related to multiphase flow. By raising the liquid velocity in the pipe, the liquid holdup, and subsequently, the wetted wall fraction increase as well.

Since NAP corrosion usually occurs in the presence of a liquid phase, a higher wetted wall fraction can only advance the NAP corrosion.

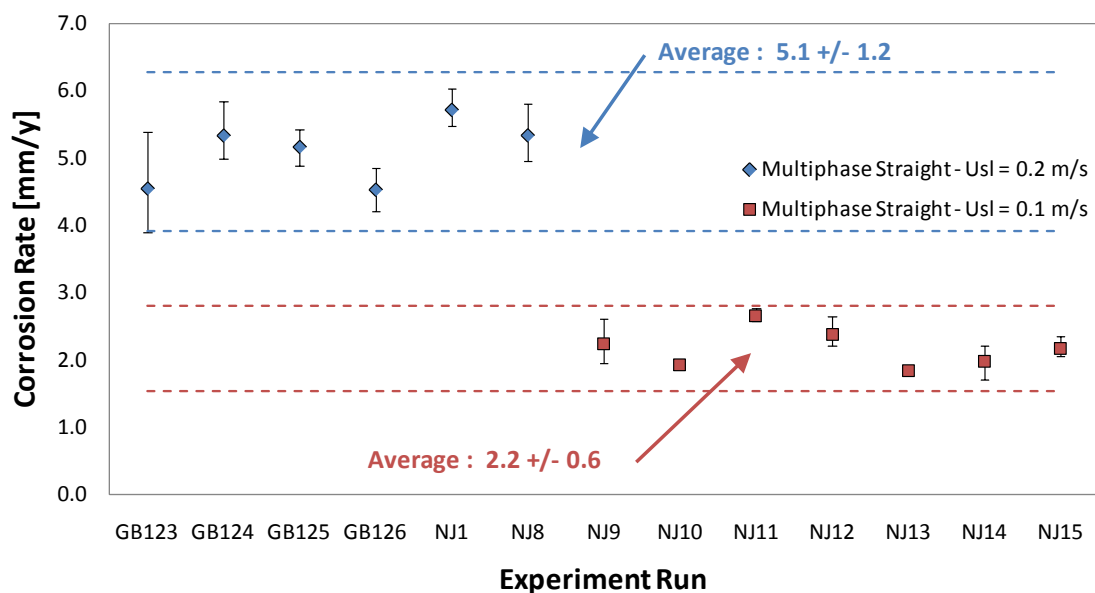


Figure 3.44: Corrosion rates under multiphase flow conditions at different superficial liquid velocities.

3.5.2.5 A comparison of corrosion rates measured in different flow systems

The corrosion rates from this study were compared with those reported from previous works done on other facilities in the ICMT laboratory, in order to demonstrate the effect of flow on NAP corrosion. Two of the facilities have been already introduced, the AFR and FTMA; the others are a rotating cylinder called here the *High Velocity Rig* (HVR) and a standard *autoclave*. The chemical operating conditions were very similar among these facilities, with an acid number TAN 4 and a temperature of 343 °C. However, the flow conditions varied among the different devices from no flow (*i.e.*,

autoclave) to high liquid flow rates (*i.e.*, AFR) or high shear stress levels (*i.e.*, HVR, AFR – multiphase flow). The main hydrodynamic parameters and respective corrosion rates are detailed in Table 3.6.

Table 3.6: Flow conditions encountered in different flow loops for pure NAP corrosion tests (TAN 4).

| Flow loop | Autoclave ^c | FTMA ^d | HVR ^e | AFR | | |
|--|------------------------|---------------------|------------------|---------------------|-------------------------|------|
| | | | | Single phase | Multiphase ^g | |
| Superficial gas velocity (m/s) | - | - | - | - | 20 | 20 |
| Refreshment rate (mL/min) | 0 | 1.5 | 8 | 80 | 80 | 185 |
| In-situ liquid velocity (m/s) | N/A | $9.0 \cdot 10^{-5}$ | 8.6^f | 0.1 | 6.0 | 8.6 |
| Residence time (s) ^a | test duration | 434 | 162 | 2 | 0.1 | 0.1 |
| Liquid Reynolds number (-) | N/A | 4.5 | $2.0 \cdot 10^6$ | 1,343 | 982 | 1236 |
| Wall-liquid shear stress (Pa) | N/A | $9.0 \cdot 10^{-6}$ | 52 | $5.0 \cdot 10^{-2}$ | 201 | 329 |
| Test duration (hrs) | 24 | 24 | 24 | 6 | 6 | 6 |
| Samples size (-) | 2 | 4 | 9 | 10 | 33 | 18 |
| Corrosion rate (mm/y) | 2.17 | 3.50 | 7.94 | 12.55 | 2.15 | 5.10 |
| Corrosion rate error (mm/y) ^b | 0.01 | 0.40 | 2.78 | 2.39 | 0.82 | 1.20 |

^a The residence time was calculated as the ratio of the liquid volume to the liquid flow rate.

^b The errors were calculated using the method min/max since there were only two measurements reported for autoclave.

^c Data from Jin (to be published).

^d The flow related parameters were calculated based on Kanukuntla's (2008) design using square samples immersed in oil.

^e Data from Bota (2010b) and Jin (to be published).

^f The liquid velocity at the steel surface was calculated based on the speed of a rotating cylinder (2000 RPM). The actual liquid flow rate should be calculated using the refreshment rate.

^g Multiphase flow characteristics were computed with the gas-liquid two-phase flow model.

Note that a distinction was made between the refreshment rate and the in-situ liquid velocity. The former represents the liquid flow rate flowing through the test section and set up for the experiment, while the latter represents the real liquid velocity as experienced by the samples. This distinction is important since the estimation of the residence time of the liquid phase in the test sections is based on the refreshment rate.

In Figure 3.45, the corrosion rates from Table 3.6 were plotted for each device ranked by refreshment rate up to 185 mL/min. Also, the corrosion rates measured in single- and multiphase flow conditions were separated in this graph because different mechanisms underline the two cases. Only the chemical operating conditions were common.

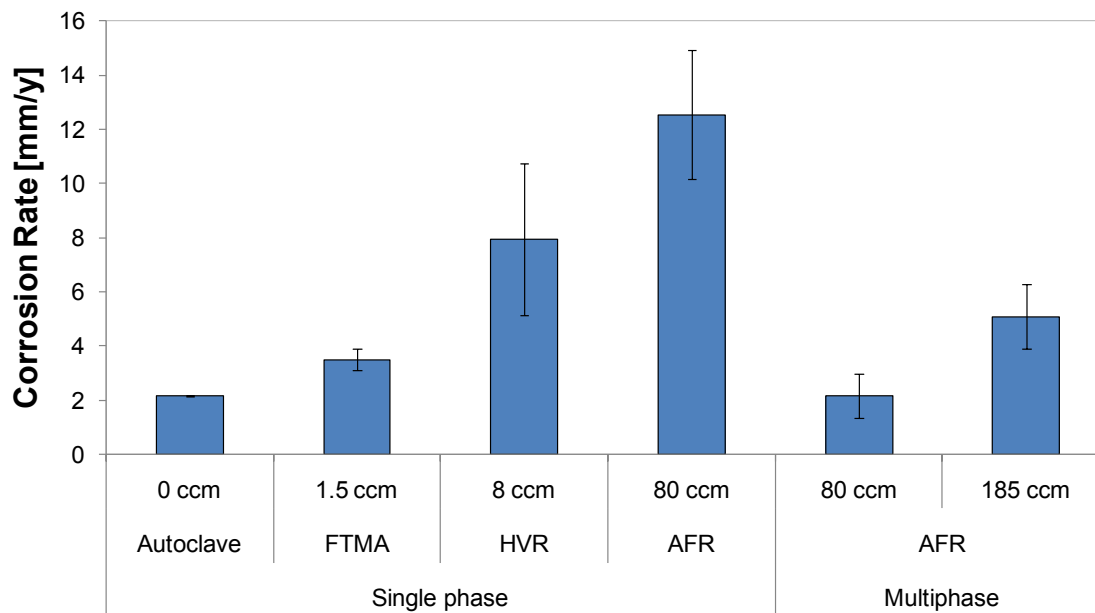


Figure 3.45: Corrosion rates by flow loops. Results are from single phase and multiphase flow conditions (TAN 4 and 343 °C).

In single phase flow, the average corrosion rate measured in the FTMA was higher by a factor of 2 than the one measured in the autoclave. Since there was no flow in the autoclave, the corrosiveness of the liquid solution weakened because of the reaction of naphthenic acids with iron. The continuous refreshment of the corrosive species in the FTMA minimized the *chemistry effect* on the resulted corrosion rates and maintained the same corrosiveness over the whole test.

Higher flow rates of liquid solutions fed the HVR and AFR in single-phase environments. The largest shear stress was generated in the HVR causing turbulence and, therefore, enhancing the transport of corrosive species to the steel surface. The average corrosion rate measured in the AFR (13 mm/y) exceeded that of the HVR (8 mm/y). The levels of shear stress, calculated for various conditions in the HVR, AFR single- and multiphase, do not correlate with corrosion rates measured in the corresponding flow loops. Although the single phase flow conditions in the AFR experienced 1000 – 6000 times less shear stress than the other flow conditions, higher flow rates were observed in these particular conditions. This finding contradicts the statement that “scales can be physically removed by shear stress” (Kapusta et al., 2004) since the highest shear stress developed under the experimental conditions in this study never exceeded 500 Pa.

Because the flow in the AFR was laminar ($Re < 2000$), it is plausible that a chemical mechanism rather than a mechanical one drove the NAP corrosion in the liquid phase. At low liquid refreshment rates, like in the HVR (8 mL/min), the corrosion by-products (i.e., iron naphthenates) could form and cause an inhibition of NAP corrosion by possible steric effects on the metal surface. At higher liquid flow rates, the corrosion by-

products, which are soluble in oil, could be easily entrained by the flowing fluid and transported away from the surface. In other works (Bota, 2010b; Craig Jr., 1995; Gutzeit, 1977; Jin, to be published; Smart et al., 2002), a rotating cylinder electrode similar to the HVR was used to run NAP corrosion experiments. In all the cited works, the operating flow rate was rather low (6 – 8 mL/min), and a partial NAP corrosion inhibition may occur leading to lower corrosion rates. In literature, the authors usually point out the velocity and shear stress as the main factors to evaluate the flow effect on NAP corrosion, but they rarely mention the flow rate. Though, one researcher (Derungs, 1956) emphasized the effect of flow rate by showing that an increase in the crude load (40 to 70 t/day) determined higher corrosion rates, but the author did not mention a critical value beyond which the corrosion could be an issue. Another researcher (Slavcheva et al., 1999) also stressed out the importance of the flow rate to maintain the same chemical medium during the experiment, as it was also done in this study. No other work, particularly focusing on NAP corrosion in pipes using high liquid flow rates, was published prior to this study. Despite recycling the liquid phase in the flow loop⁷, much higher corrosion rates could be measured in single phase flow in the AFR compared to any other case reporting high shear stresses under similar chemical conditions. By focusing on the shear stress effect only, one tends to forget that a change in chemistry may have a more important effect on the NAP corrosion process than it is often considered.

⁷ A careful monitoring of the species concentration should be performed to make sure that the chemistry is not altered to the point that inhibition or thermal degradation of corrosive species could affect the corrosion process. For these reasons, the iron and TAN concentrations in oil have to be measured.

On the other hand, the multiphase flow should be separately treated because of its complex nature. A higher liquid flow rate was required to exceed the corrosion rate found in the FTMA ($Q_L = 185$ mL/min). As shown in a previous section (section 3.5.2.4.1), lower corrosion rates in multiphase flow could be linked to the flow pattern. For example, in mist flow, a very small wetted wall fraction at the metal surface could play an “inhibition role” and be one of the key parameters controlling NAP corrosion.

3.5.3 Presulfidation-challenge corrosion

The experiments reported in this section assessed the corrosivity of naphthenic acids by using pretreated samples with an iron sulfide scale built at the metal surface. These experiments, although more complex (building the FeS scale) are more realistic because the operating conditions approach more closely those occurring in oil refineries where sulfur compounds are always present while naphthenic may be seen occasionally when opportunity crudes are processed. Results are presented below from two perspectives: the effect of TAN concentration and the effect of superficial gas velocity on corrosion rate of presulfided samples.

3.5.3.1 The effect of TAN concentration

Similarly to the pure NAP corrosion (challenge), the experiments in this section were repeated twice or three times to ensure a good reproducibility of the results. The operating conditions are given in Table 3.4.

Initially, the experiments were run using a liquid solution spiked with naphthenic acids at a concentration of TAN 4, a superficial gas velocity of 20 m/s and a superficial liquid velocity of 0.1 m/s. According to Figure 3.46, at TAN 4 and multiphase flow conditions, the measured corrosion rates on straight and 90° elbow samples were similar suggesting that the piping geometry was not important despite the high superficial gas velocity used; contrary, the number of phases seemed to be important since the highest corrosion rate (7 mm/y) was obtained in single phase flow, about 4 times higher than those in gas-oil two-phase flow (1.7–2 mm/y).

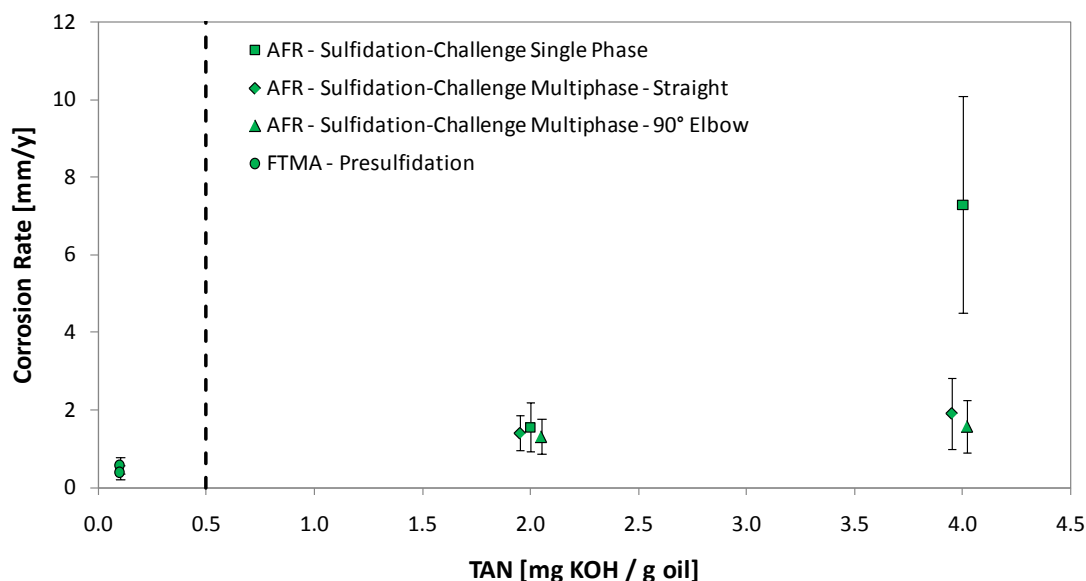


Figure 3.46: Corrosion rates measured using presulfided samples of different geometry and TAN concentrations. In multiphase flow, $U_{SG} = 20$ m/s and $U_{SL} = 0.1$ m/s. Corrosion rates displayed at TAN 0.1 represent the average sulfidation corrosion rate in the FTMA. (The point-values are slightly displaced to the left or right of the TAN corresponding tick mark for a better visualization; the actual point-values overlap).

The FeS scale built during presulfidation, from which the measured corrosion rates due to sulfidation only were less than 0.6 mm/y, did not show significant protection during the subsequent "challenge" experiments at TAN 4 in both, multiphase and single phase flow conditions. This finding supported the decision to reduce the TAN concentration from 4 to 2 in the experiments in order to have a less aggressive chemical medium in the system and, presumably, to observe if the FeS scale resisted to corrosion.

Using the same flow conditions ($U_{SG} = 20$ and $U_{SL} = 0.1$ m/s), the experiments run at TAN 2 yielded a much lower corrosion rate in single phase flow, but still higher than the sulfidation corrosion rate (Figure 3.46). The corrosion rates resulted from multiphase flow at TAN 2 were similar to those at TAN 4 in a range of 1–2 mm/y, which were also higher than those from sulfidation. In either case, TAN 2 or 4, the FeS scale did not resist the "challenge" conditions, failing to protect the samples against NAP corrosion. Furthermore, no effect of piping geometry was observed on the corrosion rates. Despite the mild chemical conditions used, the TAN concentration had a strong effect on the corrosion rate in single phase flow, but none in multiphase flow; the flow effect was further investigated by using a lower superficial gas velocity (next section 3.5.3.2).

The effect of TAN concentration was further compared among corrosion rates measured in single phase on samples with or without a FeS scale (Figure 3.47). Overall, the corrosion rates were lower (less than 6 mm/y) when samples were protected by the FeS scale regardless which TAN concentration was used. Furthermore, the corrosion rate increased about twice when the acid number in the liquid phase was doubled. However,

the levels of corrosion rates were high in both cases, with or without the FeS scale (7–13 mm/y).

A similar comparison, including piping geometry as well, was done for multiphase flow conditions in Figure 3.48. Obviously, by increasing the TAN concentration from 2 to 4, the metal samples experienced similar higher corrosion rates, regardless of the FeS scale.

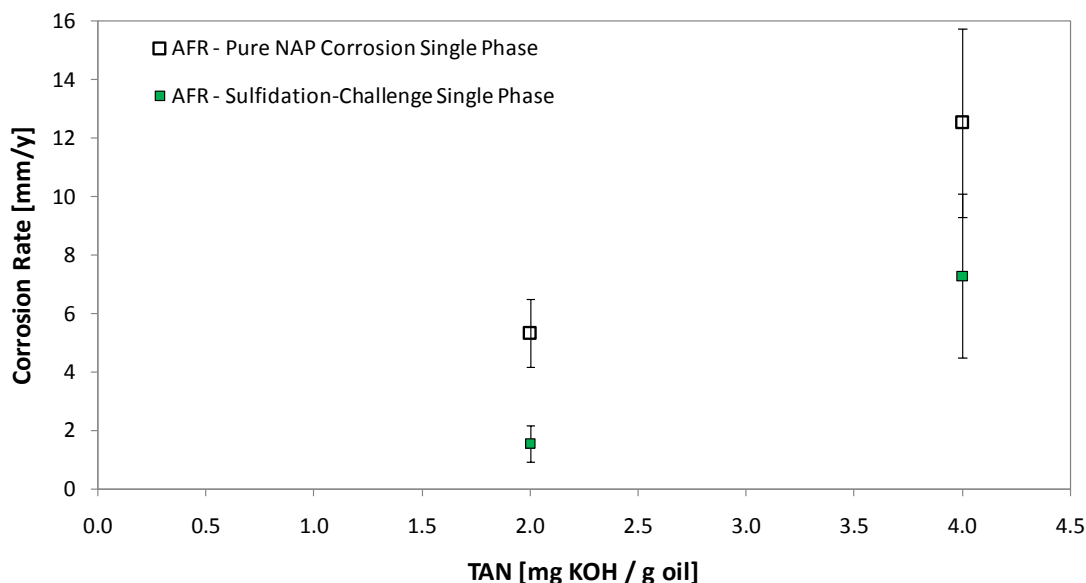


Figure 3.47: Corrosion rates measured in single phase flow conditions ($U_{SL} = 0.1$ m/s) at different TAN concentrations using non-presulfided (hollow marks) and presulfided (full marks) samples.

Apparently, the protected samples due to sulfidation exhibit slightly lower corrosion rates than those unprotected, but given the error bars a clear difference cannot be made. Moreover, an important effect of piping geometry could not be demonstrated as the corrosion rates express similar variability in both straight and elbow samples.

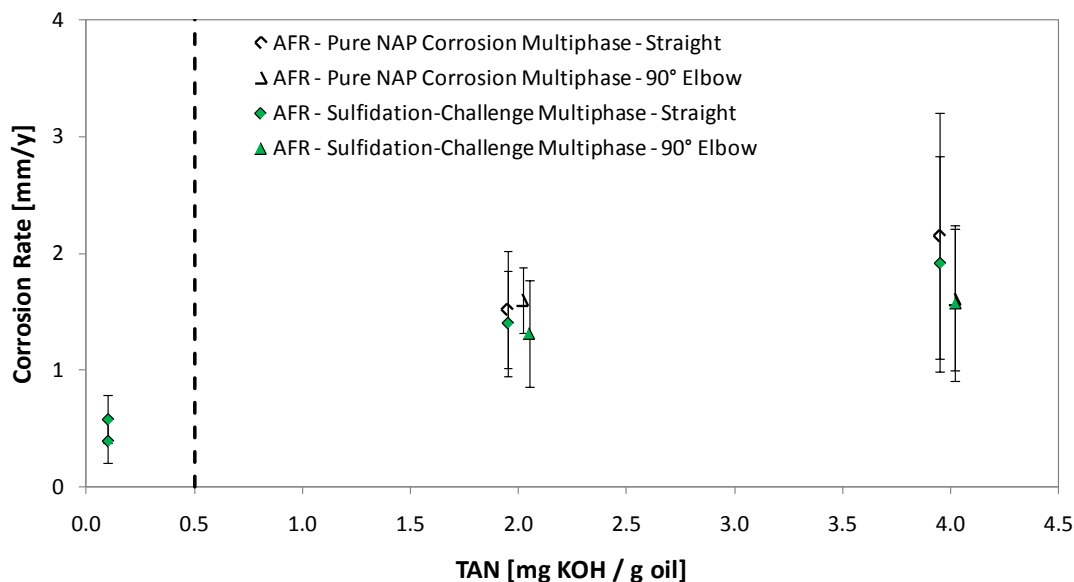


Figure 3.48: Corrosion rates measured in multiphase flow conditions ($U_{SG} = 20$ m/s; $U_{SL} = 0.1$ m/s) at different TAN concentrations using non-presulfided (hollow marks) and presulfided (full marks) samples and various piping geometries.

3.5.3.2 The effect of superficial gas velocity

Previously, it was found that the TAN concentration had no effect on the corrosion rate due to naphthenic acids in multiphase flow conditions at a superficial gas velocity of 20 m/s. In order to check if the flow had an influence on the corrosion rate, the superficial gas velocity was varied from 20 m/s to 10 m/s (the superficial liquid velocity remained 0.1 m/s). The experiments were only run at TAN 2. Corrosion rates were plotted as a function of the superficial gas velocity in Figure 3.49. As reference, in the plot was added the average corrosion rate measured in single oil phase flow on presulfided samples at $U_{SG} = 0$ m/s. Measurements showed that corrosion rates measured in single phase and multiphase flow were not significantly different regardless the increased superficial gas velocity. The FeS scale at the metal surface conferred an equal

degree of protection although the sulfidation process was performed at a lower temperature (316 °C instead of 343 °C used by Kanukuntla, 2008) to increase the FeS scale' resistance against NAP corrosion.

Another “curious” aspect of the corrosion results was that NAP corrosion was as aggressive in straight lines as it was in bends (90° elbows), while refiners usually reported severe corrosion issues only in bends (section 2.4.1).

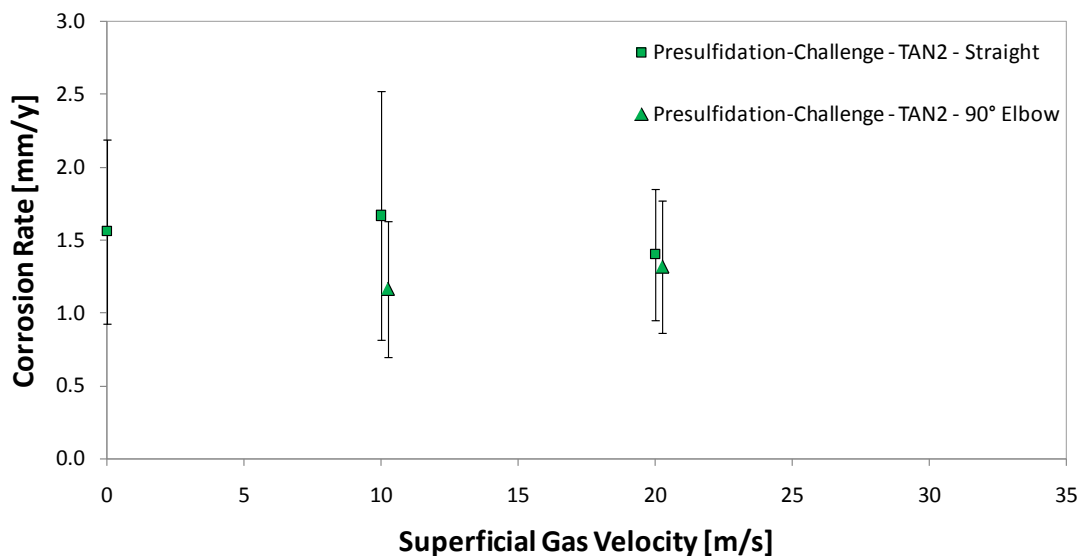


Figure 3.49: Corrosion rates expressed as a function of the superficial gas velocity using a TAN 2 solution and presulfided samples of various piping geometry in multiphase flow. The corrosion rate at $U_{SG} = 0$ m/s was measured in single phase flow conditions.

At high temperature, the presence of a mist flow implies that NAP corrosion can only come from the liquid droplets flowing in the gas core and their ability to impact on the pipe walls. It has been shown that for pipe diameters in a range 0.025–0.095 m, the volume median diameter of droplets increases with the square root of the pipe diameter

(Al-Sarkhi and Hanratty, 2002). By extrapolating these observations to smaller and larger pipe diameters, the droplet size distribution in the pipe can be reasonably assumed to be very different between the AFR test section and a transfer line of oil refinery. At a small operating scale, the droplets would not have enough kinetic energy to damage the scale present at the metal surface in bends, while their respective mass in the large pipe diameters can be much larger and have the ability to locally damage the iron sulfide scale.

The morphology of scale can inform about the exposure of samples to particular flows (single phase vs. multiphase). For instance, if two samples exhibit similar scales (shape, thickness) it can be inferred that both samples experienced the same flow conditions. Longitudinal and radial cross-sections of two samples (S1 from tests NJ41–42, M3 from tests NJ37, 41–42) were analyzed by SEM/EDX. It should be reminded that all tests were operated at similar conditions with few exceptions (tests NJ41–42 at $U_{SG} = 10$ m/s and tests NJ37 at $U_{SG} = 20$ m/s). Since the scale morphology and elemental content did not differ much among the analyzed samples, the two cross sections of sample M3 (test NJ41) were considered representative and, hence, used in all SEM/EDX images in the following figures. The radial cross section of the sample focused on the bottom and top of the tubing sample to find any difference in the scale morphology. As can be seen in Figure 3.50 and Figure 3.51 (zoom), the visible scale at the metal surface looked very similar at the bottom and the top of the sample suggesting that both surfaces were exposed to similar flow conditions.

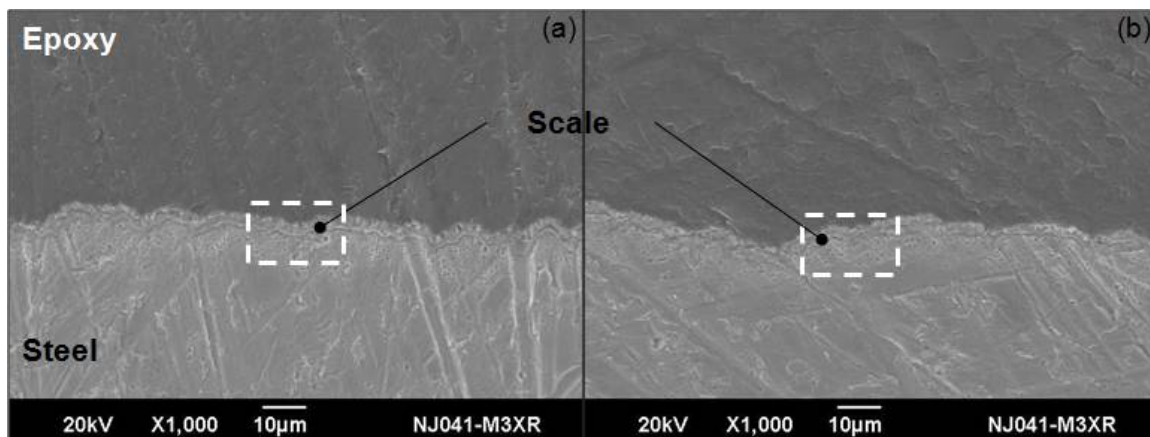


Figure 3.50: SEM images (magnified 1000X) showing the radial cross-sections of a CS sample: (a) bottom; (b) top. The FeS scale was formed with yellow oil in the FTMA for 24 hrs at 316 °C, then challenged in the AFR by a TAN 2 solution for 6 hrs at 343 °C in multiphase flow conditions ($U_{SG} = 10$ m/s; $U_{SL} = 0.1$ m/s).

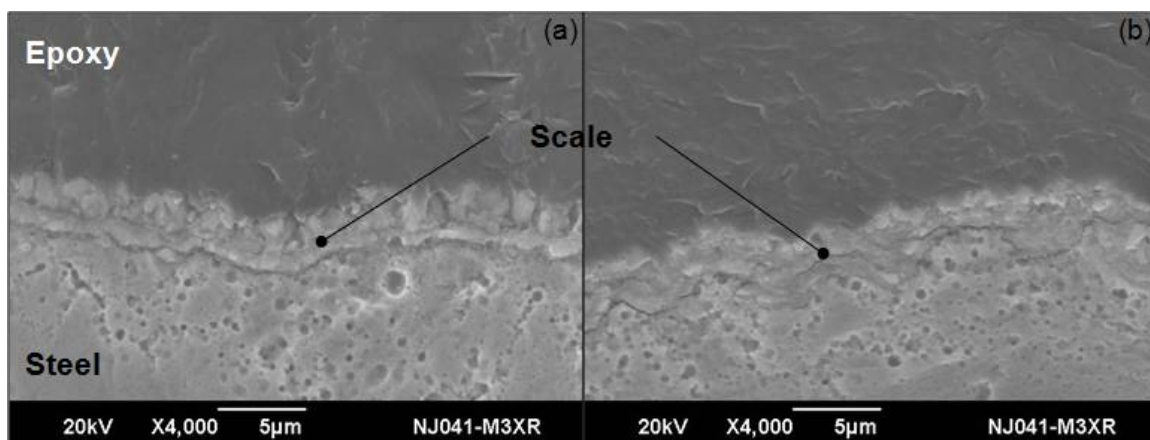


Figure 3.51: SEM images magnified 4000X to see in detail the radial cross-sections of a CS sample from Figure 3.50.

SEM backscattering (enhancing the visibility of the scale) revealed that the scale thickness was in the range of 1–3 μm at both locations on the radial cross-sections of the sample (Figure 3.52). This thickness looks similar to that of the FeS scale built during presulfidation in the FTMA.

The EDX analysis confirmed that the scale content is FeS (Figure 3.53). Regarding the oxygen content of the scale at the bottom and top of the sample, the graph in Figure 3.53b implies that only minor traces of oxygen were found at the metal surface, which is most likely the product of oxidation of the samples exposed to air prior to their insertion into the FTMA for presulfidation treatment. A longitudinal surface analysis was also performed on the same carbon steel sample M3 (test NJ41). The SEM images in Figure 3.54 pointed out a difference in the scale morphology compared to that obtained after a sulfidation test: the scale was not very adherent to the steel surface. This feature usually demonstrates a non-protectiveness of the scale against corrosive species (Nesic, 2012). Some published work confirms this finding about the non-adherence of scale although the authors did not particularly emphasize it in their research (Bota, 2010b; Kanukuntla, 2008 related to NAP corrosion; Han, 2009 related to CO₂/H₂S corrosion).

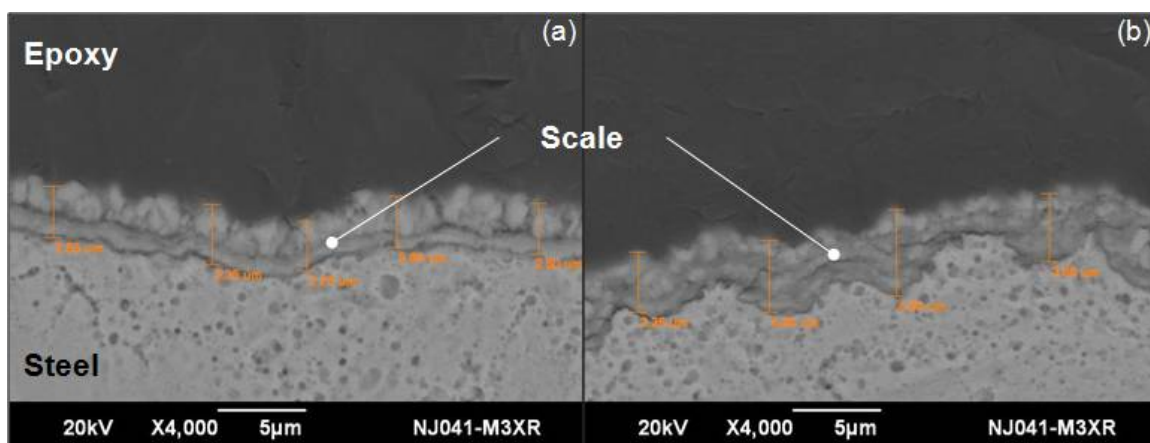


Figure 3.52: Backscattered images (magnified 4000X) showing the radial cross-sections of a CS sample: (a) bottom; (b) top. The FeS scale was formed with yellow oil in the FTMA for 24 hrs at 316 °C, then challenged in the AFR by a TAN 2 solution for 6 hrs at 343 °C in multiphase flow conditions ($U_{SG} = 10$ m/s; $U_{SL} = 0.1$ m/s). The thickness measurements appear in orange.

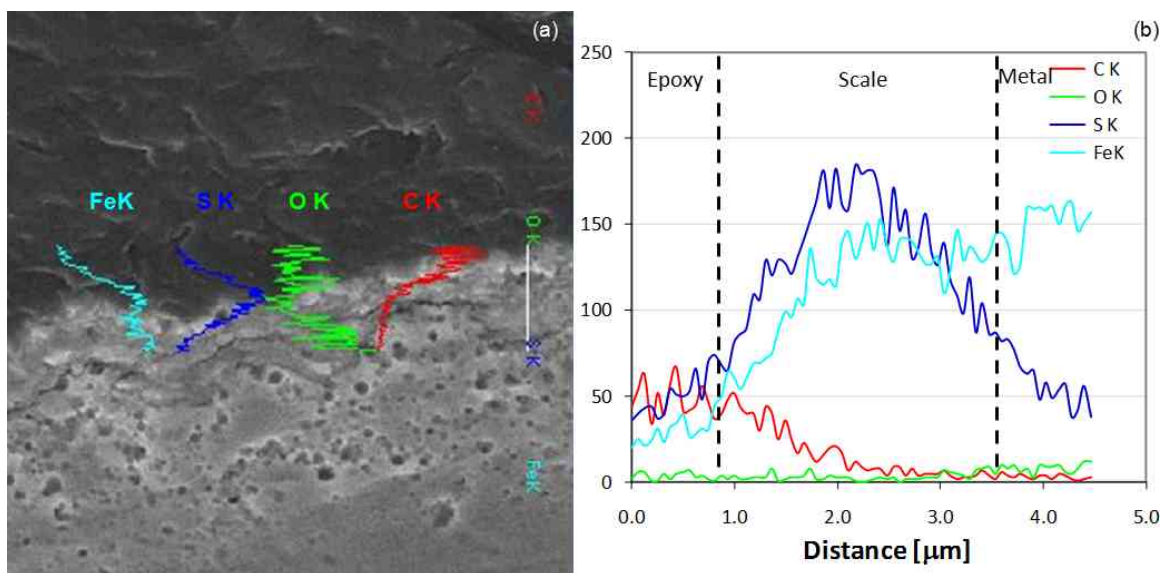


Figure 3.53: (a) EDX analysis across the top of the radial cross-section of the CS sample presented in Figure 3.51. (b) The equivalent EDX analysis re-plotted with absolute values showing that the oxygen content of the scale at this location of the sample is only an artifact.

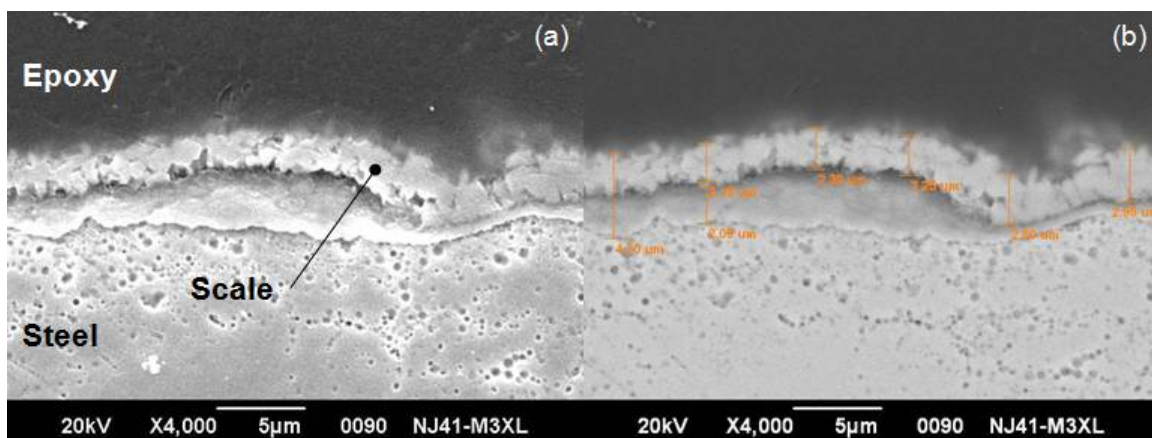


Figure 3.54: SEM image (magnified 4000X) of a longitudinal cross section of a CS sample: (a) typical SEM view; (b) backscattered SEM image with marked thickness measurements. The FeS scale was formed with yellow oil in the FTMA for 24 hrs at 316 °C, then challenged in the AFR by a TAN 2 solution for 6 hrs at 343 °C in multiphase flow conditions ($U_{SG} = 10$ m/s; $U_{SL} = 0.1$ m/s).

3.6 Summary

In single phase flow, the NAP corrosion was found to be a function of TAN concentration and consistently mitigated in the presence of an FeS scale at the metal surface. These results were in agreement with a previously published work in this field for similar conditions (Kanukuntla et al., 2008).

In multiphase flow, results showed that the piping geometry, the TAN concentration, and the presence of an FeS scale at the metal surface had no significant effect on the corrosion rate. The FeS scale was not protective against NAP corrosion during the challenge test in the AFR, although lower temperatures were used during the sulfidation process to build a more resistant scale. These findings did not agree with field observations since the corrosion rates measured in the lab pilot in multiphase flow were, in general, lower than those measured in single phase flow conditions, while in the field corrosion issues in bends of transfer lines are usually reported. Effects of both superficial gas and liquid velocities on the corrosion rate, also supported by the multiphase flow modeling, suggested that the mechanism driving NAP corrosion in multiphase flow conditions is related to the oil wetting fraction depending on the flow pattern occurring in the line.

At this stage, understanding the flow hydrodynamics and the distribution of the phases (flow patterns) in small scale pipes becomes important in order to scale-up these mechanisms to the transfer lines of oil refineries. Therefore, the hydrodynamics of the flow was studied, in parallel, on a large scale flow loop built for the purpose of this work.

CHAPTER 4 EXPERIMENTAL STUDY OF HYDRODYNAMICS

The corrosion study in the previous chapter pointed out the need to better understand the multiphase flow effects on naphthenic acid corrosion. NAP corrosion mainly occurs in the presence of a liquid phase at the steel surface, while lower corrosion rates are usually measured in vapor phase conditions (Gutzeit, 1977; Slavcheva et al., 1999). Therefore, the distribution of the liquid and gas phases in the pipe appears to be a critical factor in this study. In other words, the flow pattern(s), the flow pattern transition(s) and their associated mechanisms had to be investigated and identified in conditions similar to those encountered in transfer lines of oil refineries. A large scale flow loop, the *Cold Flow Rig* (CFR), was designed and built in the present work to study the gas-liquid two-phase flow at high gas velocities and in large pipe diameters.

This chapter starts with an overview of the CFR design and working fluids, continues with descriptions of the test sections and instrument calibration, then describes the experimental procedure and ends with a discussion of the results and a summary of the hydrodynamics study.

4.1 Overview of the Cold Flow Rig and working fluids

The CFR was designed and built to study the hydrodynamics of a liquid-gas two-phase flow mixture in straight pipes at ambient temperature and near atmospheric pressure. The study includes the characterization of the observed flow patterns and flow pattern transitions, and measurements of key hydrodynamic parameters. Because of the

obstruction imposed by existing flow loops in the lab, the construction of the rig had to be considered at a height of 4 m from the ground. All flow lines including the test sections were suspended by hangers and could be accessed only using a lift. The main flow line of the CFR consisted of a 70 m long transparent PVC schedule 40 pipe with an 0.154 m (6") inner diameter (Figure 4.1). Each of the 3.048 m (10 ft) long pipe units were flanged with 0.154 m (6") Vanstone flanges schedule 80.

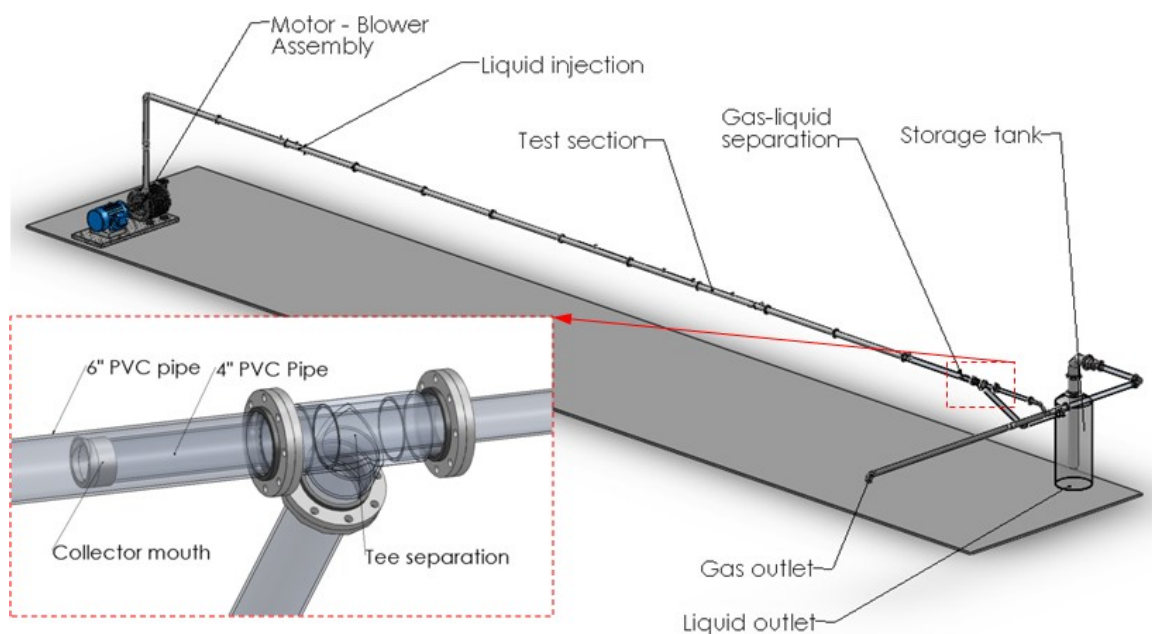


Figure 4.1: Overview of the Cold Flow Rig with a zoom on the gas-liquid separation.

The gas phase (air) was delivered by a Hoffman 38404 multistage centrifugal blower exhauster with a maximal flow rate of $1.42 \text{ m}^3/\text{s}$ (3000 scfm). The rotating speed of the 110 HP motor entraining the blower impeller was directed from a control panel where the air flow rate was set up according to the test requirements. The liquid phase (water) was delivered from the Athens City water supply. Three pipes with an 0.027 m

inner diameter were used to inject the liquid phase into the main flow line of the CFR, at different locations of the gas-liquid mixing section (top, middle, and bottom) as suggested by the diagram in Figure 4.2. The injections of the liquid phase at the top and bottom of the flow line were performed directly through the wall of the pipe, while the injection in the middle section used a nozzle to uniformly distribute the liquid in the core of the pipe.

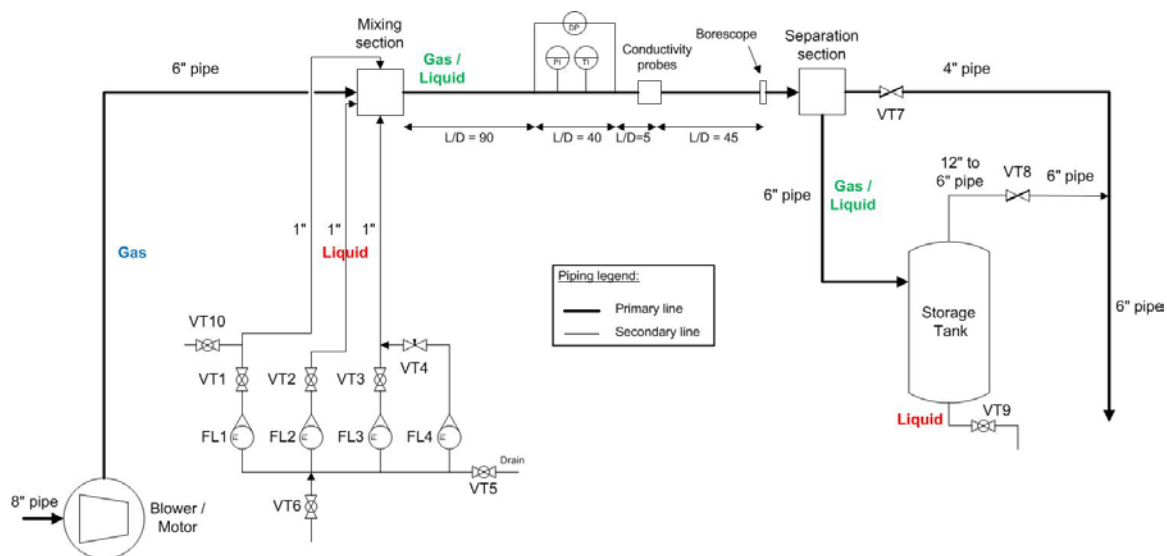


Figure 4.2: Process and flow diagram of the Cold Flow Rig.

During the preliminary testing, a minimum distance $L / D = 50$ from the location of the liquid-gas mixing section in the flow line was assessed to be in unsteady state. Therefore, any instrumentation had to be located beyond this minimum distance. A fitting was added on one of the liquid feeding line using valve VT10 to facilitate the injection of a fluorescent dye (fluorescein) in the liquid phase and also to help to record the in situ liquid velocities flowing at the bottom of the pipe. However, such records and

observations from several tests were inconclusive and were not reported in this document.

After the gas-liquid mixing section, the flow developed along the flow line until it reached the gas-liquid separation section. This latter consisted of two concentric pipes which separated the gas and liquid phases assuming an annular-mist flow pattern (at high gas flow rates). The main CFR line was used as the outer pipe; the inner pipe, with an 0.102 m inner diameter on which a collector was mounted, aimed to capture the gas phase and possible entrained liquid droplets in the gas core (see the zoomed view in Figure 4.1). The gas phase captured by the collector mouth was directed to the gas outlet while the liquid phase flowing through the outer pipe annulus flowed down, towards a collecting tank with an 117 cm inner diameter and a 300 cm height. The volume of collected water in the tank could be either recorded to estimate the flow rate of the liquid film or drained out to the sewer (using valve VT9).

4.2 Description of the CFR test section

The test section began at a distance $L / D = 90$ downstream of the liquid injection section, where temperature, pressure, pressure drop, liquid height at the bottom, and wetted wall fraction were measured and recorded. The pressures measured in the test section were near the atmospheric pressure. The pressure drop was measured between two pressure taps, located at 6.096 m one from another. A metallic graduated stick was used to measure the liquid height at the bottom of the pipe.

A set of conductivity probes was designed to measure the wettability at the internal wall of the pipe (Figure 4.3). The probes are made of epoxy-coated stainless steel pins introduced in 1.47 mm OD capillary tubes glued to the pipe into a 1.59 mm ID hole. A total of 265 probes, staggered in five rows of 53 probes, were flush-mounted around the circumference of the pipe wall, at the end of the test section. This large number of spatially distributed probes was necessary to avoid any reading error due to the “snaking” of the liquid phase around otherwise isolated probes. The probes were connected to a computer through a set of circuit boards to record the wettability.



Figure 4.3: Set up of the conductivity probes at the pipe wall, connected to the circuit board (in the background).

All the equipment related to wettability measurements (i.e., probes, circuit boards, data acquisition program) was designed and manufactured in the house (ICMT lab). The

conductivity probes, however, could not discriminate between droplets and the liquid film during the flow transition from stratified to annular. Therefore, measurements using a ruler tape were also performed to estimate the wettability due to the liquid film only.

The flow pattern in the pipe and entrainment onset of liquid droplets in the gas phase were recorded with a Hawkeye prism borescope (Figure 4.4) and completed by visual observations. The borescope was located at a distance $L / D = 180$ from the liquid injection, inserted in the pipe at the top, and positioned in the same direction of the flow.

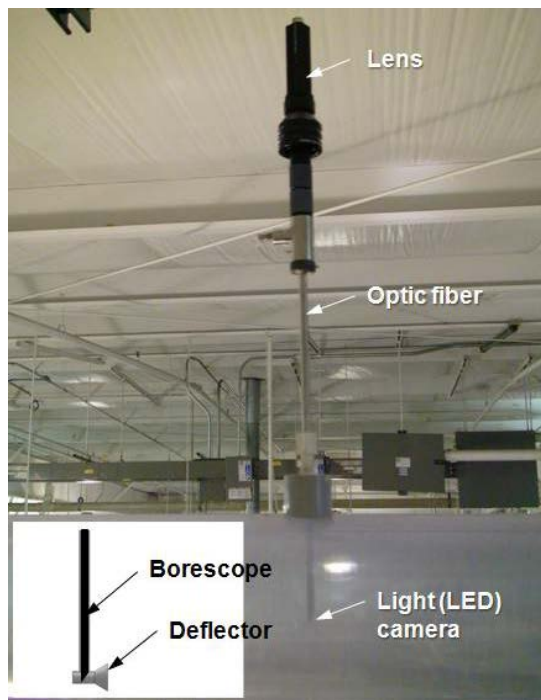


Figure 4.4: Boreprobe setup in the CFR. The PVC deflector (black) protecting the borescope camera from liquid droplets (lower left corner).

The direction-of-view of the prism had a range of $16\text{--}118^\circ$ with an 8 mm diameter glass opening. Videos and photos could be taken with a Luxor camera combined

with a portable light source. Additionally, a deflector was designed to protect the borescope camera from the liquid droplets rolling over its objective at high gas flow velocity (see the zoomed view in Figure 4.4).

Three collectors were manufactured to measure the entrainment fraction, but only two were used for the actual measurements (Jauseau, 2009). Design #1 was machined using an original 90° elbow (schedule 40 pipe), while a 45° elbow (schedule 40 pipe) was modified to obtain design #3 (Figure 4.5). The two designs can cover 31% and 48% of the cross sectional surface area of the pipe, respectively. The butterfly valve (VT7), whose opening can be manually changed, helped to maintain similar pressure conditions in the inner and outer pipes nearby the location of the collector mouth.

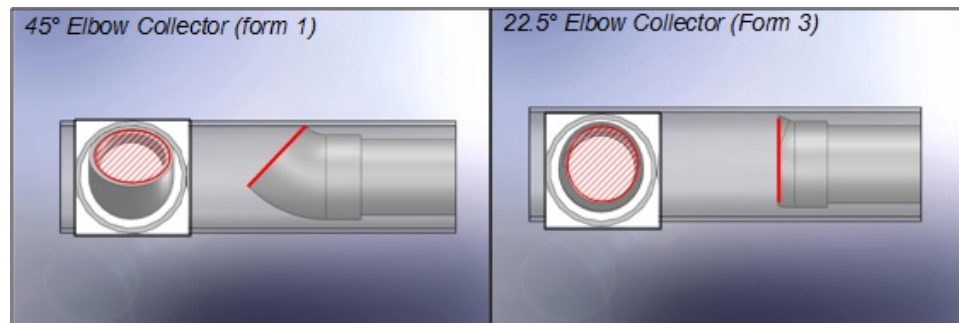


Figure 4.5: Longitudinal and radial views of the collector mouths placed at the extremity of the inner pipe in the gas-liquid separation section.

4.3 Instrument calibration

The gas flow rates were measured with an anemometer HHF92A at the inlet of the flow rig (blower location). The anemometer has an operating range of 0.4–35 m/s with a measurement uncertainty of 1.1 m/s. Calibration curves of superficial gas velocity

vs. controller frequency at different liquid flow rates are provided in APPENDIX I. The liquid flow rate was measured by three FL4400 rotameters, all calibrated by the manufacturer. The FL4400 rotameters (marked as FL1, FL2 and FL3 in Figure 4.2) have an operating range of 0–77 L with a measurement uncertainty of 4%. For very low liquid flow rate measurements, a FL7603 rotameter (FL4 in Figure 4.2) with an operating range of 0–19 L and a measurement uncertainty of 2% was used.

The temperature was measured with a type K thermocouple probe made of stainless steel AISI 304 sheath, which was connected to a DP24-T temperature controller with an accuracy of 0.5°C. The pressure and pressure drops were measured using KZ wet/wet differential pressure transducers with a pressure range of 0–2 psid, calibrated by the manufacturer with an uncertainty of 0.25%.

The metallic stick used to measure the liquid height at the bottom of the pipe has marks at every 0.25 cm. Since waves occurred at the gas-liquid interface during measurements, the liquid height oscillated from one reading to another, so that the readings were averaged over the observation time (i.e., 20–30 s). The amplitudes of the waves did not exceed a graduation unit around the measured average; therefore, the 2.5 mm graduation unit was considered as the instrument uncertainty.

The liquid perimeter was measured with a ruler tape. However, because of the difficulty to estimate the wettability of the pipe after the entrainment onset had occurred, the systematic uncertainty of the perimeter measurements was estimated at ± 3 mm.

The liquid entrainment fraction was indirectly measured by a mass balance between the total volumetric flow rate $Q_{L,T}$ measured at the rotameters and the volumetric

flow rate of the liquid film $Q_{L,F}$ recovered in the storage tank. The liquid film flow rate was estimated from the difference of water levels measured in the storage tank during the test (initial and final stages). For this purpose, a graduated tubing with a ruler tape was connected on the external side of the storage tank where it experienced the same pressure conditions to those in the storage tank. For each of the two readings, at the beginning and the end of the test, the uncertainty of the liquid level measurement was ± 1 mm. The uncertainty related to the time measurement was less significant and estimated at 1 s for each measurement.

The entrainment fraction FE was calculated using the following equation:

$$FE = \frac{Q_{L,T} - Q_{L,F}}{Q_{L,T}} = \frac{Q_{L,E}}{Q_{L,T}} \quad (4.3.1)$$

where $Q_{L,E}$ is the liquid flow rate of the droplets entrained by the gas phase (m^3/s).

4.4 Experimental procedure for CFR experiments

An experiment on the CFR started with the valves on the liquid lines (VT1 to VT6) closed, while valves on the gas and gas-liquid lines (VT7 to VT9) were open. All instrumentation and the control panel were powered up. In the first 10–15 minutes of the experiment, only a single gas phase flowed through the CFR in order to warm the motor-blower assembly. Then, the gas and liquid flow rates were set up according to the desired operating conditions from the control panel and using rotameters. Only few minutes were necessary to reach the steady state since the fluid was not recycled. For each test, a series of parameters were recorded: gas and liquid flow rates, pressure, temperature, pressure drop, entrainment fraction, liquid height at the bottom of the pipe, flow pattern

characteristics and entrainment onset. The entrainment onset was estimated from recordings of a borescope camera combined with visual observations at the top of the pipe. An arbitrary criterion to assess the entrainment onset was set that at least one liquid droplet should hit the top of the pipe or the borescope camera every ten seconds. Therefore, the borescope camera was placed close to the top of the pipe and faced the direction of the oncoming flow. For a given liquid flow rate, the gas velocity was increased in increments of 0.5 m/s to be able to observe the entrained droplets in the gas core.

For each data point at given operating conditions (U_{SG}, U_{SL}), measurements were repeated three times and then averaged. After the measurements were completed, the CFR system could be re-run for different operating conditions or shut down. Prior shutting it down, the liquid feeds were first turned off and the flow rig was dried using a superficial gas velocity of 30–40 m/s. After ca. 20 min the motor-blower was stopped, and then, all the instrumentation shut down.

A test matrix as a function of superficial gas and liquid velocities is given in Table 4.1. The test conditions for an air–water mixture are point-marked on a flow map generated with the flow model presented in CHAPTER 5 (Figure 4.6).

Table 4.1: The CFR test matrix for air-water experimental cases (EO is the Entrainment Onset).

| U_{SL} (m/s) | U_{SG} (m/s) | | | | | | | | |
|-------------------|----------------|----|----|----|----|----|----|----|----|
| | 15 | 20 | 25 | 30 | 40 | 50 | 55 | 60 | EO |
| 0.007 | 15 | 20 | 25 | 30 | 40 | 50 | 55 | 60 | EO |
| 0.017 | 15 | 20 | 25 | 30 | 40 | 50 | 55 | | EO |
| 0.034 | 15 | 20 | 25 | 30 | 40 | 50 | 55 | | EO |
| 0.068 | 15 | 20 | 25 | 30 | 40 | 50 | 55 | | EO |
| 0.102 | 15 | 20 | 25 | 30 | 40 | 50 | | | EO |
| 0.135 | 15 | 20 | 25 | 30 | 40 | 50 | | | EO |
| 0.169 | 15 | 20 | 25 | 30 | 40 | 50 | | | EO |

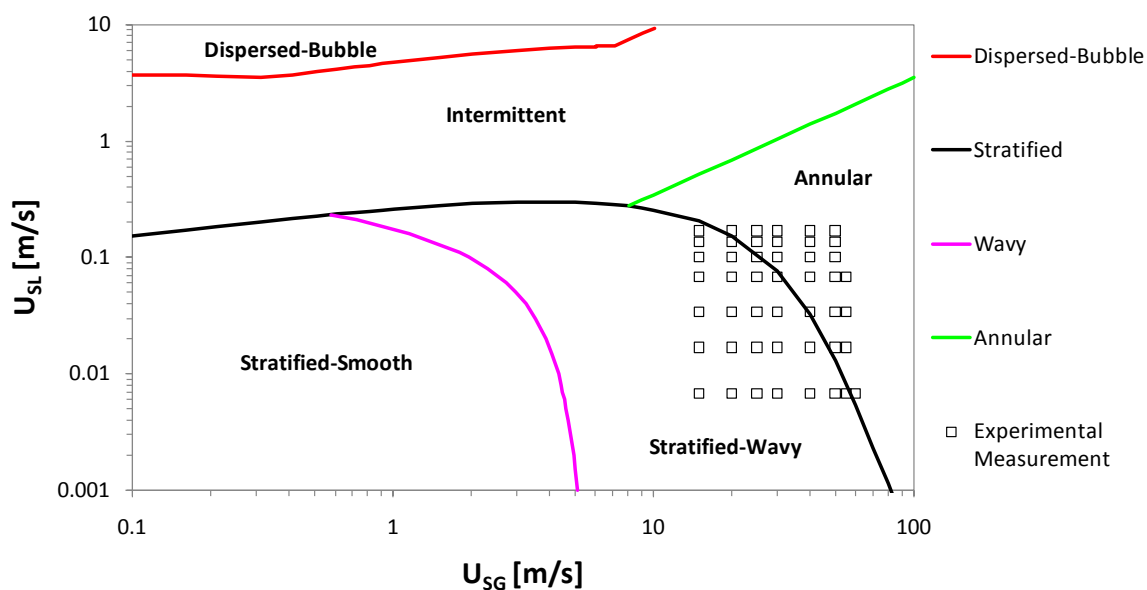


Figure 4.6: The CFR test matrix superimposed on an air-water flow map in horizontal flow using a 0.154 m pipe diameter.

4.5 Results and discussion

Descriptions of flow patterns and associated flow transitions, and all the measurements recorded to characterize the flow are presented in this section. The experimental data are available in APPENDIX J.

4.5.1 Flow patterns and entrainment onset

A qualitative assessment of the flow patterns occurring during experiments in the CFR was achieved through visual observations of the flow. The entrainment onset was assessed directly by visually observing the external pipe surface and indirectly, through a borescope camera. The superficial gas velocity was varied from 15 to 55 m/s; within this range, different flow patterns (i.e., stratified-wavy and annular-dispersed) could be observed. The flow pattern transition was characterized by a mechanism of droplets entrainment-deposition similar to that reported in literature (Andritsos, 1986; Meng et al., 2001). The following succession of flow patterns (from b to e) was observed to occur in the CFR at a constant liquid flow rate and an increasing superficial gas velocity (Figure 4.7):

- Stratified wavy flow (a)
- Droplets atomization in the gas phase (b)
- Droplets deposition at the wall of the pipe (c)
- Rivulets formation at the wall of the pipe (d/e)
- Liquid film formation at the wall of the pipe (d/e)
- Annular-dispersed flow (f)

Before the droplets started atomizing, the gas-liquid interface was wavy with a liquid film creeping slightly along the pipe because of the motion of the waves. While increasing the gas velocity, the droplets atomization was quickly followed by a deposition of small droplets just above the gas-liquid interface at the wall of the pipe.

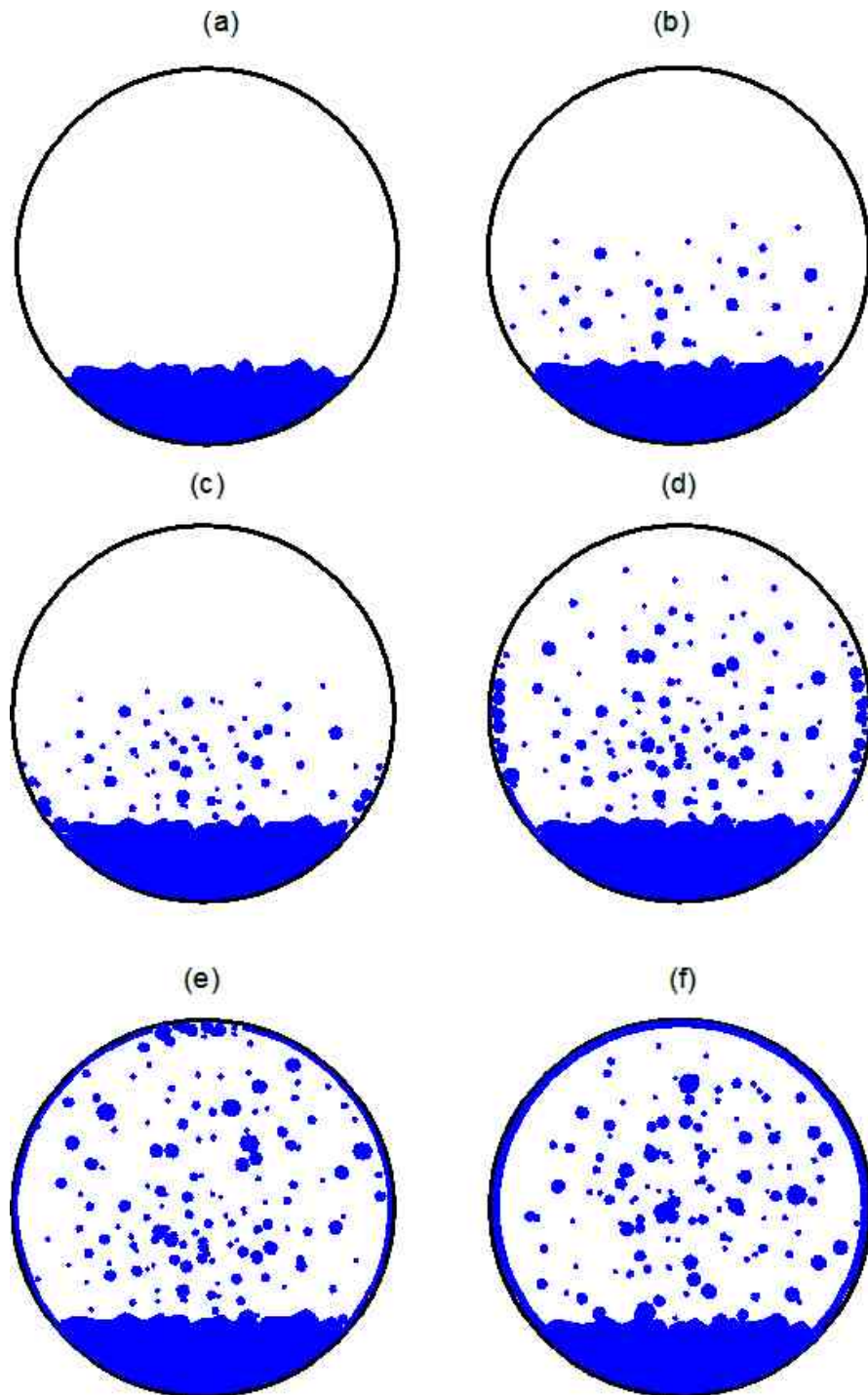


Figure 4.7: The 6-step droplets entrainment-deposition mechanism of the flow transition stratified to annular-dispersed. The pipe cross sections are: stratified-wavy flow (a), droplets atomization (b), droplets deposition (c), formation of liquid rivulets (d), continuous liquid film built along the top of the pipe wall (d/e), annular-dispersed flow (f).

A further increase in gas velocity led to the generation of more droplets. Smaller droplets started depositing on the upper part of the pipe wall, while larger droplets hit the wall in the lower section of the pipe (between h_L and $D/2$), and eventually started forming liquid rivulets. A further increase in the gas flow rate allowed the formation of a continuous liquid film at the lower part of the pipe wall. The larger droplets and, by extension, the rivulets started forming in the mid and upper sections of the pipe wall. This mechanism propagated until the top of the pipe was totally covered with a very thin yet fragile liquid film since it could be easily disrupted by any deep groove present at the top of the pipe. Because of the gravity effect, the distribution of the liquid film was asymmetric: thick at the bottom and much thinner at the top and on the sides. The velocity of the liquid film was also very similar at the top and the sides of the pipe, but much slower than that observed at the bottom of the pipe.

A flow map generated with the model in Chapter 5 summarized all the above observations in Figure 4.8. The model (lines) agreed well with the experimental data (point-marks). As can be seen, the lines define different flow pattern regions containing the corresponding empirical observations.

Contrary to the qualitative assessment of flow patterns, each entrainment onset point was quantified within an uncertainty range of gas velocity (Figure 4.9). At lower liquid flow rate, a higher superficial gas velocity was required to measure the entrainment onset. At these gas velocities, the measured entrainment onset falls within the stratified-wavy region in Figure 4.8. These results will serve for model validation in Chapter 6.

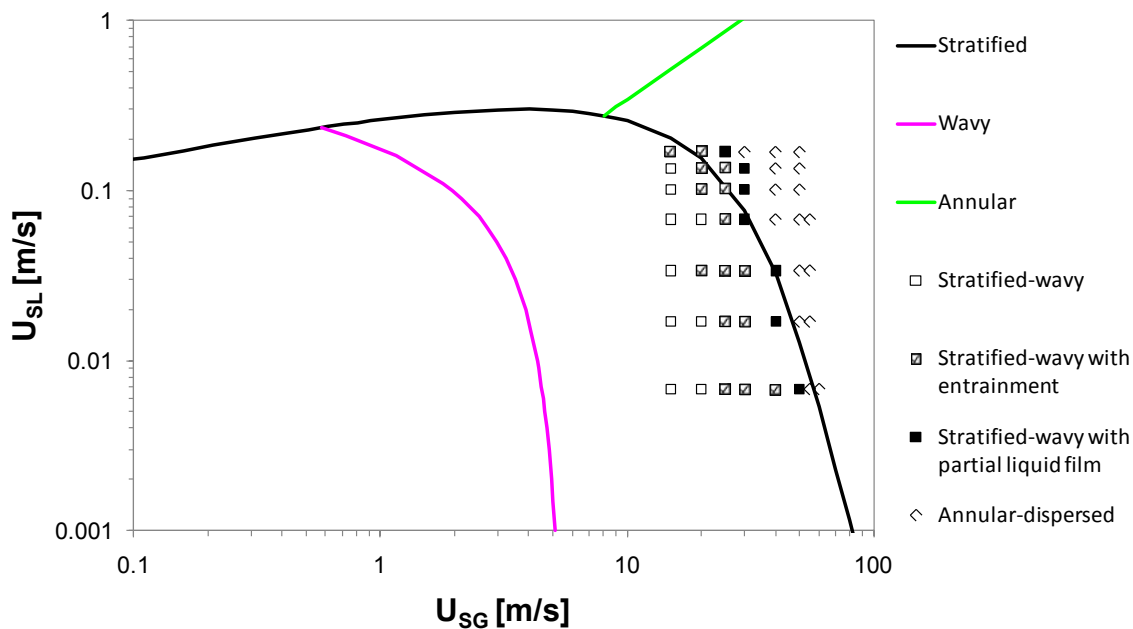


Figure 4.8: Experimental observations represented on a flow pattern map of an air / water mixture in a 0.154 m horizontal pipe.

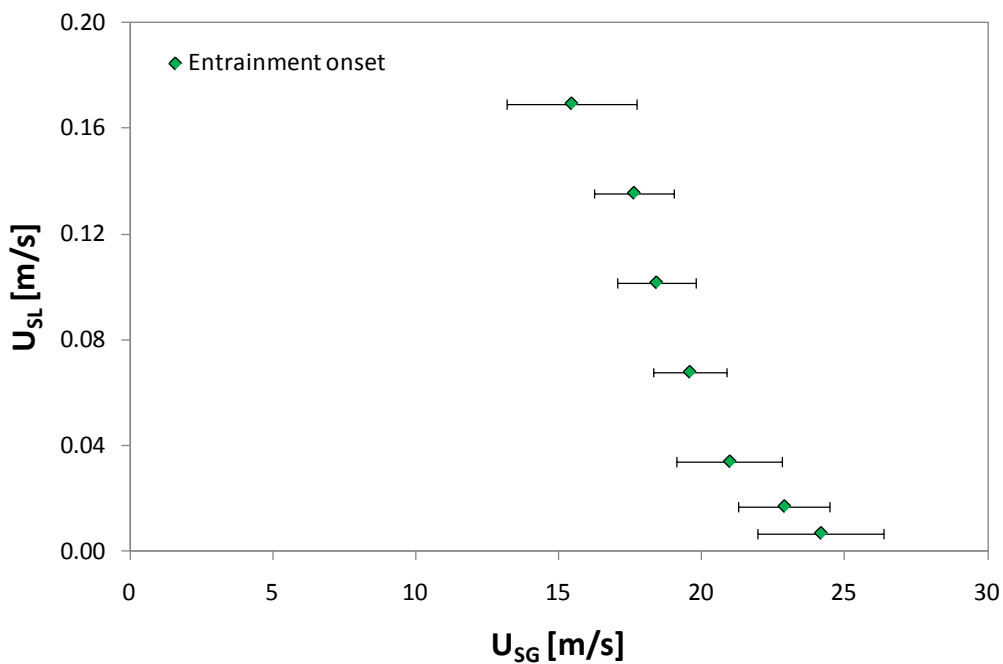


Figure 4.9: Experimental measurements of the entrainment onset.

4.5.2 Flow characteristics

The main flow characteristics analyzed in this section are: pressure drop, wetted wall fraction, liquid height and entrainment fraction.

The pressure drop

At a constant liquid flow rate, the total pressure drop increases when increasing the superficial gas velocity (Figure 4.10). This finding was also observed when increasing the superficial liquid velocity at a constant gas flow rate. In both cases, the increase in pressure drop was due to higher frictions of the liquid and the gas phases with the wall of pipe. A sharper slope in the ascending trend of the pressure drop was noticed right after the appearance of the entrainment onset.

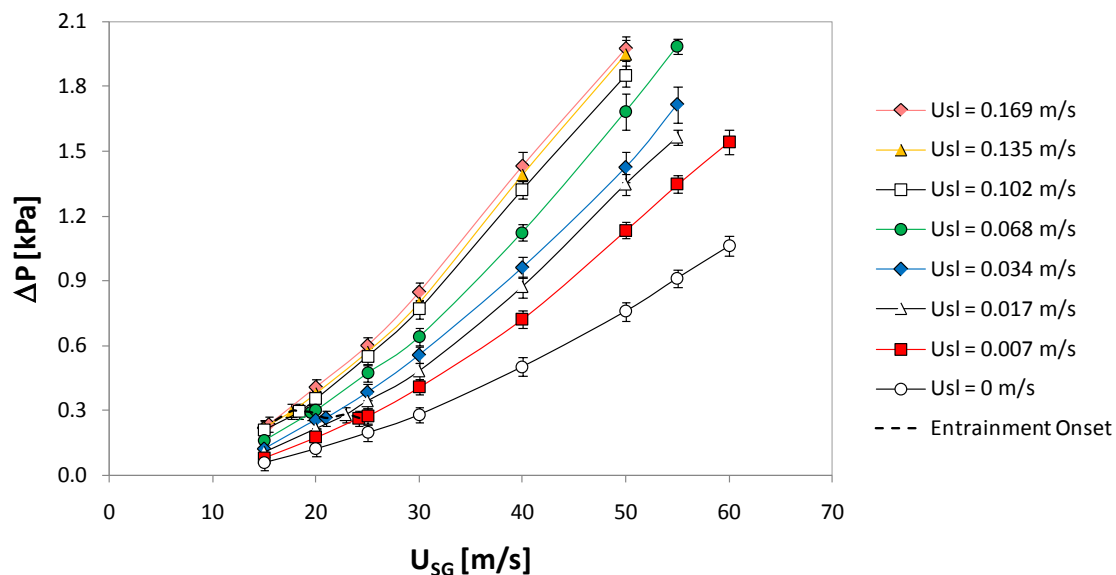


Figure 4.10: The pressure drop ΔP trends at different superficial liquid velocities.

The wetted wall fraction

This parameter could be measured when a liquid film (even a very thin one) was wetting the inner surface of the pipe. It was either recorded with a computer connected to the conductivity probes (Figure 4.11) or visually measured with a ruler tape.

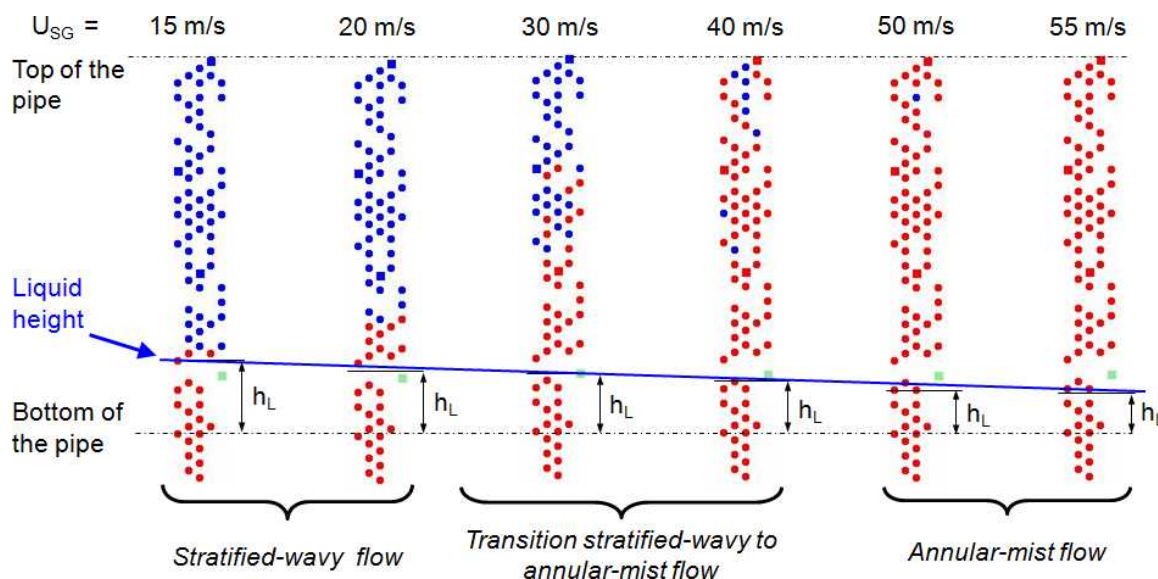


Figure 4.11: Wettability measurements at the inner wall of the pipe (red = wet, blue = dry) for a superficial gas velocity range of 15–55 m/s and at a constant liquid flow rate $Q_L = 18.92$ L/min. The liquid level at the bottom is expressed as the liquid height h_L .

Droplets or rivulets that formed on the wall were not included in the wetted wall fraction because they were not part of the liquid film. In the advanced stage of the stratified to non-stratified transition (at least 50 % of the pipe perimeter covered by the liquid film), the whole perimeter is wet and the conductivity probes do not discriminate the liquid droplets/rivulets from the liquid film. Therefore, the boundary between the continuous liquid film and the numerous rivulets formed at the inner pipe interface should be visually observed. In stratified-wavy flow conditions, it was observed that the

wetted wall fraction mainly increased due to the presence of waves at the gas-liquid interface which promoted the creeping of the liquid film along the wall.

The wetted wall fraction was plotted as a function of the superficial gas velocity for different liquid flow rates (Figure 4.12). After the entrainment onset was observed (dashed line) the wetted wall fraction sharply increased due to the deposition of droplets and the following formation of a thin liquid film at the wall until it totally covered the pipe perimeter. At a constant gas flow rate, the wetting wall fraction increased with the superficial liquid velocity.

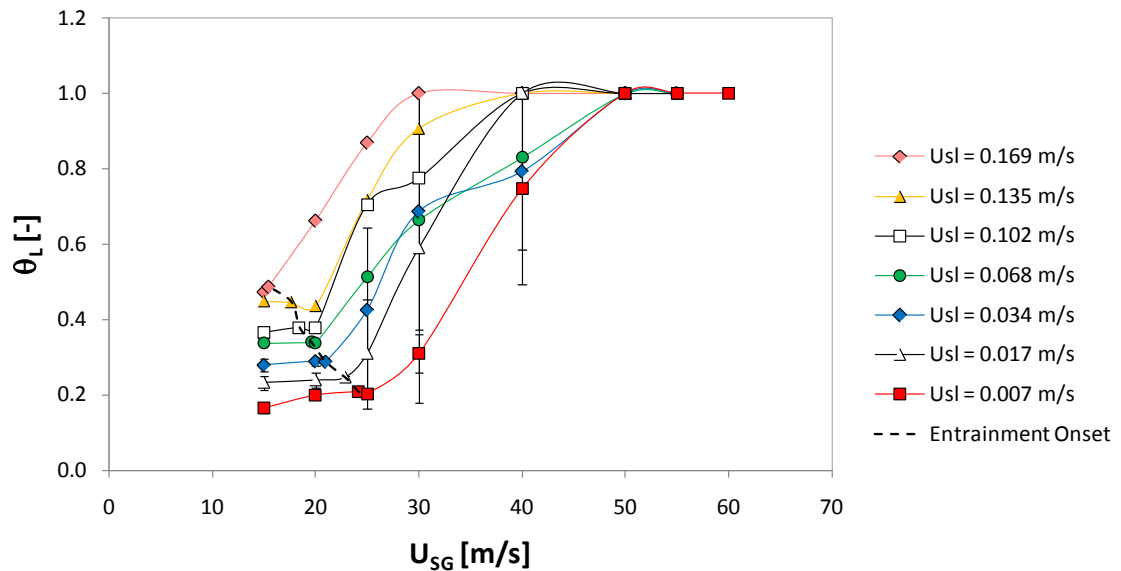


Figure 4.12: The wetted wall fraction θ_L at different superficial liquid velocities.

The liquid height at the bottom of the pipe

At a given liquid flow rate, the liquid height shrank when increasing the superficial gas velocity because of an accentuated shear stress at the gas-liquid interface

(Figure 4.13). Conversely, at a constant gas flow rate, the height of the liquid increased as a function of the superficial liquid velocity. Overall, the measured liquid height varied from 2.5 mm (0.007 m/s liquid and 40 m/s gas) to 40 mm (0.169 m/s liquid and 15 m/s gas).

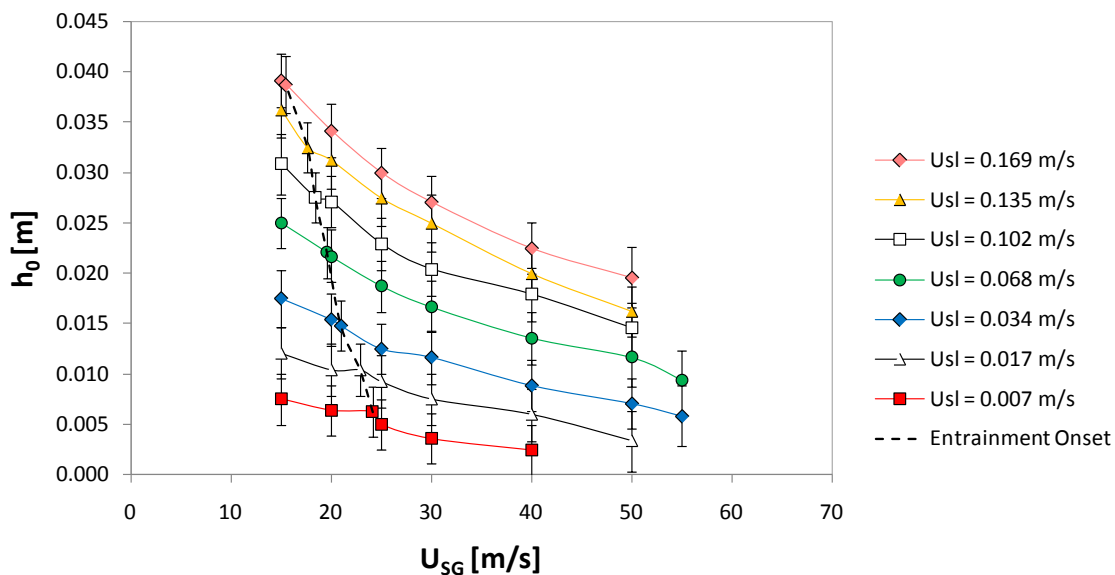


Figure 4.13: The liquid height at the bottom of the pipe h_0 at different superficial liquid velocities.

The entrainment fraction

The entrainment fraction FE was measured with two different collector mouths. However, the use of two different cross sectional areas of the collectors did not make any difference in collecting the entrained droplets in the gas core; therefore, only results obtained with collector #3 are presented in this section. Measurements were performed six times for particular flow characteristics and as a means to ensure confidence in reproducibility to get consistent data at given flow conditions. The entrainment fraction,

as a function of gas velocity, increased from the entrainment onset up to 25%, but only for low liquid loads (Figure 4.14).

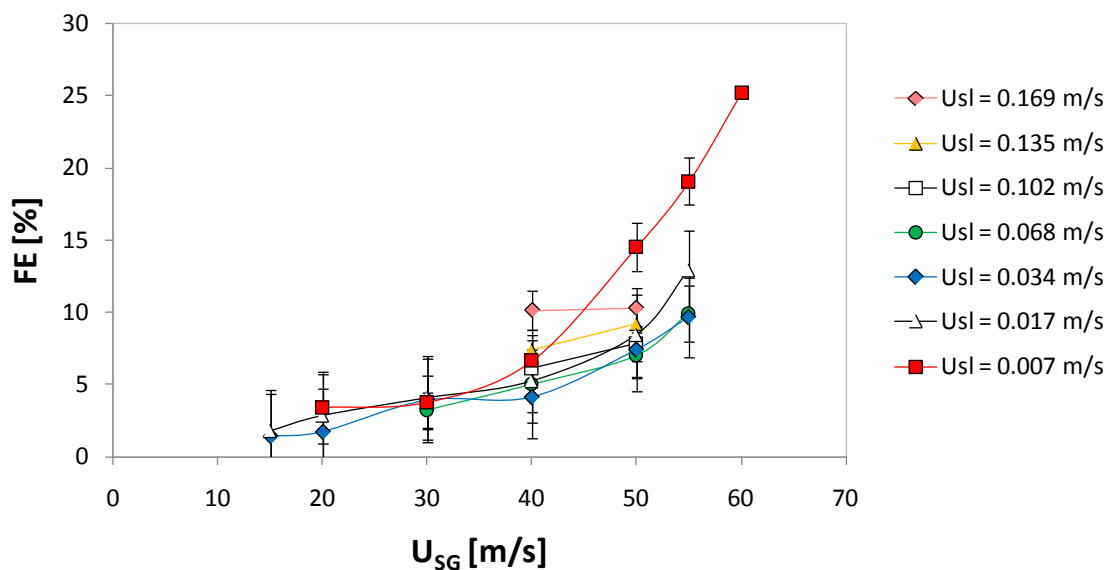


Figure 4.14: The entrainment fraction FE at different superficial liquid velocities.

The entrainment fraction shows no or little increase at higher liquid loads; therefore, no relationship with the liquid velocity could be inferred from these results. Given the measurement uncertainty, the entrainment fractions below 10% were not significantly different from each other. The inconsistent evolution of the entrainment fraction at a higher liquid flow rate can be explained by the limitation of the instrumentation used to assess the liquid film required to equalize the pressure at the collector mouth, in order to avoid the suction of the liquid by a possible pressure difference in the gas core cross section. This condition remained difficult to achieve, particularly at high liquid flows, with the present setup (a manual butterfly valve). Using

similar operating conditions (0.154 m horizontal pipe with air/water mixture) Mantilla (2008) could measure entrainment fractions in the same order of magnitude as the ones presented here at lower gas velocity. However, a film extractor was used to measure the liquid volume of the film flowing at the pipe wall.

4.6 Summary

A new experimental flow system was designed and built to study the hydrodynamics of gas-liquid two-phase flow mixtures in straight pipes, at high flow gas velocities and at low to medium liquid loadings. The dominant flow patterns observed in this system within these operating conditions were stratified-wavy and annular-dispersed. Their associated (flow pattern) transition was driven by a droplets entrainment-deposition mechanism at the pipe wall. Important flow characteristics, such as the pressure drop and the wetted wall fraction, were recorded and used for the validation of the flow model in CHAPTER 6.

CHAPTER 5 GAS-LIQUID TWO-PHASE FLOW MODELING

Although much important experimental work was done in the field of oil refinery corrosion (CHAPTER 2) in order to obtain reliable data for the validation of predictive models, there remain uncertainties related to scaling-up or scaling-down of the corrosion and flow conditions occurring in pipelines. For example, the flow patterns occurring in transfer lines of oil refineries are difficult to assess because of several factors, such as the variation in crude oil blends, operating conditions (pressure, temperature, flow rate) leading to different vaporization rates, wetted wall fractions, etc. Therefore, in this study, a new mechanistic gas-liquid two-phase flow model has been developed to predict the flow pattern and its characteristics: liquid holdup, pressure drop, and entrainment fraction. Comprising of nine sections, this chapter starts with the descriptions of different flow patterns occurring in multiphase flow, followed by the predictions of flow pattern transitions, entrainment onset modeling, flow patterns modeling and, finally, the structure of the gas-liquid two-phase flow model.

5.1 Description of flow patterns in multiphase flow

5.1.1 Stratified flow

The stratified flow is characterized by a complete stratification of the two fluids (Figure 5.1). The gas phase flows in the upper part of the pipe while the liquid phase flows at the bottom. The stratified flow pattern can take two forms, such as stratified-smooth (where the gas-liquid interface is smooth) and stratified-wavy (where the flow

ripples, then, small waves appear while increasing the superficial gas velocity). It is not observed in upward flow at pipe inclinations greater than 20° and superficial liquid velocities higher than 0.001 m/s (Barnea et al., 1985). Many studies (Chen et al., 1997; Fan et al., 2007; Meng et al., 2001) demonstrated that the stratified flow can reasonably occur at inclination angles up to 10° . The latter was considered the upper limit of pipe inclination angles in the present model.

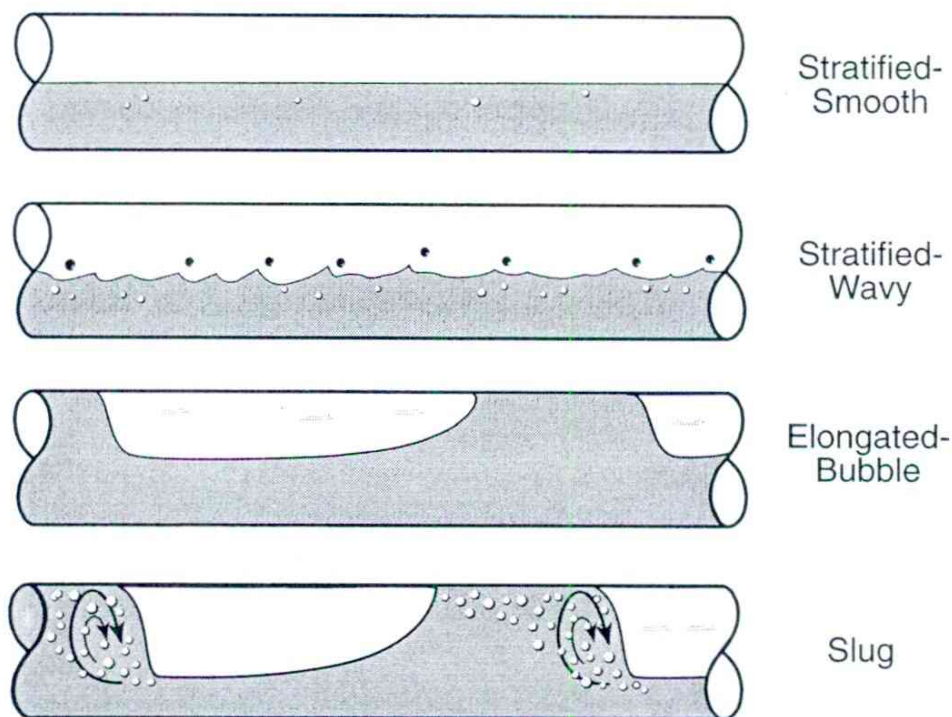


Figure 5.1: Representation of stratified and intermittent flow patterns observed at horizontal and near horizontal pipe inclinations (adapted from Shoham (2006). © 2006 Society of Petroleum Engineers)

5.1.2 Annular-dispersed flow

The annular-dispersed flow (Figure 5.2 and Figure 5.3) occurs at moderate and/or high gas velocities and can be encountered at any pipe inclination. For modeling purposes, the different configurations of fluid distribution (“annular-mist”, “mist” and “annular-wavy”) are all considered as annular-dispersed flow in order to predict the flow regime.

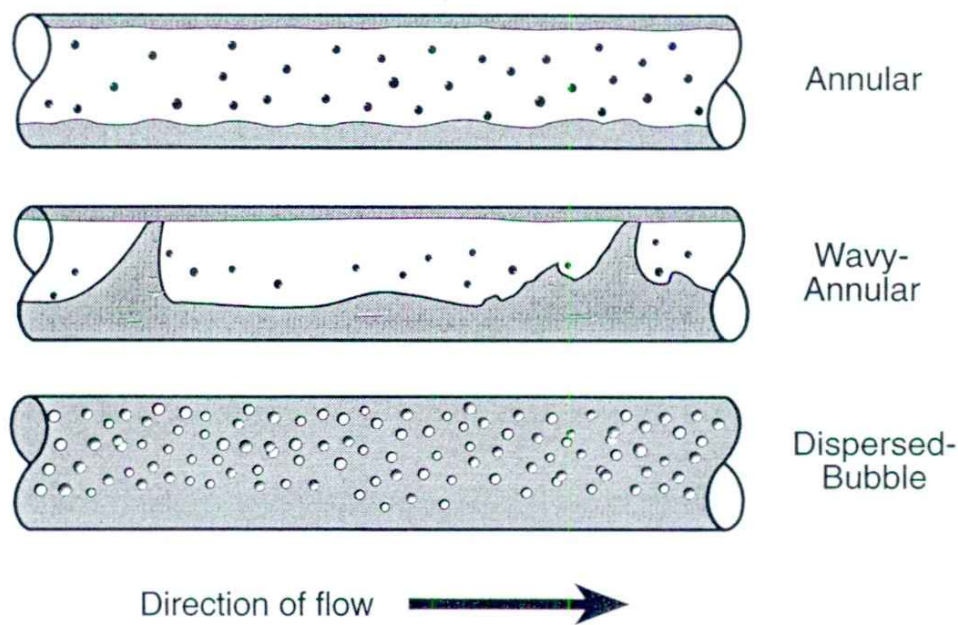


Figure 5.2: Representation of annular-dispersed (annular and wavy-annular) and dispersed-bubble flow patterns observed at horizontal and near horizontal pipe inclinations (adapted from Shoham (2006). © 2006 Society of Petroleum Engineers).

The annular-mist is characterized by a liquid film flowing at the wall of the pipe while the pipe core is occupied by the gas phase. The gas phase also contains liquid droplets (mist) entrained from the liquid film. For vertical gas-liquid flows, the thickness

of the liquid film may be considered as constant, while for horizontal and near horizontal flows, the thickness varies because of the gravity effect (thicker at the bottom than the top and sides of the pipe). The distribution of both phases is depicted in Figure 5.2 for horizontal pipes and in Figure 5.3 for vertical pipes.

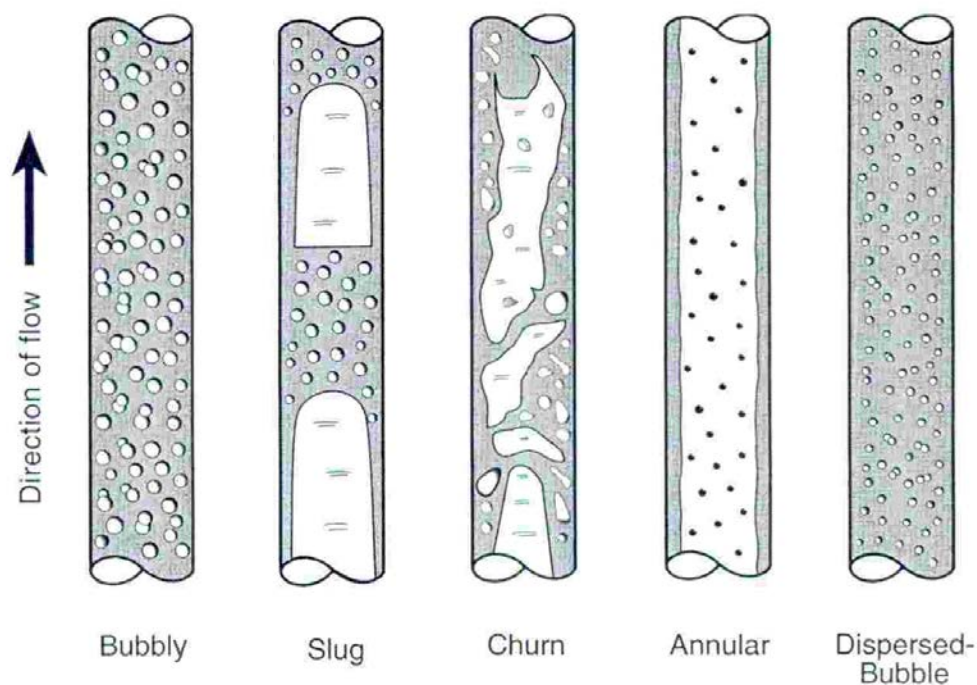


Figure 5.3: Representation of flow patterns observed at vertical and sharply vertical pipe inclinations (adapted from Shoham (2006). © 2006 Society of Petroleum Engineers).

The mist flow is very similar to annular-mist except that no annular liquid film flows at the wall of the pipe. This type of flow pattern may occur only at very high gas velocity.

The annular-wavy flow appears as an intermediate flow pattern between slug and annular flows. When the gas velocity increases, the void fraction in the liquid slug also

increases. If the slug can no longer form a strong liquid bridge, the liquid slug is called “protoslug” and the flow pattern is considered as being wavy-annular (Taitel and Barnea, 1990b).

5.1.3 Intermittent flow

The intermittent flow gathers different types of flow patterns, such as elongated bubble, slug, plug or churn. Each flow pattern is shortly described in this section, although the most common is the slug flow.

Slug flow pattern

The slug flow is an unsteady state flow and the most encountered flow pattern in upward flow. It can be characterized by a slug unit (Figure 5.1) composed of two parts: a slug body of liquid with entrained gas bubbles and a film zone (or slug tail) with a liquid layer at the bottom of the pipe. The slug body is considered to be moving as the same velocity as the gas phase. In vertical and sharply inclined upward flows, the film zone is called the "Taylor bubble". The "Taylor bubble" is a symmetrical bullet-shape gas bubble rising up while a liquid film flows down around the gas bubble at the wall of the pipe (Figure 5.3). A liquid bridge aerated with small gas bubbles separates two consecutive Taylor bubbles (Shoham, 2006).

Elongated bubble and churn flow patterns

The elongated bubble and churn flows represent two limiting cases of the slug

flow pattern. In elongated bubble flow pattern, the gas void fraction in the slug body tends to be zero. The elongated bubble pattern is encountered in horizontal and near horizontal gas-liquid flows. At low gas velocities and moderate liquid velocities, elongated gas bubbles flow in the upper part of the pipe (Figure 5.1). The second limiting case of the slug flow pattern is the churn flow, which only happens in vertical and near vertical pipes. When increasing the gas velocity, the liquid slugs become more aerated and, therefore, the liquid bridges are regularly blown up (Figure 5.3). This flow pattern is highly turbulent and described as “a coarse agitation of the liquid phase” (Govier and Aziz, 2008).

5.1.4 Bubble flow

The bubble flow is a homogenous flow pattern consisting of a continuous liquid phase with discrete gas bubbles. It can be divided into two different categories, such as dispersed bubble and bubbly if any slip or none occurs between the two phases (Brill and Mukherjee, 1999). If the gas bubbles are large and move quicker than the liquid phase, the flow is considered as bubbly (Figure 5.3). If the gas phase consists of small dispersed gas bubbles moving as fast as the liquid phase, the flow is considered as dispersed bubble (Figure 5.1 and Figure 5.3). The dispersed bubble pattern mainly occurs at high liquid velocities and low to moderate gas velocities, while bubbly, at lower liquid and gas velocities in steep upward flows.

5.2 Friction model

For each flow pattern, the friction factors used as closure relationships in the friction model are needed to solve the momentum balance equations. These factors usually depend on the Reynolds number and pipe roughness. This section starts with a general definition of the Reynolds number Re , expressed in terms of either superficial or in-situ velocity, and continues detailing the different correlations used for calculating the gas-wall friction factors.

5.2.1 Definition of the Reynolds number

The Reynolds number is defined by the general relationship:

$$Re = \frac{\rho DU}{\mu} \quad (5.2.1)$$

A Reynolds number Re_{SG} based on superficial velocity (i.e., gas velocity U_{SG}) will be defined using the pipe diameter D and fluid properties of the corresponding phase (i.e., gas phase) as:

$$Re_{SG} = \frac{\rho_G D U_{SG}}{\mu_G} \quad (5.2.2)$$

If the Reynolds number is used to describe in situ conditions, the in situ velocity (i.e., gas velocity U_G) instead of superficial velocity will be used. Furthermore, the in situ Reynolds number Re_G will be expressed as a function of the hydraulic diameter (i.e., gas hydraulic diameter D_G):

$$Re_G = \frac{\rho_G D_G U_G}{\mu_G} \quad (5.2.3)$$

By analogy, similar relationships can be applied to the liquid phase using their corresponding physical properties, velocities, and hydraulic diameters.

5.2.2 Correlations for gas-wall friction factors

Friction factors are expressed as the Fanning friction factor f in all calculations of the model (other factors, such as Darcy-Weisbach – also called Moody – friction factor D_f , is also encountered in the literature in which $D_f = 4f$). If the Reynolds number is in the transition between the laminar and turbulent regimes ($2000 \leq Re \leq 3000$), then the maximal value between the turbulent and the laminar friction factors is chosen.

If the regime is laminar, the Reynolds number is estimated as $Re \leq 2000$ and the following equation is used to calculate the friction factor:

$$f = \frac{16}{Re} \quad (5.2.4)$$

If the regime is turbulent, the Reynolds number is estimated as $3 \cdot 10^3 \leq Re \leq 3 \cdot 10^6$. Two cases should be examined here: smooth wall turbulent (SWT), and partially/fully rough wall (PFRW). For smooth surfaces (PVC or acrylic), the equation of Drew et al. (1932) is a good reference:

$$f = 0.00140 + 0.125Re^{-0.32} \quad (5.2.5)$$

For rough surfaces (steels), the roughness ε should be accounted for; hence, the equation of Zigrang and Sylvester (1985) is preferred:

$$\frac{1}{\sqrt{f}} = -4.0 \log \left\{ \frac{\varepsilon/D}{3.7} - \frac{4.518}{Re} \log \left[\left(\frac{\varepsilon/D}{3.7} \right)^{1.11} + \frac{6.9}{Re} \right] \right\} \quad (5.2.6)$$

5.3 Predictions of flow pattern transitions

5.3.1 Introduction

The first model published by Taitel and Dukler (1976) predicted the flow pattern transitions for horizontal and near horizontal gas-liquid flows. Taitel et al. (1980) developed a second mechanistic model to determine flow pattern transitions in vertical upward flow. Later, these two models were unified and extended for all pipe inclinations with downward and upward inclined flows (Barnea, 1987).

Xiao et al. (1990) built a similar model to Barnea's but for a limited range of pipe inclination angles ($\beta = [-15^\circ, +15^\circ]$). They introduced flow characteristics prediction, such as the pressure drop and liquid holdup for the following flow patterns: stratified, intermittent, annular-dispersed and bubble.

Ansari et al. (1994) published a model applied only to vertical upward flows in wellbores where flow pattern transitions and characteristics were also determined. The prediction of flow pattern transitions was also based on Barnea's model. The pressure drop and holdup for different flow patterns were determined using other published models (Caetano et al., 1992a; Caetano et al., 1992b) for bubble flow; Sylvester (1987) for slug flow using the numerical method proposed by Vo and Shoham (1989); Alves (1991) for annular-mist flow).

Petalas and Aziz (1998) published a unified mechanistic model determining flow pattern transitions and flow characteristics for a whole range of pipe inclinations. New empirical correlations for interfacial friction factors in stratified and annular-mist flows

and a correlation for the liquid droplets entrainment in annular-mist flow were introduced.

Gomez et al. (2000) presented a versatile gas-liquid model including recent correlations for liquid slug holdup for better predicting the slug flow pattern. This model can deal with a large range of pipe diameters and fluid properties from horizontal to upward vertical pipe inclinations.

Kaya et al. (2001) developed a mechanistic model for deviated wells in upward flow conditions. The model predicted holdup and pressure drop for bubbly, dispersed-bubble, slug, churn and annular-mist flow patterns. Particularly, in the slug flow model they used Chokshi et al. (1996) approach but the closure relationships were adjusted to better fit the experimental data.

More recently, Zhang et al. (2003) developed a mechanistic model based on the hydrodynamics of a slug unit. The momentum balance equations used to characterize the slug flow can be also used to calculate the flow pattern transitions since the slug flow has common boundaries with all the other flow patterns.

Except for Barnea's model, all the mechanistic models take into account the pipe roughness and droplets entrainment.

In the following sections, the physical mechanisms on which each flow pattern transition is based are described. Furthermore, the key assumptions and final equations describing each mechanism are explained for modeling purposes.

5.3.2 Transition stratified/non-stratified

This transition separates stratified from non-stratified flow patterns. The transition is based on the Kelvin-Helmholtz instability considering the growth of a finite size of a wave over the stratified interface. Using this approach Taitel and Dukler (1976) calculated the critical gas velocity at which waves on the liquid surface grow large enough to bridge the entire pipe cross section:

$$U_G > \left(1 - \frac{h_L}{D}\right) \left[\frac{(\rho_L - \rho_G) \cdot g \cos \beta \cdot A_G}{\rho_G \cdot S_i}\right]^{1/2} \quad (5.3.1)$$

Equation (5.3.1) is represented by line ❶ on the flow map shown in Figure 5.4.

Although the equation predicts the transition well, it appears that at larger pipe diameters, the experimental observations in the CFR do not support this transition mechanism. These experimental observations using a 0.154 m pipe diameter (Figure 4.7) imply that the transition stratified to annular-dispersed is based on a droplet entrainment-deposition mechanism. Other researchers (Baik and Hanratty, 2003; Jepson and Taylor, 1993; Lin and Hanratty, 1987) observed the same transition mechanism at a similar diameter. It can be reasonably concluded that the predominant transition mechanism varies with the pipe diameter. The mechanism predicting the droplets entrainment onset is presented in section 5.4.

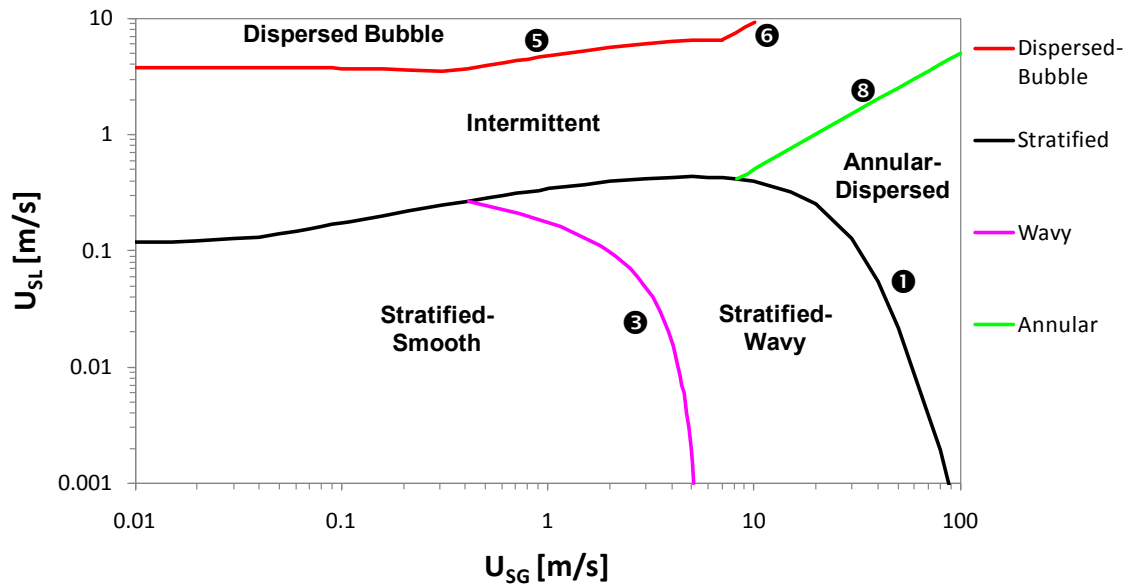


Figure 5.4: Air-water flow map at standard conditions in horizontal flow with a 0.154 m pipe diameter.

5.3.3 Transition stratified/annular at steep downward inclinations

Barnea et al. (1982a) observed that, even at low gas flow rates, the transition from stratified flow to annular-dispersed flow can be observed in downward flows at steep inclination angles ($\beta = [-88.5^\circ; -70^\circ]$). The liquid droplets are torn from the wavy interface and deposited on the upper wall. If droplets are entrained at a distance $D - h_L$ from the gas-liquid interface, the annular flow takes place. Therefore, the transition represented by line ② on the flow map shown in Figure 5.5 can be modeled with the following condition:

$$U_L^2 > \frac{gD}{f_L} \left(1 - \frac{h_L}{D}\right) \cos \beta \quad (5.3.2)$$

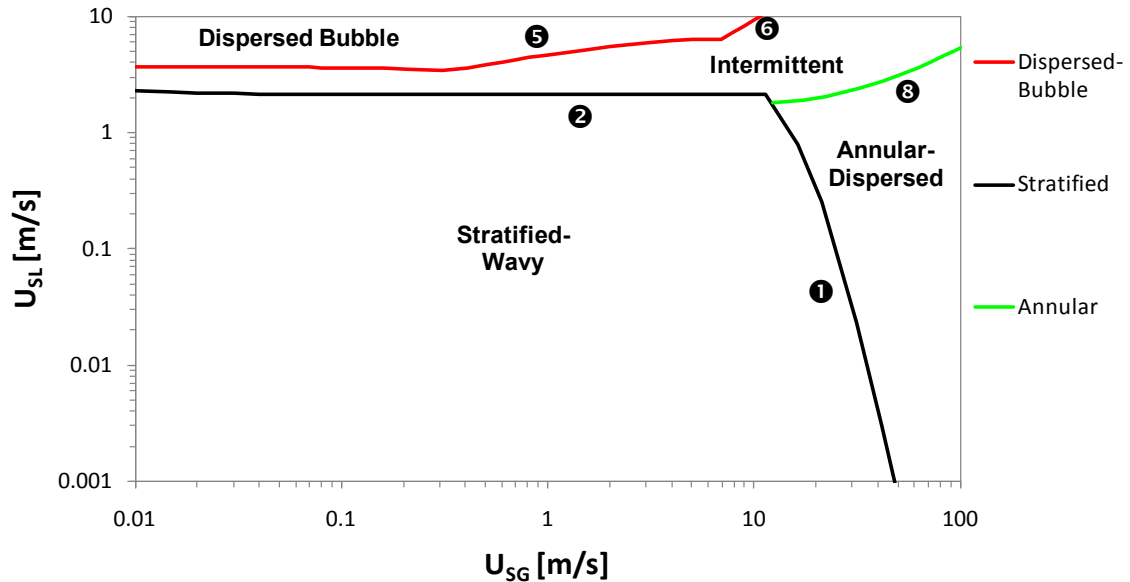


Figure 5.5: Air-water flow map at standard conditions in downward flow ($\beta = -70^\circ$) with a 0.154 m pipe diameter.

5.3.4 Transition stratified-smooth/stratified-wavy

The region called stratified flow consists of two subregions: stratified-smooth and stratified-wavy. The creation of waves arises from two different mechanisms.

The first mechanism is due to the action of the gas flowing over the liquid at the interface. Based on Jeffrey's theory (1925), Taitel and Dukler (1976) developed the equation (5.3.3) using a sheltering coefficient s equal to 0.01. Based on Andritsos' work (1986), other authors (Petalas and Aziz, 1998; Xiao et al., 1990) used a value of 0.06, which better suits high viscous liquids. In this work the value $s = 0.06$ is chosen for fluids with a liquid viscosity greater than 0.01 Pa·s while the value $s = 0.01$, for fluids with liquid viscosity less than 0.01 Pa·s. The mechanism can be modeled with equation 5.3.3, represented by line ③ on the flow map shown in Figure 5.4.

$$U_G \geq \left[\frac{4v_L(\rho_L - \rho_G) \cdot g \cos \beta}{s \cdot \rho_G \cdot U_L} \right]^{1/2} \quad (5.3.3)$$

The second mechanism is based on the effect of gravity on the liquid flow in downward flows. The following wave inception criterion using the liquid Froude number Fr_L greater than 1.5 was first proposed by Barnea et al. (1982a). However, Petalas and Aziz (1998) noticed that when the slip effect at the interface is considered, a value of 1.4 would fit much better the experimental observations:

$$Fr_L = \frac{U_L}{\sqrt{gh_L}} > 1.4 \quad (5.3.4)$$

This second mechanism was found to be irrelevant to the operating conditions used in this study, hence it was not included in the gas-liquid two-phase model.

5.3.5 Transitions from bubbly flow

5.3.5.1 Bubbly flow

The occurrence of the bubbly flow depends on the necessary and sufficient conditions requiring a minimal pipe diameter and a minimal inclination angle. The bubbly flow will occur if the rise Taylor bubble velocity is greater than the rise gas bubbles velocity in the liquid bridge (Taitel et al., 1980). In this case, no coalescence is possible. This condition imposed on the pipe diameter is expressed as:

$$D > 19 \left[\frac{(\rho_L - \rho_G) \sigma}{\rho_L^2 g} \right]^{1/2} \quad (5.3.5)$$

The other condition refers to the pipe inclination angle. If the inclination is not steep enough, the gas bubbles will rise by buoyancy effect to the upper part of the pipe, and then, will eventually coalesce together leading to an intermittent flow pattern. On the

other hand, the lift force tends to disperse the bubbles and maintain the bubble flow. Consequently, a force balance between the lift force and buoyancy leads to the following condition:

$$\frac{\cos \beta}{\sin^2 \beta} = \frac{3}{4} \cos 45^\circ \frac{U_0^2}{g} \left(\frac{C_L \gamma^2}{d} \right) \quad (5.3.6)$$

where γ is the bubble distortion coefficient, C_L is the lift coefficient, d is the bubble diameter, and U_0 is the rise velocity of the dispersed bubbles given by the following equation (Harmathy, 1960):

$$U_0 = 1.53 \left[\frac{(\rho_L - \rho_G) g \sigma}{\rho_L^2} \right]^{1/4} \quad (5.3.7)$$

Barnea et al. (1985) suggest the following ranges for three of the parameters above: $\gamma = [1.1 - 1.5]$, $C_L = [0.4 - 1.2]$ and $d = [4 - 10]$ mm. In this model, γ equaled 1.3, C_L was 0.8 and d was 7 mm.

5.3.5.2 Transition bubbly to intermittent

When the conditions for a bubbly flow existence are satisfied, the transition from bubble flow to intermittent can be determined using the equation suggested by Barnea et al. (1985). They state that at a critical void fraction α_{crit} (i.e., $\alpha_{crit} = 0.25$), the transition will take place:

$$U_{SL} = \frac{1 - \alpha_G}{\alpha_G} U_{SG} - (1 - \alpha_G) U_0 \sin \beta \quad (5.3.8)$$

The intermittent flow occurs if $\alpha_G \geq \alpha_{crit}$, while the bubbly flow happens when $\alpha_G < \alpha_{crit}$. Equation (5.3.8) is represented by line ④ on the flow map shown in Figure 5.6.

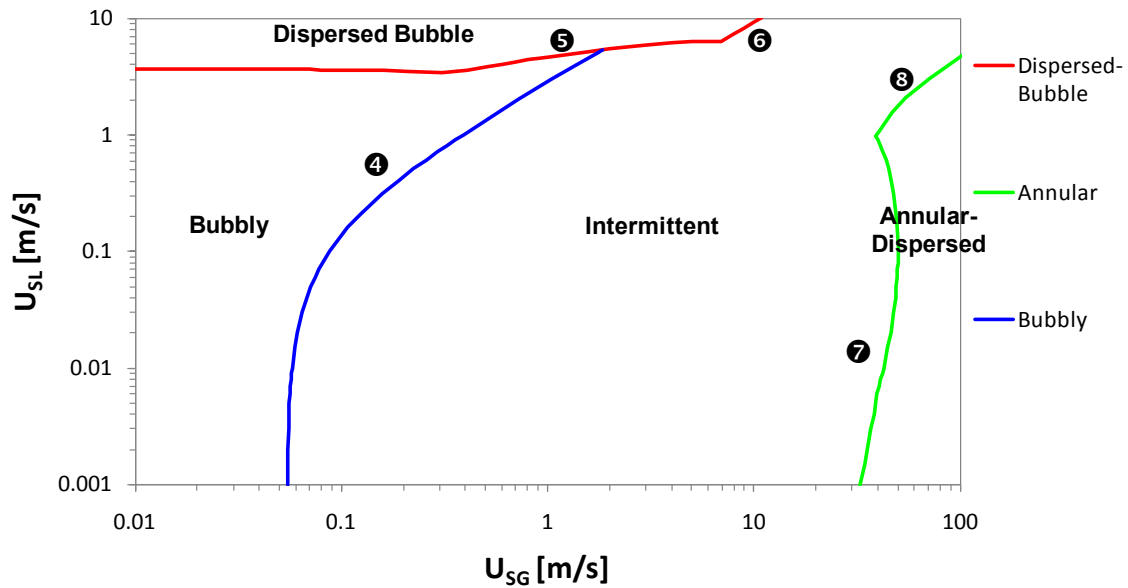


Figure 5.6: Air-water flow map at standard conditions in upward flow ($\beta = +70^\circ$) with a 0.154 m pipe diameter.

5.3.6 Transitions from dispersed bubble

Over a maximal packing density of dispersed spherical bubbles ($\alpha_{lim} = 0.52$), a dispersed bubble flow cannot exist. Two different cases are discussed here: (1) the packing density is less than 0.52 and (2) the packing density is equal to or exceeds 0.52.

Case 1: $0 < \alpha_G < \alpha_{lim}$

The H-model presented by Brauner (2001) was used in the present study to model the transition from dispersed-bubble flow. Under high liquid flow rates, the transition to dispersed-bubble flow pattern will occur if the turbulent forces can break down large bubbles into bubbles smaller than a critical size d_{crit} . Dispersed bubbles will exist even if the critical void fractional α_{crit} is exceeded. The transition criterion is:

$$d_{max} \leq d_{crit} \quad (5.3.9)$$

where d_{max} and d_{crit} are the maximal and the critical droplet diameters, respectively. Equation 5.3.9 is represented by line ⑤ on the flow map shown in Figure 5.4 to Figure 5.6. Brauner (2001) proposed the following criterion to assess the maximal droplet diameter:

$$d_{max} = \max(d_{max,0}; d_{max,\varepsilon}) \quad (5.3.10)$$

$d_{max,0}$ and $d_{max,\varepsilon}$ represent the maximal droplet sizes in dilute and dense dispersions:

$$d_{max,0} = 0.55DWe^{-0.6} \left[\frac{\rho_M f_M}{\rho_L \alpha_L} \right]^{-0.4} \quad (5.3.11)$$

$$d_{max,\varepsilon} = 2.22DC_H^{0.6}We^{-0.6} \left(\frac{\rho_M f_M}{\rho_L \alpha_L} \right)^{-0.4} \left(\frac{1-\alpha_L}{\alpha_L} \right)^{0.6} \quad (5.3.12)$$

We represents the Weber number of a dense phase and can be calculated by:

$$We = \frac{\rho_L U_M^2 D}{\sigma} \quad (5.3.13)$$

In the present model, it is assumed that all the turbulent kinetic energy available in the continuous phase is used to disperse the diluted phase. Therefore, the constant C_H is set to 1.

Note that the mixture properties are used for the modeling of droplet sizes. A mixture velocity U_M instead of a dense phase velocity is used in the calculation of Weber number since both velocities have very close values. The mixture friction factor f_M is calculated using the correlations in section 5.2, a mixture velocity U_M and a mixture Reynolds number Re_M defined as:

$$U_M = U_{SG} + U_{SL} \quad (5.3.14)$$

$$Re_M = \frac{\rho_M D U_M}{\mu_M} \quad (5.3.15)$$

The liquid holdup is determined by means of superficial velocities:

$$\alpha_L = \frac{U_{SL}}{U_{SG} + U_{SL}} \quad (5.3.16)$$

The average fluid properties depend on the liquid holdup α_L :

$$\rho_M = \alpha_L \cdot \rho_L + (1 - \alpha_L) \cdot \rho_G \quad (5.3.17)$$

$$\mu_M = \alpha_L \cdot \mu_L + (1 - \alpha_L) \cdot \mu_G \quad (5.3.18)$$

Barnea (1986) suggested that a critical droplet diameter d_{crit} can result from two different mechanisms: (a) agglomeration of deformed bubble and (b) migration of dispersed bubbles to the upper part of the pipe (creaming). If the bubble is small enough to prevent deformation, no agglomeration will occur, which does not lead to bubble flow. The critical bubble size over which the bubble is deformed d_{CD} is given by the equation (Barnea et al., 1982b):

$$d_{CD} = \left[\frac{0.4\sigma}{(\rho_L - \rho_G)g \cos \beta'} \right]^{1/2} \quad (5.3.19)$$

where:

$$\beta' = \begin{cases} |\beta| & \text{if } |\beta| < \pi/4 \\ \pi/2 - |\beta| & \text{if } |\beta| > \pi/4 \end{cases} \quad (5.3.20)$$

The second mechanism (creaming) results from a force balance between the buoyancy and turbulent forces. A critical bubble size below which the bubbles migration to the upper part of the pipe is prevented, d_{CB} , can be calculated as (Barnea, 1986):

$$d_{CB} = \frac{3}{8} \frac{\rho_L}{(\rho_L - \rho_G)} \frac{f_M U_M^2}{g \cos \beta} \quad (5.3.21)$$

Finally, the critical droplet diameter d_{crit} is selected as:

$$d_{crit} = \min(d_{CD}, d_{CB}) \quad (5.3.22)$$

Case 2: $\alpha_G \geq \alpha_{lim}$

In this case, even with high turbulence levels, the dispersed bubble flow no longer exists. The equation of the transition is given by literature (Taitel et al., 1980):

$$U_{SL} = \frac{1-\alpha_G}{\alpha_G} U_{SG} \quad (5.3.23)$$

Equation 5.3.23 can be represented by line ⑥ on the flow maps shown in Figure 5.4 to Figure 5.6.

5.3.7 Transitions annular / intermittent

As described in section 5.1, the intermittent and annular-dispersed flows are encountered over the whole range of pipe inclinations in gas-liquid flows. The transition between these two flow patterns depends on two different mechanisms described by Barnea (1986). The first mechanism is based on the instability of the annular flow liquid film due to a partial down-flow near the wall causing a blockage at the pipe entrance. It only occurs for upward flows ($\beta > 0^\circ$) and can be expressed as:

$$d\tau_i/d\tilde{\delta}_L=0 \quad (5.3.24)$$

where:

$$\tilde{\delta}_L = \delta_L/D \quad (5.3.25)$$

It can also be expressed in a dimensionless way as below:

$$Y = \frac{2-3/2\alpha_L}{(1-3/2\alpha_L)\alpha_L^3} X^2 \quad (5.3.26)$$

where:

$$X^2 = \left(\frac{dP}{dL}\right)_{SL} / \left(\frac{dP}{dL}\right)_{SG} \quad (5.3.27)$$

$$Y = \frac{(\rho_L - \rho_G)g \sin \beta}{\left(\frac{dP}{dL}\right)_{SG}} \quad (5.3.28)$$

$$-\left(\frac{dP}{dL}\right)_{SG} = \frac{2f_{SG}\rho_G U_{SG}^2}{D} \quad (5.3.29)$$

$$-\left(\frac{dP}{dL}\right)_{SL} = \frac{2f_{SL}\rho_L U_{SL}^2}{D} \quad (5.3.30)$$

$$\alpha_L = \frac{A_L}{A_p} = 4\tilde{\delta}_L(1 - \tilde{\delta}_L) \quad (5.3.31)$$

Equation 5.3.26 is represented by line ⑦ on the flow map shown in Figure 5.6.

The second mechanism is due to bridging the gas core by a thick liquid film at high liquid flow rates and can be formulated as:

$$\frac{A_L}{A_{\alpha_{LLS,min}}} = \frac{\alpha_L}{\alpha_{LLS,min}} \geq 0.5 \quad (5.3.32)$$

where $\alpha_{LLS,min}$ represents the minimum liquid holdup within the liquid slug ($\alpha_{LLS,min} = 0.48$). From here, it can be inferred a condition on the liquid holdup:

$$\alpha_L \geq 0.24 \quad (5.3.33)$$

At low pressure, a smaller liquid holdup seems to better fit the experimental data. Therefore, eq 5.3.34 is preferred for the modeling of the liquid holdup at operating pressures less than 10 bar. Equations 5.3.33 and 5.3.34 are represented as line ⑧ on the flow maps shown in Figure 5.4 to Figure 5.6.

$$\alpha_L \geq 0.20 \quad (5.3.34)$$

If any of the conditions (eq 5.3.26) or (eq 5.3.33 at high pressure, eq 5.3.34 at low pressure) is satisfied the flow is intermittent. The corresponding momentum balance to

solve the transition annular to intermittent is given by the dimensionless equation:

$$Y = \frac{1+75\alpha_L}{\alpha_L(1-\alpha_L)^{5/2}} - \frac{X^2}{\alpha_L^3} \quad (5.3.35)$$

5.4 Modeling of the entrainment onset transition

5.4.1 Description of droplets entrainment mechanisms

The entrainment of droplets in a gas phase leading to annular flow can be initiated by different mechanisms, such as: (a) bubble burst entrainment, (b) droplet impingement entrainment, and (c) wave entrainment. The first two, represented in Figure 5.7, can be considered as secondary mechanisms, while the wave entrainment described in Figure 5.8 represents the dominant entrainment mechanism leading to droplets formation (Han and Gabriel, 2007; Ishii and Grolmes, 1975; Kataoka et al., 1983; Van Rossum, 1959; Woodmansee and Hanratty, 1969).

In the case of wave entrainment, the droplets are formed from disturbances waves (3D roll waves) created at the gas-liquid interface. As shown in Figure 5.8, different mechanisms of wave entrainment may occur and can be classified in three categories: (c1) wave coalescence, (c2) wave undercutting, and (c3) ripple wave shearing-off. The dominant mechanism suggested by Woodmansee and Hanratty (1969) is represented by the ripple wave shearing-off during which a wavelet at the wave crest is torn away and generates liquid droplets. At very low liquid loadings (low Re_L), this mechanism does not occur. However, liquid droplets can still be formed by the wave undercutting mechanism if gas velocities are high enough.

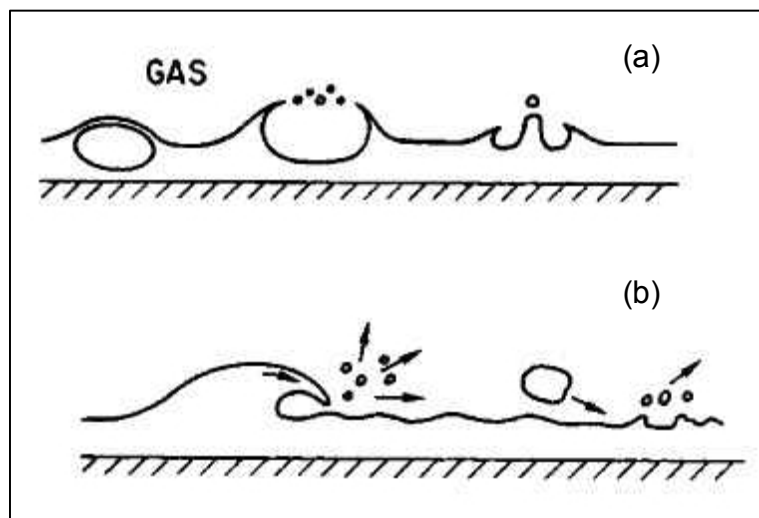


Figure 5.7: Mechanisms of droplets formation: (a) bubble burst and (b) droplet impingement at the gas-liquid interface (reprinted with permission from Ishii and Grolmes (1975). © 1975 American Institute of Chemical Engineers)

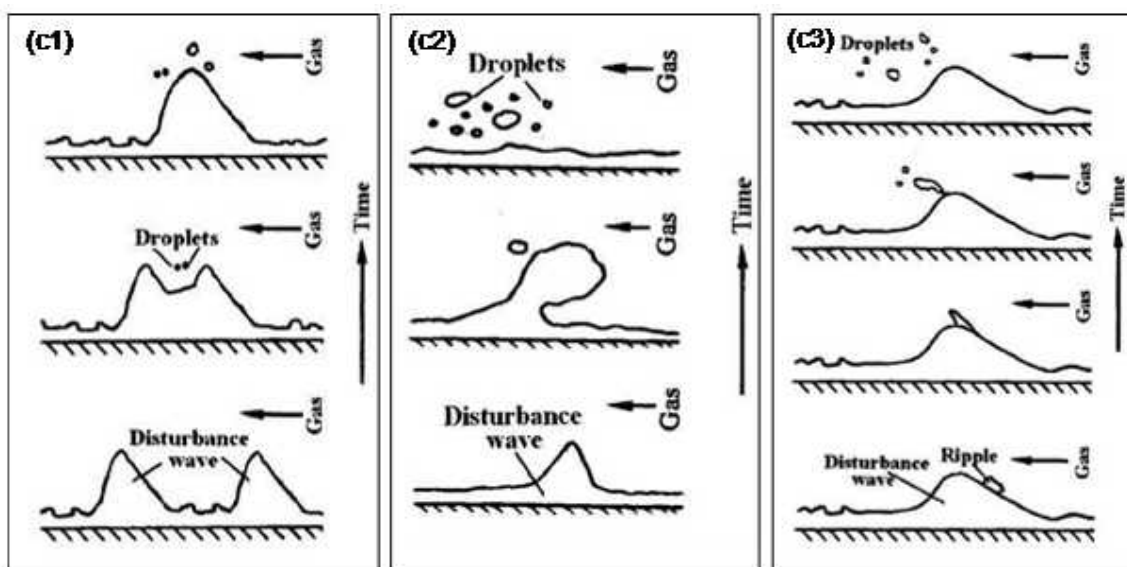


Figure 5.8: Mechanisms of droplets formation by wave entrainment: (a) wave coalescence, (b) wave undercutting, (c) ripple wave shearing-off (reprinted with permission from Han and Gabriel (2007). © 2007 American Society of Mechanical Engineers).

In this case, a disturbance wave can be sheared-off in the gas core, and then, disintegrated into smaller liquid droplets (Han and Gabriel, 2007; Ishii and Grolmes, 1975). For viscous fluids, the wave undercutting can occur at higher liquid flow rates and should be considered important and not discarded (Kataoka et al., 1983). For these reasons, the two forms of the wave entrainment mechanism, ripple wave shearing-off and wave undercutting, are considered in the present study for the modeling of entrainment onset.

5.4.2 Definition of the entrainment onset

In this work, it is considered that the entrainment onset occurs when some liquid droplets are torn from the gas-liquid interface, i.e. the atomization of liquid droplets. A second condition for the entrainment onset occurrence in horizontal pipes requires the droplets to impinge on the top of the pipe. This condition is particularly interesting because it also defines the deposition of the liquid droplets in Top of the Line Corrosion (TLC) seen in wet gas pipelines

The entrainment onset mechanism can be separated in three distinct regions. Below a critical liquid Reynolds number (low liquid flow rate), the superficial gas velocity required to initiate the droplet entrainment sharply increases reaching the entrainment limit (Hewitt and Hall-Taylor, 1970). At high liquid flow rates, no entrainment onset occurs below a critical gas velocity. Between these two limiting cases, the inception of droplet entrainment depends on both liquid and gas flow rates.

5.4.3 Modeling of the entrainment onset transition

The modeling of entrainment onset transition follows the approach initially developed by Ishii and Grolmes (1975) and completed by Mantilla and coworkers (Mantilla et al., 2009a; Mantilla et al., 2009b). A force balance described in Figure 5.9 is applied to a single wave. It consists of the drag force F_D , the surface tension force F_σ and the gravitational force F_g as in the following expression:

$$F_D \geq F_\sigma + F_g \sin(\beta) \quad (5.4.1)$$

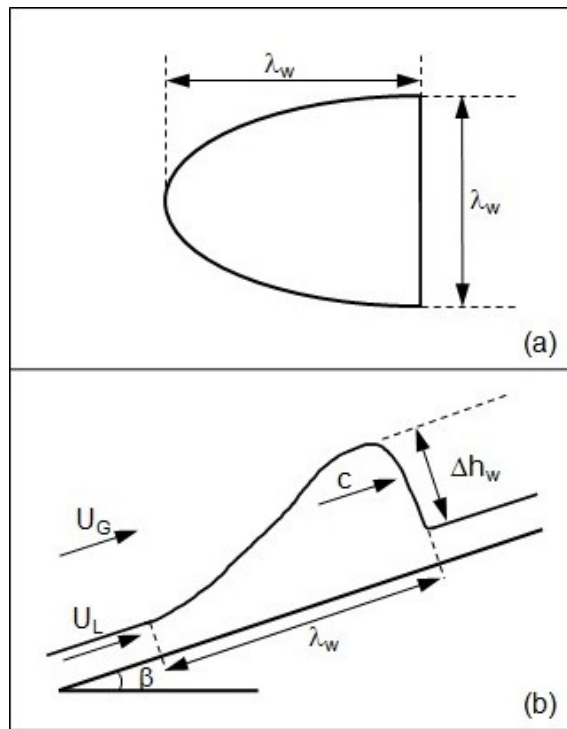


Figure 5.9: Top view (a) and side view (b) of a wave (adapted from Mantilla, 2008).

The drag force is defined as:

$$F_D = \frac{1}{2} C_D \lambda_w \Delta h_w \rho_G (U_G - U_L)^2 \quad (5.4.2)$$

C_D is the drag coefficient and estimated as $C_D = 0.95$ for irregular shapes.

The surface tension force is given by:

$$F_\sigma = C_S \lambda_w \sigma \quad (5.4.3)$$

C_S is the interfacial shape coefficient having a value of $C_S = 0.77$. This value corresponds to the average wave crest with a half elliptic base (Ishii and Grolmes, 1975).

The gravity force is calculated as:

$$F_g = \frac{\pi}{8} \lambda_w^2 \Delta h_w \rho_L g \sin(\beta) \quad (5.4.4)$$

By substituting equations 5.4.2 to 5.4.4 into equation 5.4.1, it yields:

$$C_D \Delta h_w \rho_G (U_G - U_L)^2 = 2C_S \sigma + \frac{\pi}{4} \lambda_w \Delta h_w \rho_L g \sin(\beta) \quad (5.4.5)$$

Following Ishii and Grolmes' recommendations, the interfacial shear stress at the wave crest τ_i is assumed to be proportional to the liquid film velocity:

$$\tau_i = C_w \mu_L \frac{U_L}{\Delta h_w} \quad (5.4.6)$$

C_w represents the effect of surface tension forces on the internal flow within the wave crest and can be expressed as a function of the liquid viscosity number N_μ , such as:

$$\frac{1}{3C_w} = \begin{cases} 11.78 N_\mu^{0.8} & , N_\mu \leq \frac{1}{15} \\ 1.35 & , N_\mu > \frac{1}{15} \end{cases} \quad (5.4.7)$$

where:

$$N_\mu = \mu_L \cdot \left[\rho_L \sigma \sqrt{\frac{\sigma}{(\rho_L - \rho_G)g}} \right]^{-1/2} \quad (5.4.8)$$

The interfacial shear stress τ_i can be calculated using either the liquid- or gas- interfacial friction factor, such as:

$$\tau_{Gi} = f_{Gi} \frac{\rho_G (U_G - U_L)^2}{2} \quad (5.4.9)$$

$$\tau_{Li} = f_{Li} \frac{\rho_L U_L^2}{2} \quad (5.4.10)$$

Using Hughmark (1973), the liquid-interfacial friction factor τ_{Li} is defined as:

$$f_{Li} = \sqrt{1.962 / Re_L^{1/3}} \quad (5.4.11)$$

where:

$$Re_L = \frac{\rho_L D_L U_L}{\mu_L} \quad (5.4.12)$$

The gas-interfacial friction factor f_{Gi} was initially expressed as a constant ($f_{Gi} = 0.007$). Mantilla accounted for the effect of pipe diameter since the friction factor is related to the relative roughness of the wave amplitude. In this work, a new correlation tuned with the help of randomly sampled TLC experimental data for different gas-liquid mixtures of CO₂/water and SF₆ - CO₂/water was developed:

$$f_{Gi} = K_0 \left(\frac{T}{T^0}\right)^{K_1} \left(\frac{P}{P^0}\right)^{K_2} \left(\frac{MW_G}{MW_{air}}\right)^{K_3} \left(\frac{h_L}{D}\right)^{K_4} \quad (5.4.13)$$

where: $K_0 = 0.00140820$, $K_1 = -3.41122637$, $K_2 = 0.40052095$, $K_3 = 0.33121546$, $K_4 = -0.23537017$.

In this correlation, the pressure P and temperature T are expressed in kPa and Kelvin. P^0 and T^0 are the temperature and pressure at standard conditions ($P^0 = 101.3$ kPa, $T^0 = 288.71$ K). MW_G and MW_{air} are the molecular weights of the gas phase and air, respectively ($MW_{air} = 28.97$ g/mol).

Assuming that $\tau_i = \tau_{Li}$ and using the shear stress continuity at the interface $\tau_{Li} = \tau_{Gi}$, substituting eqs 5.4.9 and 5.4.10 into eq 5.4.6 yields the following expression:

$$\Delta h_w = 2C_w \frac{\mu_L}{\rho_L} \sqrt{\frac{\rho_L}{\rho_G} \cdot \frac{1}{f_{Li} f_{Gi}}} \frac{1}{U_G - U_L} = \frac{C_r}{U_G - U_L} \quad (5.4.14)$$

where:

$$C_r = 2C_w \frac{\mu_L}{\rho_L} \sqrt{\frac{\rho_L}{\rho_G} \cdot \frac{1}{f_{Li} f_{Gi}}} \quad (5.4.15)$$

Substituting eq 5.4.14 into the force balance eq 5.4.5 gives the following expression:

$$(U_G - U_L)^2 - 2 \frac{C_S \sigma}{C_r C_D \rho_G} (U_G - U_L) - \frac{\pi \lambda_w \rho_L g \sin(\beta)}{4 C_D \rho_G} \quad (5.4.16)$$

This 2nd degree polynomial has two possible solutions. The negative solution is discarded, while the positive solution represents the entrainment onset criterion:

$$U_G - U_L = \frac{C_S \sigma}{C_r C_D \rho_G} + \sqrt{\left(\frac{C_S \sigma}{C_r C_D \rho_G}\right)^2 + \frac{\pi \lambda_w \rho_L g \sin(\beta)}{4 C_D \rho_G}} \quad (5.4.17)$$

The liquid velocity is taken as being the wave celerity c , which can be expressed as a function of the pipe inclination (Al-Sarkhi et al., 2012):

$$c/U_{SL} = \begin{cases} 2.379X^{*-0.9}, & \beta = 0^\circ \\ 2.323X^{*-0.94}, & 10^\circ \leq \beta \leq 20^\circ \\ 1.942X^{*-0.91}, & \beta \geq 45^\circ \end{cases} \quad (5.4.18)$$

X^* is defined as the Froude numbers ratio between the liquid and gas phases:

$$X^* = \frac{Fr_{SL}}{Fr_{SG}} \quad (5.4.19)$$

$$Fr_{SL} = \sqrt{\frac{\rho_L V_{SL}^2}{(\rho_L - \rho_G) g D \cos \beta}} \quad (5.4.20)$$

$$Fr_{SG} = \sqrt{\frac{\rho_G V_{SG}^2}{(\rho_L - \rho_G) g D \cos \beta}} \quad (5.4.21)$$

The wave base length λ_w is expressed with the wave spacing L_w :

$$\lambda_w = L_w/2, \quad (5.4.22)$$

while the wave spacing is defined as:

$$L_w = 2\pi\sigma^{1/2} \left[\frac{(U_G - U_L)^2}{\frac{L_G + L_L}{\rho_G + \rho_L}} - (\rho_L - \rho_G)g \cos(\beta) \right]^{-1/2} \quad (5.4.23)$$

Both L_G and L_L are geometrical properties used in stratified flow and can be written as:

$$L_G = \frac{A_G}{dA_G/dh_G} \quad (5.4.24)$$

$$L_L = \frac{A_L}{dA_L/dh_L} \quad (5.4.25)$$

5.4.4 Limiting cases

At low liquid Reynolds numbers, the roll waves start disappearing due to a lower interfacial shear stress and a sudden increase in the critical velocity necessary to entrain the droplets (Ishii and Grolmes, 1975). For low viscosity fluids, this transition occurs at a critical liquid film Reynolds number $Re_{L,crit}$, which varies with the flow inclination in pipes:

$$Re_{L,crit} = 2 \quad \text{if } \beta = -90^\circ \quad (5.4.26)$$

$$Re_{L,crit} = 160 \quad \text{if } \beta = 0^\circ \text{ or } \beta = +90^\circ \quad (5.4.27)$$

Below $Re_{L,crit}$, the ripple wave shearing off mechanism does not occur. However, liquid droplets can still be formed by the wave undercutting mechanism (Figure 5.8 – mechanism c2) when the liquid film Weber number We_L is in the range 17–22. The wave undercutting mechanism can be described by the following criterion using a Weber number of 22:

$$U_G - c = 1.5 \frac{\sigma}{\mu_L} \sqrt{\frac{\rho_L}{\rho_G} \cdot \frac{1}{Re_L}} \quad (5.4.28)$$

At high liquid Reynolds numbers ($Re_L > 5000$), the friction factor is assumed to remain constant; therefore, a value of $Re_L = 5000$ is used in eq 5.4.11.

5.5 Modeling of the stratified flow

Two different approaches were chosen for modeling the stratified flow pattern in this study. One approach was based on a modified Taitel and Dukler's (1976) model or TDM. Geometrical properties, such as the phase cross section and the perimeter or the hydraulic diameter are based on the assumption that the gas-liquid interface acts like a flat surface. However, in some situations, such as in wet gas transportation pipelines, the system operates under low liquid loading conditions, which are defined by a ratio of less than 200 STB/MMscf (Meng et al., 2001). At these particular conditions, the total liquid holdup in the pipeline is usually less than 10% and the gas-liquid interface no longer behaves like a flat surface. Although researchers (Andritsos, 1986; Chen et al., 1997; Fan et al., 2007; Grolman and Fortuin, 1997; Vlachos et al., 1999) disagreed about the shapes of the interface (flat, constant thickness, concave), the present approach to model the stratified flow pattern for low liquid loadings (LLL) was developed following the work of Fan (2005) and assuming a concave gas-liquid interface.

5.5.1 Model “Taitel Dukler Modified” (TDM)

5.5.1.1 Momentum balance equation

In stratified flow pattern, a momentum balance is applied to the gas phase (eq 5.5.1) and the liquid phase (eq 5.5.2):

$$-A_G \left(\frac{dP}{dL} \right) - \tau_{WG} S_G - \tau_i S_i - \rho_G A_G g \sin \beta = 0 \quad (5.5.1)$$

$$-A_L \left(\frac{dP}{dL} \right) - \tau_{WL} S_L + \tau_i S_i - \rho_L A_L g \sin \beta = 0 \quad (5.5.2)$$

By eliminating the pressure gradient in both equations, it leads to the following momentum equation:

$$\tau_{WG} \frac{S_G}{A_G} - \tau_{WL} \frac{S_L}{A_L} + \tau_i S_i \left(\frac{1}{A_L} + \frac{1}{A_G} \right) - (\rho_L - \rho_G) g \sin \beta = 0 \quad (5.5.3)$$

5.5.1.2 Definition of geometrical properties

Using the geometry in Figure 5.10, the cross section areas, perimeters and hydraulic diameters for a stratified flow pattern can be expressed in function of the pipe diameter D and the liquid height in the pipe h_L .

The gas and liquid cross section areas A_G and A_L are calculated as:

$$A_G = \frac{D^2}{4} \left[\pi - \cos^{-1} \left(1 - \frac{2h_L}{D} \right) + \left(1 - \frac{2h_L}{D} \right) \sqrt{1 - \left(1 - \frac{2h_L}{D} \right)^2} \right] \quad (5.5.4)$$

$$A_L = A_p - A_G \quad (5.5.5)$$

where A_p is the pipe cross section area.

The mathematical expressions of the gas and liquid perimeters S_G and S_L as well as the gas-liquid interfacial perimeter S_i are given below:

$$S_G = D \left[\pi - \cos^{-1} \left(1 - \frac{2h_L}{D} \right) \right] \quad (5.5.6)$$

$$S_L = S_p - S_G \quad (5.5.7)$$

$$S_i = D \sqrt{1 - \left(1 - \frac{2h_L}{D} \right)^2} \quad (5.5.8)$$

where S_p is the pipe perimeter.

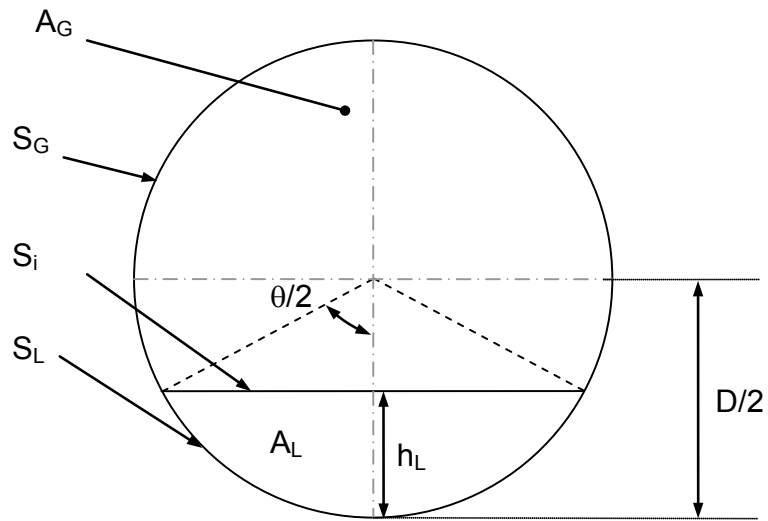


Figure 5.10: Geometry of the pipe cross section in a stratified flow pattern.

The gas and liquid hydraulic diameters D_G and D_L are calculated with the relationships (Agrawal et al., 1973):

$$D_G = \frac{4A_G}{S_G + S_i} \quad (5.5.9)$$

$$D_L = \frac{4A_L}{S_L} \quad (5.5.10)$$

5.5.1.3 Calculations of shear stress and in situ velocities

The gas-wall τ_{WG} , liquid-wall τ_{WL} and gas-liquid interface τ_i shear stresses are expressed as follows:

$$\tau_{WG} = \frac{1}{2} f_G \rho_G U_G^2 \quad (5.5.11)$$

$$\tau_{WL} = \frac{1}{2} f_L \rho_L U_L^2 \quad (5.5.12)$$

$$\tau_i = \frac{1}{2} f_i \rho_G (U_G - U_L) |U_G - U_L| \quad (5.5.13)$$

where f_G , f_L and f_i are the friction factors of gas/wall, liquid/wall and gas/liquid interface, respectively. U_G and U_L represent the in situ gas and liquid velocities and can be inferred from the following relationships:

$$U_G = \frac{U_{SG}}{1 - \alpha_L} \quad (5.5.14)$$

$$U_L = \frac{U_{SL}}{\alpha_L} \quad (5.5.15)$$

while the liquid holdup α_L can be determined from the ratio of the liquid phase cross sectional area to the pipe cross section:

$$\alpha_L = \frac{A_L}{A_p} \quad (5.5.16)$$

5.5.1.4 Friction factor correlations

The gas-wall friction factor f_G can be calculated using the correlation given in section 5.2.2, while the liquid-wall friction factor f_L using the correlation of Ouyang and Aziz (1996):

$$f_L = 1.6291 Re_L^{-0.5161} \left(\frac{U_{SG}}{U_{SL}} \right)^{0.0926} \quad (5.5.17)$$

Two different correlations were used to calculate the gas-liquid interfacial friction factor f_i . Based on the experiments run at 0.025 and 0.095 cm pipe diameters, Andritsos and Hanratty (1987) developed a correlation accounting for waves in the stratified-wavy flow pattern. A transitional superficial gas velocity $U_{SG,t}$ is used to mathematically define the interfacial friction factor:

$$f_i = \begin{cases} f_G & \text{if } U_{SG} \leq U_{SG,t} \\ f_G \left[1 + 15 \cdot \left(\frac{h_L}{D} \right)^{0.5} \right] \left[\frac{U_{SG}}{U_{SG,t}} - 1 \right] & \text{if } U_{SG} > U_{SG,t} \end{cases} \quad (5.5.15)$$

$$U_{SG,t} = 5 \cdot \left(\frac{\rho_G^0}{\rho_G} \right)^{0.5} \quad (5.5.16)$$

According to the authors above, the interfacial friction factor correlation gives a good prediction for very viscous liquids with gas velocities larger than $U_{SG,t}$. Furthermore, Xiao et al. (1990) suggested using this correlation only for small pipe diameters ($D < 0.127$ m), because the correlation overpredicts the friction factor when using large pipe diameters.

Therefore, the interfacial friction factor correlation of Baker et al. (1988), initially developed for low liquid loading mixtures ($\alpha_L < 0.10$), was used for larger pipe diameters. An effective interfacial roughness ε_i is calculated using a modified correlation proposed by Duns and Ros (1963). Two cases are defined to express ε_i as a function of Weber Number We and viscosity number N_μ , each defined as:

$$We = \frac{\rho_G U_i^2 \varepsilon_i}{\sigma} \quad (5.5.17)$$

$$N_\mu = \frac{\mu_L^2}{\rho_L \sigma \varepsilon_i} \quad (5.5.18)$$

If $We \cdot N_\mu \leq 0.005$ then

$$\varepsilon_i = \frac{34\sigma}{\rho_G U_i^2} \quad (5.5.19)$$

If $We \cdot N_\mu > 0.005$ then

$$\varepsilon_i = 170\sigma \frac{(We \cdot N_\mu)^{0.3}}{\rho_G U_i^2} \quad (5.5.20)$$

Using ε_i and the mixture Reynolds number Re_M , the interfacial friction factor is calculated from the equations given in section 5.2.2. After all, the choice of a proper correlation depends on the roughness of the pipe.

5.5.1.5 Determination of the pressure drop

By inserting eqs 5.5.4 to 5.5.16 into eq 5.5.3, the height of the stratified liquid film h_L can be calculated. Then, the liquid holdup α_L can be determined from eq 5.5.16. Once the shear stresses are calculated with eq 5.5.11 to 5.5.13, the pressure gradient dP/dL can be easily determined using either of the equations below:

$$-\left(\frac{dP}{dL}\right) = \frac{1}{A_G} [\tau_{WG} S_G + \tau_i S_i + \rho_G A_G g \sin \beta] \quad (5.5.21)$$

$$-\left(\frac{dP}{dL}\right) = \frac{1}{A_L} [\tau_{WL} S_L - \tau_i S_i + \rho_L A_L g \sin \beta] \quad (5.5.22)$$

5.5.2 Model “Low liquid Loading” (LLL)

5.5.2.1 Momentum balance equation

The model, initially developed for low liquid loadings, can be applied to all ranges of liquid holdup in horizontal and near horizontal pipes. Similarly to TDM, the same momentum balance equations are applied to the gas phase (eq 5.5.1) and the liquid

phase (eq 5.5.2). The mathematical expressions of the wall and interfacial shear stresses (eqs 5.5.11 to 5.5.13) and in situ velocities (eqs 5.5.14 and 5.5.15) are conserved from TDM as well.

5.5.2.2 Geometrical properties

The gas and liquid cross sectional areas A_G and A_L can be defined in the following way:

$$A_G = (1 - \alpha_L)A_p \quad (5.5.23)$$

$$A_L = \alpha_L A_p \quad (5.5.24)$$

The gas and liquid perimeters S_G and S_L are expressed as a function of the wetted wall fraction (section 5.5.2.4.1 for details of the calculation):

$$S_L = \pi D \theta_L \quad (5.5.25)$$

$$S_G = \pi D (1 - \theta_L) \quad (5.5.26)$$

The gas-liquid interfacial perimeter S_i is calculated assuming a concave interface and can be expressed as a function of S_{CD} and A_{CD} (Zhang et al., 2003):

$$S_i = \frac{[S_L(A_{CD} - A_L) + S_{CD}A_L]}{A_{CD}} \quad (5.5.27)$$

$$S_{CD} = D \sin(\pi \theta_L) \quad (5.5.28)$$

$$A_{CD} = \frac{D^2}{4} [\pi \theta_L - 0.5 \sin(2\pi \theta_L)] \quad (5.5.29)$$

where S_{CD} is the chord length (m) corresponding to the wetted wall fraction, and A_{CD} is the cross sectional area (m²) bounded by S_{CD} and the wetted perimeter S_L (m).

5.5.2.3 Determination of the liquid holdup

For calculating the liquid holdup, Fan et al. (2007) introduced the variable ϕ described by the relationship:

$$\phi = \frac{\alpha_L}{1-\alpha_L} \quad (5.5.30)$$

By inserting equations for shear stresses, in situ velocities, and phase cross sections (eqs 5.5.23 and 5.5.24) into eq 5.5.3, and then rearranging this equation, two new equations remained to be solved: one for downward (eq 5.5.31) and horizontal flows and another for upward flows (eq 5.5.32):

$$\phi = \left(\frac{U_{SL}}{U_{SG}} \right) \left\{ \frac{\frac{f_L \rho_L S_L}{f_G \rho_G S_G}}{\alpha_L + (1+\alpha_L) \frac{f_i S_i}{f_G S_G} \frac{2A_p \Delta \rho g \sin \beta}{f_G \rho_G S_G U_{SG}^2} \frac{\alpha_L}{(1+\alpha_L)^3}} \right\}^{1/2} \quad \text{if } \beta \leq 0 \quad (5.5.31)$$

$$\phi = \left(\frac{U_{SL}}{U_{SG}} \right) \left\{ \frac{\frac{f_L \rho_L S_L}{f_G \rho_G S_G} \left[1 + \frac{2A_p \Delta \rho g \sin \beta}{f_L \rho_L S_L U_{SL}^2} \left(\frac{\alpha_L}{1+\alpha_L} \right)^3 \right]}{\alpha_L + (1+\alpha_L) \frac{f_i S_i}{f_G S_G}} \right\}^{1/2} \quad \text{if } \beta > 0 \quad (5.5.32)$$

5.5.2.4 Closure relationships

Specific closure relationships were expressed for the wetted wall fraction θ_L , the liquid-wall friction factor f_L and the interfacial friction factor f_i .

5.5.2.4.1 Wetted wall fraction

The wetted wall fraction can be defined as the ratio of the liquid perimeter to the pipe perimeter. Some authors proposed correlations to express the wetted wall fraction assuming either a flat interface (Taitel and Dukler, 1976), a constant liquid thickness

using the *ARS/MARS* model (Grolman and Fortuin, 1997; Hart et al., 1989) or a curved interface, such as the *double circle* model proposed by Chen (1997). Others (Fan et al., 2007; Zhang et al., 2003; Zhang and Sarica, 2011) modified Chen's model and proposed correlations to express the wetted wall fraction. Fan's correlation was preferred for the development of the present model:

$$\theta_L = \begin{cases} \left[\theta_0/\pi + 0.0637 Fr_L^{0.68} \left(\frac{U_{SG}}{U_{SG,t}} \right)^{0.68} \right] \left(\frac{\sigma_W}{\sigma} \right)^{0.15} & \text{if } 0 \leq \theta_L \leq 0.5 \\ \left[\theta_0/\pi + 0.0637 Fr_L^{0.68} \left(\frac{U_{SG}}{U_{SG,t}} \right)^{0.55} \right] \left(\frac{\sigma_W}{\sigma} \right)^{0.15} & \text{if } 0.5 \leq \theta_L \leq 1 \end{cases} \quad (5.5.33)$$

θ_0 represents the wetted wall fraction when the gas-liquid interface is flat:

$$\theta_0 = \pi \alpha_L + (3\pi/2)^{1/3} [1 - 2\alpha_L + \alpha_L^{1/3} - (1 - \alpha_L)^{1/3}] \quad (5.5.34)$$

$U_{SG,t}$ is the critical superficial gas velocity at which waves start appearing:

$$U_{SG,t} = 5 \left(\frac{\rho_G^0}{\rho_G} \right)^{0.5} \quad (5.5.35)$$

The Froude number of the liquid phase Fr_L , describing the ratio between the inertia force and the gravitational force, can be defined as:

$$Fr_L = \frac{\rho_L U_L^2}{(\rho_L - \rho_G) g D \cos \beta} \quad (5.5.36)$$

5.5.2.4.2 Friction factors

The gas-wall friction factor f_G is calculated using the correlations presented in section 5.2.2. The Reynolds number is calculated with eq 5.2.3 using the gas hydraulic diameter D_G given by eq 5.5.6.

The liquid-wall friction factor f_L can be determined using the correlation proposed by Fan et al. (2007):

$$f_L = \begin{cases} 8/Re_L & \text{if } Re_L < 2100 \\ 0.0709 \cdot Re_L^{-0.2666} & \text{if } 1000 \leq Re_L < 25000 \end{cases} \quad (5.5.37)$$

in which the liquid Reynolds number can be formulated as:

$$Re_L = \frac{\rho_L U_L h_{F,a}}{\mu_L} \quad (5.5.38)$$

Note that the hydraulic diameter is not included in the calculation of the Reynolds number. An average thickness of the liquid film $h_{F,a}$ (Zhang et al., 2003) is preferred instead:

$$h_{F,a} = \frac{2A_L}{S_L + S_i} \quad (5.5.39)$$

A correlation for the interfacial friction factor f_i was developed by Fan (2005)

based on experimental data:

$$f_i = \begin{cases} f_G & \text{if } U_{SG} \leq U_{SG,t} \\ f_G \left[1 + 21 \cdot \left(\frac{h_{F,a}}{D} \right)^{0.72} \left(\frac{U_{SG}}{U_{SG,t}} - 1 \right)^{0.8} \right] & \text{if } U_{SG} > U_{SG,t} \end{cases} \quad (5.5.40)$$

5.5.3 Stability analysis on a multiple roots system

According to the operating conditions, multiple solutions (roots) that are physically meaningful can result by solving eq 5.5.10. Xiao et al. (1990) suggested choosing the root with the smallest value. Petalas and Aziz (1998) stated that if two solutions are consistent, always the same root (the highest or the smallest) must be chosen to prevent any discontinuity. Like Xiao et al. also advised the smallest root. Landman (1991) analyzed the cases when multiple root systems can occur and three different equilibria can be predicted. He concluded that only stratified flows in upward

inclined pipes are subjected to such a case and recommended to keep always the smallest root as the solution of a system of equations. The two other solutions are unstable.

In any case, it should be reminded that the choice of solutions may strongly influence the flow pattern determination. Consequently, it is advised to numerically determine the number of roots by intervals to prevent any convergence to the wrong root before determining the value of the root itself. The present gas-liquid two-phase flow model accounts for multiple roots determination up to three different roots and always selects the lowest root based on the previous suggestions from the cited literature.

5.6 Modeling of the annular flow

The development of the annular flow model was initially based on the work of Alves et al. (1991) for vertical upward flows in gas wells. The model predicted the liquid holdup and the pressure drop for a two-fluids system: a gas phase in the core of the pipe and a liquid phase consisting of a liquid film at the wall of the pipe and entrained liquid droplets flowing in the gas core. Furthermore, the model assumed a constant film thickness of the liquid film and a non-slippage condition between the core of the gas phase and the entrained liquid droplets.

5.6.1 Momentum balance equations

In an annular-dispersed flow pattern, a momentum balance is applied to both the gas core phase (eq 5.6.1) and the liquid film phase (eq 5.6.2):

$$-A_C \left(\frac{dP}{dL} \right) - \tau_i S_i - \rho_C A_C g \sin \beta = 0 \quad (5.6.1)$$

$$-A_F \left(\frac{dP}{dL} \right) - \tau_{WL} S_F + \tau_i S_i - \rho_L A_F g \sin \beta = 0 \quad (5.6.2)$$

By eliminating the pressure gradient from both equations, it results the following combined momentum balance equation:

$$\tau_{WL} \frac{S_F}{A_F} - \tau_i S_i \left(\frac{1}{A_F} + \frac{1}{A_C} \right) + (\rho_L - \rho_G) g \sin \beta = 0 \quad (5.6.3)$$

5.6.2 Definition of geometrical properties

Referring to Figure 5.11, all geometrical parameters, such as cross sectional areas, perimeters and hydraulic diameters for the annular-mist flow pattern can be expressed in function of the pipe diameter D and the liquid film thickness δ_L .

The gas core and the liquid film cross section areas A_C and A_F are expressed below:

$$A_C = \frac{\pi D^2}{4} \left(1 - \frac{2\delta_L}{D} \right)^2 \quad (5.6.4)$$

$$A_F = A_p - A_C \quad (5.6.5)$$

where A_p refers to the cross sectional area of the pipe.

The gas-liquid interface and liquid film perimeters S_i and S_F can be defined by:

$$S_i = \pi D \left(1 - \frac{2\delta_L}{D} \right) \quad (5.6.6)$$

$$S_F = \pi D \quad (5.6.7)$$

The gas core and liquid film hydraulic diameters D_C and D_F are expressed as:

$$D_C = D \left(1 - \frac{2\delta_L}{D} \right) \quad (5.6.8)$$

$$D_F = D \left[1 - \left(1 - \frac{2\delta_L}{D} \right)^2 \right] \quad (5.6.9)$$

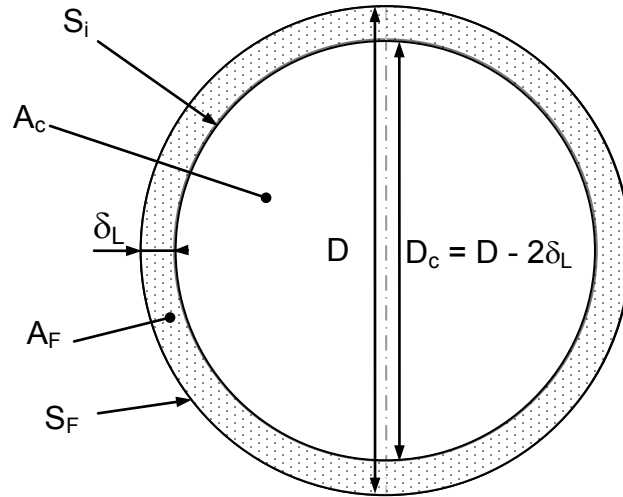


Figure 5.11: Geometry of the pipe cross section of the annular flow pattern (liquid droplets entrained in the gas core are not shown here).

5.6.3 Calculations of shear stresses and in situ velocities

The shear stresses for the liquid-wall film interface τ_{WL} and the gas core-liquid film interface τ_i can be determined from the following relationships:

$$\tau_{WL} = \frac{1}{2} f_F \rho_L U_F^2 \quad (5.6.10)$$

$$\tau_i = \frac{1}{2} f_i \rho_C (U_C - U_F) |U_C - U_F| \quad (5.6.11)$$

where f_F and f_i are the wall-liquid film and gas core-liquid film interface friction factors (section 5.6.4). In situ velocities U_F (in the liquid film) and U_C (in the gas core) can be formulated in terms of superficial velocities and the entrainment fraction FE (section 5.6.5):

$$U_F = U_{SL} \frac{(1-FE)D^2}{4\delta_L(D-\delta_L)} \quad (5.6.10)$$

$$U_C = \frac{(U_{SG} + FE \cdot U_{SL})D^2}{(D - 2\delta_L)^2} \quad (5.6.11)$$

In the present model, no slip between the entrained liquid droplets and the gas core is assumed. Therefore, the gas void fraction in the core α_C can be defined as the following:

$$\alpha_C = \frac{U_{SG}}{U_{SG} + FE \cdot U_{SL}} \quad (5.6.12)$$

The density ρ_C and the viscosity μ_C of the gas core are both functions of the gas void fraction in the core α_C :

$$\rho_C = (1 - \alpha_C) \cdot \rho_L + \alpha_C \cdot \rho_G \quad (5.6.13)$$

$$\mu_C = (1 - \alpha_C) \cdot \mu_L + \alpha_C \cdot \mu_G \quad (5.6.14)$$

5.6.4 Friction factors correlations

The film friction factor f_F is calculated using the correlations given in section 5.2.2 with the corresponding Reynolds number:

$$Re_F = \frac{\rho_L D_F U_F}{\mu_L} \quad (5.6.15)$$

The gas core/liquid film interface friction factor f_i is defined using the correlation initially developed by Asali et al. (1985) and improved by Ambrosini et al. (1991):

$$f_i = f_G \left[1 + 13.8 \cdot We_G^{0.2} \cdot Re_G^{-0.6} \left(h_F^+ - 200 \sqrt{\frac{\rho_G}{\rho_L}} \right) \right] \quad (5.6.16)$$

We_G and Re_G are the gas Weber number and the Reynolds number, each written as:

$$We_G = \frac{\rho_G U_C^2 D}{\sigma} \quad (5.6.17)$$

$$Re_G = \frac{\rho_G U_G D}{\mu_G} \quad (5.6.18)$$

The other parameters, h_F^+ (dimensionless liquid film thickness) and U_G^* (gas friction velocity) can be mathematically expressed as:

$$h_F^+ = \frac{\rho_G U_G^* h_F}{\mu_G} \quad (5.6.19)$$

$$U_G^* = \sqrt{\frac{\tau_i}{\rho_G}} \quad (5.6.20)$$

5.6.5 Entrainment fraction correlations

Numerous correlations were developed to predict the entrainment fraction of liquid droplets in the gas phase. They were all obtained from experimental data measured in horizontal pipes (Mantilla et al., 2009b; Paleev and Filippovich, 1966; Pan and Hanratty, 2002a) and vertical pipes (Cioncolini and Thome, 2010; Pan and Hanratty, 2002b; Sawant et al., 2009; Wallis, 1969).

Using statistical analysis, Magrini et al. (2010) evaluated the performance of the most used empirical correlations for different pipe inclination angles. They concluded that none could yield accurate predictions of entrainment fraction for all pipe inclinations. Relative to the pipe inclination angle, they suggested a combination of three empirical correlations that were also used in the present work: Pan and Hanratty (for horizontal pipes), Wallis (for inclined pipes), and Oliemans (for vertical pipes). These correlations are described in the next section. Although this set of correlations gave the best performance results in the statistical analysis, an absolute average error of 20–50% should be taken into consideration when predicting the entrainment fraction.

5.6.5.1 Pan and Hanratty correlation

Pan and Hanratty (2002a) developed a correlation to predict the entrainment fraction FE from experimental data measured in flow loops using an inner pipe diameter range of 0.023–0.095 m. However, the correlation can be applied only to liquids with a viscosity similar to that of water. It can be mathematically expressed as:

$$\frac{FE/FE_{max}}{1-FE/FE_{max}} = 9 \cdot 10^{-8} \frac{DU_G^3(\rho_G\rho_L)^{1/2}}{\sigma u_T} \quad (5.6.21)$$

FE_{max} represents the maximum entrainment fraction:

$$FE_{max} = 1 - \frac{W_{F,crit}}{W_F} \quad (5.6.22)$$

$W_{F,crit}$ refers to the critical film flow rate below which no droplet atomization can occur:

$$W_{F,crit} = 0.25\pi D\mu_L Re_{F,crit} \quad (5.6.23)$$

The critical film Reynolds number as a function of the film flow velocity:

$$Re_{F,crit} = 7.3 \cdot (\log\omega)^3 + 44.2 \cdot (\log\omega)^2 - 263 \cdot \log\omega + 439 \quad (5.6.24)$$

$$\omega = \frac{\mu_L}{\mu_G} \sqrt{\frac{\rho_G}{\rho_L}} \quad (5.6.25)$$

The terminal velocity of a droplet U_T can be defined as:

$$U_T = (4dg\rho_L)/(3C_D\rho_G) \quad (5.6.26)$$

where C_D represents the drag coefficient and is calculated using Morrison's (2010) equation:

$$C_D = \frac{24}{Re_d} + \frac{2.6\left(\frac{Re_d}{5}\right)}{1+\left(\frac{Re_d}{5}\right)^{1.52}} + \frac{0.411\left(\frac{Re_d}{263,000}\right)^{-7.94}}{1+\left(\frac{Re_d}{263,000}\right)^{-8.00}} + \left(\frac{Re_d^{0.80}}{461000}\right) \quad (5.6.27)$$

The Reynolds number of the liquid droplet Re_d is calculated as:

$$Re_d = \frac{\rho_G d U_T}{\mu_G} \quad (5.6.28)$$

According to Tatterson (1977), the droplet size diameter d can be expressed as a function of the Sauter diameter d_{32} :

$$d = \frac{d_{32}}{0.7} \quad (5.6.29)$$

Following the recommendation of Al-Sarkhi and Hanratty (2002) based on experimental observations, the Sauter diameter can be predicted, such as:

$$\left(\frac{\rho_G U_{SG}^2 d_{32}}{\sigma} \right)^{0.55} \left(\frac{d_{32}}{D} \right)^{0.36} = 0.154 \quad (5.6.30)$$

5.6.5.2 Wallis' correlation

Wallis (1969) modified the correlation of Paleev and Filipovich (1966) replacing the liquid viscosity by the gas viscosity, and finally proposing the following expression:

$$FE = 1 - \exp[-0.125(\phi - 1.5)] \quad (5.6.31)$$

where:

$$\phi = 10^4 \frac{U_{SG} \mu_G}{\sigma} \left(\frac{\rho_G}{\rho_L} \right)^{1/2} \quad (5.6.32)$$

5.6.5.3 Oliemans' correlation

Using a regression analysis on the HARWELL databank, Oliemans et al. (1986) developed an entrainment fraction model for vertical upward flows. The corresponding correlation is given as a function of geometrical variables, flow conditions and physical properties:

$$\frac{FE}{1-FE} = 10^{\beta_0} \rho_L^{\beta_1} \rho_G^{\beta_2} \mu_L^{\beta_3} \mu_G^{\beta_4} \sigma^{\beta_5} D^{\beta_6} U_{SL}^{\beta_7} U_{SG}^{\beta_8} g^{\beta_9} \quad (5.6.33)$$

Where: $\beta_0 = -2.52$; $\beta_1 = 1.08$; $\beta_2 = 0.18$; $\beta_3 = 0.27$; $\beta_4 = 0.28$; $\beta_5 = -1.8$; $\beta_6 = 1.72$; $\beta_7 = 0.7$; $\beta_8 = 1.44$; $\beta_9 = 0.46$.

5.6.6 Determination of pressure drop and holdup

Once the liquid film thickness δ_L is calculated by solving eq 5.6.3, the liquid holdup α_L and the liquid film holdup α_F can be determined with the equations below:

$$\alpha_L = \frac{A_L}{A} = 1 - (1 - 2\tilde{\delta}_L)^2 \frac{U_{SG}}{U_{SG} + FE \cdot U_{SL}} \quad (5.6.34)$$

$$\alpha_F = \frac{A_F}{A} = 4\tilde{\delta}_L(1 - \tilde{\delta}_L) \quad (5.6.35)$$

Once in situ velocities and shear stresses are determined, the pressure gradient dP/dL can be further calculated using either of the following equations:

$$-\left(\frac{dP}{dL}\right) = \frac{1}{A_C} [\tau_i S_i + \rho_C A_C g \sin \beta] \quad (5.6.36)$$

$$-\left(\frac{dP}{dL}\right) = \frac{1}{A_F} [\tau_{WL} S_F - \tau_i S_i + \rho_L A_F g \sin \beta] \quad (5.6.37)$$

5.7 Modeling of the bubble flow

As described in section 5.1.4, the bubble flow can have two forms: dispersed bubble and bubbly flow. For both flow regimes, determination of holdup and pressure drop follows a similar guideline. However, a no-slip condition is assumed in dispersed bubble while slippage may happen in bubbly flow. In this section, the modeling of both dispersed bubble and bubbly flow approaches is described.

5.7.1 Dispersed bubble flow

A homogenous no-slip model is used for predicting the dispersed bubble flow. The two-phase flow system is treated as a single phase flow system whose properties correspond to an average of the properties of each phase of the two-phase flow system.

The non-slip liquid holdup α_L is defined as the ratio of the superficial liquid velocity divided by the mixture velocity, such as:

$$\alpha_L = \frac{U_{SL}}{U_{SG} + U_{SL}} \quad (5.7.1)$$

Mixture average properties are used in the model to describe the fluid properties and the mixture velocity. The average velocity U_M is defined as the sum of superficial gas and liquid velocities:

$$U_M = U_{SG} + U_{SL} \quad (5.7.2)$$

Mixture density and viscosity are given as a function of the non-slip liquid holdup by the following relationships:

$$\rho_M = \alpha_L \cdot \rho_L + (1 - \alpha_L) \cdot \rho_G \quad (5.7.3)$$

$$\mu_M = \alpha_L \cdot \mu_L + (1 - \alpha_L) \cdot \mu_G \quad (5.7.4)$$

Neglecting the pressure drop generated by the acceleration of the flow, the total pressure drop can be estimated from all the contributions due to friction (first right hand side RHS term) and gravity (second RHS term):

$$-\left(\frac{dP}{dL}\right) = \frac{2f_M \rho_M U_M^2}{D} + \rho_M g \sin \beta \quad (5.7.5)$$

The mixture friction factor f_M is calculated with the correlations given in section 5.2.2. The corresponding mixture Reynolds number Re_M is based on average fluid properties and average velocity and is given by:

$$Re_M = \frac{\rho_M D U_M}{\mu_M} \quad (5.7.6)$$

5.7.2 Bubbly flow

In bubbly flow, the gas bubbles rise quicker than the liquid phase: the slippage condition must be accounted for and, hence, the homogenous model cannot be used in this case. The liquid holdup α_L is given as:

$$1 - \alpha_L = \frac{U_{SG}}{U_G} \quad (5.7.7)$$

The in situ gas velocity U_G in liquid phase is expressed by:

$$U_G = C_0 U_M + U_0 \sin \beta \cdot \alpha_L^n \quad (5.7.8)$$

where the rise velocity of the dispersed bubble U_0 can be calculated with eq 5.3.7. C_0 is a velocity distribution parameter in a range of [1.0, 1.5]. For instance, Zuber and Findlay (1965) suggested $C_0 = 1.2$, while Chokshi et al. (1996) proposed a value of 1.15. The latter was preferred for the present bubbly flow model. The average velocity U_M was described by eq 5.7.2, while α_L^n is the correction factor for bubble swarm for which n is taken as 0.5 (Ansari et al., 1994). Combining eqs 5.7.7 and 5.7.8 leads to the following for the bubbly flow model:

$$\frac{U_{SG}}{1 - \alpha_L} = C_0 U_M + U_0 \sin \beta \cdot \alpha_L^n \quad (5.7.9)$$

The liquid holdup can be assessed with the bisection method. Once it is computed, the in situ liquid U_L and gas U_G velocities can be calculated as functions of liquid holdup:

$$U_L = \frac{U_{SL}}{\alpha_L} \quad (5.7.10)$$

$$U_G = \frac{U_{SG}}{1-\alpha_L} \quad (5.7.11)$$

Similar to the homogeneous dispersed bubble flow model, the pressure drop due to acceleration is neglected. Only the friction and gravity effects are considered in the expression of pressure drop:

$$-\left(\frac{dP}{dL}\right) = \frac{2f_M \rho_M U_M^2}{D} + \rho_M g \sin \beta \quad (5.7.12)$$

where f_M is calculated with the correlations presented in section 5.2.2 using the physical properties of the gas-liquid mixture ρ_M and μ_M expressed in eqs 5.7.3 and 5.7.4, and the mixture Reynolds number Re_M given by eq 5.7.6.

5.8 Modeling of the intermittent flow (slug flow)

The intermittent flow encompasses the following patterns: elongated bubble, churn and slug. However, for simplification purposes, only the slug flow pattern will be considered for the modeling of the intermittent flow over a limited range of inclination angles, from horizontal to vertical upward flow and through inclined upward flow: $\beta = [0^\circ, +90^\circ]$. Although the slug flow pattern may also occur in downward flows, the current model has not been expanded to this range of pipe inclination.

A slug flow unit consists of two regions: the liquid slug body (region AB) and the liquid film region (BC), also called the Taylor bubble region or the slug tail (Figure 5.12).

Different mechanistic models already exist in the literature to describe the slug flow regime. The first models deal either with horizontal flows, such as Dukler and Hubbard (1975) models or vertical upward flows, such as Sylvester's (1987) model. Vo

and Shoham (1989) proposed a numerical procedure to reduce Sylvester's model to one equation with a single unknown. Bonnacaze et al. (1971) developed a model for inclined flows. Different methods concerning the numerical treatment of the Taylor bubble region are proposed in literature: (a) Kaya et al. (2001), (b) Xiao et al. (1990), and (c) Taitel and Barnea (1990a).

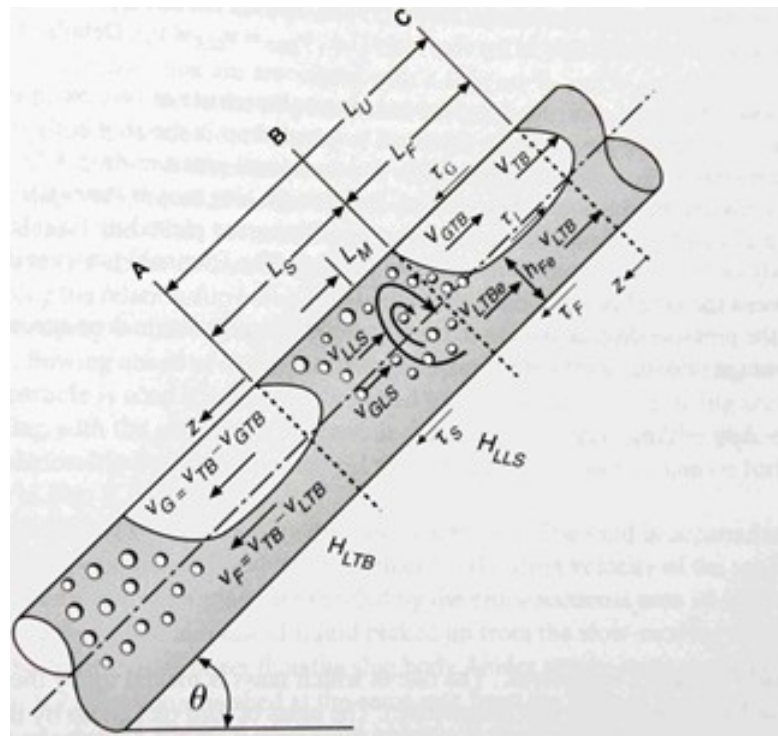


Figure 5.12: Longitudinal pipe cross section illustrating the slug flow pattern (reprinted from Shoham (2006). © 2006 Society of Petroleum Engineers).

Method (a) was used in different published models, such as Sylvester (1987), Chokshi et al. (1996) or more recently Kaya et al. (2001). It is assumed that there is no pressure gradient within the liquid film region – $(-dP / dL)_F = 0$ – but an equilibrium between gas and liquid phases. However, the height of the liquid film in the slug tail

region is not constant, such as $h_F \neq h_E$. Four empirical relationships are used to close this model.

Method (b) assumed a constant height of the liquid film in the slug tail region ($h_F = h_E$) suggesting an equilibrium between the gas and liquid phases. However, the pressure gradient in the film region is not assumed to be constant $(-dP / dL)_F \neq 0$. This model was initially applied to horizontal and near horizontal pipes. More recently, Gomez et al. (2000) developed a unified model for slug flow pattern including horizontal, upward inclined and upward vertical flows and adopted this method. Likewise method (a), four empirical relationships were used to close the model (section 5.8.4). These relationships consist of the liquid holdup in the slug body region α_{LLS} , the translational velocity of the Taylor bubble U_{TB} , the gas bubble velocity in the slug body U_{GLS} , and the length of the liquid slug body L_S . Method (b) was the one used for the slug flow model.

Method (c) appeared to be the first attempt to unify horizontal, upward inclined and upward vertical flows. This model assumed a variable liquid height ($h_F \neq 0$) in the Taylor bubble region as well as a variable pressure gradient across the same region: $(-dP / dL)_F \neq 0$. Therefore, it advanced the most accurate solution compared to the other two methods, but it is also more challenging from the programming point of view (no model simplification).

Three types of relationships are needed to model the slug flow pattern: mass balances on gas and liquid phases over a slug unit, momentum balance on the liquid film (method (b) used in the present case), and closure relationships.

5.8.1 Mass Balances

5.8.1.1 General mass balances over a slug unit

Mass balances of gas and liquid phases over a slug unit are expressed as the sum of the contributions in the liquid film (region BC) and the liquid slug (region AB) in Figure 5.12. The mass balance of the gas phase can be written as:

$$U_{SG} = \xi \cdot U_{GTB} \cdot (1 - \alpha_{LTB}) + (1 - \xi) \cdot U_{GLS} \cdot (1 - \alpha_{LLS}), \quad (5.8.1)$$

and the one for the liquid phase:

$$U_{SL} = -\xi \cdot U_{LTB} \cdot \alpha_{LTB} + (1 - \xi) \cdot U_{LLS} \cdot \alpha_{LLS} \quad (5.8.2)$$

where α_{LLS} and α_{LTB} are the liquid holdups in the slug body region and in the Taylor bubble/film region, respectively. ξ is the ratio of the liquid film length L_F to the slug unit length L_U :

$$\xi = \frac{L_F}{L_U} \quad (5.8.3)$$

5.8.1.2 Cross-sectional area mass balances

The mass balances in eqs 5.8.4 (gas phase) and 5.8.5 (liquid phase) are performed in the cross-sectional areas of the liquid slug and the liquid film regions, respectively. They are expressed using a Lagrangian coordinate system moving at the same velocity as the Taylor bubble velocity U_{TB} .

$$(U_{TB} - U_{GLS})(1 - \alpha_{LLS}) = (U_{TB} - U_{GTB})(1 - \alpha_{LTB}) \quad (5.8.4)$$

$$(U_{TB} - U_{LLS}) \cdot \alpha_{LLS} = (U_{TB} - U_{LTB}) \cdot \alpha_{LTB} \quad (5.8.5)$$

Using the mixture velocity, the cross-sectional area mass balances over the liquid slug (eq 5.8.6) and over the liquid film (eq 5.8.7) are expressed by:

$$U_M = U_{LTB} \cdot \alpha_{LTB} + U_{GTB} \cdot (1 - \alpha_{LTB}) \quad (5.8.6)$$

$$U_M = U_{LLS} \cdot \alpha_{LLS} + U_{GLS} \cdot (1 - \alpha_{LLS}) \quad (5.8.7)$$

5.8.2 Hydrodynamics in the film region

5.8.2.1 Momentum balance equations

An equilibrium and a constant film thickness are assumed along the entire liquid film region ($h_F = h_E$). Therefore, the region is treated like a stratified flow pattern and uses the same geometrical properties (cross sectional area, perimeter, hydraulic diameter) introduced in eqs 5.5.4 to 5.5.10. The momentum balance equations are expressed for the liquid film:

$$-\left(\frac{dP}{dL}\right) + \frac{\tau_F S_F}{A_F} - \frac{\tau_i S_i}{A_F} + \rho_L g \sin \beta = 0 \quad (5.8.8)$$

and for the gas pocket in the liquid film region:

$$-\left(\frac{dP}{dL}\right) + \frac{\tau_G S_G}{A_G} + \frac{\tau_i S_i}{A_G} + \rho_G g \sin \beta = 0 \quad (5.8.9)$$

Eliminating the pressure gradient, eqs 5.8.8 and 5.8.9 can be rearranged as:

$$\tau_F \frac{S_F}{A_F} - \tau_G \frac{S_G}{A_G} - \tau_i S_i \left(\frac{1}{A_F} + \frac{1}{A_G} \right) + (\rho_L - \rho_G) g \sin \beta = 0 \quad (5.8.10)$$

5.8.2.2 Shear stresses expressions

The liquid, gas and interfacial shear stresses are expressed in function of the in situ velocities in the slug unit, U_{GTB} and U_{LTB} :

$$\tau_F = \frac{1}{2} f_F \rho_L U_{LTB} |U_{LTB}| \quad (5.8.11)$$

$$\tau_G = \frac{1}{2} f_G \rho_G U_{GTB} |U_{GTB}| \quad (5.8.12)$$

$$\tau_i = \frac{1}{2} f_i \rho_G (U_{GTB} - U_{LTB}) |U_{GTB} - U_{LTB}| \quad (5.8.13)$$

The friction factors, f_G and f_F , are calculated with the equations from section 5.2.2 and their corresponding gas Reynolds numbers:

$$Re_G = \frac{\rho_G D_G U_{GTB}}{\mu_G} \quad (5.8.14)$$

$$Re_F = \frac{\rho_L D_F U_{LTB}}{\mu_L} \quad (5.8.15)$$

The interfacial friction factor f_i depends on the structure of the wavy interface. Due to its complexity, no specific correlation can accurately describe it. Therefore, the gas-liquid interface will be assessed based on the flow pattern of the liquid film region (i.e., stratified flow). In horizontal flows, the correlation proposed by Shoham and Taitel (1984) is preferred:

$$f_i = 0.0142 \quad (5.8.16)$$

while for upward vertical flow, the one developed by Wallis (1969), such as:

$$f_i = f_G \cdot (1 + 300 \delta_L/D) \quad (5.8.17)$$

In inclined pipes the interfacial friction factor will be averaged based on the pipe inclination:

$$f_i = 0.0142 \cdot \cos^2 \beta + f_G \cdot (1 + 300 \delta_L/D) \cdot \sin^2 \beta \quad (5.8.18)$$

5.8.3 Hydrodynamics in the slug region

The gas and liquid phases move at equal speed in the slug body. Assuming that the flow is incompressible, the slug velocity U_S equals the mixture velocity U_M .

Therefore, the shear stress of the slug body τ_S can be written as:

$$\tau_S = \frac{1}{2} f_S \rho_S U_S^2 = \frac{1}{2} f_S \rho_S U_M^2 \quad (5.8.19)$$

The friction factor f_S depends on the slug body Reynolds number Re_S :

$$Re_S = \frac{\rho_S D U_M}{\mu_S} \quad (5.8.20)$$

The physical properties of the slug body are averaged based on the liquid holdup in the slug region and can be calculated as follows:

$$\rho_S = \alpha_{LLS} \cdot \rho_L + (1 - \alpha_{LLS}) \cdot \rho_G \quad (5.8.21)$$

$$\mu_S = \alpha_{LLS} \cdot \mu_L + (1 - \alpha_{LLS}) \cdot \mu_G \quad (5.8.22)$$

5.8.4 Closure relationships

The present intermittent (slug) flow model still requires four closure relationships to be numerically solved. These relationships are: the Taylor bubble translational velocity U_{TB} , the slug body liquid holdup α_{LLS} , the gas-bubble velocity in slug body U_{GLS} , and the liquid slug body length L_S . Each is separately described in the subsequent sections.

5.8.4.1 Taylor bubble translational velocity U_{TB}

The translational velocity of the Taylor bubble is given by the following equation applicable to a range of pipe inclination angles of $0^\circ \leq \beta \leq 90^\circ$:

$$U_{TB} = C_0 U_M + U_D \quad (5.8.23)$$

The drift velocity U_D represents the velocity of the Taylor bubble in a stagnant liquid and C_0 is a flow distribution coefficient. For large liquid slugs ($L > 10D$),

Bendiksen et al. (1991) suggested:

$$Fr < 3.5 : \begin{cases} C_0 = 1.2 + 0.15 \cos^2 \beta \\ U_D = (0.54 \cos \beta + 0.35 \sin \beta) \sqrt{\frac{gD(\rho_L - \rho_G)}{\rho_L}} \end{cases} \quad (5.8.24)$$

$$Fr \geq 3.5 : \begin{cases} C_0 = 1.2 \\ U_D = 0.35 \sin \beta \sqrt{\frac{gD(\rho_L - \rho_G)}{\rho_L}} \end{cases} \quad (5.8.25)$$

where Fr is the Froude number which can be defined by:

$$Fr = \frac{U_M}{\sqrt{gD}} \quad (5.8.26)$$

5.8.4.2 Slug body liquid holdup α_{LLS}

The slug body liquid holdup α_{LLS} uses the correlation developed by Gomez et al. (2000) valid for horizontal and upward flows ($0^\circ \leq \beta \leq 90^\circ$):

$$\alpha_{LLS} = \exp(-7.85 \cdot 10^{-3}\beta - 2.48 \cdot 10^{-6}Re_S) \quad (5.8.27)$$

The pipe inclination angle β is expressed in radians. The Reynolds number of the liquid slug Re_S is based on the liquid phase properties, such as:

$$Re_S = \frac{\rho_L D U_M}{\mu_L} \quad (5.8.28)$$

5.8.4.3 Gas-bubble velocity in slug body U_{GLS}

The gas-bubble velocity in the slug body U_{GLS} can be calculated from:

$$U_{GLS} = 1.2 \cdot U_M + U_0 \sin \beta \cdot \alpha_{LLS}^{1/2} \quad (5.8.29)$$

where U_M is the mixture velocity and U_0 is the rise velocity of the dispersed bubbles in the slug body:

$$U_0 = 1.53 \left[\frac{(\rho_L - \rho_G)g\sigma}{\rho_L^2} \right]^{1/4} \quad (5.3.7)$$

5.8.4.4 Liquid slug body length L_S

The length of the liquid slug is averaged over a range of pipe inclinations spanning the horizontal and upward vertical flows as follows:

$$L_S = 30D \cdot \cos^2\beta + 20D \cdot \sin^2\beta \quad (5.8.30)$$

However, for large pipe diameter (12–24 inches), Scott et al. (1989) developed a correlation for horizontal flows:

$$\ln(L_S) = -25.4 + 28.5[\ln(D)]^{0.1} \quad (5.8.31)$$

where L_S and D are given in feet and inch, respectively.

5.8.5 Calculation of lengths L_U and L_F

The slug unit length L_U is expressed by the relationship:

$$L_U = L_S \frac{U_{LLS}\alpha_{LLS} - U_{LTB}\alpha_{LTB}}{U_{SL} - U_{LTB}\alpha_{LTB}} \quad (5.8.32)$$

The length of the liquid film region L_F is:

$$L_F = L_U - L_S \quad (5.8.33)$$

5.8.6 Determination of holdup and pressure drop over the slug unit

The overall liquid holdup over the slug unit α_{LSU} may be defined without using any slug characteristics:

$$\alpha_{LSU} = \frac{U_{TB}\alpha_{LLS} + U_{GLS}(1 - \alpha_{LLS}) - U_{SG}}{U_{TB}} \quad (5.8.34)$$

The overall pressure drop over the slug unit is:

$$-\left(\frac{dP}{dL}\right) = \rho_U g \sin \beta + \frac{\tau_S \pi D}{A_p} \frac{L_S}{L_U} + \frac{\tau_F S_F + \tau_G S_G}{A_p} \frac{L_F}{L_U} \quad (5.8.35)$$

where the density of the slug unit ρ_U can be calculated as below:

$$\rho_U = \alpha_{LSU} \cdot \rho_L + (1 - \alpha_{LSU}) \cdot \rho_G \quad (5.8.36)$$

The first term in the right hand side of eq 5.8.35 corresponds to the gravitational pressure gradient. The other two are the contributions of the frictional pressure gradient due to the existence of the slug region (the second term) and the film region (the third term).

5.8.7 Liquid slug frequency

In the present model, a correlation developed by Zabaras et al. (2000) is used to predict the liquid slug frequency v_S . The correlation was validated against 399 experimental points for a pipe diameter range between 0.0254 and 0.203 m, and a pipe inclination range between 0 and 11°. Note that the correlation is expressed in imperial units: U_M and U_{SL} in ft/s, D in ft, v_S in 1/s, $g = 32.2 \text{ ft/s}^2$.

$$v_S = 0.0226 \cdot \left(\frac{U_{SL}}{gD}\right)^{1.2} \left(\frac{212.6}{U_M} + U_M\right)^{1.2} [0.836 + 2.75 \cdot \sin(\beta)^{0.25}] \quad (5.8.37)$$

5.8.8 Direction of the liquid film in slug flow

The slug flow occurs over a large range of pipe inclination. For downward and

horizontal flows, the liquid layer in the film region flows in the same direction because of the effects of gravity and interfacial shear between the gas and liquid phases. In upward flows, beyond a critical angle $\beta_{S,crit}$, the liquid film may flow backwards as shown in Figure 5.12. Therefore, prior to calculate the characteristics of the slug flow unit, the critical angle shall be calculated using a force balance between gravity and the interfacial shear force between the liquid and gas phases (Moghissi et al., 2002).

5.9 Structure of the flow model

Although generically referred as “*the gas-liquid two-phase flow model*” in this dissertation, the overall flow model actually consisted of six different (sub)models to predict the flow pattern transitions and characteristics. An additional (the seventh) model for single phase flow (liquid or gas) was developed and mainly used for validation by experimental data obtained on the CFR in single gas phase flow (Figure 5.13). Each of the seven models represented in Figure 5.13 was also physically separated in the program using object-oriented programming (class module). The flow model was programmed using a VBA environment with inputs and outputs stored in Microsoft Excel® spreadsheets.

The modeling of flow pattern transitions was handled by the *FLOPAT* and the *Droplet Transport* models (Figure 5.13). The FLOPAT model which stands for FLOW PATtern transitions, consisted of three main sections. The first section predicted all the possible intersections between transitions, and the intersections between transitions and axes ($U_{SG,min}$, $U_{SG,max}$, $U_{SL,min}$, $U_{SL,max}$). The second section focused only on the flow

pattern prediction while the third section calculated the coordinates (U_{SG}, U_{SL}) of the flow pattern transitions. The Droplet Transport model was separately developed to predict the entrainment onset of liquid droplets in the gas phase (section 5.4). The model was only called if a stratified-wavy flow pattern (noted “SW”) was predicted by the *FLOPAT* model at operating conditions in horizontal pipes. Since the calculation of the transition was more complex, the algorithm of the Droplet Transport model is provided in Figure 5.14.

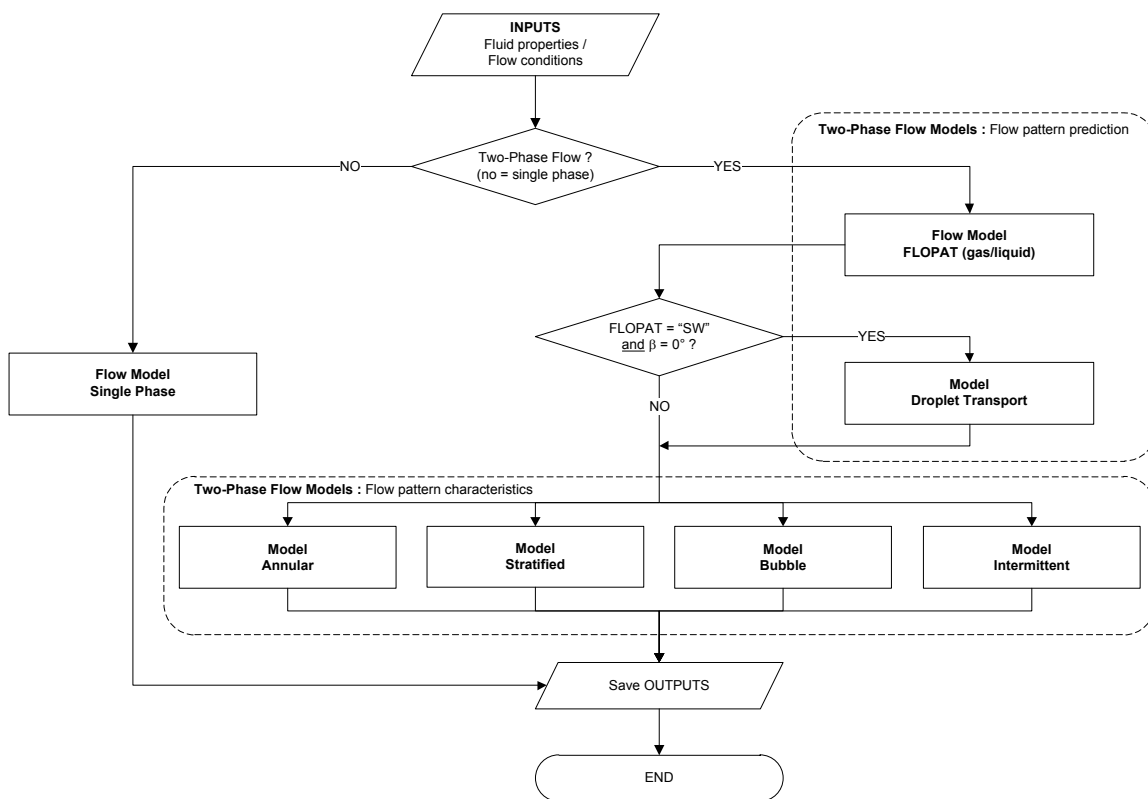


Figure 5.13: General structure of the flow model.

The characteristics of the flow pattern - a second desiderate of the overall flow model - were computed with the following models: stratified, annular, bubble, and intermittent (sections 5.5 to 5.8). Their respective algorithms are provided in Figure 5.15 to Figure 5.18. The stratified flow model proposed two algorithms (Taitel-Dukler Modified or TDM and Low Liquid Loading or LLL) whose structures are presented in Figure 5.15. The LLL model, initially developed for low liquid loading conditions, also exhibited a good performance for higher liquid holdups; therefore, its use was extended to all stratified flow cases in horizontal and near horizontal pipes for a range of inclination angles of $\beta = [-10^\circ, +10^\circ]$. For downward flows with a slope of 10° or more, the TDM model was preferred. In terms of structure, the two models were different. The LLL model was initialized by calculating the liquid holdup with the Hart et al. (1989) correlation while the TDM model solved the momentum balance equation by guessing the liquid height in the pipe. The algorithm of the annular flow model is presented in Figure 5.16 and is structurally very similar to the TDM model used in stratified flows. However, the liquid height is replaced by the liquid film thickness to solve the momentum balance. The bubble model consisting of two flow model types, dispersed-bubble and bubbly, is schematically represented in Figure 5.17. Finally, the intermittent flow model is presented in Figure 5.18. The closure relationships and critical angle defined in sections 5.8.4 and 5.8.8 are determined before solving the momentum balance equation on the liquid film region.

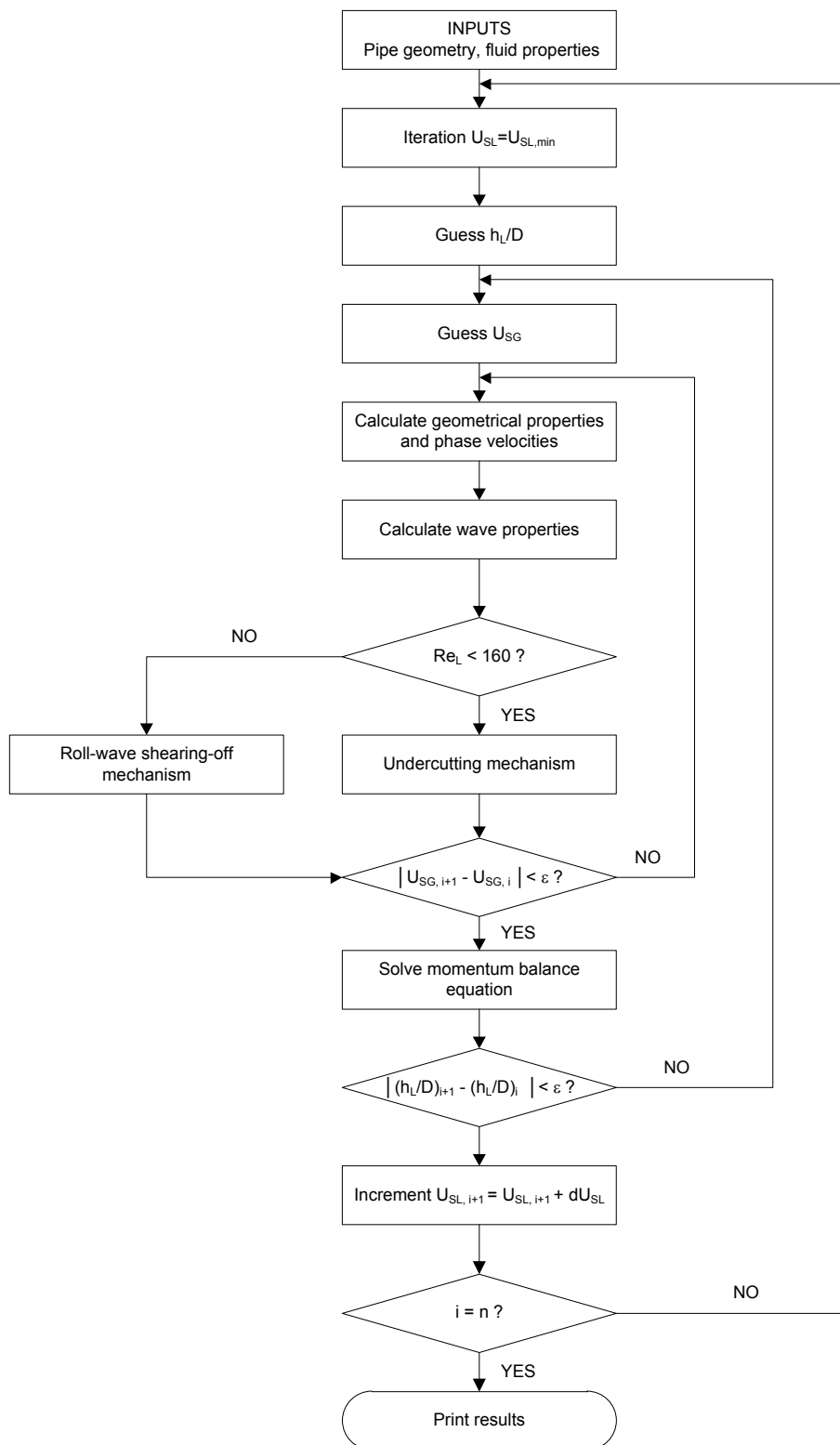


Figure 5.14: Algorithm of the entrainment onset model.

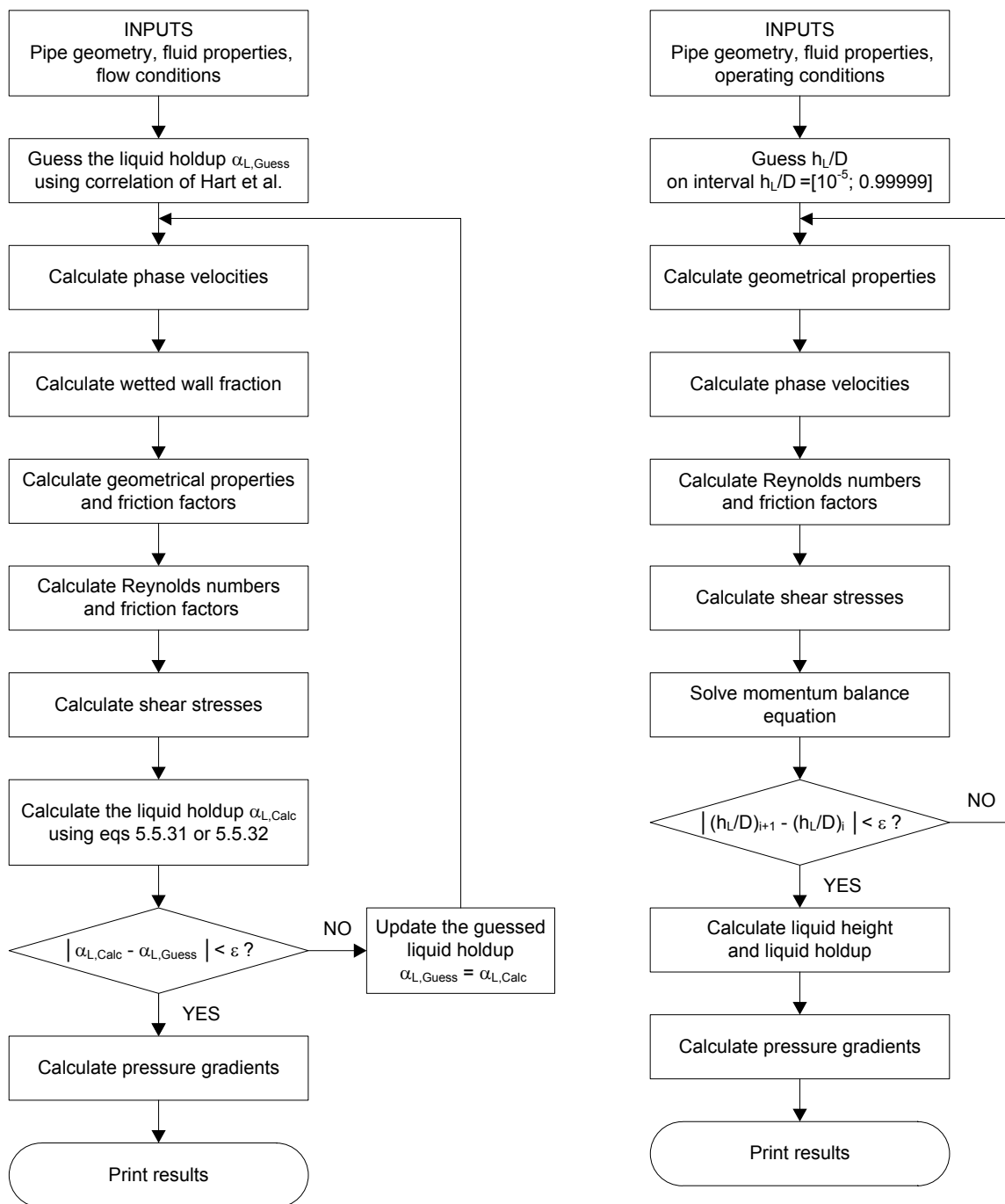


Figure 5.15: Algorithms of the stratified flow model using and the LLL approach (left) and the TDM approach (right).

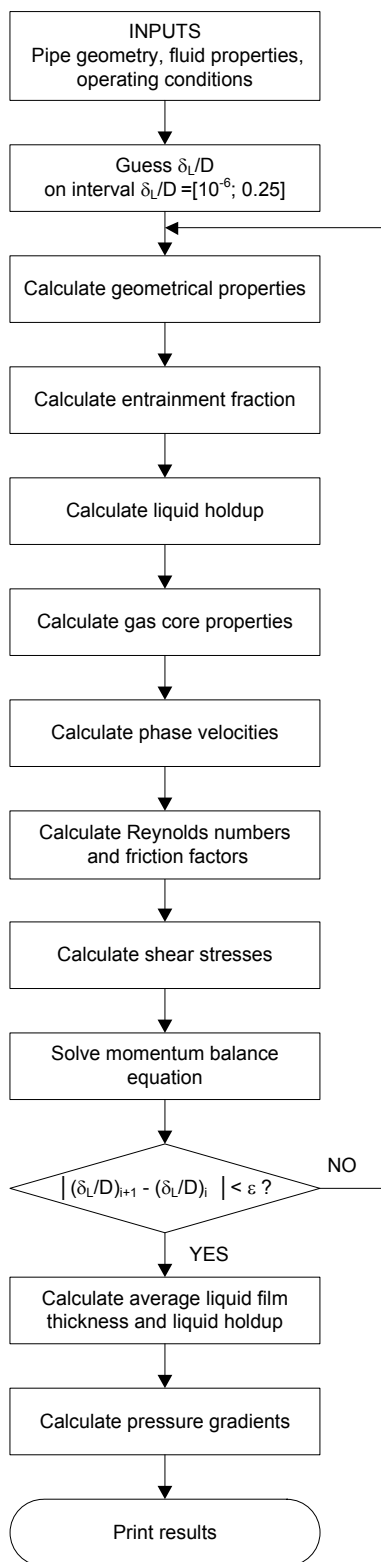


Figure 5.16: Algorithm of the annular flow model.

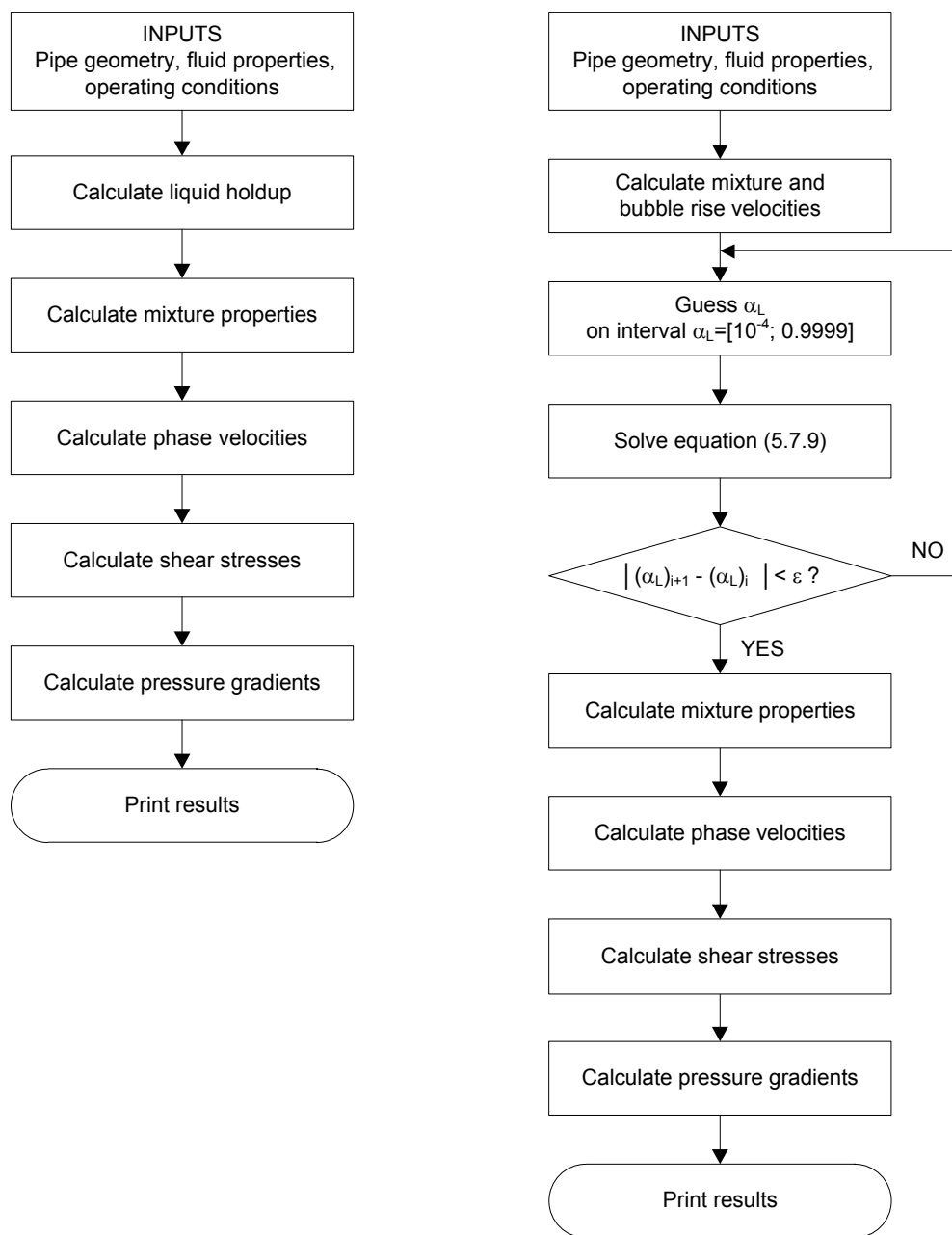


Figure 5.17: Algorithms of the dispersed-bubble (left) and the bubbly (right) flow models.

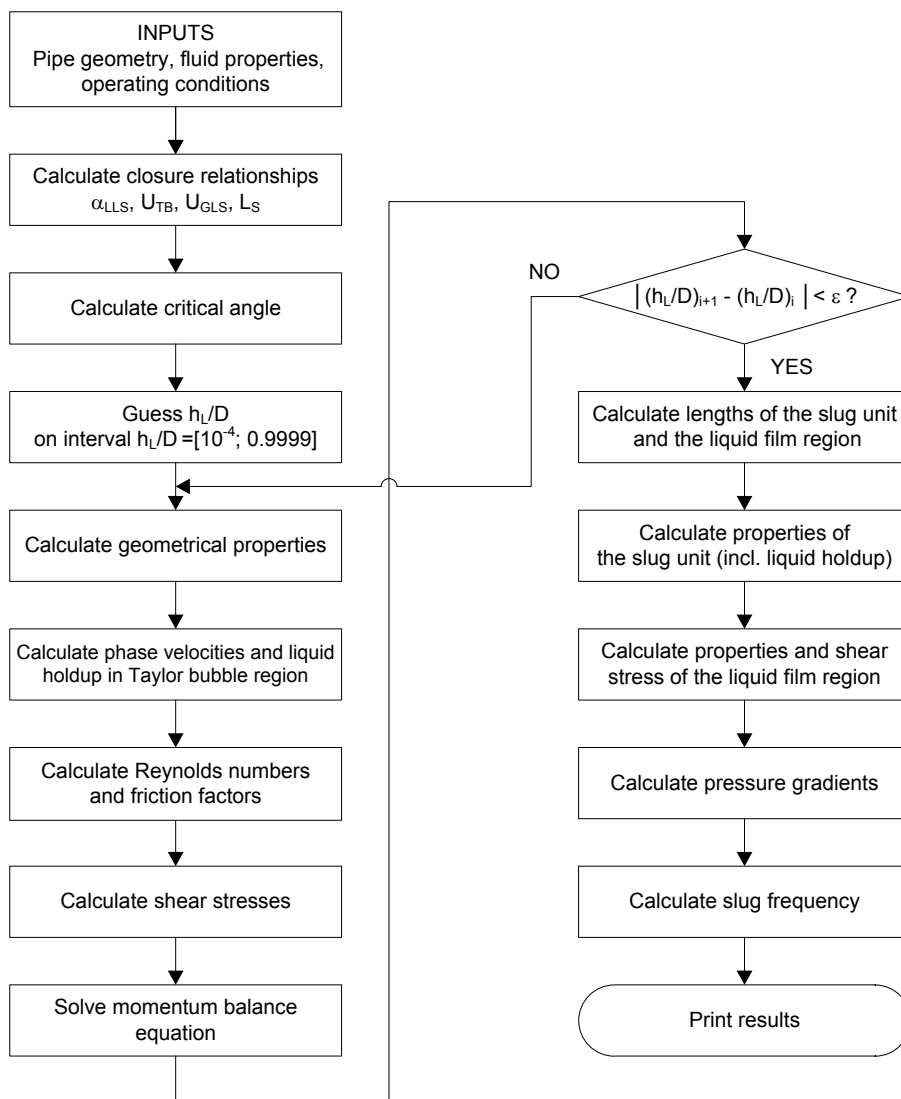


Figure 5.18: Algorithm of the intermittent (slug) flow model.

CHAPTER 6 FLOW MODEL RESULTS AND VALIDATION

The gas-liquid two-phase flow model developed in the previous chapter consisted of two parts: (1) prediction of flow patterns and (2) modeling of flow pattern characteristics (Figure 5.14). Predictions from both parts were validated by experimental data. Therefore, this chapter first describes the database creation based on literature sources and the current hydrodynamics study. Then, a short section introduces the statistical tools designed for the model validation and accuracy assessment. The chapter continues with the validation of the flow pattern predictions, entrainment onset transition, and the characteristics of each predicted flow pattern (stratified, annular, intermittent, and bubble).

6.1 The gas-liquid two-phase flow database

The experimental data generated during the flow study in CHAPTER 4 covers a narrow range of experimental conditions. Therefore, a database encompassing larger ranges of fluid properties, pipe properties, and operating conditions was built using published and proprietary data against which the model could be tested. A number of 24 datasets totalizing 8263 data points were gathered to validate the flow models and are presented in Table 6.1. Since the gas-liquid two-phase model was initially built to predict flow patterns and their characteristics similar to those encountered in transfer lines of oil refineries, the data search focused on experimental measurements obtained at low liquid

Table 6.1: The gas-liquid two-phase flow database.

| Nr. | Data source | Data points | Fluids | Pipe diameter (m) | Pipe inclination (°) | U_{SG} (m/s) | U_{SL} (m/s) |
|-----|--------------------------|-------------|--|-------------------|----------------------|----------------|----------------|
| 1 | AbdulMajeed (1996) | 88 | Air / Kerosene | 0.053 | 0 | 0.20 - 49 | 0.002 - 1.83 |
| 2 | Andritsos (1986) | 393 | Air / Water, Water-Glycerine | 0.025, 0.095 | 0 | 1.00 - 163 | 0.0001 - 0.33 |
| 3 | Beggs (1972) | 58 | Air / Water | 0.025, 0.038 | 0 | 0.30 - 25 | 0.023 - 2.63 |
| 4 | Caetano (1985) | 71 | Air / Kerosene, Water | 0.063 | +90 | 0.03 - 1.2 | 0.002 - 3.05 |
| 5 | Dallman (1978) | 137 | Air / Water | 0.023 | 0 | 17.6 - 92 | 0.008 - 0.91 |
| 6 | Fan (2005) | 351 | Air / Water | 0.051, 0.150 | -2, 0, +2 | 4.90 - 26 | 0.0003 - 0.05 |
| 7 | Felizola (1992) | 89 | Air / Kerosene | 0.053 | 0 to +90 | 0.39 - 3.4 | 0.049 - 1.49 |
| 8 | Govier & Aziz (2008) | 16 | Air / Water | 0.026 | 0 | 0.06 - 27 | 0.030 - 3.05 |
| 9 | Govier & Omer (1962) | 15 | Air / Water | 0.026 | 0 | 0.05 - 16 | 0.009 - 0.92 |
| 10 | Hewitt & Owen (1987) | 42 | Air / Water | 0.032 | 90 | 1.02 - 56 | 0.298 |
| 11 | Laurinat (1982) | 189 | Air / Water | 0.025, 0.051 | 0 | 9.70 - 136 | 0.015 - 1.12 |
| 12 | Magrini (2009) | 168 | Air / Water | 0.076 | 0 to +90 | 36.6 - 82 | 0.003 - 0.04 |
| 13 | Mantilla (2008) | 144 | Air / Water, Water-Glycerine, Water-Butanol | 0.049, 0.152 | 0 | 1.50 - 82 | 0.003 - 0.10 |
| 14 | Meng (1999) | 180 | Air / Lubsnap 40 | 0.051 | -2 to +2 | 4.60 - 27 | 0.001 - 0.05 |
| 15 | Minami (1982) | 111 | Air / Kerosene, Water | 0.078 | 0 | 0.47 - 17 | 0.005 - 0.95 |
| 16 | Palmer (1979) | 144 | Natural gas / Water | 0.051 | -6 to +7 | 0.32 - 6.7 | 0.112 - 0.74 |
| 17 | Paras & Karabelas (1991) | 17 | Air / Water | 0.051 | 0 | 31.1 - 66 | 0.020 - 0.20 |
| 18 | McLeod (1971) | 12 | Natural gas / Crude oil | 0.154 | 0 | 3.10 - 3.5 | 0.073 - 0.08 |
| 19 | Shoham (1982) | 5685 | Air / Water | 0.025, 0.051 | -90 to +90 | 0.02 - 40 | 0.002 - 6.50 |
| 20 | Tayebi (2000) | 22 | SF ₆ / Exxsol D80, Water | 0.102 | 0 | 3.35 - 7 | 0.220 - 0.26 |
| 21 | Singer et al. (2009) | 258 | CO ₂ , SF ₆ -CO ₂ / Water | 0.095 | 0 | 5.88 - 11 | 0.004 - 0.07 |
| 22 | Williams (1986) | 12 | Air / Water | 0.095 | 0 | 30.8 - 46 | 0.030 - 0.12 |
| 23 | Williams (1990) | 7 | Air / Water | 0.095 | 0 | 67.1 - 90 | 0.030 - 0.12 |
| 24 | This work | 54 | Air / Water | 0.154 | 0 | 15.0 - 60 | 0.007 - 0.17 |

loading conditions. In other words, the database is centered on empirical observations made in stratified and annular flow conditions.

6.2 Statistical tools

The accuracy of the flow model predictions was quantified using statistical analysis. The following statistical parameters were used for this purpose: relative error e_R , average relative error ε_1 , absolute average relative error ε_2 and percent standard deviation ε_3 .

The relative error e_R between the model prediction and the experimental data is given by the following equation:

$$e_R = \frac{X_{pred} - X_{exp}}{X_{exp}} \quad (6.2.1)$$

where X represents the variable assessed during the statistical analysis, predicted by the model (X_{pred}) and experimentally measured (X_{exp}).

The average relative error ε_1 measures the overall accuracy of the model based on individual relative errors within a range of predictions. The sign of ε_1 indicates the underprediction ($\varepsilon_1 < 0$) or overprediction ($\varepsilon_1 > 0$) of the model.

$$\varepsilon_1 = \frac{1}{n} (\sum_{i=1}^n e_{R,i} \times 100) \quad (6.2.2)$$

Because the average errors may cancel out, the absolute average relative error ε_2 is also calculated:

$$\varepsilon_2 = \frac{1}{n} (\sum_{i=1}^n |e_{R,i}| \times 100) \quad (6.2.3)$$

Finally, a quantification of relative errors scattering with respect to their average relative error is given by the percent standard deviation ε_3 :

$$\varepsilon_3 = \sum_{i=1}^n \sqrt{\frac{(e_{R,i} \times 100 - \varepsilon_1)^2}{n-1}} \quad (6.2.4)$$

For the visualization of the model agreement with experimental data, parity plots of predicted (y-axis) vs. experimental (x-axis) are used. The 1:1 line represents the ideal agreement between the model and data, while the two dashed lines represent the 20% deviation from the ideal agreement.

6.3 Evaluation of flow pattern prediction models

6.3.1 Evaluation of the FLOPAT model

As mentioned in the previous section, a large number of experimental data points (7314) with flow patterns observations were recorded in the database. Among these observations, only 160 were identified as the “atomization” flow pattern; hence, they were discarded from the analysis. The remaining (7066) data points were further used for the validation. Since 80% of the experimental data comes from Shoham’s dataset, the other datasets were separately analyzed against model predictions to confirm a similar model agreement found with Shoham's data.

Note that the flow pattern data provided by Abdulmajeed (1996) was deduced from Mandhane et al. (1974) flow map instead of being experimentally recorded on the flow loop; for this reason, these data are not taken into account for the performance assessment of the flow pattern prediction model.

6.3.1.1 Shoham dataset

The experimental data reported by Shoham (1982) are the main source of flow pattern observations (5685 points) at small pipe diameters (0.025 and 0.051 m), covering the whole range of pipe inclinations. Overall, 81% of the observed flow patterns were correctly predicted as can be seen in Table 6.2. The predicted flow patterns (regions) defined by the transition lines can be visualized on the flow maps in Figure 6.1 to Figure 6.3 along with the corresponding experimental data.

Table 6.2: Flow pattern predictions using Shoham's (1982) experimental data.

| | Flow Pattern | Predicted | | | | Data points | Model performance |
|-----------------|--------------|------------|--------------|---------|--------|-------------|-------------------|
| | | Stratified | Intermittent | Annular | Bubble | | |
| Observed | Stratified | 769 | 81 | 280 | 0 | 1130 | 68% |
| | Intermittent | 30 | 2324 | 269 | 91 | 2714 | 86% |
| | Annular | 33 | 154 | 953 | 0 | 1140 | 84% |
| | Bubble | 24 | 114 | 0 | 563 | 701 | 80% |
| Total : | | | | | 5685 | 81% | |

The model uncertainty is usually higher near the flow pattern transitions (the lines on the flow maps). It was noticed during validation that the choice of closure relationships (i.e., interfacial and liquid-wall friction factors) can significantly shift some of the transitions. The most recurrent prediction errors are found at the flow pattern transitions stratified/non-stratified, annular/intermittent, and bubbly/intermittent. The prediction of the stratified flow pattern seems to be less accurate since only 68% of the experimental observations were correctly predicted by the model (Table 6.2). This can be

attributed to the uncertainty of predicting the transition stratified/non-stratified in downward flows ($\beta \leq -10^\circ$) in 53% of the cases studied (151 out of 280), when the annular flow pattern was predicted instead of stratified flow. Another important source of uncertainty, concerning 59% of the cases (159 out of 269), comes from the underprediction of the transition intermittent/annular flow patterns due to the mechanism of liquid film instability in slightly upward flows ($\beta =]0^\circ, 10^\circ]$) as shown in Figure 6.2.

Figure 6.3 shows a couple of flow maps portraying an air-water mixture at standard conditions in horizontal pipes at two different diameters (0.025 and 0.051 m). The stratified to non-stratified flow pattern transition is particularly sensitive to a change in pipe diameter; an increase in the diameter tends to expand the stratified flow region at the expense of other flow pattern regions, particularly, the annular flow.

Oil refiners usually design the transfer lines to prevent the gas from reaching sonic velocities and, therefore, they increase the diameter of the pipes from the furnace to the distillation tower. Some of the flow pattern transitions, such as the stratified to non-stratified transition, are particularly affected by a change in diameter. As an example to illustrate this phenomenon, three flow maps were generated using experimental conditions on the AFR with larger pipe diameters (0.154 m, 0.609 m and 1.524 m), similar to those encountered in transfer lines of oil refineries.

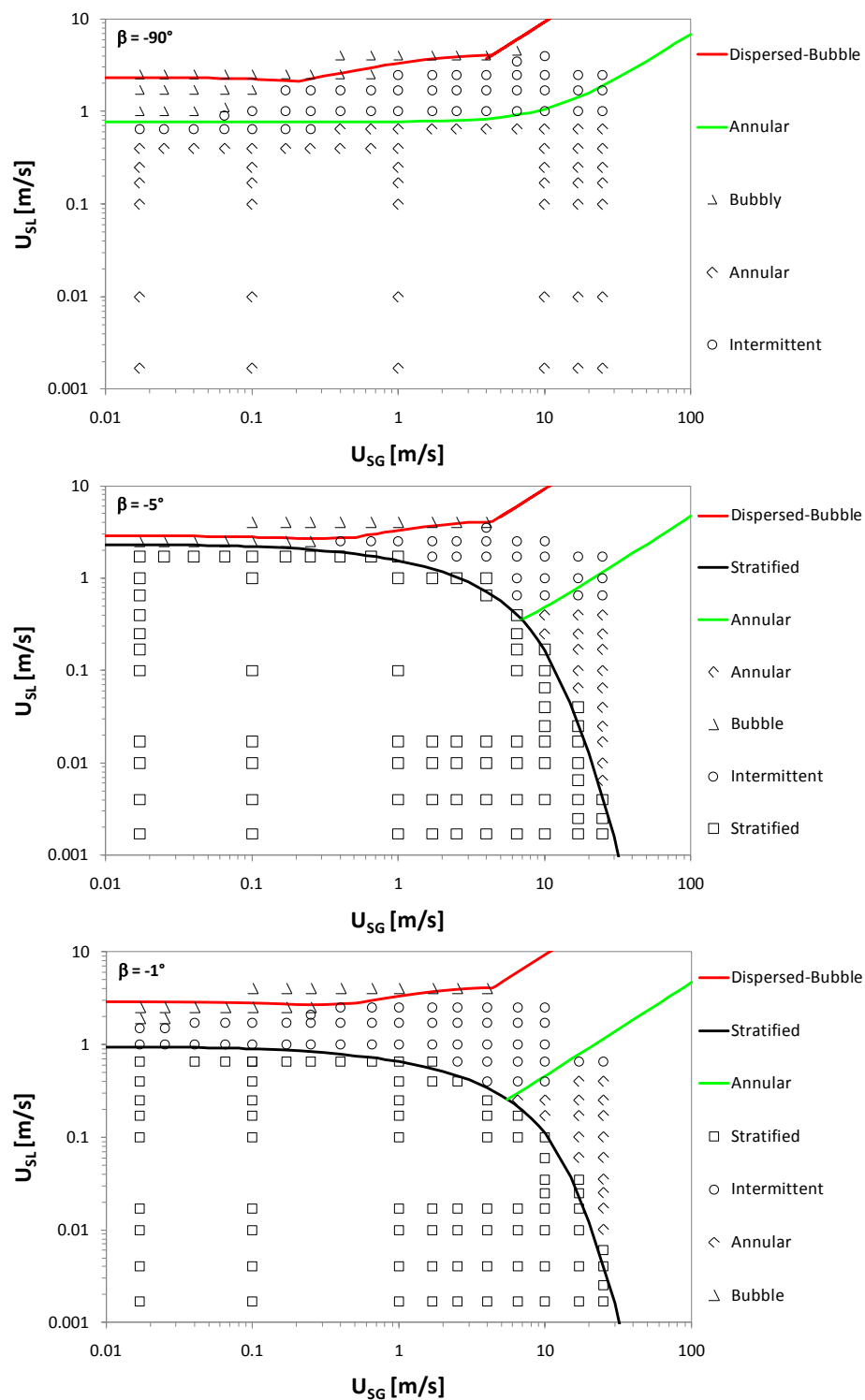


Figure 6.1: Flow pattern maps for downward inclinations (-90° , -5° , -1°) of a 0.051 m pipe diameter at standard conditions. The points represent experimental observations of flow patterns. The transitions lines are generated with the FLOPAT model.

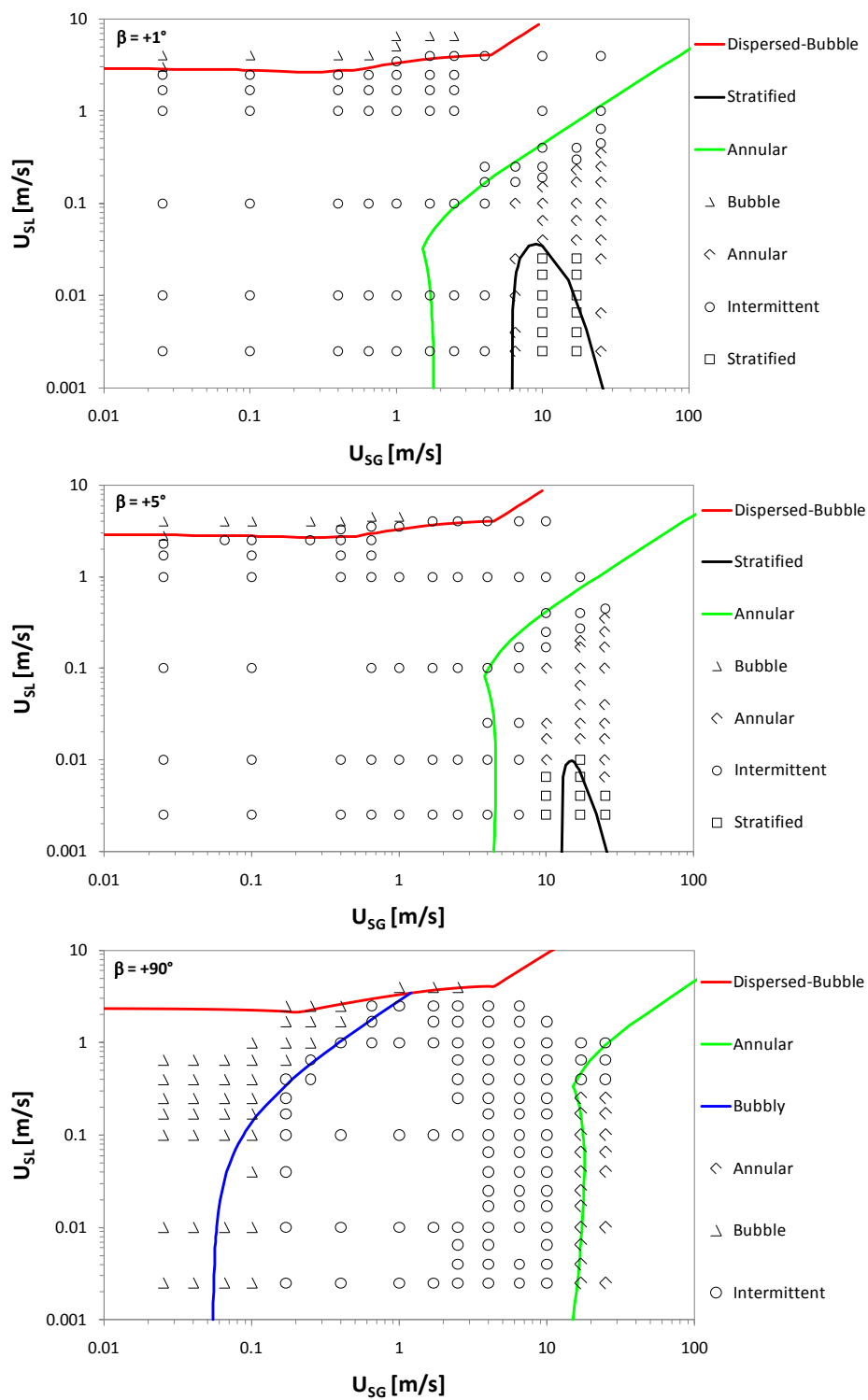


Figure 6.2: Flow pattern maps for upward inclinations ($+1^\circ$, $+5^\circ$, $+90^\circ$) of a 0.051 m pipe diameter at standard conditions. The points represent experimental observations of flow patterns. The transitions lines are generated with the FLOPAT model.

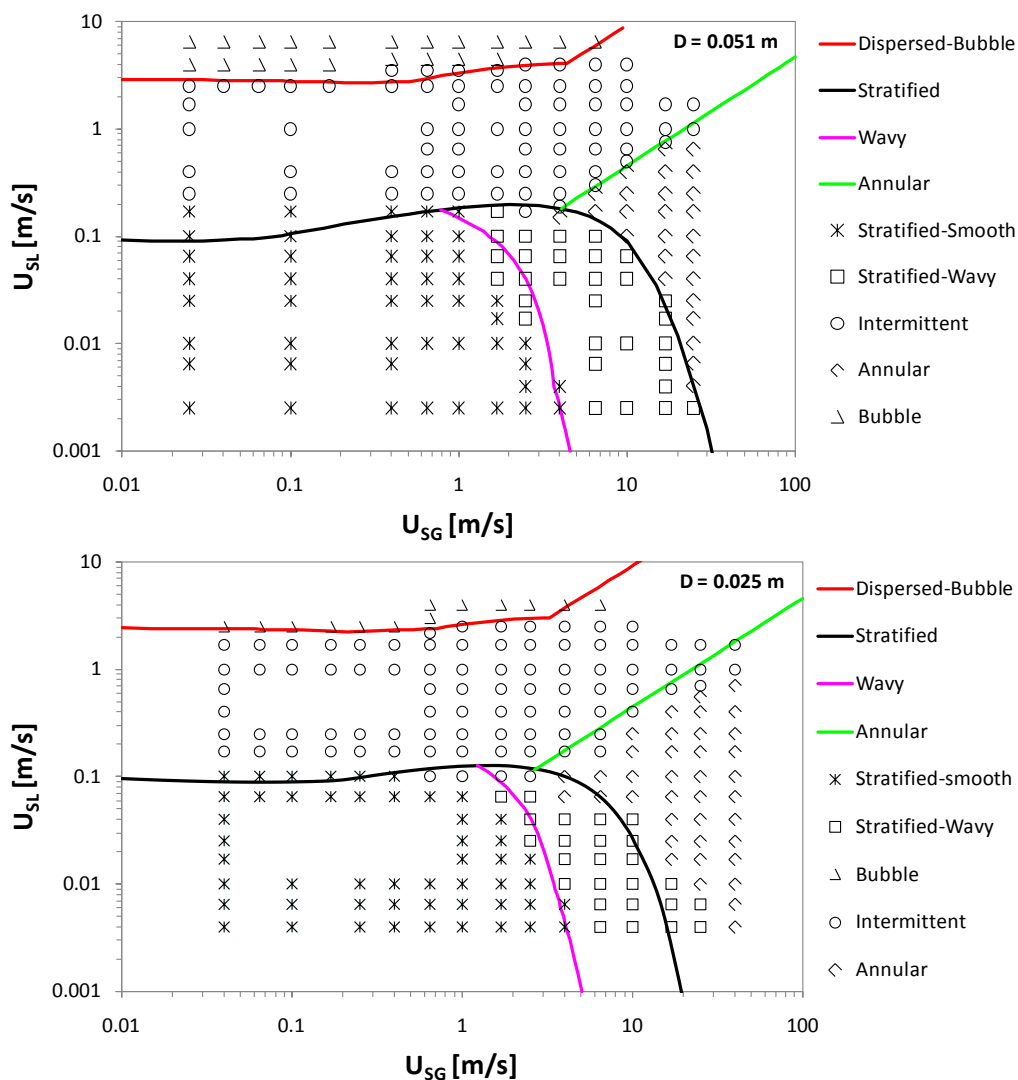


Figure 6.3: Flow pattern maps for horizontal pipes of 0.051 m and 0.025 m diameters at standard conditions. The points represent experimental observations of flow patterns. The transitions lines are generated by the FLOPAT model.

These flow maps are superimposed in Figure 6.4. Results show that while increasing the diameter, the stratified region expands (SS / SW / SW-E) and the other flow regions patterns shrink. For a range of superficial gas velocity of $U_{SG} = [20-100]$ m/s and superficial liquid velocity of $U_{SL} = [0.001-0.1]$ m/s, covering the operating conditions in transfer lines (defined by the red rectangle), a stratified flow with entrained

droplets in the gas phase (SW-E) represents the dominant flow pattern. An increase in pipe diameter shifts the formation of the continuous liquid film (i.e., annular flow) towards higher superficial gas velocities and the liquid droplets can easily impinge on the wall of the pipe, which is only partially covered by the liquid film. These operating conditions correspond to a mechanism of droplet entrainment-deposition, described in CHAPTER 4.

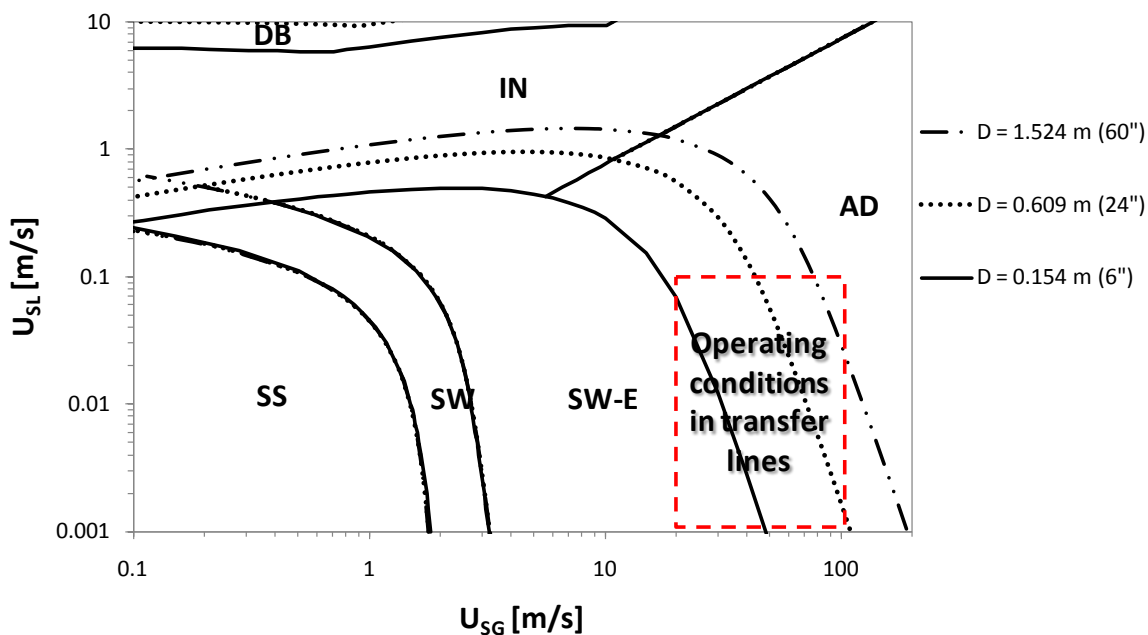


Figure 6.4: The effect of pipe diameter on flow pattern transitions using the same conditions encountered in the AFR (CO_2 / Tufflo mixture at $T = 343$ °C and $P = 377$ kPa). The operating conditions in transfer lines of oil refineries are contained in the red rectangle.

6.3.1.2 Other datasets

An analysis of the flow pattern prediction was performed against other datasets reported in Table 6.1 (1381 data points). Overall, the model correctly predicted 86% of

the experimentally observed flow patterns (Table 6.3). This dataset included 54 observations of flow pattern recorded during the experiments done in this work. Although, most of the recorded observations in this study fell within the transition stratified/non-stratified region, the model reasonably predicted 83% of them (Figure 4.8).

Overall, these results reinforce the conclusions drawn from the comparison with Shoham's dataset. They point out the difficulty⁸ to predict the transition stratified to non-stratified at high gas velocities. As shown in the flow study, this transition can cover a band of superficial gas velocity as wide as 20–30 m/s; the flow pattern observations may be very subjective, depending on the experience of the user. Therefore, the model prediction of the flow pattern transition falling into this gas velocity band is in good agreement with experimental observations. Other authors (Andritsos, 1986; Fan, 2005; Mantilla, 2008; Meng, 1999) who gathered a considerable amount of data in this region as well as the present flow study confirm this observation.

Table 6.3: Flow pattern predictions of other datasets than Shoham's.

| Flow Pattern | Predicted | | | | Data points | Model performance | |
|--------------|--------------|--------------|---------|--------|-------------|-------------------|-----|
| | Stratified | Intermittent | Annular | Bubble | | | |
| Observed | Stratified | 599 | 3 | 115 | 0 | 717 | 84% |
| | Intermittent | 2 | 119 | 19 | 0 | 140 | 85% |
| | Annular | 42 | 4 | 402 | 0 | 448 | 90% |
| | Bubble | 0 | 9 | 0 | 67 | 76 | 88% |
| Total : | | | | | 1381 | 86% | |

⁸ 157 cases with a predicted flow pattern different from the experimental observation were identified related to the present issue in Table 6.3.

6.3.2 Evaluation of the entrainment onset model

6.3.2.1 Experimental observations of entrainment onset

The literature reporting entrainment onset data measured in horizontal pipes is scarce. In general, the measurements, including those from the present hydrodynamics study (CHAPTER 4), were obtained from low pressure systems and do not capture the effect of pressure on droplet entrainment. To capture the effect of pressure on the entrainment onset, empirical observations performed with high density gases, such as those from the Top-of-the-Line Corrosion Joint Industry Project (TLCJIP) (Singer et al., 2009) were added to the database. For the TLCJIP data, the Kay's mixing rules and Bromley's mixing rules (Perry and Green, 1999) were used to calculate the gas density and viscosity of the CO₂/SF₆ mixture. The surface tension was calculated using the Jasper (1972) correlation.

The entrainment onset database initially contained 303 data points. From this total, 33 points were randomly selected and used for model tuning; this sample was not included in the model validation. The remaining 270 points were used for model validation (Table 6.4).

In the flow study described in Figure 6.5, the entrainment onset was observed at higher superficial gas velocities than those predicted by the model. This shift can be attributed to the prevailing method used to record the entrainment onset. When the user relied on the borescope camera, droplets could not always be clearly observed despite the good lighting at the top of the pipe; in this case, the visual observations were found to be more reliable.

Table 6.4: Experimental data used for the entrainment onset model validation.

| Authors | Data points | Fluids | Pipe diameter (m) |
|------------------|-------------|--|-------------------|
| Andritsos (1986) | 14 | Air / Water | 0.025, 0.095 |
| Andritsos (1986) | 10 | Air / Water-glycerine | 0.025, 0.095 |
| Mantilla (2008) | 14 | Air / Water | 0.049, 0.152 |
| Mantilla (2008) | 4 | Air / Water-glycerine | 0.049 |
| Mantilla (2008) | 3 | Air / Water-butanol | 0.049 |
| TLCJIP (2009) | 97 | CO ₂ / Water | 0.095 |
| TLCJIP (2009) | 161 | SF ₆ -CO ₂ / Water | 0.095 |
| This work | 7 | Air / Water | 0.154 |

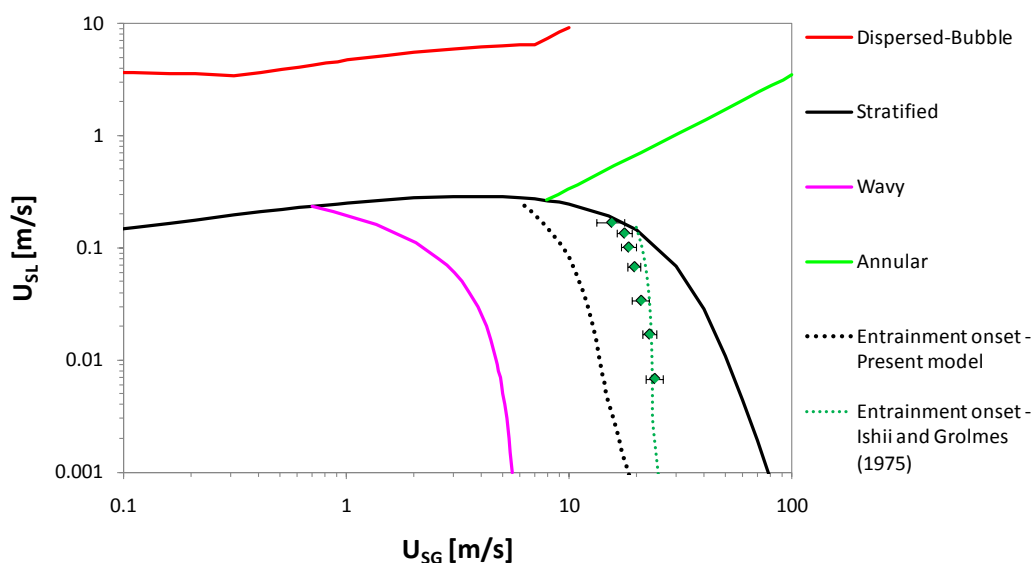


Figure 6.5: Experimental measurements of the entrainment onset (this work) plotted on a flow map with entrainment onset predictions generated by the model in this study and another model from literature

When using an intrusive method, such as the borescope camera, the entrainment onset is generally measured at a lower gas velocity because droplets impinging the pipe wall can be detected at an earlier stage. The entrainment onset model developed by Ishii

and Grolmes (1975), using a gas-interfacial friction factor of $f_{Gi} = 0.007$, seems to better predict the data measured in this study.

6.3.2.2 Model validation and accuracy

Following the statistical analysis described in section 6.2, the relative errors of model predictions were calculated as the difference between predicted and experimental superficial gas velocities at a given superficial liquid velocity (experimental value was chosen), then averaged for each dataset and the entire database.

As shown in Table 6.5, the model predicted most accurately the TLCJIP data (2.9%), with consistent prediction errors (3.8 %) that are comparable to those from this study (4.3%).

Table 6.5: Performance evaluation of the entrainment onset model.

| Authors | Data points | Statistics | | |
|------------------|-------------|---------------------|---------------------|---------------------|
| | | ε_1 (%) | ε_2 (%) | ε_3 (%) |
| TLCJIP (2009) | 225 | 0.2 | 2.9 | 3.8 |
| Andritsos (1986) | 24 | -9.9 | 26.7 | 32.6 |
| Mantilla (2009) | 21 | 10.9 | 22.9 | 28.4 |
| Present study | 7 | -46.8 | 46.8 | 4.3 |
| All data | 277 | -1.1 | 7.6 | 15.2 |

However, the underprediction of this work's entrainment onset, mentioned in the previous section, was confirmed by a relative error of 46.8%. Andritsos' data was also underestimated by 9.9%, but based on a larger sample size. At the other extreme, the model overpredicted the measured entrainment onset by 10.9% for Mantilla's dataset that

is comparable to Andritsos' in terms of overall accuracy (22.9%) and error variability (28.4%). Regardless of which data set is referred to, in general, the model underpredicts the measured entrainment onset by 1.1%, has an overall accuracy of 7.6% and a scatter of errors equal to 15.2%.

Figure 6.6 shows the agreement between predicted and measured entrainment onset expressed as superficial gas velocity. The $\pm 20\%$ deviations from the ideal case (the 1:1 line) are marked as dashed lines. Data from this study are in red. Most of the data points fall within the $\pm 20\%$ interval from the ideal agreement. The model tends to be in a better agreement with the entrainment onset data observed with the borescope camera (Mantilla, 2008; Singer et al., 2009) than those measured from outside the pipe through visual observations (Andritsos, 1986; present work).

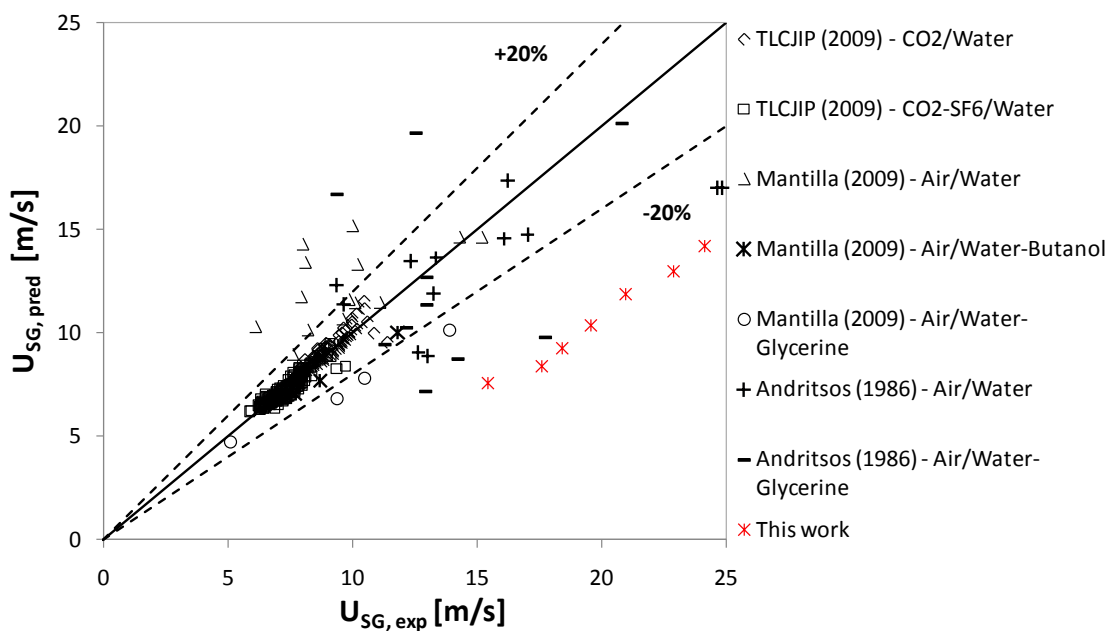


Figure 6.6: Comparison between predicted and experimental entrainment onset values expressed as superficial gas velocity U_{SG} .

The evaluation of the model also revealed that the entrainment onset observed in small pipe diameters ($D < 0.05$ m) using viscous fluids ($\mu_L > 4 \cdot 10^{-3}$ Pa·s) was poorly predicted. For more accurate entrainment onset predictions, only measurements from fluids with a viscosity of $\mu_L < 4 \cdot 10^{-3}$ Pa·s should be used to validate this model.

6.4 Evaluation of flow pattern models

Four individual flow pattern models (stratified, annular, intermittent, bubble) were built to predict flow pattern characteristics, such as pressure drop, liquid holdup, wetted wall fraction, and liquid height at the bottom of the pipe. Predictions of these characteristics for each flow pattern were compared to corresponding experimental observations. Data points were selected for validation if the same flow pattern had been identified through observations during the experiments. When the flow pattern could not be identified because no data was available, it was predicted by the FLOPAT model. Once known which flow pattern occurred, the corresponding flow pattern model was run. A total of 2286 data points were used for validating the four flow models as reported in Table 6.6.

Table 6.6: Validation data for each flow pattern model.

| Flow model | Stratified | Annular | Intermittent | Bubble |
|-------------------|-------------------|----------------|---------------------|---------------|
| Data points | 1126 | 831 | 252 | 77 |

The performance of each flow pattern model was evaluated through measurements of characteristics specific to each flow pattern. In general, the pressure

drop and liquid holdup were two common variables among flow patterns that were mainly considered in the validation. Additionally, the wetted wall fraction, the liquid height at the bottom of the pipe, the entrainment fraction of liquid droplets in the gas phase, and the slug frequency complete the analysis but are only calculated for their specific flow regimes.

6.4.1 Stratified flow model

A substantial sample of data points obtained at low liquid loadings using horizontal or near horizontal pipes ($\beta = [-5, +5]^\circ$) was acquired and assigned to validate the stratified flow model since important changes in flow pattern and characteristics are observed at this range of inclination angles. Furthermore, these pipe inclinations are commonly found in upstream oil and gas industry. The model accuracy was tested against measurements of pressure drop, liquid holdup, wetted wall fraction, and liquid height at the bottom of the pipe. For each of these flow pattern characteristics, the corresponding number of data points and statistical parameters are provided in Table 6.7.

Table 6.7: Performance evaluation of the stratified flow model.

| Variables | Data points | Statistics | | |
|---------------------------|-------------|---------------------|---------------------|---------------------|
| | | ε_1 (%) | ε_2 (%) | ε_3 (%) |
| Pressure drop | 874 | 1.6 | 16.9 | 22.5 |
| Liquid holdup | 647 | 8.0 | 20.0 | 27.6 |
| Wetted wall fraction | 440 | 1.2 | 14.3 | 18.4 |
| Pipe bottom liquid height | 538 | 9.6 | 34.6 | 54.0 |

The highest accuracy was achieved when predicting the wetted wall fraction (14.3%), followed by the pressure drop (16.9%). In both cases, the model slightly overpredicted the measured values in stratified flow (1.2% and 1.6%, respectively). The relative errors were less scattered in the case of wetted wall fraction prediction (18.4%). The less accurate values were the predictions of the liquid height at the bottom of the pipe (34.6%), an aspect also reflected by the large scatter in the errors (54%). However, the prediction of the film thickness closely depends on the shape of the gas-liquid interface assumed in the stratified model. Even though Zhang et al. (2003) provided a rather realistic description of it compared to a flat interface (Taitel and Dukler, 1976) or a constant liquid film (Hart et al., 1989), the effects of waves are not accounted for in the present case. For these reasons, an accurate prediction (i.e., ~10%) remains challenging. Overall, the absolute average error was less than 35% for any of the flow pattern characteristics.

Predictions of the stratified flow model for all these variables are plotted in Figure 6.7 to Figure 6.10. The variables measured on the CFR, excepting the liquid holdup (not directly measured in this study) are marked differently to separate them from the rest of the database.

Most of the pressure drop predictions fall within the $\pm 20\%$ error from the 1:1 line, suggesting an excellent model agreement (Figure 6.7). The red squares follow the general trend like the rest of the data.

The predictions of liquid holdup in Figure 6.8 are more scattered at values greater than 0.2, confirmed by an errors scatter of 27.6%, but the overall accuracy is good (20%).

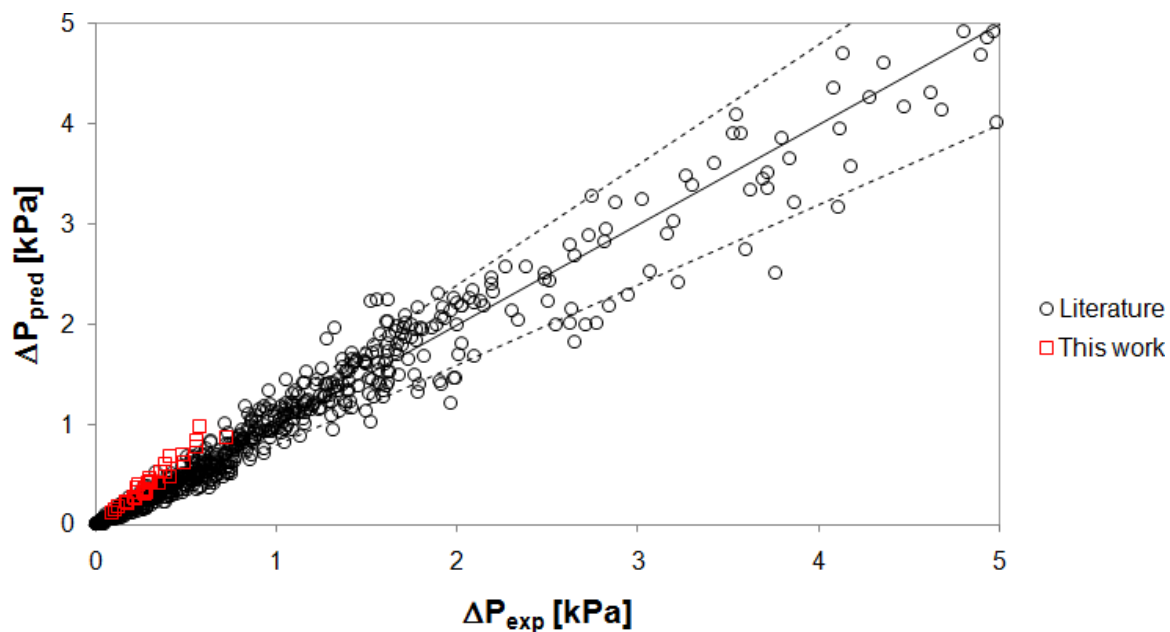


Figure 6.7: Comparison between predicted and measured pressure drop in stratified flow conditions (Data source: Table 6.1, Ref. Nr. 2-3; 6; 9; 11; 13-14; 20; 24).

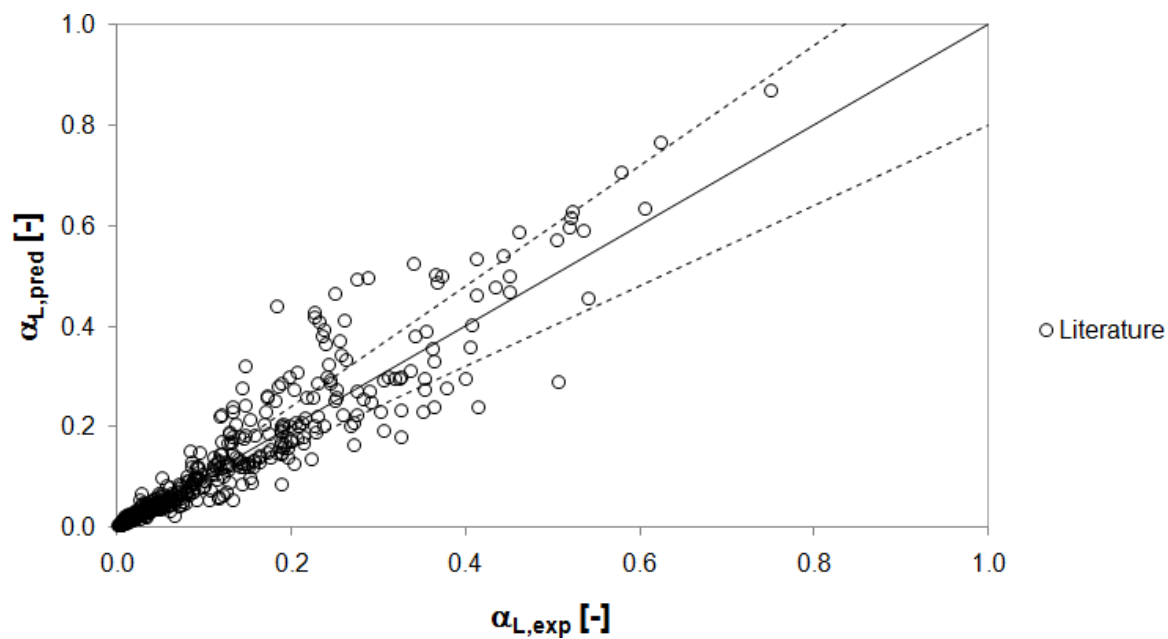


Figure 6.8: Comparison between predicted and measured liquid holdup in stratified flow conditions (Data source: Table 6.1, Ref. Nr. 1; 3; 6; 8-9; 14-16; 20).

The model agreement with measured wetted wall fraction in stratified flow (Figure 6.9) is one of the best among the variables tested for this particular flow pattern (the smallest absolute average relative error, 14.3%). In Figure 6.9, all the predictions follow closely the 1:1 line, excepting 6 data points (3 from this work and 3 from other sources). Although underpredicted, these outliers do not impair the excellent performance of the model. Regarding this work, in stratified flow operating conditions, the liquid droplets were already depositing at the top of pipe with plenty of rivulets flowing on the sides of the pipe. Therefore, the interface between the liquid film and these rivulets was difficult to assess.

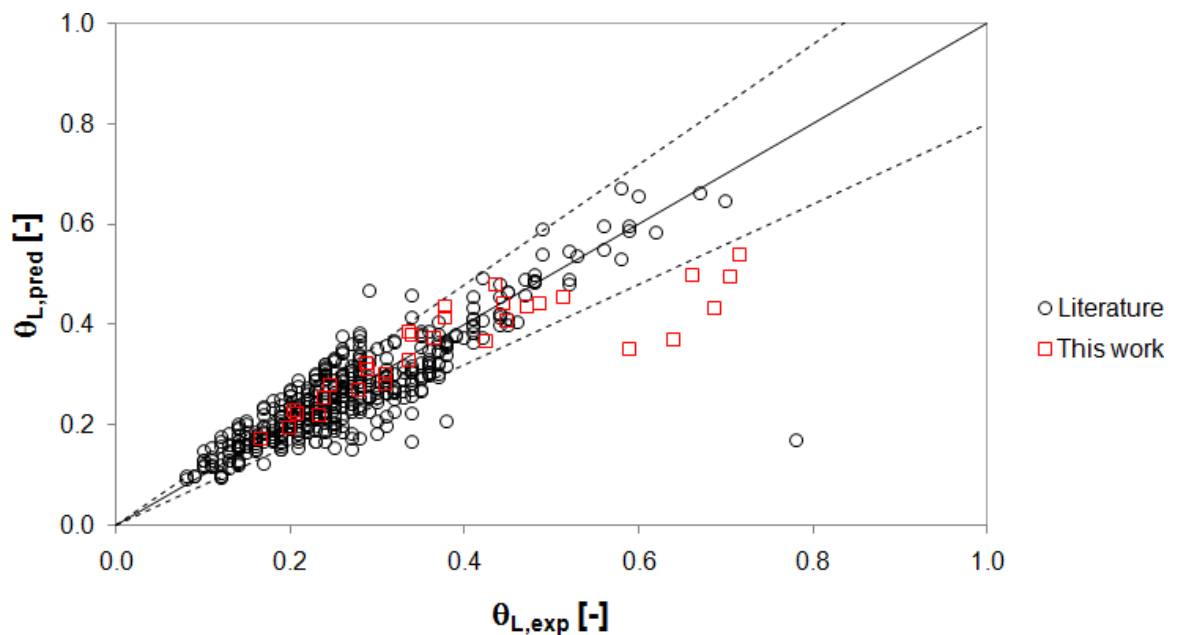


Figure 6.9: Comparison between predicted and measured wetted wall fraction in stratified flow conditions (Data source: Table 6.1, Ref. Nr. 6; 14; 24).

The remaining variable used to evaluate the stratified model is the liquid height at

the bottom of the pipe (Figure 6.10). In the present flow study, given some instrument limitations, the observations of the liquid height were averaged from repeated readings made on a simple metal stick with marks every 2.5 mm, inserted in the pipe.

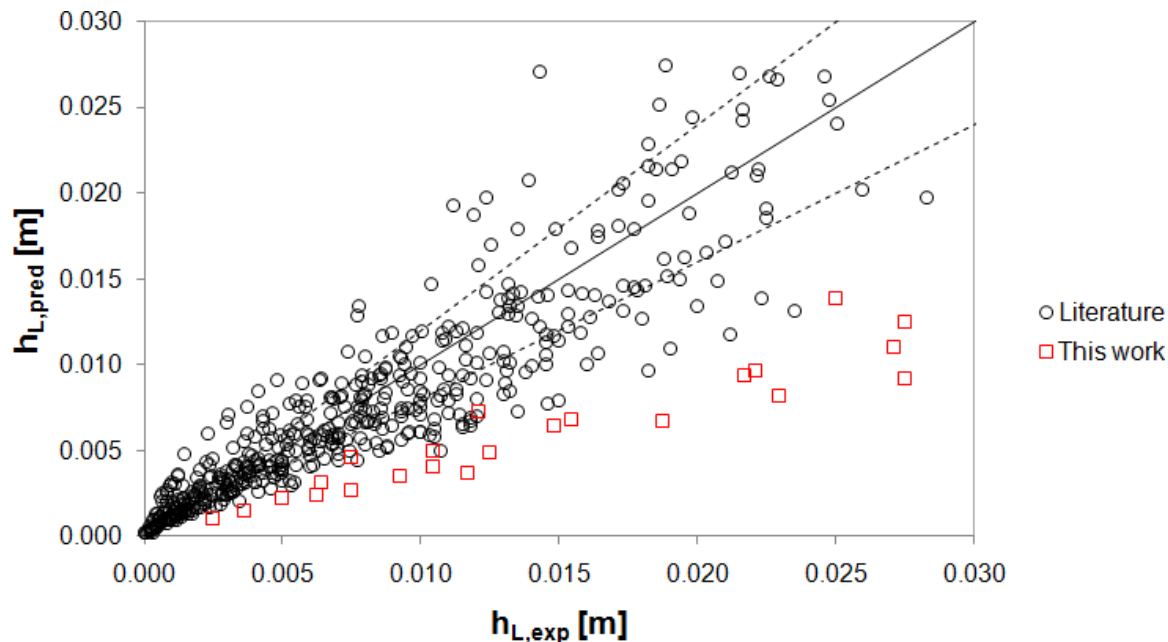


Figure 6.10: Comparison between predicted and measured liquid height in stratified flow conditions (Data source: Table 6.1, Ref. Nr. 2; 6; 13; 14; 24).

Because of the presence of waves during measurements, this method obviously was prone to uncertainty. Note that small liquid film heights (less than 2.5 mm) were systematically discarded because they were considered unreliable. Thus, the measurement method explains the deviated but consistent trend on the parity plot (red squares). Compared to other data sources, accurate measurements of this variable are usually obtained using conductivity probes (Andritsos, 1986; Fan, 2005; Laurinat, 1982; Mantilla, 2008; Williams, 1986; Williams, 1990). Overall, the model performance is

acceptable, with an absolute average relative error of predictions less than 35%.

6.4.2 Annular flow model

The annular flow model was evaluated with the database from Table 6.8, for three flow pattern characteristics, such as the pressure drop, liquid holdup and entrainment fraction. The best model agreement was achieved in the case of liquid holdup and entrainment fraction, with absolute average errors of 26.4% and 30.5%, respectively. The pressure drop predictions did not reasonably agree with the measurements, considering the large average error (56.7%) and scatter (83.7%).

Table 6.8: Performance evaluation of the annular flow model.

| Variables | Data points | Statistics | | |
|----------------------|-------------|---------------------|---------------------|---------------------|
| | | ε_1 (%) | ε_2 (%) | ε_3 (%) |
| Pressure drop | 555 | 18.4 | 56.7 | 83.7 |
| Liquid holdup | 352 | -19.1 | 26.4 | 26.0 |
| Entrainment fraction | 485 | 10.7 | 30.5 | 49.4 |

In Figure 6.11, it is shown that the annular flow model slightly underpredicted most of the pressure drop data at low liquid loadings ($U_{SL} < 0.1$ m/s). At the other extreme, the model overpredicted the pressure drop measured at higher superficial liquid velocities ($U_{SL} > 0.1$ m/s). This disagreement is considered to be related to the choice of the closure relationship for the interfacial friction factor f_i (Ambrosini et al., 1991) used in the model, since the changes in the other closure relationships (the cases of

entrainment fraction and liquid-wall friction factor) did not drastically affect the model prediction as f_i did. The use of other f_i correlations (Wallis, 1969; Whalley and Hewitt, 1978; Gomez et al., 1999 based on Henstock and Hanratty's (1976) work) did not improve the performance of the annular flow model since the model still overestimated the pressure drop at high liquid loadings. Data from this study (red squares) exhibited similar trends at high liquid flow rate conditions.

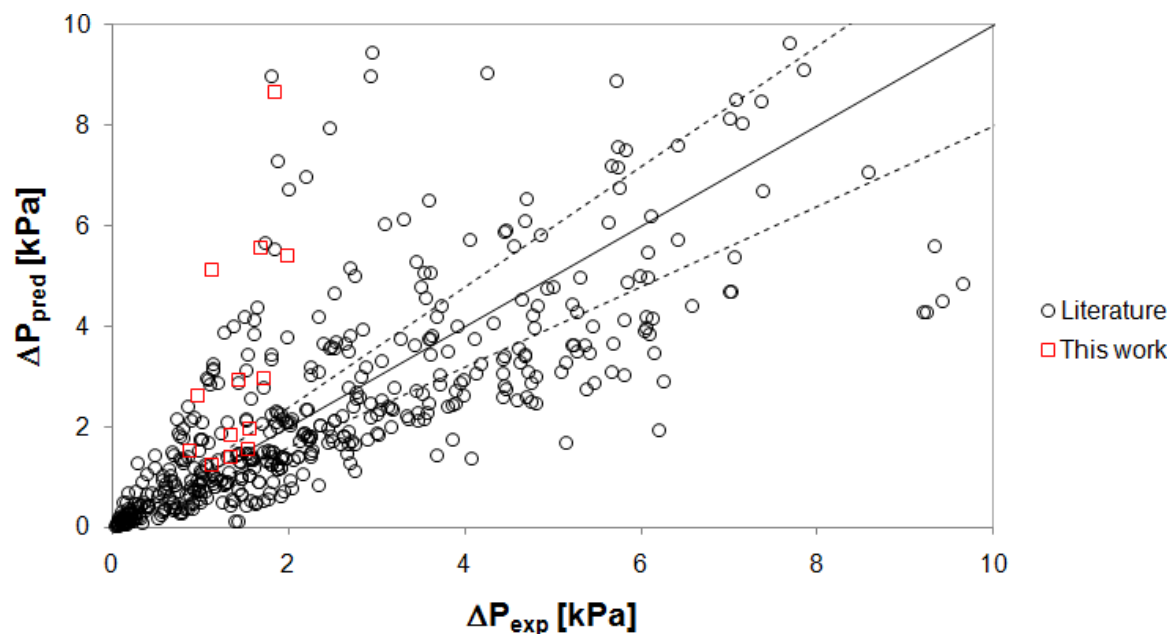


Figure 6.11: Comparison between predicted and measured pressure drop in annular flow conditions (Data source: Table 6.1, Ref. Nr. 2-3; 9; 11-14; 24).

As shown in Figure 6.12, the liquid holdup measured in annular flow was in good agreement with just a few underestimations, which contributed to an absolute average error of 26.4%, otherwise the smallest among the other annular flow pattern characteristics. All the measurements come from the available literature.

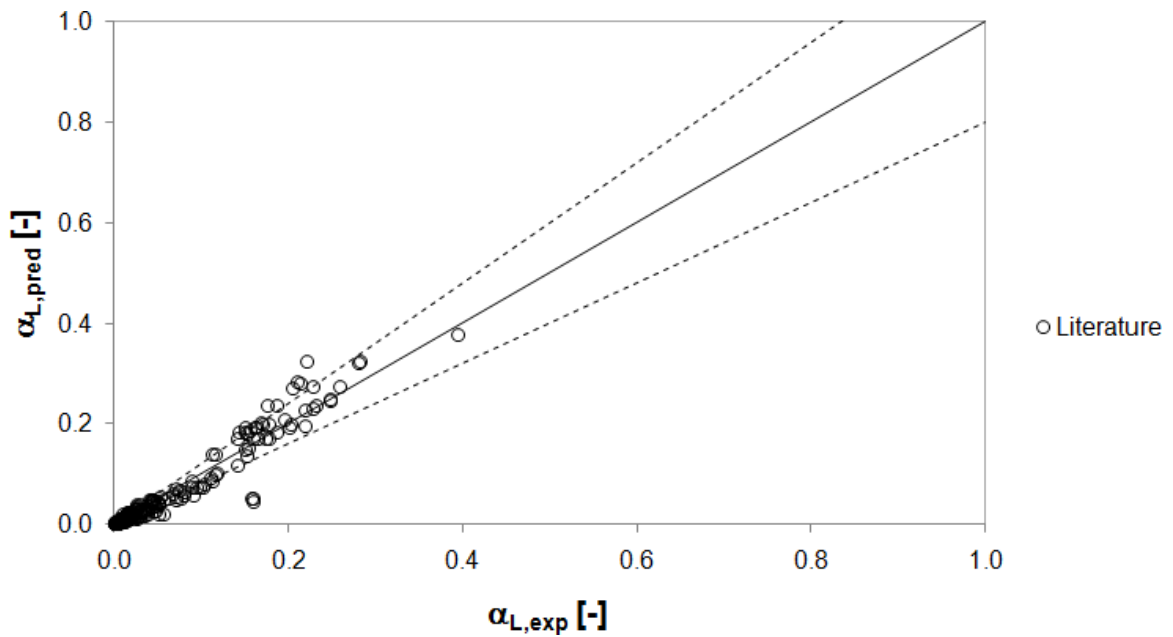


Figure 6.12: Comparison between predicted and measured liquid holdup in annular flow conditions (Data source: Table 6.1, Ref. Nr. 1; 3; 8-9; 12; 14; 16).

Figure 6.13 shows the prediction of the entrainment fraction of liquid droplets in the gas core of an annular flow pattern. The model overpredicts the measured values by 10.7%, but the overall accuracy is acceptable (30.5%). Using a set of three correlations, Magrini (2010) recently demonstrated that the prediction of the entrainment fraction had an accuracy between 20 and 50%. Note that the entrainment fraction measured in this study (CHAPTER 4) was not included in the model validation because it is the result of some limitations of the instruments used in the CFR, such as the control of pressure nearby the collector mouth, but it was plotted in Figure 6.13 (red squares) along with the rest of the data.

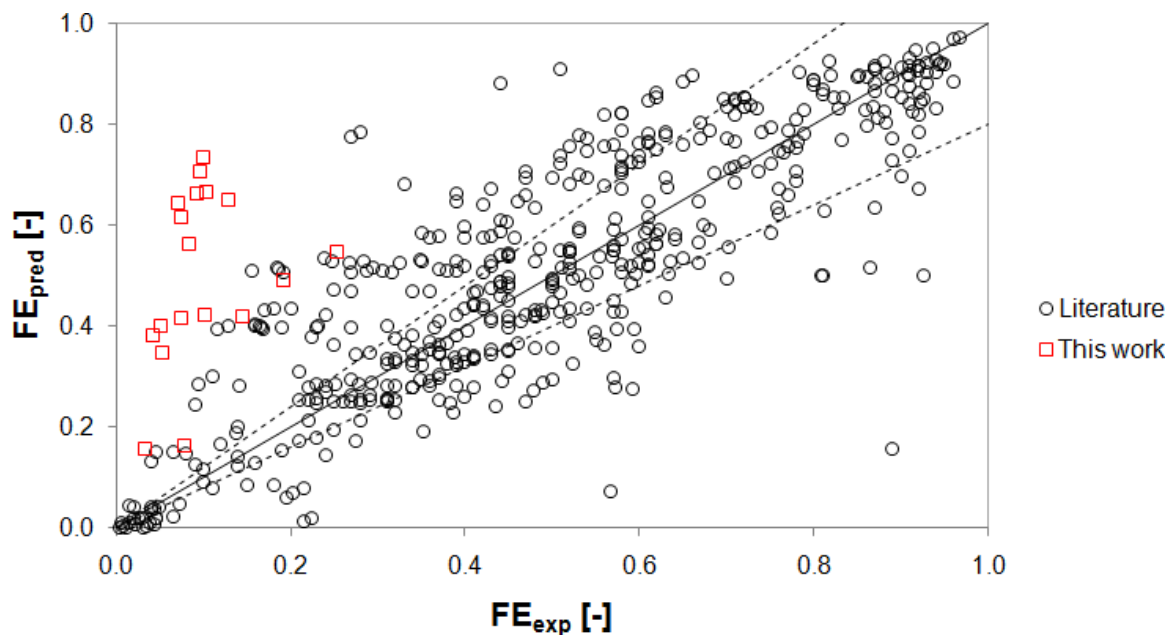


Figure 6.13: Comparison between predicted and measured entrainment fraction in annular flow conditions (Data source: Table 6.1, Ref. Nr. 5; 10-14; 17; 22-24).

6.4.3 Intermittent flow model

Higher superficial liquid velocities than those encountered in transfer lines of oil refineries are required to form the slug flow in the pipe. This flow pattern was not the main focus of this work, but was added to expand the capability of the gas-liquid two-phase flow model. Therefore, a less extensive model validation was performed compared to stratified and annular flow models. Furthermore, the model was only developed and validated for horizontal to upward vertical flows. Additional closure relationships would be needed before validating the model for downward flow cases. The corresponding analysis of the slug model performance for pressure drop, liquid holdup and slug frequency is detailed in Table 6.9.

Table 6.9: Performance evaluation of the intermittent flow model.

| Variables | Data points | Statistics | | |
|--|-------------|---------------------|---------------------|---------------------|
| | | ε_1 (%) | ε_2 (%) | ε_3 (%) |
| Pressure drop | 123 | 41.6 | 53.6 | 53.4 |
| Liquid holdup | 196 | 3.6 | 13.8 | 17.2 |
| Slug frequency ($\beta = [0, 11]^\circ$) | 20 | 8.4 | 51.4 | 67.9 |

The pressure drop predictions of the intermittent flow model were not satisfactory regardless of the datasets used for validation. The model overpredicts experimental data by 41.6% and has a large variability of errors (53.4%). The model has an excellent agreement of liquid holdup predictions (13.8%); the errors are less scattered than those from pressure drop predictions. Regarding the slug frequency, the accuracy of the model can be improved as the absolute average error is high (51.4%).

In Figure 6.14, the overprediction of pressure drop can also be visualized and, so, the scatter of the data points. Only few observations fall within the $\pm 20\%$ agreement with the 1:1 line.

Figure 6.15 shows the excellent agreement of the model with the expected liquid holdup. A sample of 104 data points from three different datasets (Beggs and Brill, 1973; Felizola, 1992; Govier and Omer, 1962) was commonly used to validate both the liquid holdup and the pressure drop. Furthermore, the experimental data from Beggs, and Govier and Omer were very well predicted (absolute average error of 8.2% with a standard deviation of 6.9%) suggesting that the calculation of pressure drop in the intermittent flow model could be improved.

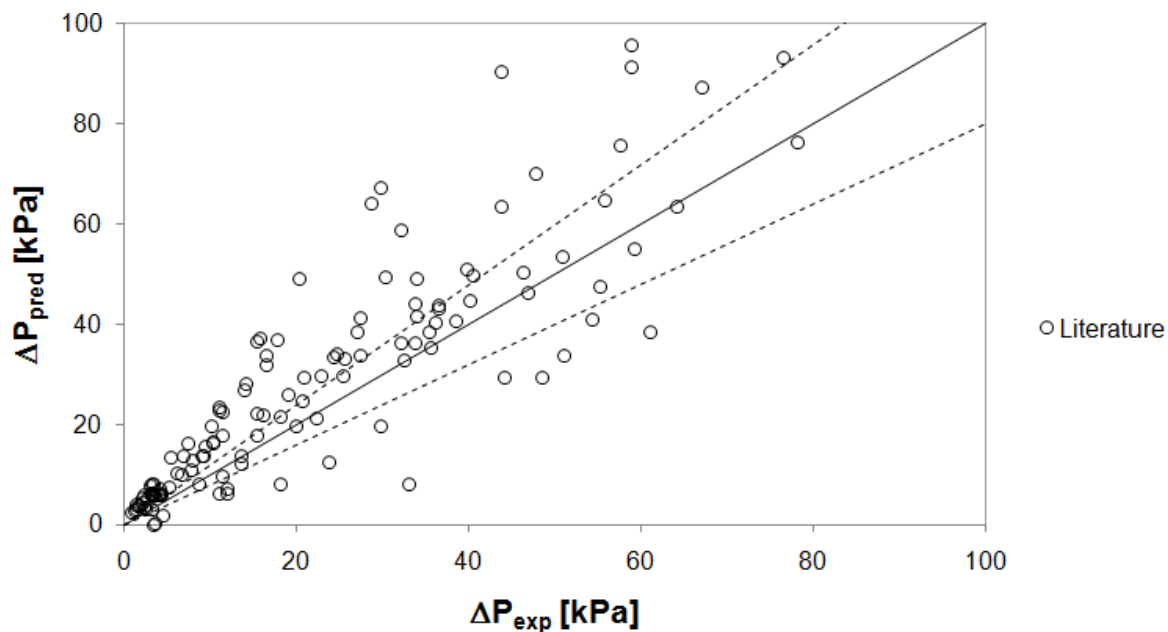


Figure 6.14: Comparison between predicted and measured pressure drop in intermittent flow conditions (Data source: Table 6.1, Ref. Nr. 2-3; 7; 9-11).

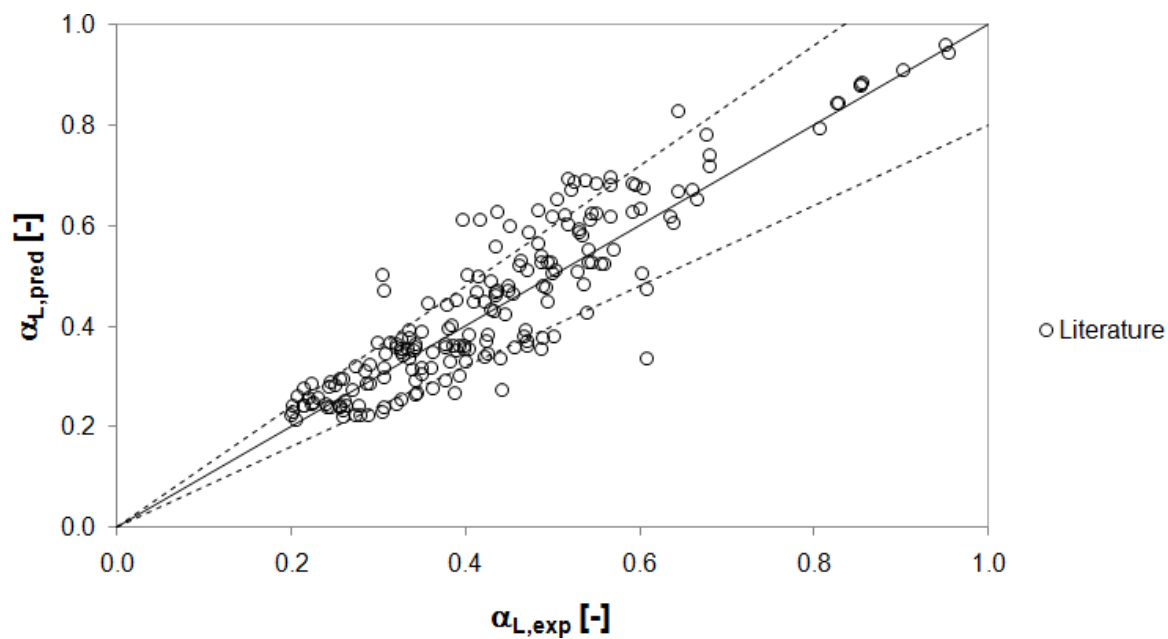


Figure 6.15: Comparison between predicted and measured liquid holdup in intermittent flow conditions (Data source: Table 6.1, Ref. Nr. 1; 3; 7-9; 16).

The slug frequency represented the third set of flow pattern characteristics used to evaluate the performance of the intermittent model. Only 20 data points out of 91 from the database corresponded to pipe inclinations in the range of 0–11° and were used for validation. The original correlation (Zabaras, 2000) developed with 399 experimental data points gave an absolute average error of 60% and a standard deviation of 80%, which are slightly higher than those from this study (51.4% and 67.9% respectively). Still, these ranges of uncertainty remain very large and the prediction of the slug frequency difficult. Recently, Al-Safran (2012) pointed out that none of the actual correlations is able to correctly predict the slug frequency and suggested the use of probabilistic modeling in order to evaluate the error related to the predicted slug frequency.

6.4.4 Bubble flow model

The main bubble flow pattern characteristic for the model validation is the liquid holdup. Note that the data from Caetano (1985) was measured in an annulus configuration. For bubbly and dispersed bubble flow patterns, an equivalent diameter obtained with the same cross-sectional area of the annulus and equivalent superficial velocities were calculated for the model validation. Figure 6.16 shows an excellent agreement of predictions with Caetano's measured liquid holdup (74 points). Statistical analysis estimated an absolute average error of 3.1% and a variability of errors equal to 4.6%.

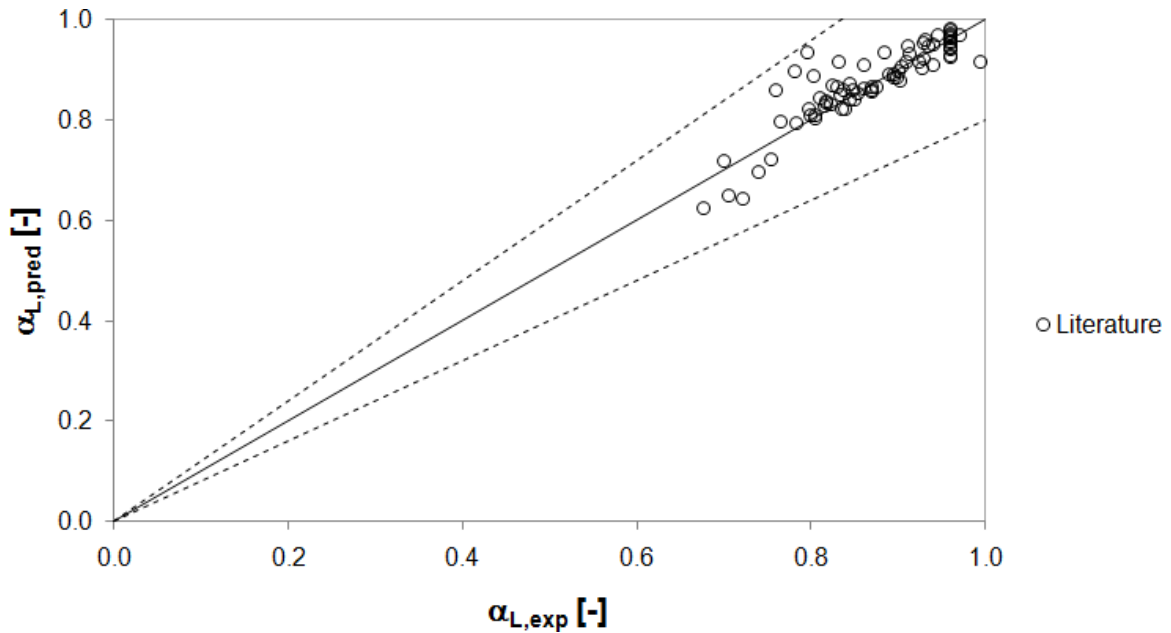


Figure 6.16: Comparison between predicted and measured liquid holdup in bubble flow conditions (Data source: Table 6.1, Ref. Nr. 3-4; 8).

6.5 Summary

A large database from literature, proprietary data and this work (CHAPTER 4) was built to validate the gas-liquid two-phase flow model developed in this study (CHAPTER 5). The model predicting the flow pattern transitions (FLOPAT) was validated against 7066 data points with a prediction rate of 82%. A second flow model predicting the entrainment onset of liquid droplets in the gas phase was also successful (absolute average error of 7.6%). For each of the predicted flow patterns (stratified, annular, intermittent and bubble), a flow model was built to estimate flow pattern characteristics. The resultant models were individually validated for their corresponding characteristics. An additional statistical analysis was done to evaluate the overall performance of these models in terms of flow pattern characteristics, such as pressure

drop, liquid holdup, wetted wall fraction and liquid height (stratified flow), as well as the entrainment fraction (annular flow) and slug frequency (slug flow). Table 6.10 summarizes the final results of this validation. All flow pattern characteristics were predicted within an absolute average error less than 35%, except for slug frequency.

Table 6.10: Overall performance of the gas-liquid two-phase flow model.

| Variables | Data points | Statistics | | |
|--|-------------|---------------------|---------------------|---------------------|
| | | ε_1 (%) | ε_2 (%) | ε_3 (%) |
| Pressure drop | 1566 | 11.2 | 34.4 | 56.4 |
| Liquid holdup | 1269 | -0.6 | 19.8 | 27.5 |
| Wetted wall fraction | 440 | 1.2 | 14.3 | 18.4 |
| Pipe bottom liquid height | 538 | 9.6 | 34.6 | 54.0 |
| Entrainment fraction | 485 | 10.7 | 30.5 | 49.4 |
| Slug frequency ($\beta = [0, 11]^\circ$) | 20 | 8.4 | 51.4 | 67.9 |

CHAPTER 7 CORROSION MODEL VALIDATION

A particular contribution of the experimental corrosion study presented in CHAPTER 3 is the validation of an existing corrosion simulator named *Crudecorp*, which has been developed to predict the corrosion of crude oils in refinery environments. The AFR flow loop on which the naphthenic acid corrosion experiments were run is the only facility of the ICMT lab that can simulate multiphase flow conditions under high temperatures and flow velocities. Therefore, the data generated in this study, along with data from other sources, helped to test the corrosion model. Thus, this chapter will give an overview of the mechanisms on which the corrosion model is based, and then, show an evaluation of the model using the aforementioned data.

7.1 Description of the corrosion model

A mechanistic model was developed to predict corrosion due to naphthenic acids and sulfur compounds in oil refinery environments (Bota, 2010b). It is constituted from two parts: a corrosion module and a scale growth module.

The corrosion module describes the physicochemical processes related to sulfidation and naphthenic acid corrosions, and their corresponding corrosion rates. Similar to the work of Sun and Nescic (2009) regarding the H₂S corrosion mechanisms, the sulfidation process - involving more generally, sulfur compounds - is primarily based on a “heterogeneous solid state reaction” at the steel surface. The model assumes the presence of two layers acting as diffusion barriers to the transportation of corrosive

species to the metal surface (Figure 7.1). The inner layer is a thin ($< 1 \mu\text{m}$) and dense film of sulfides present directly at the metal surface (Nesic and Qu, 2008). The outer layer is generated from the inner layer by a transient cyclic process of scale growth, cracking and delamination. Its structure is usually more porous, thicker ($> 1 \mu\text{m}$) and looser compared to that of the inner layer. The naphthenic acid attack (CHAPTER 2 eq 2.2.1) is also a heterogeneous reaction occurring at the metal surface between naphthenic acid species diffusing through the scale layers and iron. Similarly to the experimental corrosion rates measured in the presulfidation-challenge testing, the overall corrosion rate CR_T can be described in terms of sulfidation corrosion rate CR_{Sulf} and naphthenic acid corrosion rate CR_{NAP} in:

$$CR_T = CR_{NAP} + CR_{Sulf} \quad (3.4.5)$$

with:

$$CR_{NAP} = \varphi(TAN, T, U_L, \delta_{OS}, \dots) \quad (7.1.1)$$

$$CR_{Sulf} = \varphi(TS, T, U_L, \delta_{OS}, \dots) \quad (7.1.2)$$

where T is the temperature (K), U_L is the in-situ liquid velocity at the pipe wall (m/s), δ_{OS} is the outer scale thickness (m), and TS refers to the total content of sulfur compounds (wt%).

The scale growth module describes the mechanisms of scale growth at the metal surface and scale removal. The scale growth is determined by the sulfidation rate CR_{Sulf} . The scale removal results from a combination of mechanical effects (noted SR_{mech}), such as flow turbulence, and chemical effects (noted SR_{chem}), such as the NAP attack. The overall scale retention rate SR_T is expressed as:

$$SR_T = CR_{Sulf} - (SR_{chem} + SR_{mech}) \quad (7.1.3)$$

where:

$$SR_{chem} = \varphi(TAN, T, U_L, \dots) \quad (7.1.4)$$

$$SR_{mech} = \varphi(U_L, \delta_{OS}, \dots) \quad (7.1.5)$$

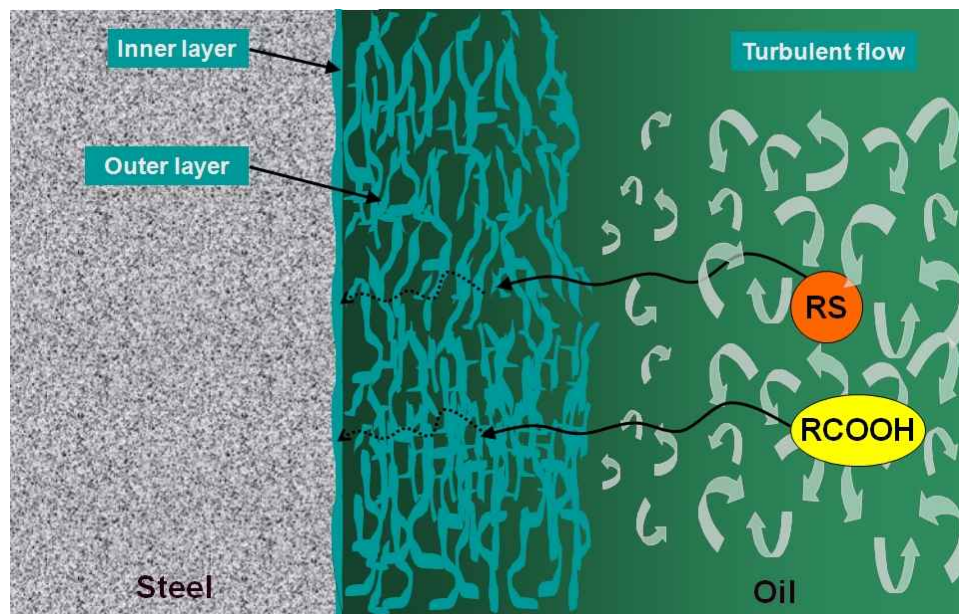


Figure 7.1: Corrosion processes occurring at the metal surface in naphthenic acid (RCOOH) and organo-sulfur compounds (RS) containing environments (adapted from Nestic and Qu, 2008).

7.2 Model evaluation

The corrosion model presented in the previous section was evaluated and tuned with experimental data using a large range of fluids, such as model oils, 650+ cuts, and VGO cuts (Bota, 2010b). The model, implemented in the corrosion simulator Crudecorp V5.1, was tested separately from previous validations and only using new experimental data, including data from this study; data used for model tuning in previous works was

disregarded as well. The chemical and flow operating conditions of the experimental data used in the validation are provided in Table 7.1 to Table 7.3 unless specified otherwise.

The predictive tool allowed the user to enter a set of inputs as shown in Figure 7.2, and calculate trends of variables, such as the corrosion rate at the metal surface. This validation focused on separate predictions of corrosion rates due to sulfidation corrosion and pure NAP corrosion (challenge). In the case of presulfidation-challenge (section 3.4.5), only the operating conditions of the presulfidation step could be reasonably simulated by Crudecorp. Some program limitations allowed the user to change the chemical conditions, but prevented any modification of the flow conditions (hydraulic diameter, liquid velocity) that were used in the "challenge" experiments. For these reasons, no presulfidation-challenge could be reasonably simulated with this corrosion model.

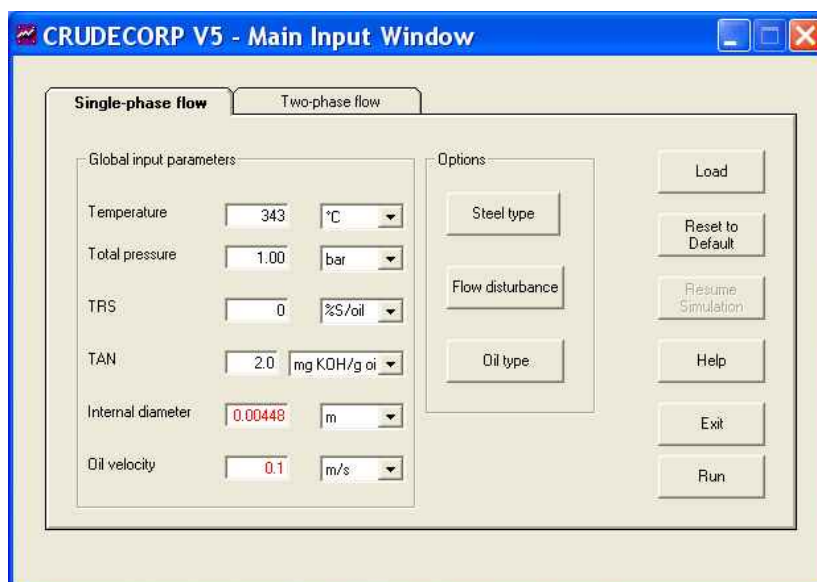


Figure 7.2: Overview of the inputs window of Crudecorp V5.1 for single phase flow conditions.

Table 7.1: Experimental conditions for sulfidation used for corrosion model validation.

| Data source | Flow loop | Refreshment rate (mL/min) | TAN (mg KOH / g oil) | Sulfur content (%wt) | Temperature (°C) | Test duration (hrs) | Data points (-) |
|--------------------------|----------------------|---------------------------|----------------------|----------------------|------------------|---------------------|-----------------|
| Qu and Nestic (2006) | Autoclave | 0 | 0.1 | 0.25 | 288–343 | 24 | 4 |
| Kanukuntla et al. (2008) | FTMA ^a | 1.5 | 0.1 | 0.25 | 232–343 | 24 | 8 |
| Present study | FTMA ^a | 1.5 | 0.1 | 0.25 | 343 | 24 | 2 |
| Present study | FTMA NJ ^b | 1.5 | 0.1 | 0.25 | 343 | 24 | 47 |

Table 7.2: Experimental conditions for pure NAP corrosion used for corrosion model validation.

| Data source | Flow loop | Refreshment rate (mL/min) | TAN (mg KOH / g oil) | Sulfur content (%wt) | Temperature (°C) | Test duration (hrs) | Data points (-) |
|-----------------------|--------------------|---------------------------|----------------------|----------------------|------------------|---------------------|-----------------|
| Jin (to be published) | Autoclave | 0 | 4 | 0 | 343 | 24 | 2 |
| Huang (2008) | FTMA ^a | 1.5 | 1–8 | 0 | 343 | 24 | 14 |
| Present study | AFR – single phase | 80 | 2, 4 | 0 | 343 | 6 | 36 |
| Present study | AFR – multiphase | 80–185 | 2, 4 | 0 | 343 | 6 | 87 |

Table 7.3: Flow characteristics conditions encountered in the autoclave, the FTMA, and the AFR.

| Flow loop | In-situ gas velocity (m/s) | Refreshment rate (mL/min) | In-situ liquid velocity (m/s) | Residence time (s) ^d | Liquid Reynolds number (-) ^e | Wall-liquid friction factor (-) ^f | Wall-liquid shear stress (Pa) |
|-------------------------------|----------------------------|---------------------------|-------------------------------|---------------------------------|---|--|-------------------------------|
| Autoclave | N/A | 0 | N/A | test duration | N/A | N/A | N/A |
| FTMA ^a | N/A | 1.5 | 9.0E-05 | 434 | 4 | 3.585 | 9E-06 |
| FTMA NJ ^b | N/A | 1.5 | 1.5E-03 | 420 | N/A | N/A | 5 |
| AFR – single phase | N/A | 80 | 0.1 | 2.0 | 1,343 | 0.012 | 5E-02 |
| AFR – multiphase ^c | 1.5–33 | 80 | 2.2 | 0.2 | 77 | 0.209 | 336 |

^a The calculations were based on Kanukuntla's (2008) design using square samples immersed in oil.

^b The calculations were based on the design proposed in the present study (noted design #3 in section 3.1.2).

^c Multiphase flow characteristics were computed with the gas-liquid two-phase flow model.

^d The calculation of the residence time was based on the oil volume contained in the respective test sections: volume of both coupon holders (FTMA); the volume of 8 samples arranged in series (FTMA NJ); the volume of samples type S (AFR – single phase); the volume of samples type M and E (AFR – multiphase flow).

^e The liquid Reynolds number is based on the superficial liquid velocity (except for the AFR – multiphase flow).

^f The friction factors were calculated using the correlations provided in section 5.2.

7.2.1 Prediction of the sulfidation corrosion rate

In this present study, the sulfidation experiments were done only at a temperature of 316 °C. Results from other experimental works concerning sulfidation in the FTMA with Kanukuntla set up or in autoclaves, and the effect of temperature on sulfidation and NAP corrosions were added to the model validation (Kanukuntla et al., 2008; Qu and Nestic, 2006). The measured corrosion rates associated to these experiments and their corresponding model predictions (plotted as trend lines) against temperature are presented in Figure 7.3.

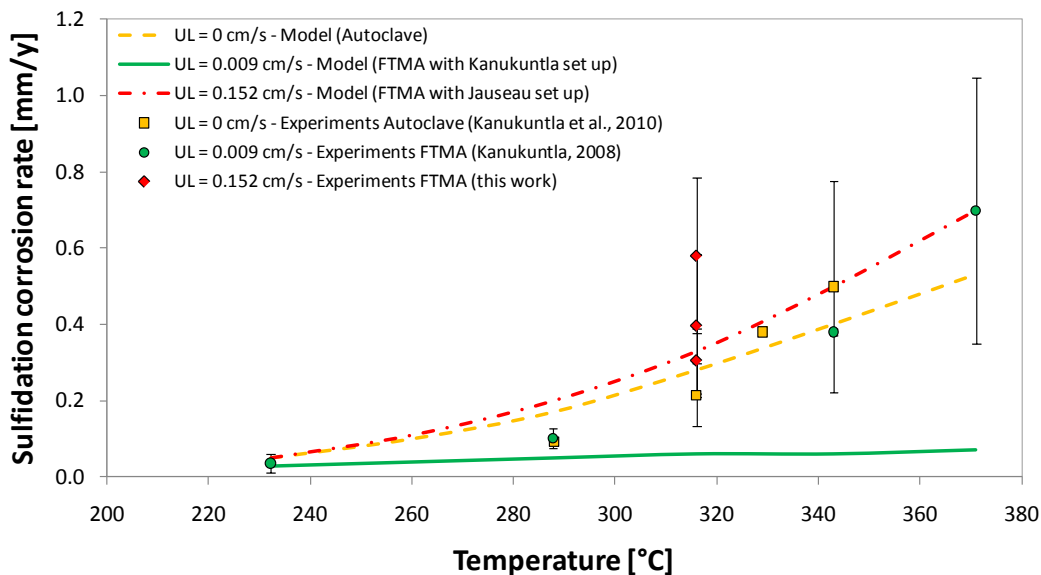


Figure 7.3: Sulfidation corrosion rates as a function of temperature. Experimental data were measured in autoclave and in the FTMA using either Kanukuntla (2008) set up or this study's set up (tubing samples).

The three corrosion rates (red dots) measured in this work come from Table 3.5. Relative to these points, the model predicted very well the corrosion rates due to

sulfidation given the low values of corrosion rates measured ($CR < 0.8$ mm/y) that are subject to uncertainty. In static conditions (autoclave), the trend and magnitude of the corrosion rates were also well predicted by the model. A slightly effect of flow on corrosion rates can be inferred from the two FTMA (the author's setup) and autoclaves simulations; this inference is supported by the higher corrosion rates measured in the former case at 316 °C (red dots).

Under the laminar flow regime ($Re \sim 5$), the corrosion rates measured in the FTMA with Kanukutla setup (green dots) increased as a function of fluid temperature. The model, however, did not predict well at these conditions suggesting that the temperature has no effect on the corrosion rate during sulfidation at temperatures greater than 280 °C. An explanation can be the physics of the flow implemented in *Crudecorp*, which assumes turbulent flow conditions. In the case of a laminar regime, very large boundary layer thicknesses would be predicted by the model. It would limit the diffusion of corrosive species to the steel surface, and therefore, considerably lower the corrosion rate of iron.

7.2.2 Prediction of the pure NAP corrosion rate

For validating the *Crudecorp* simulations for specific pure NAP corrosion conditions, the choice of the variables having an effect on NAP corrosion rate was driven by the present study. Therefore, the TAN concentration and flow velocity were chosen for the parametric study. Data recorded at similar conditions on other flow loops were also included in the validation.

7.2.2.1 Effect of TAN concentration

The corrosion rates measured at quiescent or low flow rate conditions in the liquid phase are plotted in Figure 7.4. In quiescent conditions, the model (yellow line) predicted an increase in corrosion rate when the corrosiveness of the fluid was enhanced. The diameter of the autoclave ($D = 10$ cm) was chosen as the characteristic length (hydraulic diameter) for the model inputs. For static conditions, this assumption may not be very representative, artificially increases the Reynolds number and generates friction. For this particular case, more data is necessary to strengthen the model validation. Based on the single experimental point, the model overpredicted the corrosion rate by a factor of 3 at an acidity of TAN 4.

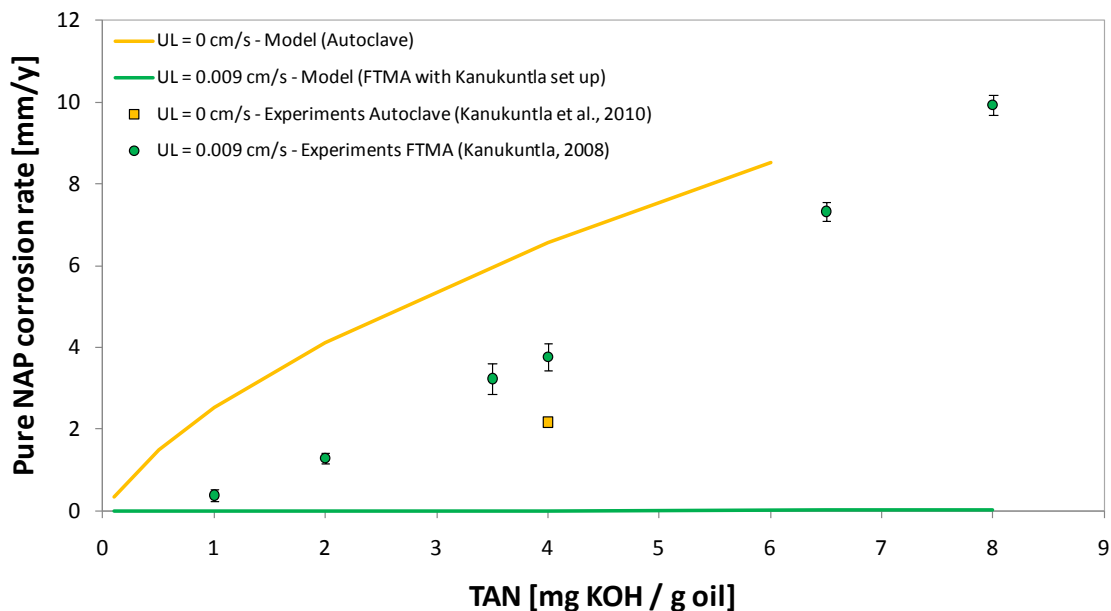


Figure 7.4: Pure NAP corrosion rates as a function of TAN concentration in autoclaves and FTMA operating conditions.

Under low flow conditions in FTMA (laminar regime), the model failed to predict the corrosion rate because, as mentioned in section 7.2.1, the model assumes a turbulent flow in the pipe. Experimentally, although the flow rate was very small, it could provide a continuous refreshment of the corrosive species at the steel surface so that the corrosion rate increased while enhancing the TAN concentration.

At higher liquid flow rates, conditions were much more aggressive with corrosion rates four times higher than those measured in the FTMA (Figure 7.5).

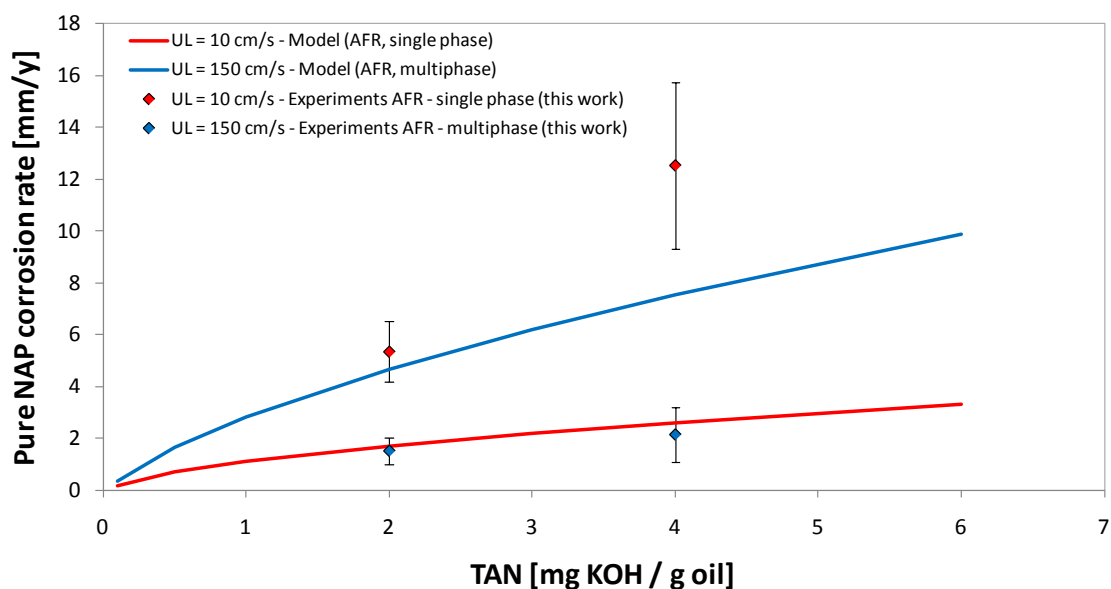


Figure 7.5: Pure NAP corrosion rates as a function of TAN concentration. Measurements were taken in the AFR in single phase and multiphase flow conditions (superficial velocities $U_{SG} = 20$ m/s; $U_{SL} = 0.1$ m/s).

The model, which accounts for flow turbulence through the velocity effect, also predicted higher corrosion rates in the AFR than in the FTMA or the autoclave. Similarly to FTMA conditions, the single phase flow conditions in the AFR were also under

laminar regime and the model underpredicted the corrosion rates by a factor of 3 to 6. Furthermore, the model was tuned with experimental data measured in the HVR, where an undesired corrosion inhibition was earlier demonstrated (section 3.5.2.5). Consequently, the corrosion inhibition introduced the systematic error in the model prediction, which would tend to lower the corrosion rate prediction as well.

In multiphase flow conditions, the model overpredicted the corrosion rate by a factor of 2 to 3 (Figure 7.5). One explanation can be that this trend can be attributed to the high velocity values specified as inputs in the corrosion simulator. The velocity feeding the model was not the superficial liquid velocity U_{SL} , usually measured in single phase flow, but the in situ liquid velocity U_L , calculated by the flow model (section 5.6.3). In multiphase flow conditions, U_L could be larger than U_{SL} by an order of magnitude. Therefore, the model, by using U_L instead of U_{SL} , would account for some of the multiphase flow effects (i.e., phase slippage), which can increase the liquid velocity under high gas flow conditions. A higher liquid velocity at the steel surface would simultaneously lead to an increase in shear stress, mass transfer, and therefore, corrosion rate.

7.2.2.2 Effect of velocity

The effect of flow velocity on NAP corrosion was also tested during the validation of Crudecorp simulation. To account for multiphase flow effects, the corrosion rates were plotted as a function of the in situ liquid (oil) velocity (Figure 7.6).

The in situ oil velocity was calculated with the flow model based on a liquid flow rate of 80 mL/min. The change in oil velocity was due to the phase slippage since the experimental tests were run at different gas flow rates. Contrary to single phase flow conditions (given at $U_L = 0.1$ m/s), the corrosion rate exhibited a decreasing trend as the velocity was increased. However, the corrosion model does not include any physics related to the oil wetting of the steel surface. A smaller wetted wall fraction may contribute to a decrease in corrosion rate since less oil contained naphthenic acids come in direct contact with the steel surface of the sample. Therefore, for multiphase flow cases, the model predicted similar corrosion rates to single phase flow because it does not account for multiphase flow effects.

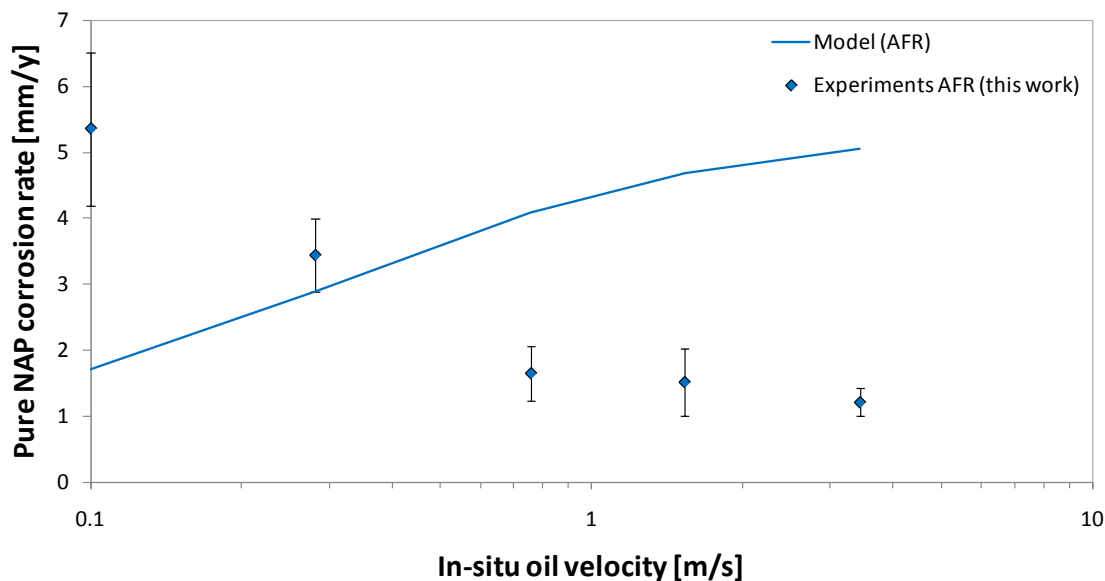


Figure 7.6: Pure NAP corrosion rates expressed as a function of the in situ oil velocity. Experiments were performed in the AFR with a liquid flow rate $Q_L = 80$ mL/min. The corrosion rate corresponding to the in situ velocity $U_L = 0.1$ m/s represents single phase flow conditions.

CHAPTER 8 CONCLUSIONS AND RECOMMENDATIONS

Overall, this project achieved its research goal and objectives. Consisting of both experimental and modeling works, this research produced results that can inform the fields of internal corrosion and multiphase flow in oil refineries. A technical challenge was to reproduce the operating conditions in the transfer lines of oil refineries, such as hydrodynamics (single and multiphase flows) and chemistry (naphthenic acids, sulfurs) at high temperature. The flow conditions were achieved in a large-scale flow rig, which was entirely designed and built in this study; the high temperature corrosive medium was simulated in a small-scale flow loop, also revamped during this research. The flow model designed from “scratch” to predict the flow patterns transitions and characteristics for similar conditions used in the experimental flow study, was satisfactory built and validated. The mechanistic understanding of the flow pattern and its characteristics in a large pipe guided the investigation of the flow effect on corrosion rate in a smaller pipe.

The main goal of this research project was to contribute to the understanding of corrosion processes occurring in transfer lines of oil refineries by studying the multiphase flow effect on naphthenic acid corrosion of carbon steel at high temperature and gas velocity. The general objectives covered two experimental studies and one modeling study. The experimental study focused on two main objectives: (1) the characterization of a gas-liquid two-phase flow in a straight pipe section using “cold flow” conditions and (2) the assessment of the naphthenic acid corrosiveness on carbon steel at high temperature, conditions similar to those encountered in crude distillation units.

A new lab flow system (CFR) was especially designed and built for studying the hydrodynamics of an air-water two-phase flow using low liquid loading conditions, similar to those from transfer lines. The stratified-wavy and annular flow patterns were observed in a 0.154 m inner diameter flow rig, with a dominant flow pattern featuring a stratified-wavy interface with liquid droplets transported in the gas phase. The associated transition between the stratified and annular flow regimes was driven by a mechanism of droplets entrainment-deposition at the wall of the pipe, able to promote droplets impingement on the pipe wall. Since naphthenic acid corrosion mainly occurs in the presence of a liquid phase in contact with the internal wall of the pipe, a particular attention was given to the distribution of both liquid and gas phases in the pipe by measuring the flow characteristics, such as the wetted wall fraction, the liquid height at the bottom of the pipe and the entrainment fraction.

A novel aspect of the corrosion study lay in the design of the AFR test sections, which are the actual piping of the flow loop and in direct contact with a corrosive gas-oil mixture flowing at high velocity. Furthermore, the experimental procedures developed in this study included the use of presulfided samples, accounting for the chemical activity of sulfur compounds usually present in refining media.

The experimental results confirmed that, in the absence of an iron sulfide scale at the metal surface and at increasing TAN concentration and/or temperature, the corrosivity of naphthenic acids on carbon steel accelerated in single phase flow conditions. In multiphase flow conditions, NAP corrosion displayed a very different and unexpected behavior since the measured corrosion rates were either equal to or lower than those

measured in single phase flow conditions. The TAN concentration, the geometry of the piping, and the pretreatment of the metal samples by presulfidation showed no or little effect on the corrosion rate.

The superficial phase velocities differently influenced the NAP corrosion. The corollary of the superficial velocities, the oil wetted wall fraction, was found to be the key parameter controlling NAP corrosion in multiphase flow. An increase in the corrosion rate coincided with an increase in the liquid volume fraction for a superficial gas velocity below 10 m/s; beyond this critical value, the corrosion rate did not significantly vary.

The gas-liquid two-phase flow model supported these findings by predicting a change in the flow pattern in the region where the critical superficial velocity was found. At these high gas velocities, the liquid phase was mainly transported as a mist in the gas core, which limited the contact of the corrosive species with the steel surface and, therefore, decelerated the NAP corrosion process. At lower gas velocities (below the critical value), the change in the predicted flow pattern led to a transitional intermittent/annular flow regime. In this flow regime, the presence of a more continuous liquid film at the steel surface helped to increase the wetted wall fraction, and thus, enhanced NAP corrosion. The use of flow modeling also helped to disregard the shear stress as a major contributing factor to NAP corrosion. Multiphase flow conditions, where higher liquid-wall shear stresses were generated due to a phase slippage, exhibited less corrosive conditions than those in single phase flow.

The set up of the AFR flow loop (recycling) and the operating (flow) conditions used during the experimental work also emphasized the presence of two concurrent physicochemical processes controlling the NAP corrosion. One mechanism inhibited the NAP corrosion due to the presence of corrosion by-products in the liquid stream, while another mechanism (the fluid flow) promoted the NAP corrosion by enhancing the mass transfer near the surface.

Data obtained with the two experimental studies served to develop and/or validate flow and corrosion models. For instance, the measured corrosion rates helped to evaluate the refining corrosion simulator Crudecorp V5 and to identify its potential limitations. Overall, the model predictions agreed well with the experimental data measured in single phase flow, although the physics of the model, assuming a turbulent flow regime, was not adapted for predicting corrosion rates in a laminar fluid flow. In multiphase flow conditions, the trend of predictions relative to the measured corrosion rates suggested that the model does not account for flow characteristics, such as the phase slippage or wetted wall fraction.

A steady state point model was developed to predict the transitions and flow patterns of a gas-liquid two-phase flow occurring in a straight pipe section. Special attention was given to the transition predicting the entrainment onset of liquid droplets in the gas phase. Once the flow model (FLOPAT) determined which flow pattern occurred at given conditions, separate (sub)models were built for each flow pattern (stratified, annular, intermittent, bubble) to predict their respective flow characteristics. The good overall accuracy of the gas-liquid two-phase flow model (absolute average error less than

35%) was evaluated by individually validating the flow pattern characteristics for each predicted flow pattern against a database of 8263 experimental points including data generated during the hydrodynamics study (CHAPTER 4). The main flow characteristics analyzed along with their accuracy were: the wetted wall fraction ($\pm 14.3\%$), the liquid holdup ($\pm 19.8\%$) and the pressure drop ($\pm 34.4\%$). The validation demonstrated a reliable mechanistic understanding of flow patterns and their characteristics that is not only complementary to the corrosion study of this research, but also is a valuable asset whose features have been implemented into an integrated multiphase flow engine available in the corrosion simulators Multicorp V5 and Topcorp V5, both developed in the Institute for Corrosion and Multiphase Technology.

In a broader context, the present research, in which both experimental methods and modeling tools were developed, supports the development of a more reliable refining corrosion simulator as a final research product beyond this dissertation. The author foresees further publication of this work (NAP corrosion and multiphase flow modeling) in peer reviewed journals and offers some recommendations for future research that could continue to broaden the understanding of issues related to this research topic.

The validation addressed the limitations of the corrosion model to handle multiphase flow systems, particularly because this model was developed and tuned with data measured from a single liquid phase. Therefore, some work would be required to fill this gap; the fluid flow effects, such as the phase slippage, oil wall wetting, liquid load at low flow rate conditions (since it favors the NAP corrosion inhibition) could be considered as starting points for future development of Crudecorp.

Regarding the gas-liquid two-phase model, further developments are recommended, such as the modeling of the slug flow in downward flows by the addition of new closure relationships and the elimination of discontinuities at flow pattern transition boundaries (i.e., slug to annular, bubble to slug). Furthermore, the model was initially developed for low pressure systems, as the transfer lines of oil refineries, and its reliability for upstream applications, such as transportation pipelines, cannot be always guaranteed. Development of other capabilities that would better predict the multiphase flow in high pressure systems can be anticipated since the industry goes towards higher temperature and pressure conditions to produce oil and gas. As an example, the giant deepwater field in Campos Basin (Brazil), with variable CO₂ contents, illustrates an application of corrosion modeling to high pressure environments (Henriques et al., 2012).

The improvement of the models can be achieved with good quality data. In general, the results from the flow model validation support the need to improve some of the instrumentation used in the CFR. The measurements of the liquid height at the bottom of the pipe were consistently underestimated by the model and differed from other data at similar operating conditions (i.e., lower values). In this case, upgrading the conductivity probes to measure the liquid film thickness at the internal wall of the pipe would allow more accurate measurements. Poor results were obtained when measuring the entrainment fraction; a liquid film extractor or an isokinetic probe are recognized tools and would be better for measuring the fraction of droplets entrained by the gas phase (Magrini et al., 2010; Mantilla et al., 2009a).

The AFR, redesigned and repeatedly tested during this research, shows a great potential in evaluating the corrosiveness of naphthenic acids in multiphase flow at high velocity. The experimental design presented in this study can be further extended. If the effect of superficial gas velocity was investigated over the whole range of velocities, the superficial liquid velocities $U_{SL} = [0.1 - 0.2]$ m/s used in this study represented only the upper boundary of low liquid loadings. Therefore, exploring lower ranges, such as $U_{SL} = [0.02 - 0.1]$ m/s, at low superficial gas velocities ($U_{SG} < 10$ m/s) is strongly recommended in order to refine the understanding of the effect on NAP corrosion in the transfer lines of oil refineries.

According to the field experience and published failure reports in refining processes, higher corrosion rates are usually located in the bends of transfer lines. However, in multiphase flow conditions, the corrosion rates from the present study did not confirm a difference between straight pipe sections and 90° elbows. At this stage, two hypotheses could be proposed to explain this field-based observation.

One hypothesis can be that the iron sulfide scale generated during the sulfidation process is not sufficiently adherent to resist high flow conditions in straight sections, making NAP corrosion as aggressive in straight sections as it is in 90° elbows. In this case, a lower operating temperature during the sulfidation process or the use of potentially less aggressive fractions that can confer superior scale retention is recommended to build a more coherent and protective FeS corrosion product layer.

Another opposing hypothesis would assume that the FeS scale resists NAP corrosion equally likely in straight and elbow sections because of a smaller droplets size

distribution existing in small-scale pipes. Since the drop size usually increases as a function of the pipe diameter, larger droplets could be entrained and hit the pipe wall in larger diameter pipes, possibly leading to a more aggressive erosion-corrosion. Since the flow effects were shown to be significant in multiphase flow conditions, this assumption may also be plausible. However, doubling the diameter would be an important technical challenge since the redesign of heating devices would be required to maintain the same superficial velocities in larger pipes.

REFERENCES

- (1) Abdul-Majeed, G. H. Liquid Holdup in Horizontal Two-Phase Gas-Liquid Flow. *J. Pet. Sci. Eng.* **1996**, *15*, 271-280.
- (2) Agrawal, S. S.; Gregory, G. A.; Govier, G. W. An Analysis of Horizontal Stratified Two Phase Flow in Pipes. *Can. J. Chem. Eng.* **1973**, *51*, 280-286.
- (3) Al-Safran, E. Probabilistic Modeling of Slug Frequency in Gas/Liquid Pipe Flow using Poisson Probability Theory. *Proceedings of The 8th North American Conference on Multiphase Technology*, BHR Group: Cranfield, UK, 2012.
- (4) Al-Sarkhi, A.; Hanratty, T. J. Effect of Pipe Diameter on the Drop Size in a Horizontal Annular Gas-Liquid Flow. *Int. J. Multiphase Flow* **2002**, *28*, 1617-1629.
- (5) Al-Sarkhi, A.; Sarica, C.; Magrini, K. L. Inclination Effects on Wave Characteristics in Annular Gas-Liquid Flows. *AIChE J.* **2012**, *58*, 1018-1029.
- (6) Altgelt, K. H.; Boduszynski, M. M. Composition of Heavy Petroleums. 3. an Improved Boiling Point-Molecular Weight Relation. *Energy Fuels* **1992**, *6*, 68-72.
- (7) Alves, I. N.; Caetano, E. F.; Minami, K.; Shoham, O. Modeling Annular Flow Behavior for Gas Wells. *SPE Prod. Eng.* **1991**, *6*, 435-440.
- (8) Ambrosini, W.; Andreussi, P.; Azzopardi, B. J. A Physically Based Correlation for Drop Size in Annular-Flow. *Int. J. Multiphase Flow* **1991**, *17*, 497-507.
- (9) Andritsos, N. Effect of Pipe Diameter and Liquid Viscosity on Horizontal Stratified Flow. Ph.D. Dissertation, University of Illinois, Urbana-Champaign, IL, 1986.
- (10) Andritsos, N.; Hanratty, T. J. Influence of Interfacial Waves in Stratified Gas-Liquid Flows. *AIChE J.* **1987**, *33*, 444-454.
- (11) Ansari, A.; Sylvester, N.; Sarica, C.; Shoham, O.; Brill, J. P. A Comprehensive Mechanistic Model for Upward Two-Phase Flow in Wellbores. *SPE Prod. Fac.* **1994**, *9*, 143-152.
- (12) Asali, J. C.; Hanratty, T. J.; Andreussi, P. Interfacial Drag and Film Height for Vertical Annular Flow. *AIChE J.* **1985**, *31*, 895-902.
- (13) ASTM International. ASTM D5705 - 12 Standard Test Method for Measurement of Hydrogen Sulfide in the Vapor Phase Above Residual Fuel Oils. <http://www.astm.org/Standards/D5705.htm> (accessed September 6, 2012).

- (14) ASTM International. ASTM D974: Standard Test Method for Acid Number and Base Number by Color-Indicator Titration. <http://www.astm.org/Standards/D974.htm> (accessed July 17, 2012).
- (15) ASTM International. ASTM D664: 11a Standard Test Method for Acid Number of Petroleum Products by Potentiometric Titration. <http://www.astm.org/Standards/D664.htm> (accessed July 17, 2012).
- (16) ASTM International. ASTM G1-03: Standard Practice for Preparing, Cleaning, and Evaluating Corrosion Test Specimens. <http://www.astm.org/Standards/G1.htm> (accessed July 17, 2012).
- (17) ASTM International. ASTM D2887-08: Standard Test Method for Boiling Range Distribution of Petroleum Fractions by Gas Chromatography. <http://www.astm.org/Standards/D2887.htm> (accessed October 7, 2012).
- (18) Babaian-Kibala, E.; Craig Jr., H. L.; Rusk, G. L.; Blanchard, K. V.; Rose, T.; Uehlein, B. L.; Quinter, R.; Summers, M. A. Naphthenic Acid Corrosion in Refinery Settings. *Mater. Perform.* **1993**, *32*, 50-55.
- (19) Babaian-Kibala, E.; Petersen, P. R.; Humphries, M. J. Corrosion by Naphthenic Acids in Crude Oils. *Proceedings of The 215th National Meeting American Chemical Society*, American Chemical Society: Washington, DC, 1998.
- (20) Baik, S.; Hanratty, T. J. Effects of a Drag Reducing Polymer on Stratified Gas-Liquid Flow in a Large Diameter Horizontal Pipe. *Int. J. Multiphase Flow* **2003**, *29*, 1749-1757.
- (21) Baker, A.; Nielsen, K.; Gabb, A. Pressure Loss, Liquid Holdup Calculations Developed. *Oil Gas J.* **1988**, *86*, 55-59.
- (22) Barnea, D. A Unified Model for Predicting Flow-Pattern Transitions for the Whole Range of Pipe Inclinations. *Int. J. Multiphase Flow* **1987**, *13*, 1-12.
- (23) Barnea, D. Transition from Annular Flow and from Dispersed Bubble Flow – Unified Models for the Whole Range of Pipe Inclinations. *Int. J. Multiphase Flow* **1986**, *12*, 733-744.
- (24) Barnea, D.; Shoham, O.; Taitel, Y. Flow Pattern Transition for Downward Inclined Two Phase Flow - Horizontal to Vertical. *Chem. Eng. Sci.* **1982a**, *37*, 735-740.
- (25) Barnea, D.; Shoham, O.; Taitel, Y. Flow Pattern Transition for Vertical Downward Two Phase Flow. *Chem. Eng. Sci.* **1982b**, *37*, 741-744.

- (26) Barnea, D.; Shoham, O.; Taitel, Y.; Dukler, A. E. Gas-Liquid Flow in Inclined Tubes: Flow Pattern Transitions for Upward Flow. *Chem. Eng. Sci.* **1985**, *40*, 131-136.
- (27) Barrow, M. P.; McDonnell, L. A.; Feng, X.; Walker, J.; Derrick, P. J. Determination of the Nature of Naphthenic Acids Present in Crude Oils using Nanospray Fourier Transform Ion Cyclotron Resonance Mass Spectrometry: The Continued Battle Against Corrosion. *Anal. Chem.* **2003**, *75*, 860-866.
- (28) Beggs, H. D. An Experimental Study of Two-Phase Flow in Inclined Pipes. Ph.D. Dissertation, University of Tulsa, Tulsa, OK, 1972.
- (29) Beggs, H. D.; Brill, J. P. A Study of Two-Phase Flow in Inclined Pipes. *J. Pet. Technol.* **1973**, *25*, 607-617.
- (30) Bendiksen, K. H.; Malnes, D.; Moe, R.; Nuland, S. Dynamic Two-Fluid Model OLGA. Theory and Application. *SPE Prod. Eng.* **1991**, *6*, 171-180.
- (31) Blanco F., E.; Hopkinson, B. E. Experience with Naphthenic Acid Corrosion in Refinery Distillation Process Units. *Proceedings of The NACE International Corrosion Conference and Expo*, NACE International: Houston, TX, 1983; No. 99.
- (32) Blum, S., Clinton, NJ. Personal communication, 2011.
- (33) Bonnecaze, R. H.; Erskine Jr, W.; Greskovich, E. J. Holdup and Pressure Drop for Two-Phase Slug Flow in Inclined Pipelines. *AIChE J.* **1971**, *17*, 1109-1113.
- (34) Bota, G. M. Ohio University, Athens, OH. Personal communication, 2010a.
- (35) Bota, G. M. Corrosion of Steel at High Temperature in Naphthenic Acid and Sulfur Containing Crude Oil Fractions. Ph.D. Dissertation, Ohio University, Athens, OH, 2010b.
- (36) Bota, G. M.; Qu, D. R.; Nestic, S.; Wolf, H. A. Naphthenic Acid Corrosion of Mild Steel in the Presence of Sulfide Scales Formed in Crude Oil Fractions at High Temperature. *Proceedings of The NACE International Corrosion Conference and Expo*, NACE International: Houston, TX, 2010; No. 10353.
- (37) Brauner, N. The Prediction of Dispersed Flows Boundaries in Liquid-Liquid and Gas-Liquid Systems. *Int. J. Multiphase Flow* **2001**, *27*, 885-910.
- (38) Brill, J. P.; Mukherjee, H. *Multiphase Flow in Wells*, Monograph Series 17; SPE: Richardson, TX, 1999.

- (39) Caetano, E. F. Upward Vertical Two-Phase Flow through an Annulus. Ph.D. Dissertation, University of Tulsa, Tulsa, OK, 1985.
- (40) Caetano, E. F.; Shoham, O.; Brill, J. P. Upward Vertical 2-Phase Flow through an Annulus. 1. Single-Phase Friction Factor, Taylor Bubble Rise Velocity, and Flow Pattern Prediction. *J. Ener. Res. Tech. Trans. ASME* **1992a**, *114*, 1-13.
- (41) Caetano, E. F.; Shoham, O.; Brill, J. P. Upward Vertical 2-Phase Flow through an Annulus. 2. Modeling Bubble, Slug, and Annular-Flow. *J. Ener. Res. Tech. Trans. ASME* **1992b**, *114*, 14-30.
- (42) Canto, C. Effect of Wall Shear Stress on Corrosion Inhibitors Film Performance. Ph.D. Dissertation, Ohio University, Athens, OH, to be published.
- (43) Chambers, B. D.; Srinivasan, S.; Kane, R. D.; Blades, M. A. An Experimental Method for Evaluation of Crude Corrosivity - Naphthenic Acid and Sulfidic Corrosion of Oil Fractions. *Proceedings of The NACE International Corrosion Conference and Expo*, NACE International: Houston, TX, 2012; No. 2012-1564.
- (44) Chen, X. T.; Cai, X. D.; Brill, J. P. Gas-Liquid Stratified-Wavy Flow in Horizontal Pipelines. *J. Ener. Res. Tech. Trans. ASME* **1997**, *119*, 209-216.
- (45) Chokshi, R. N.; Schmidt, Z.; Doty, D. R. Experimental Study and the Development of a Mechanistic Model for Two-Phase Flow through Vertical Tubing. *Proceedings of The 66th Annual Western Regional Meeting of the Society of Petroleum Engineers*, SPE: Richardson, TX, 1996; SPE 35676-MS.
- (46) Cioncolini, A.; Thome, J. R. Prediction of the Entrained Liquid Fraction in Vertical Annular Gas-Liquid Two-Phase Flow. *Int. J. Multiphase Flow* **2010**, *36*, 293-302.
- (47) CITGO Petroleum Corp. Chemical and Physical Properties of the Tufflo® Process Oil 6056. http://www.docs.citgo.com/msds_pi/10116.pdf (accessed January 7, 2012).
- (48) CITGO Petroleum Corp. Material Safety Data Sheet of the Tufflo® Process Oil 6056. http://www.docs.citgo.com/msds_pi/669376001.pdf (accessed January 7, 2012).
- (49) Clemente, J. S.; Fedorak, P. M. A Review of the Occurrence, Analyses, Toxicity, and Biodegradation of Naphthenic Acids. *Chemosphere* **2005**, *60*, 585-600.
- (50) Colfax Corp. Technical Specifications of the Zenith Pump. <http://www.zenithpumps.com/9000-series-pumps> (accessed January 7, 2012).

- (51) Craig Jr., H. L. Temperature and Velocity Effects in Naphthenic Acid Corrosion. *Proceedings of The NACE International Corrosion Conference and Expo*, NACE International: Houston, TX, 1996; No. 603.
- (52) Craig Jr., H. L. Naphthenic Acid Corrosion in the Refinery. *Proceedings of The NACE International Corrosion Conference and Expo*, NACE International: Houston, TX, 1995; No. 333.
- (53) Dallman, J. C. Investigation of Separated Flow Model in Annular Gas-Liquid Two-Phase Flows. Ph.D. Dissertation, University of Illinois, Urbana-Champaign, IL, 1978.
- (54) Derungs, W. A. Naphthenic Acid Corrosion - Old Enemy of Petroleum Industry. *Corros.* **1956**, *12*, 41-46.
- (55) Dettman, H. D.; Li, N.; Luo, J. Refinery Corrosion, Organic Acid Structure, and Athabasca Bitumen. *Proceedings of The NACE International Corrosion Conference and Expo*, NACE International: Houston, TX, 2009; No. 09336.
- (56) Dettman, H. D.; Li, N.; Wickramasinghe, D.; Xu, Z.; Chen, X. N.; Elliott, G. R. D.; Luo, J. The Influence of Naphthenic Acid and Sulfur Compound Structure on Global Crude Corrosively Under Vacuum Distillation Conditions. *Proceedings of The NACE International Corrosion Conference and Expo*, NACE International: Houston, TX, 2012; No. C2012-1326.
- (57) Drew, T. B.; Koo, E. C.; McAdams, W. H. The Friction Factor for Clean Round Pipes. *Trans. AIChE* **1932**, *28*, 56-72.
- (58) Dukler, A. E.; Hubbard, M. G. A Model for Gas-Liquid Slug Flow in Horizontal and Near Horizontal Tubes. *Ind. Eng. Chem. Fund.* **1975**, *14*, 337-347.
- (59) Duns, J., H.; Ros, N. C. J. Vertical Flow of Gas and Liquid Mixtures in Wells. *Proceedings of The 6th World Petroleum Congress on Drilling and Production*, World Petroleum Congress: London, UK, 1963.
- (60) Dzidic, I.; Somerville, A. C.; Raia, J. C.; Hart, H. V. Determination of Naphthenic Acids in California Crudes and Refinery Wastewaters by Fluoride Ion Chemical Ionization Mass Spectrometry. *Anal. Chem.* **1988**, *60*, 1318-1323.
- (61) Efird, K. D. Flow Accelerated Corrosion Testing Basics. *Proceedings of The NACE International Corrosion Conference and Expo*, NACE International: Houston, TX, 2006; No. 06689.

- (62) Efird, K. D.; Wright, E. J.; Boros, J. A.; Hailey, T. G. Correlation of Steel Corrosion in Pipe Flow with Jet Impingement and Rotating Cylinder Tests. *Corros.* **1993**, *49*, 992-1003.
- (63) Eldex Laboratories Inc. Eldex® ReciPro Metering Pumps Operator's Manual. <http://www.eldex.com/pdf/recipro/pumpmanual.pdf> (accessed January 17, 2012).
- (64) Fan, Y. An Investigation of Low Liquid Loading Gas-Liquid Stratified Flow in Near Horizontal Pipes. Ph.D. Dissertation, University of Tulsa, Tulsa, OK, 2005.
- (65) Fan, Y.; Wang, Q.; Zhang, H.; Danielson, T. J.; Sarica, C. A Model to Predict Liquid Holdup and Pressure Gradient of Near-Horizontal Wet-Gas Pipelines. *SPE Proj. Fac. Const.* **2007**, *2*, 1-8.
- (66) Farraro, T.; Stellina Jr., R. M. Materials of Construction for Refinery Applications. *Proceedings of The NACE International Corrosion Conference and Expo*, NACE International: Houston, TX, 1996; No. 614.
- (67) Felizola, H. Slug Flow in Extended Reach Directional Wells. MS Thesis, University of Tulsa, Tulsa, OK, 1992.
- (68) Gabetta, G.; Mancini, N.; Montanari, L.; Oddo, G. Preliminary Results of a Project on Crude Oil Corrosion. *Proceedings of The NACE International Corrosion Conference and Expo*, NACE International: Houston, TX, 2003; No. 03644.
- (69) Gallo, G.; Edmondson, J. The Effect of Molybdenum on Stainless Steels and Naphthenic Acid Corrosion Resistance. *Proceedings of The NACE International Corrosion Conference and Expo*, NACE International: Houston, TX, 2008; No. 08555.
- (70) Gomez, L. E.; Shoham, O.; Schmidt, Z.; Chokshi, R. N.; Northug, T. Unified Mechanistic Model for Steady-State Two-Phase Flow: Horizontal to Vertical Upward Flow. *Proceedings of The SPE Annual Technical Conference and Exhibition*, Society of Petroleum Engineers: Richardson, TX, 1999; SPE 56520.
- (71) Gomez, L. E.; Shoham, O.; Taitel, Y. Prediction of Slug Liquid Holdup: Horizontal to Upward Vertical Flow. *Int. J. Multiphase Flow* **2000**, *26*, 517-521.
- (72) Govier, G. W.; Aziz, K. *The Flow of Complex Mixtures in Pipes*; 2nd ed.; SPE: Richardson, TX, 2008.
- (73) Govier, G. W.; Omer, M. M. The Horizontal Pipeline Flow of Air-Water Mixtures. *Can. J. Chem. Eng.* **1962**, *40*, 93-104.

- (74) Grolman, E.; Fortuin, J. M. H. Gas-Liquid Flow in Slightly Inclined Pipes. *Chem. Eng. Sci.* **1997**, *52*, 4461-4471.
- (75) Groysman, A.; Brodsky, N.; Penner, J.; Goldis, A.; Savchenko, N. Study of Corrosiveness of Acidic Crude Oil and its Fractions. *Proceedings of The NACE International Corrosion Conference and Expo*, NACE International: Houston, TX, 2005; No. 05568.
- (76) Groysman, A.; Brodsky, N.; Penner, J.; Shmulevich, D. Low Temperature Naphthenic Acid Corrosion Study. *Proceedings of The NACE International Corrosion Conference and Expo*, NACE International: Houston, TX, 2007; No. 07569.
- (77) Gutzeit, J. Naphthenic Acid Corrosion in Oil Refineries. *Mater. Perform.* **1977**, *16*, 24-35.
- (78) Han, H.; Gabriel, K. S. A Numerical Study of Entrainment Mechanism in Axisymmetric Annular Gas-Liquid Flow. *J. Fluids Eng. Trans. ASME* **2007**, *129*, 293-301.
- (79) Han, J. Galvanic Mechanism of Localized Corrosion for Mild Steel in Carbon Dioxide Environments. Ph.D. Dissertation, Ohio University, Athens, OH, 2009.
- (80) Harmathy, T. Z. Velocity of Large Drops and Bubbles in Media of Infinite Or Restricted Extent. *AIChE J.* **1960**, *6*, 281-288.
- (81) Harrell, B. G.; Babic-Samardzija, K.; Sandu, C. L.; Zetlmeisl, M. J. Naphthenic Acid Corrosion: The Effect of Phosphorus and Non-Phosphorus Inhibitors on Carbon Steel Surfaces. *Proceedings of The NACE International Corrosion Conference and Expo*, NACE International: Houston, TX, 2009; No. 09344.
- (82) Hart, J.; Hamersma, P. J.; Fortuin, J. M. H. Correlations Predicting Frictional Pressure-Drop and Liquid Holdup during Horizontal Gas-Liquid Pipe-Flow with a Small Liquid Holdup. *Int. J. Multiphase Flow* **1989**, *15*, 947-964.
- (83) Hau, J. L. Predicting Sulfidic and Naphthenic Acid Corrosion. *Corros.* **2009**, *65*, 831-844.
- (84) Hau, J. L.; Yopez, O.; Specht, M. I.; Lorenzo, R. The Iron Powder Test for Naphthenic Acid Corrosion Studies. *Proceedings of The NACE International Corrosion Conference and Expo*, NACE International: Houston, TX, 1999; No. 379.
- (85) Heitz, E. Chemo-Mechanical Effects of Flow on Corrosion. *Corros.* **1991**, *47*, 135-145.

- (86) Henriques, C. C. D.; Joia, C. J. B. M.; Baptista, I. P.; Guedes, F. M. F. Material Selection for Brazilian Presalt Fields. *Proceedings of The Offshore Technology Conference*, Society of Petroleum Engineers: Richardson, TX, 2012; 23320-MS.
- (87) Henstock, W. H.; Hanratty, T. J. Interfacial Drag and Height of Wall Layer in Annular Flows. *AIChE J.* **1976**, *22*, 990-1000.
- (88) Hewitt, G. F.; Hall-Taylor, N. S. *Annular Two-Phase Flow*; 1st ed.; Pergamon Press: Oxford, UK, 1970.
- (89) Hewitt, G. F.; Owen, D. G. Experimental Data Set #1: Pressure Drop and Entrained Fraction in Fully Developed Flow. *Multiphase Sci. Tech.* **1987**, *3*, 145-154.
- (90) Hopkinson, B. E.; Penuela, L. E. Naphthenic Acid Corrosion by Venezuelan Crudes. *Proceedings of The NACE International Corrosion Conference and Expo*, NACE International: Houston, TX, 1997; No. 502.
- (91) Hsu, C. S.; Dechert, G. J.; Robbins, W. K.; Fukuda, E. K. Naphthenic Acids in Crude Oils Characterized by Mass Spectrometry. *Energy Fuels* **2000**, *14*, 217-223.
- (92) Huang, J. Pure NAP Corrosion Experiments in FTMA. *Proceedings of The NACE International Corrosion Conference and Expo*, NACE International: Houston, TX, 2008; Poster.
- (93) Hughmark, G. A. Film Thickness, Entrainment, and Pressure Drop in Upward Annular and Dispersed Flow. *AIChE J.* **1973**, *19*, 1062-1065.
- (94) Imperial Oil. Chemical and Physical Properties of the Oil Americas Core 600. http://www.imperialoil.ca/Canada-English/Files/Products_Lubes/IOCAENBSKESAmericas_core.pdf (accessed January 7, 2012).
- (95) Ishii, M.; Grolmes, M. A. Inception Criteria for Droplet Entrainment in Two-Phase Concurrent Film Flow. *AIChE J.* **1975**, *21*, 308-318.
- (96) Jasper, J. J. The Surface Tension of Pure Liquid Compounds. *J. Phys. Chem. Ref. Data* **1972**, *1*, 841-1009.
- (97) Jauseau, N. AFR Progress Report (Period June-December 2010). Unpublished report 2011CO-01311; Ohio University, Athens, OH, 2011.
- (98) Jauseau, N. CFR Measurements Updated for the EMRE Board Meeting. Unpublished report 2009FM-06044; Ohio University, Athens, OH, 2009.

- (99) Jayaraman, A.; Singh, H.; Lefebvre, Y. Naphthenic Acid Corrosion in Petroleum Refineries. A Review. *Revue IFP* **1986**, *41*, 265-274.
- (100) Jeffreys, H. On the Formation of Water Waves by Wind. *Proc. Royal Soc. London* **1925**, *107*, 189-206.
- (101) Jepson, W. P.; Taylor, R. E. Slug Flow and its Transitions in Large-Diameter Horizontal Pipes. *Int. J. Multiphase Flow* **1993**, *19*, 411-420.
- (102) Jin, P. Mechanism of Corrosion by Naphthenic Acids and Organo-Sulfur Compounds at High Temperatures. Ph.D. Dissertation, Ohio University, Athens, OH, to be published.
- (103) Johnson, D.; McAteer, G.; Zuk, H. The Safe Processing of High Naphthenic Acid Content Crude Oils - Refinery Experience and Mitigation Studies. *Proceedings of The NACE International Corrosion Conference and Expo*, NACE International: Houston, TX, 2003; No. 03645.
- (104) Jones, D. S. J.; Pujado, P. R. *Handbook of Petroleum Processing*; 1st ed.; Springer: Dordrecht, The Netherlands, 2006.
- (105) Kane, R. D. Corrosion: Environments and Industries. In *ASM Handbook*; Cramer, S. D., Covino, B. S., Jr., Eds.; ASM International, 2006; Vol. 13C, pp 967-1014.
- (106) Kane, R. D.; Cayard, M. S. A Comprehensive Study on Naphthenic Acid Corrosion. *Proceedings of The NACE International Corrosion Conference and Expo*, NACE International: Houston, TX, 2002; No. 02555.
- (107) Kane, R. D.; Cayard, M. S. Understanding Critical Factors that Influence Refinery Crude Corrosiveness. *Mater. Perform.* **1999**, *38*, 48-54.
- (108) Kanukuntla, V. Formation of Sulfide Scales and their Role in Naphthenic Acid Corrosion of Steels. MS Thesis, Ohio University, Athens, OH, 2008.
- (109) Kanukuntla, V.; Qu, D. R.; Nescic, S.; Wolf, H. A. Experimental Study of Concurrent Naphthenic Acid and Sulfidation Corrosion. *Proceedings of The 17th International Corrosion Congress*, NACE International: Houston, TX, 2008; No. 2764.
- (110) Kapusta, S. D.; Ooms, A.; Smith, A.; Van Den Berg, F.; Fort, W. Safe Processing of Acid Crudes. *Proceedings of The NACE International Corrosion Conference and Expo*, NACE International: Houston, TX, 2004; No. 04637.

- (111) Kataoka, I.; Ishii, M.; Mishima, K. Generation and Size Distribution of Droplet in Annular Two-Phase Flow. *J. Fluids Eng. Trans. ASME* **1983**, *105*, 230-238.
- (112) Kaya, A. S.; Sarica, C.; Brill, J. P. Mechanistic Modeling of Two-Phase Flow in Deviated Wells. *SPE Prod. Fac.* **2001**, *16*, 156-165.
- (113) Landman, M. J. Non-Unique Holdup and Pressure Drop in Two-Phase Stratified Inclined Pipe Flow. *Int. J. Multiphase Flow* **1991**, *17*, 377-394.
- (114) Laurinat, J. E. Studies of the Effect of Pipe Size on Horizontal Annular Two-Phase Flows. Ph.D. Dissertation, University of Illinois, Urbana-Champaign, IL, 1982.
- (115) Lin, P. Y.; Hanratty, T. J. Effect of Pipe Diameter on Flow Patterns for Air Water-Flow in Horizontal Pipes. *Int. J. Multiphase Flow* **1987**, *13*, 549-563.
- (116) Lywood, B. H₂S Measurement in Crude. http://www.coqa-inc.org/20120301_Lywood.pdf (accessed March 1, 2012).
- (117) Magrini, K. L. Liquid Entrainment in Annular Gas-Liquid Flow in Inclined Pipes. MS Thesis, University of Tulsa, Tulsa, OK, 2009.
- (118) Magrini, K. L.; Sarica, C.; Al-Sarkhi, A.; Zhang, H. Liquid Entrainment in Annular Gas/Liquid Flow in Inclined Pipes. *Proceedings of The SPE Annual Technical Conference and Exhibition*, Society of Petroleum Engineers: Richardson, TX, 2010; SPE 134765.
- (119) Mandhane, J. M.; Gregory, G. A.; Aziz, K. Flow Pattern Map for Gas-Liquid Flow in Horizontal Pipes. *Int. J. Multiphase Flow* **1974**, *1*, 537-553.
- (120) Mantilla, I. Mechanistic Modeling of Liquid Entrainment in Gas in Horizontal Pipes. Ph.D. Dissertation, University of Tulsa, Tulsa, OK, 2008.
- (121) Mantilla, I.; Gomez, L. E.; Mohan, R. S.; Shoham, O.; Kouba, G. E.; Roberts, R. Experimental Investigation of Liquid Entrainment in Gas in Horizontal Pipes. *Proceedings of The ASME Fluids Engineering Division Summer Conference*, American Society of Mechanical Engineers: New York, 2009a; FEDSM2009-78420.
- (122) Mantilla, I.; Gomez, L. E.; Mohan, R. S.; Shoham, O.; Kouba, G. E.; Roberts, R. Modeling of Liquid Entrainment in Gas in Horizontal Pipes. *Proceedings of The ASME Fluids Engineering Division Summer Conference*, American Society of Mechanical Engineers: New York, 2009b; FEDSM2009-78459.

- (123) McConomy, H. F. High Temperature Sulfidic Corrosion in Hydrogen Free Environment. *Proceedings of The 28th Midyear Meeting of the American Petroleum Institute*, API: Washington, DC, 1963.
- (124) McLeod, W. R.; Rhodes, D. F.; Day, J. J. Radiotracers in Gas-Liquid Transportation Problems - A Field Case. *J. Pet. Technol.* **1971**, *23*, 939-947.
- (125) Meng, W. Low Liquid Loading Gas-Liquid Two-Phase Flow in Near Horizontal Pipes. PhD. Dissertation, University of Tulsa, Tulsa, OK, 1999.
- (126) Meng, W.; Chen, X. T.; Kouba, G. E.; Sarica, C.; Brill, J. P. Experimental Study of Low-Liquid-Loading Gas-Liquid Flow in Near-Horizontal Pipes. *SPE Prod. Fac.* **2001**, *16*, 240-249.
- (127) Messer, B.; Tarleton, B.; Beaton, M.; Phillips, T. New Theory for Naphthenic Acid Corrosivity of Athabasca Oil Sands Crudes. *Proceedings of The NACE International Corrosion Conference and Expo*, NACE International: Houston, TX, 2004; No. 04634.
- (128) Minami, K. Liquid Holdup in Wet-Gas Pipelines. MS Thesis, University of Tulsa, Tulsa, OK, 1982.
- (129) Moghissi, O. C.; Norris, L.; Dusek, P. J.; Cookingham, B. Internal Corrosion Direct Assessment of Gas Transmission Pipelines. *Proceedings of The NACE International Corrosion Conference and Expo*, NACE International: Houston, TX, 2002; No. 02087.
- (130) Morrison, F. A. Data Correlation for Drag Coefficient for Sphere. <http://www.chem.mtu.edu/~fmorriso/DataCorrelationForSphereDrag2010.pdf> (accessed August 22, 2011).
- (131) Murray, D. H₂S Measurement in Crude - Project Update. http://www.coqa-inc.org/20100211_Murray_H2S_Measurement.pdf (accessed September 15, 2010).
- (132) NACE International. *Crude Distillation Unit - Distillation Tower Overhead System Corrosion*; Report 34109; NACE International: Houston, TX, 2009.
- (133) NACE International. *Overview of Sulfidic Corrosion in Petroleum Refining*; Report 34103; NACE International: Houston, TX, 2004.
- (134) Nestic, S. Ohio University, Athens, OH. Personal communication, 2012.
- (135) Nestic, S.; Qu, D. R. Crudecorp V5.0. Unpublished presentation, Advisory Board Meeting; Ohio University, Athens, OH, 2008.

- (136) Nesic, S.; Solvi, G. T.; Skjerve, S. Comparison of Rotating Cylinder and Loop Methods for Testing CO₂ Corrosion Inhibitors. *Br. Corros. J.* **1997**, *32*, 269-276.
- (137) Nugent, M. J.; Dobis, J. D. Experience with Naphthenic Acid Corrosion in Low TAN Crudes. *Proceedings of The NACE International Corrosion Conference and Expo*, NACE International: Houston, TX, 1998; No. 577.
- (138) Oliemans, R. V. A.; Pots, B. F. M.; Trompe, N. Modelling of Annular Dispersed Two-Phase Flow in Vertical Pipes. *Int. J. Multiphase Flow* **1986**, *12*, 711-732.
- (139) Omega Engineering Inc. Technical Specifications of the Rotameter Series F3000. <http://www.omega.com/Green/pdf/FLT.pdf> (accessed January 7, 2012).
- (140) Ouyang, L. B.; Aziz, K. Development of New Wall Friction Factor and Interfacial Friction Factor Correlations for Gas-Liquid Stratified Flow in Wells and Pipelines. *Proceedings of The SPE 66th Annual Western Regional Meeting*, Society of Petroleum Engineers: Richardson, TX, 1996; SPE 35679-MS.
- (141) Paleev, I. I.; Filippovich, B. S. Phenomena of Liquid Transfer in Two-Phase Dispersed Annular Flow. *International Journal of Heat and Mass Transfer* **1966**, *9*, 1089-1093.
- (142) Pan, L.; Hanratty, T. J. Correlation of Entrainment for Annular Flow in Horizontal Pipes. *Int. J. Multiphase Flow* **2002a**, *28*, 385-408.
- (143) Pan, L.; Hanratty, T. J. Correlation of Entrainment for Annular Flow in Vertical Pipes. *Int. J. Multiphase Flow* **2002b**, *28*, 363-384.
- (144) Paras, S. V.; Karabelas, A. J. Droplet Entrainment and Deposition in Horizontal Annular-Flow. *Int. J. Multiphase Flow* **1991**, *17*, 455-468.
- (145) Payne, G. A.; Palmer, C. M.; Brill, J. P.; Beggs, H. D. Evaluation of Inclined-Pipe, Two-Phase Liquid Holdup and Pressure-Loss Correlation using Experimental Data. *J. Pet. Technol.* **1979**, *31*, 1198-1208.
- (146) Perry, R. H.; Green, D. W., Eds.; In *Chemical's Engineers' Handbook*, 7th ed.; McGraw-Hill: New York, 1999, pp 9-10, 16-20.
- (147) Petalas, N.; Aziz, K. A Mechanistic Model for Multiphase Flow in Pipes. *Proceedings of The 49th Annual Technical Meeting of the Petroleum Society of the Canadian Institute of Mining, Metallurgy and Petroleum*, 1998; No. 98-39.
- (148) Piehl, R. L. Naphthenic Acid Corrosion in Crude Distillation Units. *Mater. Perform.* **1988**, *27*, 37-43.

- (149) Poulson, B. Electrochemical Measurements in Flowing Solutions. *Corros. Sci.* **1983**, *23*, 391-430.
- (150) Qian, K.; Edwards, K. E.; Dechert, G. J.; Jaffe, S. B.; Green, L. A.; Olmstead, W. N. Measurement of Total Acid Number (TAN) and TAN Boiling Point Distribution in Petroleum Products by Electrospray Ionization Mass Spectrometry. *Anal. Chem.* **2008**, *80*, 849-855.
- (151) Qu, D. R. Annular Flow Rig - New Design. Unpublished presentation; Ohio University, Athens, OH, 2008.
- (152) Qu, D. R.; Nestic, S. Autoclave Tests of Sulfidation Corrosion and Naphthenic Acid Corrosion. Unpublished report; Ohio University, Athens, OH, 2006.
- (153) Qu, D. R.; Zheng, Y. G.; Jing, H. M.; Jiang, X.; Ke, W. Erosion-Corrosion of Q235 and 5Cr1/2Mo Steels in Oil with Naphthenic Acid and/or Sulfur Compound at High Temperature. *Mater. Corros.* **2005**, *56*, 533-541.
- (154) Qu, D. R.; Zheng, Y. G.; Jing, H. M.; Yao, Z. M.; Ke, W. High Temperature Naphthenic Acid Corrosion and Sulphidic Corrosion of Q235 and 5Cr1/2Mo Steels in Synthetic Refining Media. *Corros. Sci.* **2006**, *48*, 1960-1985.
- (155) Quann, R. J.; Jaffe, S. B. Structure-Oriented Lumping. Describing the Chemistry of Complex Hydrocarbon Mixtures. *Ind. Eng. Chem. Res.* **1992**, *31*, 2483-2497.
- (156) Rebak, R. B. Sulfidic Corrosion in Refineries - A Review. *Corr. Rev.* **2011**, *29*, 123-133.
- (157) Ritter, R. B.; Lenoir, J. M.; Schweppe, J. L. Find Specific Gravities by Nomograph. *Pet. Refiner* **1958**, *37*, 225-232.
- (158) Robbins, W. K. Challenges in the Analytical Characterization of Non-Thiophenic and Thiophenic Sulfur Compounds in Petroleum. *Am. Chem. Soc. - Division Pet. Chem.* **2000**, *45*, 68-71.
- (159) Roberge, P. *Erosion-Corrosion*, Corrosion Testing Made Easy; 1st ed.; NACE International: Houston, TX, 2004.
- (160) Rogers, V. V.; Liber, K.; MacKinnon, M. D. Isolation and Characterization of Naphthenic Acids from Athabasca Oil Sands Tailings Pond Water. *Chemosphere* **2002**, *48*, 519-527.
- (161) Sawant, P.; Ishii, M.; Mori, M. Prediction of Amount of Entrained Droplets in Vertical Annular Two-Phase Flow. *Int. J. Heat Fluid Flow* **2009**, *30*, 715-728.

- (162) Scattergood, G. L.; Strong, R. C.; Lindley, W. A. Naphthenic Acid Corrosion, an Update of Controls Methods. *Proceedings of The NACE International Corrosion Conference and Expo*, NACE International: Houston, TX, 1987; No. 197.
- (163) Schmitt, G.; Gudde, T.; Strobel-Effertz, E. Fracture Mechanical Properties of CO₂ Corrosion Product Scales and their Relation to Localized Corrosion. *Proceedings of The NACE International Corrosion Conference and Expo*, NACE international: Houston, TX, 1996; No. 96009.
- (164) Schubert, A. Ohio University, Athens, OH. Personal communication, 2008.
- (165) Scott, S. L.; Shoham, O.; Brill, J. P. Prediction of Slug Length in Horizontal, Large-Diameter Pipes. *SPE Prod. Eng.* **1989**, *4*, 335-340.
- (166) Seifert, W. K. Carboxylic Acids in Petroleum and Sediments. *Prog. Chem. Org. Nat. Products* **1975**, *32*, 1-49.
- (167) Sheverev, V.; Nestic, S.; Brown, B. Direct Measurement of Shear Stress in Single- and Multiphase Flows. <http://www.lenterra.com/company/publications/> (accessed September 15, 2012).
- (168) Shoham, O. *Mechanistic Modeling of Gas-Liquid Two-Phase Flow in Pipes*; SPE: Richardson, TX, 2006.
- (169) Shoham, O. Flow Pattern Transition and Characterization in Gas- Liquid Two Phase Flow in Inclined Pipes. Ph.D. dissertation, Tel-Aviv University, Tel-Aviv, Israel, 1982.
- (170) Shoham, O.; Taitel, Y. Stratified Turbulent-Turbulent Gas-Liquid Flow in Horizontal and Inclined Pipes. *AIChE J.* **1984**, *30*, 377-385.
- (171) Silverman, D. C. The Rotating Cylinder Electrode for Examining Velocity-Sensitive Corrosion - A Review. *Corros.* **2004**, *60*, 1003-1023.
- (172) Silverman, D. C. Technical Note: Simplified Equation for Simulating Velocity-Sensitive Corrosion in the Rotating Cylinder Electrode at Higher Reynolds Numbers. *Corros.* **2003**, *59*, 207-211.
- (173) Silverman, D. C. Rotating Cylinder Electrode for Velocity Sensitivity Testing. *Corros.* **1984**, *40*, 220-226.
- (174) Singer, M., Pojtanabuntoeng, T., Kaewpradap, U., Addis, K.; Nestic, S. Top of the Line Corrosion Joint Industry Project. Experimental Results and Modeling Updates. Unpublished report; Ohio University, Athens, OH, 2009.

- (175) Singh, B.; Mutyala, S.; Puttagunta, V. R. Viscosity Range from One Test. *Hydrocarbon Process.* **1990**, *69*, 39-41.
- (176) Slavcheva, E.; Shone, B.; Turnbull, A. Review of Naphthenic Acid Corrosion in Oil Refining. *Br. Corros. J.* **1999**, *34*, 125-131.
- (177) Smart, N. R.; Rance, A. P.; Pritchard, A. M. Laboratory Investigation of Naphthenic Acid Corrosion Under Flowing Conditions. *Proceedings of The NACE International Corrosion Conference and Expo*, NACE International: Houston, TX, 2002; No. 02484.
- (178) Sun, W.; Nestic, S. A Mechanistic Model of Uniform Hydrogen Sulfide/Carbon Dioxide Corrosion of Mild Steel. *Corros.* **2009**, *65*, 291-307.
- (179) Sylvester, N. D. A Mechanistic Model for Two-Phase Vertical Slug Flow in Pipes. *J. Ener. Res. Tech. Trans. ASME* **1987**, *109*, 206-215.
- (180) Taitel, Y.; Barnea, D. A Consistent Approach for Calculating Pressure-Drop in Inclined Slug Flow. *Chem. Eng. Sci.* **1990a**, *45*, 1199-1206.
- (181) Taitel, Y.; Barnea, D. Two-Phase Slug Flow. *Adv. Heat Transfer* **1990b**, *20*, 83-132.
- (182) Taitel, Y.; Barnea, D.; Dukler, A. E. Modelling Flow Pattern Transitions for Steady Upward Gas-Liquid Flow in Vertical Tubes. *AIChE J.* **1980**, *26*, 345-354.
- (183) Taitel, Y.; Dukler, A. E. A Model for Predicting Flow Regime Transitions in Horizontal and Near Horizontal Gas-Liquid Flow. *AIChE J.* **1976**, *22*, 47-55.
- (184) Tatterson, D. F.; Dallman, J. C.; Hanratty, T. J. Drop Sizes in Annular Gas-Liquid Flows. *AIChE J.* **1977**, *23*, 68-76.
- (185) Tayebi, D.; Nuland, S.; Fuchs, P. Droplet Transport in Oil/Gas and Water/Gas Flow at High Gas Densities. *Int. J. Multiphase Flow* **2000**, *26*, 741-761.
- (186) Tebbal, S. Critical Review of Naphthenic Acid Corrosion. *Proceedings of The NACE International Corrosion Conference and Expo*, NACE International: Houston, TX, 1999; No. 380.
- (187) Tebbal, S.; Kane, R. D. Assessment of Crude Oil Corrosivity. *Proceedings of The NACE International Corrosion Conference and Expo*, NACE International: Houston, TX, 1998; No. 578.

- (188) Tebbal, S.; Kane, R. D. Assessment of the Corrosivity of Crude Fractions from Varying Feedstock. *Proceedings of The NACE International Corrosion Conference and Expo*, NACE International: Houston, TX, 1997; No. 498.
- (189) Tebbal, S.; Kane, R. D. Review of Critical Factors Affecting Crude Corrosivity. *Proceedings of The NACE International Corrosion Conference and Expo*, NACE International: Houston, TX, 1996; No. 607.
- (190) Tokyo Chemical Industry Corp. Chemical and Physical Properties of the Naphthenic Acids Solution. <http://www.tciamerica.com/catalog/N0343.html> (accessed January 7, 2012).
- (191) Turnbull, A.; Slavcheva, E.; Shone, B. Factors Controlling Naphthenic Acid Corrosion. *Corros.* **1998**, *54*, 922-930.
- (192) Van Rossum, J. J. Experimental Investigation of Horizontal Liquid Films : Wave Formation, Atomization, Film Thickness. *Chem. Eng. Sci.* **1959**, *11*, 35-52.
- (193) Vlachos, N. A.; Paras, S. V.; Karabelas, A. J. Prediction of Holdup, Axial Pressure Gradient and Wall Shear Stress in Wavy Stratified and Stratified/Atomization Gas/Liquid Flow. *Int. J. Multiphase Flow* **1999**, *25*, 365-376.
- (194) Vo, D. T.; Shoham, O. A Note on the Existence of a Solution for Two-Phase Slug Flow in Vertical Pipes. *J. Ener. Res. Tech. Trans. ASME* **1989**, *111*, 64-65.
- (195) Wallis, G. B. *One-Dimensional Two-Phase Flow*; Mc Graw-Hill: New York, 1969; pp 318-321.
- (196) Weber, J. Flow Induced Corrosion: 25 Years of Industrial Research. *Br. Corros. J.* **1992**, *27*, 193-199.
- (197) Whalley, P. B.; Hewitt, G. F. *The Correlation of Liquid Entrainment Fraction and Entrainment Rate in Annular Two-Phase Flow*; Report AERE-R9187; UKAEA, 1978.
- (198) Williams, L. R. Effect of Pipe Diameter on Horizontal Annular Two-Phase Flow. Ph.D. Dissertation, University of Illinois, Urbana-Champaign, IL, 1990.
- (199) Williams, L. R. Entrainment Measurements in a 4-Inch Horizontal Pipe. MS Thesis, University of Illinois, Urbana-Champaign, IL, 1986.
- (200) Wolf, H. A. ExxonMobil Research and Engineering, Clinton, NJ. Corrosion - Field observations, Personal communication, 2011.

- (201) Wolf, H. A. ExxonMobil Research and Engineering, Clinton, NJ. Oil samples analysis data, Personal communication, 2010a.
- (202) Wolf, H. A. ExxonMobil Research and Engineering, Clinton, NJ. Boiling points distribution of naphthenic acids, Personal communication, 2010b.
- (203) Woodmansee, D. E.; Hanratty, T. J. Mechanism for Removal of Droplets from Liquid Surface by Parallel Air Flow. *Chem. Eng. Sci.* **1969**, *24*, 299-307.
- (204) Wu, X. Q.; Jing, H. M.; Zheng, Y. G.; Yao, Z. M.; Ke, W. Erosion-Corrosion of various Oil-Refining Materials in Naphthenic Acid. *Wear* **2004a**, *256*, 133-144.
- (205) Wu, X. Q.; Jing, H. M.; Zheng, Y. G.; Yao, Z. M.; Ke, W. Resistance of Mo-Bearing Stainless Steels and Mo-Bearing Stainless-Steel Coating to Naphthenic Acid Corrosion and Erosion-Corrosion. *Corros. Sci.* **2004b**, *46*, 1013-1032.
- (206) Wu, X. Q.; Jing, H. M.; Zheng, Y. G.; Yao, Z. M.; Ke, W. Study on High-Temperature Naphthenic Acid Corrosion and Erosion-Corrosion of Aluminized Carbon Steel. *J. Mater. Sci.* **2004c**, *39*, 975-985.
- (207) Wu, X. Q.; Jing, H. M.; Zheng, Y. G.; Yao, Z. M.; Ke, W. Corrosion and Erosion-Corrosion Behaviors of Carbon Steel in Naphthenic Acid Media. *Mater. Corros.* **2002**, *53*, 833-844.
- (208) Xiao, J. J.; Shoham, O.; Brill, J. P. A Comprehensive Mechanistic Model for Two-Phase Flow in Pipelines. *Proceedings of The 65th SPE Annual Technical Conference and Exhibition*, Society of Petroleum Engineers: Richardson, TX, 1990; SPE 20631.
- (209) Xiong, Y. AFM Studies of the Metallicity of Single-Walled Carbon Nanotubes and Corrosion Inhibitor Adsorption. Ph.D. Dissertation, Ohio University, Athens, OH, 2011.
- (210) Zabararas, G. J. Prediction of Slug Frequency for Gas/Liquid Flows. *SPE J.* **2000**, *5*, 252-258.
- (211) Zhang, H.; Sarica, C. Low Liquid Loading Gas/Liquid Pipe Flow. *J. Nat. Gas Sci. Eng.* **2011**, *3*, 413-422.
- (212) Zhang, H.; Wang, Q.; Sarica, C.; Brill, J. P. Unified Model for Gas-Liquid Pipe Flow Via Slug Dynamics - Part 1: Model Development. *J. Ener. Res. Tech. Trans. ASME* **2003**, *125*, 266-273.
- (213) Zigrang, D. J.; Sylvester, N. D. A Review of Explicit Friction Factor Equations. *J. Ener. Res. Tech. Trans. ASME* **1985**, *107*, 280-283.

- (214) Zuber, N.; Findlay, J. A. Average Volumetric Concentration in Two-Phase Flow Systems. *J. Heat Transfer Trans. ASME* **1965**, *87*, 453-468.

NOMENCLATURE

Latin Symbols

- A : Pipe cross sectional area (m^2)
- C_H : Constant in the H-model (-)
- C_L : Lift coefficient ($C_L = 0.8$)
- c : Wave celerity (m/s)
- C_0 : Velocity profile distribution parameter in bubbly model ($C_0 = 1.15$)
- C_0 : Flow distribution coefficient in slug model (-)
- C_D : Drag coefficient ($C_D = 0.95$)
- C_r : Parameter used in the ripple wave shearing-off mechanism equation (m^2/s)
- C_S : Interfacial shape coefficient ($C_S = 0.77$)
- C_w : Coefficient function of the liquid viscosity number N_μ (-)
- CR : Corrosion rate (mm/y)
- d : Bubble diameter (m)
- d_{32} : Sauter diameter (m)
- d_{CB} : Critical bubble size below which migration of bubbles to the upper part of the pipe is prevented (m)
- d_{CD} : Critical bubble size over which the bubble is deformed (m)
- $d_{max,0}$: Maximal stable diameter of dispersed bubbles in a dilute dispersion (m)
- $d_{max,\varepsilon}$: Maximal stable diameter of dispersed bubbles in a dense dispersion (m)
- D : Pipe diameter or hydraulic diameter (m)

| | |
|------------|---|
| D_f | : Darcy-Weisbach friction factor ($D_f = 4f$) |
| E | : Relating to equilibrium conditions |
| e_R | : Relative error (-) |
| f | : Fanning friction factor (-) |
| F_D | : Drag force (N) |
| F_g | : Gravity force (N) |
| F_σ | : Surface tension force (N) |
| FE | : Entrained liquid droplets fraction in gas phase (-) |
| g | : Gravity constant ($g = 9.81 \text{ m/s}^2$) |
| h | : Height (m) |
| K | : Empirical constant (-) |
| L | : Length (m) |
| m | : Mass (g) |
| \dot{m} | : Mass flow rate (kg/s) |
| MW | : Molecular weight (g/mol) |
| n | : Integer (-) |
| n | : Sample size (-) |
| dP/dL | : Pressure gradient (Pa/m) |
| P | : Pressure (kPa or bar) |
| PCV | : Process control value (-) |
| Q | : Volume flow rate (m^3/s) |
| S | : Perimeter (m) |

| | |
|-----------|---|
| s | : Sheltering coefficient ($s = 0.01$ or $s = 0.06$) |
| t | : Time (s) |
| T | : Temperature ($^{\circ}C$ or K) |
| TS | : Total content of sulfur compounds ($wt\%$) |
| U | : Velocity (m/s) |
| U_0 | : Rise velocity of dispersed bubbles (m/s) |
| X | : Martinelli parameter (-) |
| Y | : Dimensionless parameter (-) |
| \bar{x} | : Sample mean (-) |
| X^* | : Froude number ratio between the liquid and gas phases (-) |

Greek Symbols

| | |
|------------------|--|
| α | : Phase fraction (-) |
| β | : Pipe inclination angle (degree) |
| β' | : Angle in Brauner's H-model (degree) |
| γ | : Bubble distortion coefficient ($\gamma = 1.3$) |
| δ | : Film thickness in annular-mist flow pattern (m) |
| $\tilde{\delta}$ | : Dimensionless factor $\tilde{\delta} = \delta/D$ (-) |
| ε | : Pipe roughness (m) |
| ε_1 | : Average relative error (%) |
| ε_2 | : Absolute average relative error (%) |
| ε_3 | : Standard deviation of relative error (%) |

| | |
|------------|--|
| λ | : Length (m) |
| μ | : Dynamic viscosity ($kg/m/s$) |
| ν | : Kinematic viscosity (m^2/s) |
| ν | : Frequency ($1/s$) |
| ξ | : Length ratio in slug flow pattern (-) |
| θ_0 | : Wetted wall fraction when the gas-liquid interface is flat (-) |
| θ_L | : Wetted wall fraction (-) |
| ρ | : Density (kg/m^3) |
| σ | : Surface tension (N/m) |
| σ | : Standard deviation of the mean (based on units of the mean) |
| τ | : Shear stress (Pa) |
| ϕ | : Constant in Wallis correlation (-) |
| ϕ | : Holdup function in stratified model LLL (-) |
| ω | : Constant used in Oliemans correlation for entrainment (-) |

Subscripts

| | |
|--------|--|
| a | : Based on average properties |
| a | : Based on real flow conditions (only in APPENDIX G) |
| air | : Based on air gas |
| C | : Relating to the gas core |
| CD | : Relating to the chord |
| $crit$ | : Relating to critical conditions |

| | |
|-------------|--|
| <i>d</i> | : Relating to droplets |
| <i>D</i> | : Based on drift properties |
| <i>E</i> | : Based on entrainment |
| <i>exp</i> | : Relating to experimental measurements |
| <i>f</i> | : Based on final conditions |
| <i>F</i> | : Relating to the liquid film |
| <i>FM</i> | : Based on the flow meter location |
| <i>G</i> | : Relating to the gas phase |
| <i>GLS</i> | : Relating to the gas phase in the slug body region |
| <i>GTB</i> | : Relating to the gas phase in the film region |
| <i>i</i> | : Relating to the gas-liquid interface |
| <i>i</i> | : Based on initial conditions |
| <i>L</i> | : Relating to the liquid |
| <i>LLS</i> | : Relating to the liquid phase in the slug body region |
| <i>LTB</i> | : Relating to the liquid phase in the film region |
| <i>LSU</i> | : Relating to the liquid slug unit |
| <i>M</i> | : Relating to the mixture |
| <i>max</i> | : Relating to maximum |
| <i>min</i> | : Relating to minimum |
| <i>NAP</i> | : Relating to naphthenic acid species |
| <i>p</i> | : Based on pipe conditions |
| <i>pred</i> | : Relating to predicted values |

| | |
|-------------|---|
| <i>pump</i> | : Based on the pump |
| <i>R</i> | : Relating to the random error (statistics) |
| <i>S</i> | : Relating to the systematic error (statistics) |
| <i>S</i> | : Relating to the slug body |
| <i>SG</i> | : Based on the superficial gas |
| <i>SL</i> | : Based on the superficial liquid |
| <i>Sulf</i> | : Relating to sulfur compounds |
| <i>t</i> | : Relating to the transitional velocity |
| <i>T</i> | : Relating to the terminal velocity |
| <i>T</i> | : Based on total values |
| <i>TB</i> | : Relating to the Taylor bubble |
| <i>TS</i> | : Based on the test section location |
| <i>U</i> | : Based on the slug unit |
| <i>w</i> | : Relating to the wave |
| <i>W</i> | : Relating to water |
| <i>WG</i> | : Relating to the wall-gas interface |
| <i>WL</i> | : Relating to the wall-liquid interface |

Superscript

| | |
|---|--|
| 0 | : Based on standard conditions ($T = 15.6\text{ }^{\circ}\text{C}$, $P = 101.3\text{ kPa}$) established by the Society of Petroleum Engineers |
|---|--|

Dimensionless numbers

Fr : Froude number (ratio inertia forces / gravity forces)

N_μ : Viscosity number

Re : Reynolds number (ratio inertia forces / viscous forces)

We : Weber number (ratio inertia forces / surface tension forces)

APPENDIX A PROCEDURE OF PROCESSING METAL SAMPLES FOR SEM/EDX
ANALYSES

Step1: The preparation of Epoxy

1. Identify the coupons using the laboratory notebook reference format “xxxx-xxx-xx” for “notebook-page-sample#”.

Example: 0053-NJ038-M3XL (NJ038 stands for test ID, M3 for sample ID, and XL/XR for radial or longitudinal cross sections).
2. Photograph the samples using digital photography and ensuring the inclusion of the sample ID in each corresponding image or make copies of notebook-page-sample-formats in which the images were placed and labeled with the sample ID and associated operating conditions.
3. Clamp the sample in a vise and cut it with the tubing cutter (do not use the electrical saw or a dremel) as close as possible to the ¼” nut. Remove both nuts from the sample. Cut again with the tubing cutter a piece of 15-20 mm long tubing section and save it for the longitudinal cross section (XL) analysis. In the end, cut a piece of 15-20 mm long tubing section with the tubing cutter and save it for the radial cross section (XR) analysis.
4. Label 1-1/4" sample cups with sample IDs and coat the interior of the cups with a mold release liquid. Allow to dry before placing the samples in the cups.
 - a. XL samples: use a sample clip to indicate the orientation of the sample (top vs. bottom) and place the sample in the cup accordingly.

- b. XR samples: cut a piece of tygon tubing as straight as possible (use a blade to cut the tygon, not a knife). Make two triangular-shape incisions at the base of the cylinder to let the trapped air escape more easily when the epoxy is added. Insert the tubing slightly in the tygon support. Place the sample in the cup using the tygon piece as a stand. Use a sample clip to indicate the orientation of the sample (top vs. bottom) and place the sample in the cup accordingly.
5. Wearing gloves, mix 15 mL of low viscosity epoxy mixture per sample mount, in a paper cup, according to manufacturers mixing guidelines. Do not prepare more than 75 mL per batch (prepare 70–75 g epoxy).
6. Fill up a syringe with epoxy.
7. Fill all cups with epoxy using the syringe as slowly as possible to avoid trapping gas inside the sample, up to the top of the cup for the XR samples.
8. Place the epoxy mixture and the cups with samples into a vacuum bell jar. Pull vacuum on the bell jar to degas the epoxy mixture. Cycle pressure between atmospheric and vacuum to remove bubbles from the epoxy. Modulate the vacuum to prevent the boiling of epoxy (no longer than 15–20s under vacuum conditions). The operation should be repeated 5 to 10 times depending on how easy the gas trapped in the samples is withdrawn. Vent the bell jar, and then fill each sample cup to 5 mm from the cup top. Pull vacuum on the bell jar until the samples are completely degassed (ca. 10-15 min.), then vent the bell jar.
9. After curing the epoxy mounts (24 hrs), remove the mounts from the sample cups and identify the sides with the notebook-page-sample format.

Step2: Polishing the samples:

For the following steps, the “back face” corresponds to:

- a. the face at the bottom of the cup (tygon tubing side) for XL samples,
- b. the face at the top of the epoxy cup for both XR samples.

For the following steps, the “front face” corresponds to the opposite of the "back face".

10. Write the sample ID with a marker on the back face and the front face for samples XL and XR, respectively. Place the samples in the plate head of the polishing machine.
11. Grind the samples using 120 grit SiC abrasive paper on a rotary grinder at 350 rpm speed with water cooling using 12 lbs. pressure during 30s–1min (polishing check step). During the polishing check, if the head is rotating in the z-direction (gravity), the surface won't be flat. If this happens, untighten the samples and tighten them again to avoid the rotational motion. Rotating the mount and applying a light pressure during grinding will help to keep the sample plane and perpendicular.
12. Repeat the grinding for 2–3 min following the previous step in order to get a rough flat surface. Dry the samples and write their names on the polished surface. Set up the samples in the polishing machine head to grind the faces which will be analyzed by SEM.
13. Repeat step 10.
14. Set up the grinding time to 10 min. Repeat this step using 15 lbs. pressure as long as needed until both samples are visible (XL sample is always taken as a reference). A fairly estimated time is around 1hrs 40 min. The metal surface of the sample should

be grinded and the epoxy inside the sample should be visible all along the cross section.

15. Grind the samples using:

- a. 180 grit SiC abrasive paper on rotary grinder at 300 rpm speed with water cooling using 8 lbs. pressure during twice 10 min.
- b. 240 grit SiC abrasive paper on rotary grinder at 300 rpm speed with water cooling using 8 lbs. pressure during 15 min, then at 250 rpm speed with water cooling using 5 lbs. pressure during 15 min.
- c. 320 grit SiC abrasive paper on rotary grinder at 250 rpm speed with water cooling using 5 lbs. pressure during 10 min, then using 6 lbs. pressure during 5 min.
- d. 400 grit SiC abrasive paper on rotary grinder at 250 rpm speed with water cooling using 5 lbs. pressure during twice 5 min.
- e. Grind with each grit size until scratches from the previous grinding step are completely removed (1–2 min.).

16. Dry the samples with a paper towel and replace SiC paper on grinding wheel with silk cloth. Apply 9 μm water based diamond abrasive to cloth and begin the coarse polishing using 150 rpm wheel speed and 8 lbs. pressure. Continue the coarse polishing step until all grinding scratches from the 400 grit step are removed (2 times 5 min).

- a. During polishing, replenish the diamond suspension as needed to keep the cloth damp with suspension.

17. Clean the sample mount of all the polishing suspension using cotton batting and DI water (do not use tap water), and dry with nitrogen.
18. Replace the silk cloth on polishing wheel by a non-woven textile. Apply 3 μ m water based diamond abrasive to the cloth and begin the intermediate polishing using 150 rpm speed and 5 lbs. pressure. Continue the intermediate polishing step until all polishing scratches from the 9 μ m polishing step are removed (6 to 9 min by series of 3 min).
 - a. Clean the sample mount of all the polishing suspension using cotton batting and DI water and dry with nitrogen.
19. Replace the non-woven cloth on the polishing wheel by a flocked cloth. Apply 0.25 μ m water based diamond abrasive to the cloth and begin the intermediate polishing using 150 rpm speed and 5 lbs. pressure. Continue the intermediate polishing step until all polishing scratches from the 3 μ m polishing step are removed (1 min then 3 min).
 - a. Clean the sample mount of all polishing suspension using cotton batting and DI water and dry with nitrogen.
 - b. Inspect the samples using an optical microscope with reflected light bright field illumination to determine if the polishing is adequate.
20. Gold coat each sample after polishing using a gold coating machine. Follow the procedure accompanying the device for better results. Set up a coating time of 1 min.

21. Store the polished samples in a dessicator to prevent them from rusting. The samples should be analyzed by the SEM/EDX as soon as possible right after the ended preparation despite the presence of the protective gold layer.

APPENDIX B CHEMICAL ANALYSIS OF OIL SAMPLES

Table B.1: Chemical analysis of oil samples (NJ05 to NJ46) after the challenge in the AFR.

| Parameters | TAN (mg KOH / g oil) | | Copper (ppm) | | Iron (ppm) | | Sodium (ppm) | | Nickel (ppm) | | Vanadium (ppm) | | Sulfur (wt%) |
|------------|----------------------|------|--------------|------|------------|------|--------------|------|--------------|------|----------------|------|--------------|
| | Column | Tank | Column | Tank | Column | Tank | Column | Tank | Column | Tank | Column | Tank | Tank |
| Start NJ05 | 3.90 | N/A | N/A | N/A | N/A | N/A | N/A | N/A | N/A | N/A | N/A | N/A | N/A |
| End NJ05 | 3.78 | 3.86 | N/A | N/A | N/A | N/A | N/A | N/A | N/A | N/A | N/A | N/A | N/A |
| End NJ06 | 1.01 | N/A | N/A | N/A | N/A | N/A | N/A | N/A | N/A | N/A | N/A | N/A | N/A |
| End NJ08 | 0.48 | 4.72 | N/A | N/A | N/A | N/A | N/A | N/A | N/A | N/A | N/A | N/A | N/A |
| Start NJ09 | 0.25 | 4.67 | N/A | N/A | N/A | N/A | N/A | N/A | N/A | N/A | N/A | N/A | N/A |
| End NJ09 | 0.41 | 4.68 | N/A | N/A | N/A | N/A | N/A | N/A | N/A | N/A | N/A | N/A | N/A |
| End NJ10 | 0.39 | 4.68 | N/A | N/A | N/A | N/A | N/A | N/A | N/A | N/A | N/A | N/A | N/A |
| End NJ11 | 0.16 | 5.04 | 0.2 | 0.2 | 2.4 | 31.9 | <0.1 | <0.1 | 0.1 | 0.2 | <0.1 | <0.1 | N/A |
| Start NJ12 | 0.09 | 5.04 | <0.1 | N/A | 0.4 | N/A | <0.1 | N/A | <0.1 | N/A | <0.1 | N/A | N/A |
| End NJ12 | 0.27 | 4.64 | <0.1 | 0.2 | 0.2 | 39.9 | <0.1 | <0.1 | <0.1 | 0.2 | <0.1 | <0.1 | N/A |
| End NJ13 | 0.34 | 4.43 | <0.1 | 0.1 | 0.2 | 46.3 | <0.1 | <0.1 | <0.1 | 0.2 | <0.1 | <0.1 | N/A |
| Start NJ14 | 6.35 | 4.43 | <0.1 | N/A | 0.5 | N/A | <0.1 | N/A | <0.1 | N/A | <0.1 | N/A | N/A |
| End NJ14 | 4.22 | 5.15 | <0.1 | 0.1 | 3.8 | 55.6 | <0.1 | <0.1 | 0.1 | 0.2 | <0.1 | <0.1 | N/A |
| Start NJ15 | 0.05 | 3.80 | <0.1 | <0.1 | 0.2 | 1.2 | <0.1 | <0.1 | 0.2 | <0.1 | <0.1 | <0.1 | 0.0016 |
| End NJ15 | 0.14 | 3.78 | 0.2 | 0.1 | 0.3 | 8.1 | <0.1 | <0.1 | 0.1 | <0.1 | <0.1 | <0.1 | 0.0015 |
| End NJ16 | 0.14 | 3.90 | <0.1 | <0.1 | 0.3 | 10.3 | <0.1 | <0.1 | 0.2 | <0.1 | <0.1 | <0.1 | 0.0015 |
| End NJ17 | 0.20 | 3.91 | <0.1 | <0.1 | 0.2 | 12.8 | <0.1 | <0.1 | 0.1 | <0.1 | <0.1 | <0.1 | 0.0019 |
| Start NJ24 | 0.40 | 0.30 | 1.6 | 0.1 | 0.3 | 12.2 | <0.1 | <0.1 | 0.5 | 0.4 | <0.1 | <0.1 | N/A |
| End NJ24 | 0.37 | 3.86 | 0.2 | 0.1 | 0.4 | 14.2 | <0.1 | <0.1 | 0.5 | 0.6 | <0.1 | <0.1 | 0.0012 |
| End NJ25 | 0.36 | 3.68 | 0.5 | 0.1 | 0.3 | 17.3 | <0.1 | <0.1 | 0.6 | 0.4 | <0.1 | <0.1 | 0.0012 |
| End NJ26 | <0.05 | 3.66 | 0.2 | 0.1 | 0.2 | 21.4 | <0.1 | <0.1 | 0.3 | 0.4 | <0.1 | <0.1 | 0.0012 |

Table B.1: continued.

| Parameters | TAN (mg KOH / g oil) | | Copper (ppm) | | Iron (ppm) | | Sodium (ppm) | | Nickel (ppm) | | Vanadium (ppm) | | Sulfur (wt%) |
|---------------|-------------------------|------|--------------|------|------------|------|--------------|------|--------------|------|-------------------|------|-----------------|
| | Column | Tank | Column | Tank | Column | Tank | Column | Tank | Column | Tank | Column | Tank | Tank |
| End NJ27 | <0.05 | 3.64 | 0.2 | 0.1 | 0.2 | 24.9 | <0.1 | <0.1 | 0.4 | 0.4 | <0.1 | <0.1 | 0.0012 |
| End NJ28 | 0.38 | 3.68 | 0.2 | 0.2 | <0.1 | 28.4 | <0.1 | <0.1 | <0.1 | 0.1 | <0.1 | <0.1 | 0.0011 |
| End NJ29 | 0.27 | 3.72 | 0.2 | 0.2 | <0.1 | 31.7 | <0.1 | <0.1 | <0.1 | <0.1 | <0.1 | <0.1 | 0.0011 |
| End NJ30 | 0.38 | 3.66 | 0.2 | 0.2 | <0.1 | 36.2 | <0.1 | <0.1 | <0.1 | <0.1 | <0.1 | <0.1 | 0.0011 |
| End NJ31 | 0.43 | 3.63 | 0.2 | 0.2 | <0.1 | 38.1 | <0.1 | <0.1 | <0.1 | 0.1 | <0.1 | <0.1 | 0.0011 |
| Start NJ32 | 0.1 | 1.84 | 0.1 | 0.1 | <0.1 | 0.5 | <0.1 | <0.1 | <0.1 | <0.1 | <0.1 | <0.1 | 0.0007 |
| End NJ32 | 0.08 | 1.89 | 0.2 | <0.1 | 0.1 | 3 | <0.1 | <0.1 | <0.1 | <0.1 | <0.1 | <0.1 | 0.0007 |
| End NJ33 | N/A | 1.97 | N/A | <0.1 | N/A | 4.9 | N/A | <0.1 | N/A | <0.1 | N/A | <0.1 | 0.0006 |
| End NJ34 | N/A | 2.07 | N/A | <0.1 | N/A | 6.1 | N/A | <0.1 | N/A | <0.1 | N/A | <0.1 | 0.0005 |
| End NJ35 | N/A | 1.97 | N/A | <0.1 | N/A | 6.5 | N/A | <0.1 | N/A | <0.1 | N/A | <0.1 | 0.0006 |
| End NJ36 | N/A | 2.02 | N/A | <0.1 | N/A | 7.3 | N/A | <0.1 | N/A | <0.1 | N/A | <0.1 | 0.0005 |
| End NJ37 | N/A | 1.85 | N/A | 0.1 | N/A | 7.7 | N/A | <0.1 | N/A | <0.1 | N/A | <0.1 | 0.0006 |
| End NJ39 | N/A | 1.72 | N/A | 0.2 | N/A | 9.2 | N/A | <0.1 | N/A | 0.1 | N/A | <0.1 | 0.0009 |
| End NJ40 | N/A | 1.75 | N/A | 0.2 | N/A | 10.9 | N/A | <0.1 | N/A | 0.1 | N/A | <0.1 | 0.0008 |
| End NJ41 | N/A | 1.92 | N/A | 0.2 | N/A | 11.2 | N/A | <0.1 | N/A | 0.1 | N/A | <0.1 | 0.0007 |
| End NJ42 | N/A | 1.71 | N/A | 0.2 | N/A | 11.7 | N/A | <0.1 | N/A | 0.1 | N/A | <0.1 | 0.0007 |
| Start NJ43 | 2.69 | 1.93 | 0.2 | 0.2 | 0.1 | 0.4 | <0.1 | <0.1 | 0.2 | 0.2 | <0.1 | <0.1 | 0.0006 |
| NJ43 (15 min) | N/A | 5.24 | N/A | 0.3 | N/A | 8.2 | N/A | <0.1 | N/A | 0.2 | N/A | <0.1 | 0.0013 |
| NJ43 (3 hrs) | N/A | 2.01 | N/A | 0.1 | N/A | 4.3 | N/A | <0.1 | N/A | <0.1 | N/A | <0.1 | 0.0006 |
| End NJ43 | 0.23 | 2.03 | 0.2 | 0.2 | 3.2 | 4.2 | <0.1 | <0.1 | 0.2 | 0.2 | <0.1 | <0.1 | <0.0003 |
| Start NJ44 | N/A | 1.83 | N/A | 0.2 | N/A | 0.4 | N/A | <0.1 | N/A | 0.2 | N/A | <0.1 | 0.0006 |
| End NJ44 | N/A | 2.02 | N/A | 0.2 | N/A | 4.1 | N/A | <0.1 | N/A | 0.2 | N/A | <0.1 | 0.0006 |
| End NJ45 | N/A | 1.93 | N/A | <0.1 | N/A | 7.6 | N/A | <0.1 | N/A | <0.1 | N/A | <0.1 | 0.0007 |
| End NJ46 | N/A | 1.99 | N/A | <0.1 | N/A | 9.4 | N/A | <0.1 | N/A | <0.1 | N/A | <0.1 | 0.0007 |

Table B.3: Chemical analysis of oil samples (NJ50 only).

| Parameters | TAN (mg KOH / g oil) | | Copper (ppm) | | Iron (ppm) | | Sodium (ppm) | | Nickel (ppm) | | Vanadium (ppm) | | Sulfur (wt%) |
|-----------------|----------------------|-------|--------------|------|------------|------|--------------|------|--------------|------|----------------|------|--------------|
| | Column | Tank | Column | Tank | Column | Tank | Column | Tank | Column | Tank | Column | Tank | Tank |
| Start NJ50 | 2.81 | 1.91 | <0.1 | <0.1 | <0.1 | <0.1 | <0.1 | <0.1 | <0.1 | <0.1 | <0.1 | <0.1 | N/A |
| #1 - t=15 min | N/A | 47.23 | N/A | <0.1 | N/A | 2.3 | N/A | <0.1 | N/A | <0.1 | N/A | <0.1 | N/A |
| #2 - t=20 min | N/A | 17.04 | N/A | <0.1 | N/A | 6.1 | N/A | <0.1 | N/A | <0.1 | N/A | <0.1 | N/A |
| #11 - t=70 min | N/A | 2.42 | N/A | <0.1 | N/A | 5.1 | N/A | <0.1 | N/A | <0.1 | N/A | <0.1 | N/A |
| #12 - t=75 min | N/A | 2.33 | N/A | <0.1 | N/A | 4.9 | N/A | <0.1 | N/A | <0.1 | N/A | <0.1 | N/A |
| #14 - t=80 min | N/A | 2.29 | N/A | <0.1 | N/A | 4.8 | N/A | <0.1 | N/A | <0.1 | N/A | <0.1 | N/A |
| #15 - t=90 min | N/A | 2.18 | N/A | <0.1 | N/A | 4.7 | N/A | <0.1 | N/A | <0.1 | N/A | <0.1 | N/A |
| #27 - t=150 min | N/A | 2.02 | N/A | <0.1 | N/A | 4.2 | N/A | <0.1 | N/A | <0.1 | N/A | <0.1 | N/A |
| #28 - t=155 min | N/A | 1.99 | N/A | <0.1 | N/A | 4.2 | N/A | <0.1 | N/A | <0.1 | N/A | <0.1 | N/A |
| #30 - t=165 min | N/A | 1.99 | N/A | <0.1 | N/A | 4.2 | N/A | <0.1 | N/A | <0.1 | N/A | <0.1 | N/A |
| #31 - t=170 min | N/A | 1.98 | N/A | <0.1 | N/A | 4.2 | N/A | <0.1 | N/A | <0.1 | N/A | <0.1 | N/A |
| #43 - t=230 min | N/A | 2.05 | N/A | <0.1 | N/A | 4.1 | N/A | <0.1 | N/A | <0.1 | N/A | <0.1 | N/A |
| #44 - t=235 min | N/A | 2.20 | N/A | <0.1 | N/A | 4.0 | N/A | <0.1 | N/A | <0.1 | N/A | <0.1 | N/A |
| #46 - t=245 min | N/A | 2.15 | N/A | <0.1 | N/A | 4.1 | N/A | <0.1 | N/A | <0.1 | N/A | <0.1 | N/A |
| #47 - t=250 min | N/A | 2.08 | N/A | <0.1 | N/A | 4.0 | N/A | <0.1 | N/A | <0.1 | N/A | <0.1 | N/A |
| #58 - t=305 min | N/A | 2.08 | N/A | <0.1 | N/A | 3.9 | N/A | <0.1 | N/A | <0.1 | N/A | <0.1 | N/A |
| #59 - t=310 min | N/A | 1.93 | N/A | <0.1 | N/A | 4.0 | N/A | <0.1 | N/A | <0.1 | N/A | <0.1 | N/A |
| #61 - t=320 min | N/A | 1.98 | N/A | <0.1 | N/A | 3.9 | N/A | <0.1 | N/A | <0.1 | N/A | <0.1 | N/A |
| #62 - t=325 min | N/A | 1.92 | N/A | <0.1 | N/A | 3.9 | N/A | <0.1 | N/A | <0.1 | N/A | <0.1 | N/A |
| #29 - t=365 min | N/A | 2.06 | N/A | <0.1 | N/A | 3.9 | N/A | <0.1 | N/A | <0.1 | N/A | <0.1 | N/A |
| #29 - t=368 min | 0.36 | 1.88 | N/A | <0.1 | N/A | 3.9 | N/A | <0.1 | N/A | <0.1 | N/A | <0.1 | N/A |

Note: The analytical techniques used are: ASTM D664 for TAN, ICP for metal content, and X-Ray Fluorescence (XRF) for sulfur content.

APPENDIX C UNCERTAINTY ANALYSIS OF THE AFR AND CFR
EXPERIMENTS

Sample average

For all experiments, the sample average \bar{x} is calculated with the following equation:

$$\bar{x} = \frac{1}{n} \sum_i^n x_i \quad (\text{C.1})$$

where n is the sample size.

Random error

The random error Δx_R describes the scatter between the repeated experimental measurements. The errors related to the instrumentation used on the AFR and the CFR are reported in Table C.1 and Table C.2.

When measuring the corrosion rates, limited data is usually generated because the experiments are long, tedious and expensive. In the present study, two to four corrosion rates were measured for each sample type (S/E/M) after each experiment. Therefore, the random error due to the weight loss measurements, which directly concerns the calculation of the random error of corrosion rate, was handled differently: (a) single experiment and (b) multiple experiments.

For a single experiment, the lower boundary of the random error $\Delta x_{R,min}$ was chosen as the smallest value among the observations, while the upper boundary of the

random error $\Delta x_{R,max}$ was chosen as the highest value among the observations.

Mathematically, this can be written as:

$$\Delta x_{R,min} = |\bar{x} - \min(x_i)| \quad (C.2)$$

$$\Delta x_{R,max} = |\bar{x} - \max(x_i)| \quad (C.3)$$

In general, $\Delta x_{R,min}$ and $\Delta x_{R,max}$ are similar within an experiment.

For multiple experiments, the random error was calculated as two standard deviation or 2σ :

$$\Delta x_R = 2\sigma \quad (C.4)$$

$$\sigma = \sqrt{\frac{\sum_i^n (x_i - \bar{x})^2}{n}} \quad (C.5)$$

Systematic error

For all measurements, the systematic error Δx_S was calculated based on the instrument accuracy provided by the supplier. These respective values are given in Table C1 and Table C2 in the column “Systematic error”.

Propagation error

The propagation error Δx_T represents the addition of all random and systematic errors:

$$\Delta x_T = \sqrt{(\Delta x_R^2 + \Delta x_S^2)} \quad (C.6)$$

Table C.1: Propagation error related to the instrumentation used on the AFR and the FTMA.

| Parameter | Instrument | Random error | Systematic error | Propagation error |
|------------------|---------------------------------|---------------|------------------|-------------------|
| Pressure | Pressure gauge (0-20 barg) | ± 0.3 bar | ± 0.5 bar | ± 0.6 bar |
| Pressure | Pressure gauge (0-70 barg) | ± 0.7 bar | ± 1.8 bar | ± 1.9 bar |
| Temperature | Thermocouple/Controller CN7800 | ± 0.5 °C | ± 3.8 °C | ± 3.8 °C |
| Temperature | Thermocouple/Controller CN76000 | ± 0.5 °C | ± 2.8 °C | ± 2.8 °C |
| Temperature | Thermocouple/Controller CN77000 | ± 0.5 °C | ± 0.6 °C | ± 0.8 °C |
| Gas flow rate | Rotameter FL-5681T | ± 0.7 % | ± 3.0 % | ± 3.1 % |
| Gas flow rate | Rotameter FL-5671ST | ± 0.7 % | ± 3.0 % | ± 3.1 % |
| Gas flow rate | Rotameter FL5651G | ± 0.7 % | ± 3.0 % | ± 3.1 % |
| Liquid flow rate | Calibration curve | ± 0.5 % | ± 0.8 % | ± 0.9 % |
| Weight loss | Analytical balance | N/A | ± 0.02 mg | ± 0.02 mg |
| Surface analysis | SEM JEOL 3690 LV | N/A | N/A | N/A |

Table C.2: Propagation error related to the instrumentation used on the CFR.

| Parameter | Instrument | Random error | Systematic error | Propagation error |
|--------------------------|---------------------|--------------|------------------|-------------------|
| Pressure / Pressure drop | Pressure transducer | ± 1.00 % | ± 0.25 % | ± 1.03 % |
| Temperature | Controller | ± 0.1 °C | ± 0.5 °C | ± 0.5 °C |
| Liquid flow rate | Rotameter FL7603 | ± 1.0 % | ± 2.0 % | ± 2.2 % |
| Liquid flow rate | Rotameter FL4403 | ± 1.0 % | ± 4.0 % | ± 4.1 % |
| Gas flow rate | Anemometer HHF92A | N/A | ± 1.1 m/s | ± 1.1 m/s |
| Liquid level (tank) | Graduated ruler | ± 1.0 mm | ± 1.0 mm | ± 1.4 mm |
| Pipe liquid height | Ruler | ± 1.0 mm | ± 2.5 mm | ± 2.7 mm |
| Wetted wall fraction | Taped ruler (mm) | ± 3.0 mm | ± 1.0 mm | ± 3.2 mm |

APPENDIX D SULFIDATION EXPERIMENTAL DATA (FTMA)

Table D.1: Sulfidation reference corrosion rates¹.

| Test ID | Sample ID | Oil flow rate (mL/min) | Corrosion rate (mm/y) | Test ID | Sample ID | Oil flow rate (mL/min) | Corrosion rate (mm/y) |
|---------|-----------|------------------------|-----------------------|---------|-----------|------------------------|-----------------------|
| NJ18 | M1 | 1.5 | 0.25 | NJ21 | E1 | 1.5 | 0.39 |
| NJ18 | M2 | 1.5 | 0.49 | NJ21 | E2 | 1.5 | 0.32 |
| NJ18 | M3 | 1.5 | 0.69 | NJ21 | S1 | 1.5 | 0.44 |
| NJ18 | M4 | 2.5 | 0.59 | NJ21 | S2 | 1.5 | 0.33 |
| NJ19 | M1 | 1.5 | 0.32 | NJ22 | M1 | 1.5 | 0.26 |
| NJ19 | M2 | 1.5 | 0.59 | NJ22 | M2 | 1.5 | 0.50 |
| NJ19 | M3 | 1.5 | 0.93 | NJ22 | M3 | 1.5 | 0.55 |
| NJ19 | M4 | 1.5 | 0.93 | NJ22 | M4 | 1.5 | 0.50 |
| NJ19 | E1 | 1.5 | 0.45 | NJ22 | S1 | 1.5 | 0.35 |
| NJ19 | E2 | 1.5 | 0.66 | NJ22 | S2 | 1.5 | 0.27 |
| NJ19 | S1 | 1.5 | 0.38 | NJ23 | M1 | 1.5 | 0.34 |
| NJ19 | S2 | 1.5 | 0.35 | NJ23 | M2 | 1.5 | 0.49 |
| NJ20 | M1 | 1.5 | 0.36 | NJ23 | M3 | 1.5 | 0.66 |
| NJ20 | M2 | 1.5 | 0.55 | NJ23 | M4 | 1.5 | 0.60 |
| NJ20 | M3 | 1.5 | 0.73 | NJ23 | E1 | 1.5 | 0.37 |
| NJ20 | M4 | 1.5 | 0.58 | NJ23 | E2 | 1.5 | 0.36 |
| NJ20 | E1 | 1.5 | 0.40 | NJ23 | S1 | 1.5 | 0.33 |
| NJ20 | E2 | 1.5 | 0.44 | NJ23 | S2 | 1.5 | 0.27 |
| NJ20 | S1 | 1.5 | 0.62 | NJ38 | M2 | 1.6 | 0.45 |
| NJ20 | S2 | 1.5 | 0.41 | NJ38 | M4 | 1.6 | 0.47 |
| NJ21 | M1 | 1.5 | 0.30 | NJ38 | E1 | 1.6 | 0.41 |
| NJ21 | M2 | 1.5 | 0.53 | NJ38 | E2 | 1.6 | 0.41 |
| NJ21 | M3 | 1.5 | 0.85 | NJ38 | S2 | 1.6 | 0.39 |
| NJ21 | M4 | 1.5 | 0.64 | | | | |

¹ The operating conditions are exclusively based on the test matrix provided in Table 3.2.

APPENDIX E PURE NAP CORROSION EXPERIMENTAL DATA (AFR)

Table E.1: Corrosion rates in single phase flow conditions.

| Test ID | Number of samples | Sample geometry (-) | TAN (mg KOH / g oil) | Pressure (bar) | Temperature (°C) | U_{SG} (m/s) | U_{SL} (m/s) | Corrosion rate (mm/y) | Corrosion rate error (mm/y) |
|---------|-------------------|---------------------|----------------------|----------------|------------------|----------------|----------------|-----------------------|-----------------------------|
| NJ09 | 2 | Straight | 4 | 3.1 | 319 | N/A | 0.12 | 14.41 | 0.39 |
| NJ10 | 2 | Straight | 4 | 2.7 | 281 | N/A | 0.11 | 8.00 | 0.30 |
| NJ11 | 2 | Straight | 4 | 2.8 | 346 | N/A | 0.12 | 12.67 | 0.31 |
| NJ12 | 2 | Straight | 4 | 3.2 | 347 | N/A | 0.11 | 11.16 | 0.11 |
| NJ13 | 2 | Straight | 4 | 3.4 | 348 | N/A | 0.12 | 10.56 | 0.41 |
| NJ14 | 2 | Straight | 4 | 3.4 | 351 | N/A | 0.12 | 13.39 | 0.41 |
| NJ15 | 2 | Straight | 4 | 3.0 | 348 | N/A | 0.12 | 13.92 | 0.08 |
| NJ32 | 2 | Straight | 2 | 3.8 | 344 | N/A | 0.12 | 5.59 | 0.06 |
| NJ33 | 2 | Straight | 2 | 3.8 | 344 | N/A | 0.12 | 5.17 | 0.23 |
| NJ34 | 2 | Straight | 2 | 4.1 | 344 | N/A | 0.12 | 4.52 | 0.25 |
| NJ43 | 2 | Straight | 2 | 3.0 | 343 | N/A | 0.12 | 5.22 | 0.05 |
| NJ44 | 2 | Straight | 2 | 1.0 | 343 | N/A | 0.12 | 6.10 | 0.19 |
| NJ45 | 2 | Straight | 2 | 1.4 | 343 | N/A | 0.12 | 5.41 | 0.07 |
| NJ46 | 2 | Straight | 2 | 6.5 | 343 | N/A | 0.12 | 4.91 | 0.21 |
| NJ47 | 2 | Straight | 2 | 2.9 | 343 | N/A | 0.12 | 4.23 | 0.00 |
| NJ48 | 2 | Straight | 2 | 3.5 | 344 | N/A | 0.12 | 5.29 | 0.46 |
| NJ49 | 2 | Straight | 2 | 3.5 | 344 | N/A | 0.12 | 5.68 | 0.45 |
| NJ50 | 2 | Straight | 2 | 3.4 | 343 | N/A | 0.12 | 5.24 | 0.22 |

Table E.2: Corrosion rates in multiphase flow conditions.

| Test ID | Number of samples | Sample geometry (-) | TAN (mg KOH / g oil) | Pressure (bar) | Temperature (°C) | U_{SG} (m/s) | U_{SL} (m/s) | Corrosion rate (mm/y) | Corrosion rate error (mm/y) |
|---------|-------------------|---------------------|----------------------|----------------|------------------|----------------|----------------|-----------------------|-----------------------------|
| GB123 | 3 | Straight | 4 | 5.3 | 328 | 18.6 | 0.20 | 4.54 | 0.85 |
| GB124 | 3 | Straight | 4 | 5.2 | 323 | 19.0 | 0.20 | 5.33 | 0.51 |
| GB125 | 3 | Straight | 4 | 5.2 | 310 | 18.6 | 0.20 | 5.16 | 0.27 |
| GB126 | 3 | Straight | 4 | 4.5 | 334 | 22.9 | 0.20 | 4.52 | 0.33 |
| NJ01 | 3 | Straight | 4 | 4.4 | 337 | 23.5 | 0.20 | 5.71 | 0.32 |
| NJ08 | 3 | Straight | 4 | 5.3 | 332 | 20.8 | 0.26 | 5.33 | 0.47 |
| NJ09 | 3 | Straight | 4 | 3.5 | 342 | 19.4 | 0.12 | 2.24 | 0.37 |
| NJ10 | 3 | Straight | 4 | 3.1 | 322 | 17.4 | 0.11 | 1.92 | 0.07 |
| NJ11 | 3 | Straight | 4 | 2.8 | 342 | 18.6 | 0.12 | 2.66 | 0.11 |
| NJ12 | 3 | Straight | 4 | 2.6 | 339 | 19.8 | 0.11 | 2.39 | 0.26 |
| NJ13 | 3 | Straight | 4 | 2.8 | 340 | 22.2 | 0.12 | 1.84 | 0.05 |
| NJ14 | 3 | Straight | 4 | 2.6 | 340 | 26.2 | 0.12 | 1.99 | 0.22 |
| NJ15 | 3 | Straight | 4 | 2.9 | 341 | 25.5 | 0.12 | 2.17 | 0.18 |
| NJ29 | 4 | Straight | 4 | 2.9 | 341 | 22.9 | 0.12 | 2.69 | 1.18 |
| NJ29 | 2 | 90° Elbow | 4 | 2.9 | 343 | 23.5 | 0.12 | 1.43 | 0.10 |
| NJ30 | 4 | Straight | 4 | 2.8 | 341 | 22.3 | 0.12 | 1.90 | 0.29 |
| NJ30 | 2 | 90° Elbow | 4 | 2.8 | 343 | 22.4 | 0.12 | 1.92 | 0.08 |
| NJ31 | 4 | Straight | 4 | 2.7 | 340 | 24.7 | 0.12 | 1.74 | 0.50 |
| NJ31 | 2 | 90° Elbow | 4 | 2.7 | 343 | 23.7 | 0.12 | 1.48 | 0.26 |
| NJ32 | 4 | Straight | 2 | 3.6 | 341 | 19.3 | 0.12 | 1.72 | 0.22 |
| NJ32 | 2 | 90° Elbow | 2 | 3.6 | 343 | 19.3 | 0.12 | 1.73 | 0.03 |
| NJ33 | 4 | Straight | 2 | 3.6 | 341 | 19.5 | 0.12 | 1.48 | 0.13 |
| NJ33 | 2 | 90° Elbow | 2 | 3.6 | 343 | 19.1 | 0.12 | 1.52 | 0.04 |
| NJ34 | 4 | Straight | 2 | 3.4 | 341 | 20.1 | 0.12 | 1.35 | 0.48 |
| NJ34 | 2 | 90° Elbow | 2 | 3.4 | 343 | 19.7 | 0.12 | 1.55 | 0.15 |
| NJ39 | 4 | Straight | 2 | 2.4 | 341 | 9.8 | 0.12 | 1.65 | 0.08 |
| NJ39 | 2 | 90° Elbow | 2 | 2.4 | 343 | 10.3 | 0.12 | 1.61 | 0.08 |
| NJ40 | 4 | Straight | 2 | 2.2 | 342 | 10.6 | 0.12 | 1.66 | 0.42 |
| NJ40 | 2 | 90° Elbow | 2 | 2.2 | 343 | 10.6 | 0.12 | 1.50 | 0.08 |

Table E.2: continued.

| Test No. | Number of samples | Sample geometry (-) | TAN (mg KOH / g oil) | Pressure (bar) | Temperature (°C) | U _{SG} (m/s) | U _{SL} (m/s) | Corrosion rate (mm/y) | Corrosion rate error (mm/y) |
|----------|-------------------|---------------------|----------------------|----------------|------------------|-----------------------|-----------------------|-----------------------|-----------------------------|
| NJ43 | 4 | Straight | 2 | 3.0 | 343 | 8.4 | 0.12 | 2.22 | 0.27 |
| NJ43 | 2 | 90° Elbow | 2 | 3.0 | 343 | 8.4 | 0.12 | 2.15 | 0.16 |
| NJ44 | 4 | Straight | 2 | 1.0 | 346 | 1.5 | 0.12 | 3.56 | 0.16 |
| NJ44 | 2 | 90° Elbow | 2 | 1.0 | 346 | 1.5 | 0.12 | 3.60 | 0.14 |
| NJ45 | 4 | Straight | 2 | 1.0 | 345 | 1.5 | 0.12 | 3.33 | 0.50 |
| NJ45 | 2 | 90° Elbow | 2 | 1.0 | 345 | 1.5 | 0.12 | 3.06 | 0.02 |
| NJ46 | 4 | Straight | 2 | 6.4 | 344 | 32.5 | 0.12 | 1.21 | 0.15 |
| NJ46 | 2 | 90° Elbow | 2 | 6.4 | 344 | 33.3 | 0.12 | 1.16 | 0.40 |
| NJ47 | 4 | Straight | 2 | 2.9 | 343 | 9.6 | 0.12 | 1.79 | 0.04 |
| NJ47 | 2 | 90° Elbow | 2 | 2.9 | 337 | 9.7 | 0.11 | 1.79 | 0.06 |
| NJ48 | 4 | Straight | 2 | 3.5 | 344 | 10.2 | 0.12 | 2.32 | 0.21 |
| NJ48 | 2 | 90° Elbow | 2 | 3.5 | 344 | 10.2 | 0.12 | 2.02 | 0.09 |
| NJ49 | 4 | Straight | 2 | 3.5 | 348 | 10.9 | 0.12 | 2.02 | 0.35 |
| NJ49 | 2 | 90° Elbow | 2 | 3.5 | 346 | 10.9 | 0.12 | 1.92 | 0.05 |
| NJ50 | 4 | Straight | 2 | 3.4 | 345 | 11.9 | 0.12 | 2.06 | 0.17 |
| NJ50 | 2 | 90° Elbow | 2 | 3.4 | 344 | 11.9 | 0.12 | 1.98 | 0.12 |

APPENDIX F PRESULFIDATION-CHALLENGE EXPERIMENTAL DATA (FTMA – AFR)

Table F.1: Corrosion rates in single phase flow conditions.

| Test ID | Number of samples | Sample geometry (-) | TAN (mg KOH / g oil) | Pressure (bar) | Temperature (°C) | U _{SG} (m/s) | U _{SL} (m/s) | Corrosion rate (mm/y) | Corrosion rate error (mm/y) |
|---------|-------------------|---------------------|----------------------|----------------|------------------|-----------------------|-----------------------|-----------------------|-----------------------------|
| NJ25 | 2 | Straight | 4 | 2.9 | 347 | N/A | 0.00 | 5.90 | 2.20 |
| NJ26 | 2 | Straight | 4 | 3.7 | 354 | N/A | 0.00 | 8.78 | 0.25 |
| NJ27 | 2 | Straight | 4 | 3.0 | 346 | N/A | 0.00 | 6.61 | 0.48 |
| NJ28 | 2 | Straight | 4 | 3.0 | 347 | N/A | 0.00 | 6.20 | 1.49 |
| NJ35 | 2 | Straight | 2 | 4.2 | 345 | N/A | 0.00 | 1.93 | 0.24 |
| NJ36 | 1 | Straight | 2 | 4.1 | 344 | N/A | 0.00 | 1.30 | N/A |
| NJ37 | 2 | Straight | 2 | 4.1 | 345 | N/A | 0.00 | 1.37 | 0.31 |
| NJ41 | 1 | Straight | 2 | 2.4 | 346 | N/A | 0.00 | 1.45 | N/A |
| NJ42 | 1 | Straight | 2 | 2.4 | 345 | N/A | 0.00 | 0.92 | N/A |

Table F.2: Corrosion rates in multiphase flow conditions.

| Test ID | Number of samples | Sample geometry (-) | TAN (mg KOH / g oil) | Pressure (bar) | Temperature (°C) | U_{SG} (m/s) | U_{SL} (m/s) | Corrosion rate (mm/y) | Corrosion rate error (mm/y) |
|---------|-------------------|---------------------|----------------------|----------------|------------------|----------------|----------------|-----------------------|-----------------------------|
| NJ24 | 4 | Straight | 4 | 2.6 | 342 | 20.7 | 0.12 | 1.81 | 1.06 |
| NJ24 | 2 | 90° Elbow | 4 | 2.6 | 343 | 23.7 | 0.12 | 1.19 | 0.73 |
| NJ25 | 4 | Straight | 4 | 2.8 | 342 | 24.5 | 0.12 | 1.93 | 0.38 |
| NJ25 | 2 | 90° Elbow | 4 | 2.8 | 344 | 24.6 | 0.12 | 1.40 | 0.34 |
| NJ26 | 4 | Straight | 4 | 3.6 | 346 | 21.1 | 0.12 | 2.21 | 0.83 |
| NJ26 | 2 | 90° Elbow | 4 | 3.6 | 345 | 20.6 | 0.12 | 2.00 | 0.24 |
| NJ27 | 4 | Straight | 4 | 2.8 | 342 | 23.2 | 0.12 | 1.83 | 0.80 |
| NJ27 | 2 | 90° Elbow | 4 | 2.8 | 343 | 22.6 | 0.12 | 1.62 | 0.36 |
| NJ28 | 4 | Straight | 4 | 2.6 | 342 | 24.5 | 0.12 | 1.98 | 0.75 |
| NJ28 | 2 | 90° Elbow | 4 | 2.6 | 343 | 23.8 | 0.12 | 1.22 | 0.25 |
| NJ35 | 3 | Straight | 2 | 3.8 | 341 | 18.3 | 0.12 | 1.81 | 1.05 |
| NJ35 | 2 | 90° Elbow | 2 | 3.8 | 343 | 18.3 | 0.12 | 1.09 | 0.25 |
| NJ36 | 4 | Straight | 2 | 3.6 | 342 | 19.0 | 0.12 | 1.37 | 0.39 |
| NJ36 | 2 | 90° Elbow | 2 | 3.6 | 343 | 18.8 | 0.12 | 1.33 | 0.25 |
| NJ37 | 3 | Straight | 2 | 3.6 | 342 | 19.0 | 0.12 | 1.44 | 0.28 |
| NJ37 | 2 | 90° Elbow | 2 | 3.6 | 343 | 19.9 | 0.12 | 1.53 | 0.22 |
| NJ41 | 3 | Straight | 2 | 2.4 | 342 | 10.3 | 0.12 | 1.72 | 0.73 |
| NJ41 | 2 | 90° Elbow | 2 | 2.4 | 344 | 10.6 | 0.12 | 0.98 | 0.23 |
| NJ42 | 3 | Straight | 2 | 2.4 | 342 | 10.9 | 0.12 | 1.69 | 0.62 |
| NJ42 | 2 | 90° Elbow | 2 | 2.4 | 343 | 10.4 | 0.12 | 1.35 | 0.20 |

APPENDIX G CALCULATION OF THE SUPERFICIAL GAS VELOCITY (AFR)

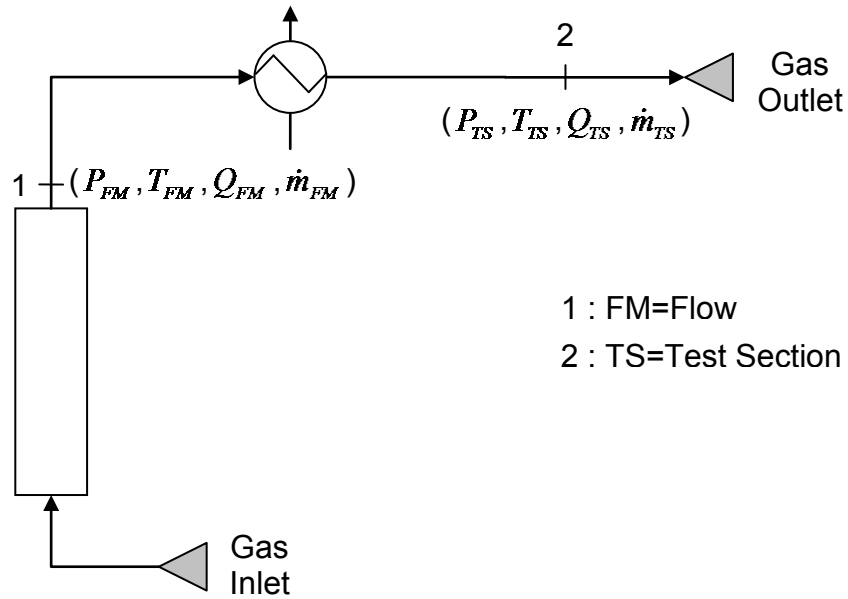


Figure G.1: Simplified P&F Diagram of the main AFR gas line.

Step 1: Calculation of the gas flow rate under standard conditions at the flow meter:

$$Q_{FM}^0 = \frac{h_{exp}}{h_{max}} \cdot Q_{FM,max} \quad (G1)$$

where Q_{FM}^0 is the gas flow rate at the flow meter location under standard conditions (mL/min), h_{exp} is the actual reading at the flow meter (-), h_{max} is the maximum reading at the flow meter ($h_{max} = 150$), and $Q_{FM,max}$ is the maximum flow rate value for the air flow meters (mL/min):

$$\text{for FL-5681T-HRV, } Q_{FM,max} = 66370 \text{ mL/min;}$$

for FL-5671ST-HRV, $Q_{FM,max} = 17810$ mL/min;

for FL5651G-HRV, $Q_{FM,max} = 2290$ mL/min.

Step 2: Calculation of the gas flow rate at the flow meter Q_{FM}

Using the formula given for the FL3000 series rotameters (Omega Engineering Inc., 2010) applied to the gas phase:

$$Q_a = Q_G \sqrt{SG \frac{T_a P^0}{T^0 P_a}} \quad (G2)$$

where Q_a is the equivalent air flow scale reading at standard conditions (mL/min), Q_G is the true flow of metered gas (mL/min), SG is the specific gravity of metered gas (for CO₂, $SG = 1.526$), T_a is the absolute temperature at flow conditions (deg R), and P_a is the pressure at flow conditions (psia). For this specific equation, the standard conditions P^0 and T^0 are taken as $P^0 = 14.7$ psia and $T^0 = 530$ R.

The gas flow rate at the flow meter location Q_{FM} (equivalent to Q_a in eq G2) is calculated with the relationship:

$$Q_{FM} = Q_{FM}^0 \left(SG \frac{T_{FM} P^0}{T^0 P_{FM}} \right)^{1/2} \quad (G3)$$

where Q_{FM} is the gas flow rate at the flow meter location under experimental conditions (mL/min), T_{FM} is the absolute temperature at flow conditions (R), and P_{FM} is the pressure at flow conditions (psia).

Step 3: Calculation of the gas flow rate at the test section Q_{TS}

Assuming that CO₂ is an ideal gas, the ideal gas law $PV = nRT$ can be applied.

Furthermore, the CO₂ mass flow rate is supposed to be constant between the flow meter location and the test section location, such as:

$$\dot{m}_{TS} = \dot{m}_{FM} \quad (G4)$$

$$Q_{TS} = Q_{FM} \cdot \frac{T_{TS}}{T_{FM}} \cdot \frac{P_{FM}}{P_{TS}} \quad (G5)$$

Step 4: Calculation of the superficial gas velocity U_{SG} at the test section location

The superficial gas velocity U_{SG} is expressed as a function of the pipe cross section A_P :

$$U_{SG,TS} = \frac{Q_{TS}}{A_P} \quad (G6)$$

APPENDIX H CALCULATION OF THE SUPERFICIAL LIQUID VELOCITY (AFR)

Step 1: Calculation of the liquid flow rate in the test section

For each test on the AFR, the liquid flow rate was measured at room temperature and ambient pressure. The physical conditions at the test section during the experiments exhibited much higher temperatures and slightly higher pressures than the atmospheric pressure. At these operating conditions, the liquid density of white oil was, therefore, different as well as the volumetric flow rate Q_L and the superficial liquid velocity U_{SL} .

However, the liquid mass flow rate \dot{m}_L remained constant at any conditions:

$$\dot{m}_{L,exp} = \dot{m}_{L,TS} \quad (H1)$$

where $\dot{m}_{L,exp}$ is the liquid mass flow rate measured at room temperature (kg/s), and $\dot{m}_{L,TS}$ is the liquid mass flow rate in the test section during the experiment.

The liquid mass flow rate measured is given by:

$$\dot{m}_{L,exp} = \rho_{L,exp} \cdot Q_{L,exp} \quad (H2)$$

$$\dot{m}_{L,TS} = \rho_{L,TS} \cdot Q_{L,TS} \quad (H3)$$

In one experiment (NJ17), the room temperature and the ambient pressure conditions were $T = 21 \text{ }^\circ\text{C}$ and $P = 1.013 \text{ bar}$, respectively. The liquid flow rate measured was $Q_L = 85 \text{ mL/min}$. In the test section, temperature and pressure were $T = 343 \text{ }^\circ\text{C}$ and $P = 2.9 \text{ bar}$. Therefore:

$$\rho_{L,exp} = \rho_L(T = 21 \text{ }^\circ\text{C}) = 872 \text{ kg/m}^3$$

$$Q_{L,exp} = 85 \text{ mL/min}$$

$$\rho_{L,TS} = \rho_L(T = 650^\circ\text{F}) = 683.7 \text{ kg/m}^3$$

we get $Q_{L,TS} = 109$ mL/min.

Step 2: Calculation of the superficial liquid velocity U_{SL} in the test section

The test section is made of carbon steel ¼” tubing with a thickness of 0.035”. The ID tubing is 0.18”. The cross section is: $A_p = 1.64 \cdot 10^{-5}$ m².

Therefore, using the superficial liquid velocity in the test section:

$$U_{SL} = \frac{Q_{L,TS}}{A_p} \quad (\text{H4})$$

we get $U_{SL} = 0.11$ m/s.

APPENDIX I CALIBRATION CURVES OF THE SUPERFICIAL GAS VELOCITY
(CFR)

The calibration curves of superficial gas velocity were determined using the CFR design with collector mouth #3 and different liquid flow rate conditions.

For a given liquid flow rate, several measurements (usually $n = 21$) of the superficial gas velocity were randomly performed at different controller frequencies ν (range 0–60 Hz), which controls the rotating speed of the motor. Then, a linear regression was applied to extract the calibration constant K at each liquid flow rate:

$$U_{SG} = K\nu \quad (II)$$

Table I.1: Empirical constants used for calibrating the superficial gas velocity for a given liquid flow rate.

| Liquid flow rate (GPM) | Superficial liquid velocity (m/s) | Empirical constant K (m/s/Hz) | 95% confidence interval (m/s/Hz) |
|------------------------|-----------------------------------|---------------------------------|----------------------------------|
| 0 | 0 | 1.041 | 0.050 |
| 2 | 0.007 | 1.016 | 0.041 |
| 5 | 0.017 | 0.985 | 0.033 |
| 10 | 0.034 | 0.969 | 0.038 |
| 20 | 0.068 | 0.933 | 0.054 |
| 30 | 0.102 | 0.894 | 0.067 |
| 40 | 0.135 | 0.859 | 0.066 |
| 50 | 0.169 | 0.846 | 0.083 |

APPENDIX J STUDY OF HYDRODYNAMICS – EXPERIMENTAL DATA (CFR)

Table J.1: Flow characteristics and flow patterns observed during the CFR experiments.

| U_{SG} (m/s) | U_{SL} (m/s) | T (°C) | P (kPa) | ρ_L (kg/m ³) | ρ_G (kg/m ³) | ΔP (kPa) | h_L (m) | Θ_L (-) | FE (%) | Flow pattern | Flow observations |
|-------------------|-------------------|-----------|------------|----------------------------------|----------------------------------|---------------------|--------------|-------------------|-----------|-----------------|--|
| 15.0 | 0.000 | 17.3 | 101.9 | 954.0 | 1.21 | 0.059 | - | - | - | Gas | Single gas phase flow |
| 20.0 | 0.000 | 16.8 | 102.3 | 956.0 | 1.24 | 0.123 | - | - | - | Gas | Single gas phase flow |
| 25.0 | 0.000 | 16.8 | 102.8 | 958.0 | 1.21 | 0.197 | - | - | - | Gas | Single gas phase flow |
| 30.0 | 0.000 | 17.7 | 103.4 | 958.0 | 1.21 | 0.281 | - | - | - | Gas | Single gas phase flow |
| 40.0 | 0.000 | 20.5 | 104.8 | 954.0 | 1.20 | 0.503 | - | - | - | Gas | Single gas phase flow |
| 50.0 | 0.000 | 29.3 | 106.7 | 961.0 | 1.22 | 0.760 | - | - | - | Gas | Single gas phase flow |
| 55.0 | 0.000 | 36.7 | 107.7 | 952.0 | 1.21 | 0.913 | - | - | - | Gas | Single gas phase flow |
| 60.0 | 0.000 | 42.7 | 108.8 | 954.0 | 1.19 | 1.060 | - | - | - | Gas | Single gas phase flow |
| 15.0 | 0.007 | 29.5 | 101.9 | 951.0 | 1.21 | 0.084 | 0.008 | 0.17 | - | SW | Stratified wavy |
| 20.0 | 0.007 | 25.0 | 102.3 | 948.0 | 1.19 | 0.178 | 0.006 | 0.20 | 3.41 | SW | Stratified wavy |
| 24.2 | 0.007 | 16.7 | 102.8 | 952.0 | 1.21 | 0.266 | 0.006 | 0.21 | - | Onset | Entrainment onset |
| 25.0 | 0.007 | 19.3 | 102.9 | 951.0 | 1.19 | 0.276 | 0.005 | 0.20 | - | SW-E | A few drops at the G/L interface |
| 30.0 | 0.007 | 14.8 | 103.6 | 954.0 | 1.22 | 0.409 | 0.004 | 0.31 | 3.77 | SW-E | Droplets at 0.5D (plenty) |
| 40.0 | 0.007 | 16.2 | 105.2 | 961.0 | 1.23 | 0.725 | 0.003 | 0.75 | 6.62 | SW-E | Rivulets at the top (plenty) |
| 50.0 | 0.007 | 18.8 | 107.4 | 953.0 | 1.21 | 1.134 | - | 1.00 | 14.54 | SW-AD | Continuous liquid film |
| 55.0 | 0.007 | 21.2 | 108.6 | 956.0 | 1.23 | 1.347 | - | 1.00 | 19.09 | AD | Continuous liquid film |
| 60.0 | 0.007 | 23.1 | 109.8 | 951.0 | 1.21 | 1.544 | - | 1.00 | 25.25 | AD | Continuous liquid film |
| 15.0 | 0.017 | 20.0 | 101.9 | 952.0 | 1.22 | 0.109 | 0.012 | 0.23 | 1.76 | SW | No entrainment |
| 20.0 | 0.017 | 17.0 | 102.4 | 952.0 | 1.22 | 0.217 | 0.010 | 0.24 | 2.83 | SW | A few drops at the G/L interface |
| 22.9 | 0.017 | 13.7 | 102.7 | 952.0 | 1.21 | 0.281 | 0.010 | 0.25 | - | Onset | Entrainment onset |
| 25.0 | 0.017 | 13.7 | 103.0 | 953.0 | 1.22 | 0.345 | 0.009 | 0.31 | - | SW-E | Droplets at 0.5D (plenty); some at the top |
| 30.0 | 0.017 | 13.7 | 103.7 | 952.0 | 1.21 | 0.483 | 0.008 | 0.59 | 4.06 | SW-E | Rivulets at the top (plenty) |

Table J.1: (continued).

| U_{SG} (m/s) | U_{SL} (m/s) | T (°C) | P (kPa) | ρ_L (kg/m ³) | ρ_G (kg/m ³) | ΔP (kPa) | h_L (m) | Θ_L (-) | FE (%) | Flow pattern | Flow observations |
|-------------------|-------------------|-----------|------------|----------------------------------|----------------------------------|---------------------|--------------|-------------------|-----------|-----------------|---|
| 40.0 | 0.017 | 14.7 | 105.6 | 953.0 | 1.22 | 0.873 | 0.006 | 1.00 | 5.22 | SW-AD | Continuous liquid film |
| 50.0 | 0.017 | 17.0 | 108.0 | 953.0 | 1.21 | 1.347 | 0.003 | 1.00 | 8.40 | AD | Continuous liquid film |
| 55.0 | 0.017 | 19.7 | 109.5 | 952.0 | 1.21 | 1.564 | - | 1.00 | 12.87 | AD | Continuous liquid film |
| 15.0 | 0.034 | 19.3 | 101.9 | 950.0 | 1.21 | 0.123 | 0.018 | 0.28 | 1.41 | SW | Stratified wavy |
| 20.0 | 0.034 | 15.7 | 102.4 | 949.0 | 1.22 | 0.256 | 0.015 | 0.29 | 1.72 | SW-E | A few drops at the G/L interface |
| 21.0 | 0.034 | 13.6 | 102.5 | 953.0 | 1.25 | 0.266 | 0.015 | 0.29 | - | Onset | Entrainment onset |
| 25.0 | 0.034 | 13.8 | 103.1 | 949.0 | 1.21 | 0.385 | 0.013 | 0.42 | - | SW-E | Droplets at the top; Rivulets at 0.5D |
| 30.0 | 0.034 | 13.8 | 103.8 | 954.0 | 1.24 | 0.557 | 0.012 | 0.69 | 3.91 | SW-E | Rivulets at the top (plenty) |
| 40.0 | 0.034 | 14.9 | 105.7 | 950.0 | 1.21 | 0.962 | 0.009 | 0.79 | 4.12 | SW-AD | Continuous liquid film |
| 50.0 | 0.034 | 16.6 | 108.3 | 952.0 | 1.24 | 1.425 | 0.007 | 1.00 | 7.40 | AD | Continuous liquid film |
| 55.0 | 0.034 | 18.3 | 109.9 | 952.0 | 1.21 | 1.716 | 0.006 | 1.00 | 9.65 | AD | Continuous liquid film |
| 15.0 | 0.068 | 14.4 | 102.1 | 952.0 | 1.23 | 0.163 | 0.025 | 0.34 | - | SW | A few drops at the G/L interface |
| 19.6 | 0.068 | 13.4 | 102.5 | 952.0 | 1.23 | 0.291 | 0.022 | 0.34 | - | Onset | Entrainment onset |
| 20.0 | 0.068 | 13.5 | 102.6 | 953.0 | 1.23 | 0.301 | 0.022 | 0.34 | - | SW | Droplets at 0.5D (a few); some at the top |
| 25.0 | 0.068 | 13.3 | 103.2 | 949.0 | 1.25 | 0.474 | 0.019 | 0.51 | - | SW-E | Droplets at the top; Rivulets at 0.75D |
| 30.0 | 0.068 | 13.2 | 104.0 | 951.0 | 1.22 | 0.641 | 0.017 | 0.66 | 3.25 | SW-AD | Rivulets at the top (plenty) |
| 40.0 | 0.068 | 13.7 | 106.1 | 950.0 | 1.24 | 1.125 | 0.014 | 0.83 | 5.02 | AD | Continuous liquid film |
| 50.0 | 0.068 | 14.5 | 109.2 | 949.0 | 1.22 | 1.682 | 0.012 | 1.00 | 7.00 | AD | Continuous liquid film |
| 55.0 | 0.068 | 16.8 | 110.2 | 950.0 | 1.23 | 1.983 | 0.009 | 1.00 | 9.92 | AD | Continuous liquid film |
| 15.0 | 0.102 | 16.0 | 102.3 | 955.0 | 1.24 | 0.212 | 0.031 | 0.36 | - | SW | Stratified wavy |
| 18.4 | 0.102 | 13.3 | 102.6 | 952.0 | 1.23 | 0.296 | 0.028 | 0.38 | - | Onset | Entrainment onset |
| 20.0 | 0.102 | 14.0 | 102.8 | 953.0 | 1.24 | 0.355 | 0.027 | 0.38 | - | SW-E | Droplets at 0.5D (a few) |
| 25.0 | 0.102 | 13.3 | 103.6 | 954.0 | 1.25 | 0.552 | 0.023 | 0.71 | - | SW-E | Droplets at the top; Rivulets at 0.5D |
| 30.0 | 0.102 | 13.3 | 104.4 | 954.0 | 1.24 | 0.769 | 0.020 | 0.77 | - | SW-AD | Rivulets at the top (plenty) |
| 40.0 | 0.102 | 13.7 | 106.7 | 952.0 | 1.27 | 1.322 | 0.018 | 1.00 | 6.14 | AD | Continuous liquid film |
| 50.0 | 0.102 | 15.3 | 110.0 | 950.0 | 1.21 | 1.850 | 0.015 | 1.00 | 7.82 | AD | Continuous liquid film |

Table J.1: (continued).

| U_{SG} (m/s) | U_{SL} (m/s) | T (°C) | P (kPa) | ρ_L (kg/m ³) | ρ_G (kg/m ³) | ΔP (kPa) | h_L (m) | Θ_L (-) | FE (%) | Flow pattern | Flow observations |
|-------------------|-------------------|-----------|------------|----------------------------------|----------------------------------|---------------------|--------------|-------------------|-----------|-----------------|--|
| 15.0 | 0.169 | 14.5 | 102.5 | 949.0 | 1.22 | 0.222 | 0.039 | 0.47 | - | SW-E | Droplets at 0.5D (a few) |
| 15.5 | 0.169 | 13.5 | 102.6 | 960.0 | 1.20 | 0.237 | 0.039 | 0.49 | - | Onset | Entrainment onset |
| 20.0 | 0.169 | 14.0 | 103.2 | 963.0 | 1.24 | 0.409 | 0.034 | 0.66 | - | SW-E | Droplets at 0.5D (plenty); some at the top |
| 25.0 | 0.169 | 13.7 | 104.2 | 973.0 | 1.27 | 0.602 | 0.030 | 0.87 | - | SW-AD | Rivulets at the top (plenty) |
| 30.0 | 0.169 | 13.7 | 105.4 | 957.0 | 1.23 | 0.848 | 0.027 | 1.00 | - | AD | Continuous liquid film |
| 40.0 | 0.169 | 13.7 | 108.2 | 959.0 | 1.20 | 1.430 | 0.023 | 1.00 | 10.14 | AD | Continuous liquid film |
| 50.0 | 0.169 | 14.5 | 110.2 | 955.0 | 1.20 | 1.973 | 0.020 | 1.00 | 10.29 | AD | Continuous liquid film |
| 15.0 | 0.135 | 15.0 | 102.4 | 952.0 | 1.26 | 0.222 | 0.036 | 0.45 | - | SW | Stratified wavy |
| 17.6 | 0.135 | 13.6 | 102.8 | 950.0 | 1.20 | 0.296 | 0.033 | 0.45 | - | Onset | Entrainment onset |
| 20.0 | 0.135 | 13.5 | 103.1 | 953.0 | 1.26 | 0.380 | 0.031 | 0.44 | - | SW-E | Droplets at 0.5D (just a few) |
| 25.0 | 0.135 | 13.4 | 104.0 | 952.0 | 1.23 | 0.572 | 0.028 | 0.72 | - | SW-E | Droplets at the top; Rivulets at 0.75D |
| 30.0 | 0.135 | 13.4 | 105.0 | 953.0 | 1.27 | 0.799 | 0.025 | 0.91 | - | SW-AD | Rivulets at the top (plenty) |
| 40.0 | 0.135 | 13.6 | 107.4 | 952.0 | 1.23 | 1.391 | 0.020 | 1.00 | 7.40 | AD | Continuous liquid film |
| 50.0 | 0.135 | 14.7 | 110.2 | 951.0 | 1.26 | 1.948 | 0.016 | 1.00 | 9.20 | AD | Continuous liquid film |

Note: in the “Flow pattern” column SW, Onset, SW-E, SW-AD, and AD respectively stand for Stratified-Wavy, Entrainment Onset, Stratified-Wavy with droplet Entrainment, Stratified-Wavy/Annular-Dispersed (stratified-wavy with a liquid film covering more than half of the pipe perimeter), and Annular-Dispersed.



OHIO
UNIVERSITY

Thesis and Dissertation Services